

# Fundamentals for Routined Utilization of Tomography in Beam Diagnostics

Dissertation  
submitted to attain the degree of doctor of natural science  
at the departement of Physics  
of the Johann Wolfgang Goethe Universität  
Frankfurt am Main

Institute of Applied Phsysics

by  
Hermine Reichau  
from Gummersbach



Frankfurt am Main  
2011

---

**vom Fachbereich Physik der Johann Wolfgang Goethe Universität  
als Dissertation angenommen**

*Dekan:* Prof.Dr. M.Huth

*Gutachter:*

Prof.Dr. U.Ratzinger  
Prof.Dr. J.Struckmeier

*Datum der Disputation:* 08.02.2012

# Grundlagen für die routinemäßige Implementierung der Tomografie in der Stahldiagnose

Dissertation  
zur Erlangung des Doktorgrades der Naturwissenschaften  
vorgelegt beim Fachbereich Physik  
der Johann Wolfgang Goethe Universität  
Frankfurt am Main

Institut für Angewandte Physik

von  
Hermine Reichau  
aus Gummersbach



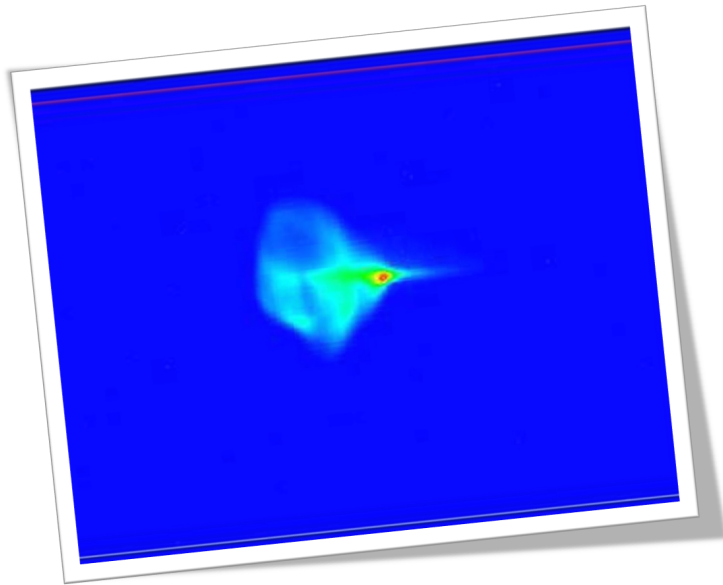
Frankfurt am Main  
2011



To my Parents  
Ilona Eleonore and Jürgen Reichau



Linac beams do not occur in distributions named after  
dead mathematicians...



...but they look like humming birds.  
P.O'Shea/P.Evtushenko





# Contents

<b>Zusammenfassung</b>	i
1 Vorbereitungen für die Tomographie zur Strahldiagnose	iii
2 Tomographie	v
3 Strahltheorie und Analyse	vii
4 Strahlprofilmessung, Emittanzbestimmung und ungewöhnliche Parameter	viii
5 Grundlegende Schritte für die Implementierung einer Strahltomografie	xi
<b>1 Preparations for Beam Diagnostics using Tomography</b>	<b>1</b>
1.1 Review of Tomography for Beam Diagnostics and Outline of Thesis	2
1.2 The Frankfurt Neutron Source (FRANZ)	4
1.3 Diagnostic Device	6
1.3.1 Preliminary Specification of Tomography Environment at FRANZ	7
1.3.2 Rotatable Vacuum Chamber	8
1.4 Object of Measurements	14
1.5 Data Recording and Preprocessing	17
1.6 Diagnostic Pipeline	22
<b>2 Tomography</b>	<b>29</b>
2.1 Properties and Conditions of the Dataset $M_p$	30
2.2 Tomography with Filtered Backprojection	30
2.2.1 Derivation of Algorithm	31
2.2.2 Examples and Representations	36
2.3 Artefacts and Noise	41
2.3.1 Distortions in Fourier Space	42
2.3.2 Filter Performance for Measurement and Simulation	45
2.3.3 Ghost Particles	47
2.3.4 Image Defects	50
2.4 Other Tomography Algorithms in a Nutshell	51
2.4.1 Algebraic Reconstruction Technique	52
2.4.2 Maximum Entropy Method	54
2.5 Comparison of Algorithms	57
2.5.1 Space and Time Requirements	57

## Contents

---

2.5.2	Projections	58
2.5.3	Noise and Image Defects	58
2.5.4	Choosing a Reconstruction Algorithm	59
<b>3</b>	<b>Beam Theory and Analysis</b>	<b>61</b>
3.1	Spaces and Subspaces of six-dimensional Phase Space	62
3.2	Phase Space Ellipse	65
3.3	Ellipse Representations	66
3.3.1	Geometric Representation	66
3.3.2	Courant-Snyder and Parametric Notation	67
3.4	Ellipse Transformations	70
3.4.1	Simple Drift	71
3.4.2	Thin Lens	73
3.4.3	Solenoid	74
3.5	Artificial Beam Edges	78
3.5.1	Fixed ABE's	79
3.5.2	Fractional ABE's	79
3.5.3	IRF-Method	83
<b>4</b>	<b>Beam Profiling</b>	<b>89</b>
4.1	Beam Width	89
4.1.1	Profile Width and Beam Diameter	90
4.1.2	Maximal and Minimal Beam Diameter	91
4.1.3	Diameter Determination for Measurement Data	96
4.2	Beam Position	99
4.2.1	Center of Gravity	99
4.2.2	Direction of Main Axis	100
4.2.3	The Two-Beam Example and the Limits of Optical Diagnosis	103
<b>5</b>	<b>Emittance Determination</b>	<b>107</b>
5.1	Tomography in Phase Space	107
5.2	RMS-Emittance	111
5.3	Discretisation of the RMS-Emittance for Phase Space Tomography	113
5.4	Effective Emittance	114
5.5	Direct Determination of Effective Emittance	115
5.5.1	Effective Emittance with Three Profiles in Longitudinal Direction	118
5.5.2	Effective Emittance with Three Different Focal Lengths of a Thin Lens	119
5.5.3	Effective Emittance with More than Three Profiles	120
5.5.4	Estimation of Expected Angle Resolutions	122
5.6	Determining Effective and RMS-Emittance	130

<b>6</b>	<b>Summary and Outlook</b>	137
<hr/>		
	<b>Appendix</b>	141
<hr/>		
1	Simulated Datasets	141
1.1	Seven-Point Extraction (S1)	141
1.2	Single Direction Projection (S2)	142
1.3	Two Dispersing Beams (S3)	142
2	Measured Datasets	147
2.1	Preliminary Measurement (M1)	147
2.2	First Measurements with Rotatable Vacuum Chamber (M2)	147



# Zusammenfassung

Die Tomographie wurde Ende der 70er Jahre durch Minerbo [Min77] am Los Alamos Scientific Laboratory zum ersten Mal für die Diagnose von Teilchenstrahlen angewendet, fünf Jahre nach der Einführung des ersten kommerziellen, medizinischen Computertomographen. Der entscheidende Unterschied zur medizinischen Tomographie ergab sich aus der wesentlich geringeren Anzahl von Projektionen für die Rekonstruktion. Die Methode der gefilterten Rückprojektion (FBP), die sich direkt aus dem Vortrag Radons [Rad17] und dem darin bereits enthaltenen Fourier-Scheiben-Theorem<sup>1</sup> ergibt, konnte bei einer Anzahl von zwei oder drei Projektionen nicht effektiv angewendet werden. Minerbo bediente sich daher der Methode der Maximalen Entropie (MEM). Ein Jahr später führte Fraser [Fra78] dann auch die Methode der Algebraischen Rekonstruktion (ART) für die Strahltomografie ein. Im Anhang seiner Untersuchungen findet sich ein Beweis dafür, dass für die Rekonstruktion des transversalen Ortsraumes eines Strahls drei Projektionen hinreichend sind. Für die Rekonstruktion des transversalen Phasenraumes mit drei Profilen verweist er auf einen Beweis von Metzger [Met73]. Beide Beweise treffen eine nicht zu unterschätzende Annahme. Für den transversalen Ortsraum wird angenommen, dass der Strahl annähernd eine bivariate Gaussverteilung aufweist. Für die Phasenraumfläche wird die Annahme getroffen, dass die Verteilung in einem Kreis mit dem Radius  $\sqrt{\epsilon\pi}$  (wobei  $\epsilon$  die Emittanz des Strahls ist) enthalten ist. Obwohl diese Annahmen bis heute gängig sind und viele Methoden der Parameterbestimmung mit ihnen arbeiten, treffen sie in den problematischen und interessanten Fällen häufig nicht zu. Durch das Treffen dieser Annahmen verschwindet dann der signifikante Informationsgehalt, und die Analyse dieser Fälle kann entweder nicht durchgeführt werden oder führt zur Fehlinterpretation. Dass die Rekonstruktion zu dieser Zeit und unter diesen Umständen überhaupt durchführbar war und auch zu Strahl Diagnosezwecken eingesetzt wurde [Fra79, Min79, Mot85], war jedoch ein sehr großer Fortschritt. Bald entdeckte man die Möglichkeit den vier-dimensionalen transversalen Phasenraum zu rekonstruieren [Min81]. Die Rekonstruktion des longitudinalen Phasenraums wurde 1987 von Jackson [Jac87] entwickelt, zusammen mit Ideen für eine Online-Tomographie und den Entwurf eines *Phase Space Tomography Monitor* (kurz: PST Monitor). Jackson war überzeugt, dass dieser PST Monitor ideal dazu geeignet wäre, die Bunchdynamik besser und detaillierter über die Rekonstruktion des longitudinalen Phasenraumes zu verstehen. 1993 präsentierte er die Ergebnisse der Implementierung und Messung des PST am Fermi Lab Hauptring [Jac93]. Aufgegriffen wurde die Idee der longitudinalen Phasenraumrekonstruktion jedoch erst 1997 von Hancock und Mane [Han97, Man97] und fand damit in vielen darauffolgenden Veröffentlichungen Einzug. 2001 war ein PST für die longitudinale Online-Tomographie im PS Complex des Cern implementiert. In den Jahren 2000 bis 2009 wurde die Strahltomografie an verschiedenen Orten zur Rekonstruktion der transversalen Phasenräume wie auch des longitudinalen Phasenraumes eingerichtet [Kos01, Hue02, Yak03, Hon05, Hol06, SD06, SD07]. Die Aufnahme der Projektionen erfolgte entweder durch mehrere fixierte CCD-Kameras entlang der Strahlstrecke beziehungsweise an einer longitudinalen Position an drei verschiedenen Ports (Multi-

---

<sup>1</sup>diesen Namen bekam es allerdings erst viel später

Port-Technik (MP)) oder durch die zu dieser Zeit neu eingeführte Technik des Quad-Scan (Quad) bei welcher der Strahl unter Verwendung von drei bis vier Quadrupolen oder zwei Solenoiden gedreht wird. Auf diese Weise kann eine höhere Anzahl von Projektionswinkeln gewonnen werden, die dann mit der wesentlich exakteren Methode der gefilterten Rückprojektion rekonstruiert werden konnten und auch eine Rekonstruktion des transversalen Ortsraumes zuließen. Das Hauptaugenmerk der Entwicklungen in dieser Zeit galt jedoch dem Umgang mit nicht linearen Effekten wie sie von Raumladung oder transversalen Kopplungen in Solenoiden hervorgerufen werden. Dies war deshalb so wichtig, weil die Phasenraumtomografie auf die Anwendung der Transportmatrix angewiesen ist, die sich aus den Matrizen der jeweiligen ionenoptischen Elemente der Strahlstrecke berechnen lässt. Bei der Anwesenheit von Raumladung weicht der tatsächliche Weg der Partikel des Strahls von der berechneten und in der Tomographie verwendeten Transportmatrix ab. Bei der transversalen Kopplung durch Solenoiden ergibt sich das Problem, dass die Transportmatrix zwar für den vier-dimensionalen transversalen Phasenraum gilt, bei der Tomographie aber zwei-dimensionale Unterräume berechnet werden, was nur erlaubt ist, wenn die beiden transversalen Richtungen nicht miteinander gekoppelt sind. Bei der vier-dimensionalen Phasenraumtomografie ergibt sich das Problem ebenfalls, da der vier-dimensionale Raum aus den beiden transversalen zwei-dimensionalen Phasenräumen und optional dem Ortsraum berechnet wird. Hierzu wurden in der angegebenen Literatur zahlreiche Lösungen entwickelt. Trotz all dieser Errungenschaften der letzten 30 Jahre ist die Tomographie bisher keine Standardanwendung für die Strahldiagnose geworden.

Auf der einen Seite hatte man bisher immer die Wahl zwischen einer geringen Anzahl von Projektionen, die sich auf relativ geringem Raum mit der MP-Technik gewinnen ließen, oder einer großen Anzahl von Projektionen, die sich sehr aufwendig und unter großem Platzaufwand durch die Quad-Scan-Technik messen ließen. Zusätzlich fordert die Tomographie ein breites Spektrum an Techniken aus der Mathematik, Informatik, Ionenoptik und Teilchenphysik, so dass erst einmal ein großer Aufwand an Ressourcen benötigt wird.

Auf der anderen Seite wurde trotz des großen Aufwands die Breite der Möglichkeiten der Tomographie bei weitem nicht ausgenutzt. Die meisten Untersuchungen zielten berechtigter Weise darauf ab, eine zerstörungsfreie Emittanzmessmethode zu entwickeln, da diese für hochenergetische Stahlen bis heute ein sehr wichtiges, zu lösendes Problem darstellt.

Die Tomographie unterstützt einerseits eine zerstörungsfreie Form der Strahldiagnose im Beschleunigerbetrieb. Durch die Möglichkeit den sechs-dimensionalen Phasenraum zu rekonstruieren bietet sie die Möglichkeit sowohl transversale Ortsraumparameter wie den Strahldurchmesser, Strahlform und die Strahlposition zu bestimmen, sowie gleichzeitig auch transversale und longitudinale Phasenraumparameter wie die Emittanz, Bunchform und Bunchdurchmesser. Andererseits erlaubt die Tomographie einen tieferen Einblick in die Strahldynamik als jede andere derzeitige Technik. Die Strahldynamik kann einwirkungsfrei beobachtet und analysiert werden, wobei die Genauigkeit der Ergebnisse je nach Analyseziel im Ortsraum über die Anzahl und Wahl der Projektionen und Winkel steuerbar ist, im Phasenraum zusätzlich von der Validität der Transportmatrix oder der Güte ihrer Abschätzung abhängt. Die durch die Tomographie aufbereiteten Daten sind allgemein und flexibel genug, so dass auf ihrer Basis ein breites Spektrum an Untersuchungen möglich ist, die weit über die Bestimmung von Standardparametern hinaus gehen.

Was bisher fehlt, ist eine systematische Prozedur, welche zu einer passenden Konfiguration der Tomographie für eine gegebene Anordnung führt und damit eine routinemäßige Installation und Anwendung

der Tomographie für die Strahldiagnose möglich macht.

In dieser Arbeit werden anhand einer Implementierung der Tomographie für die Frankfurter Neutronenquelle (FRANZ) die grundlegenden Fragen für eine solche systematische Prozedur diskutiert und zusammengefasst.

## 1 Vorbereitungen für die Tomographie zur Strahldiagnose

In einem ersten Schritt muss spezifiziert werden was unter welchen Bedingungen und zu welchem Zweck gemessen werden soll. Die Tomographie am Institut für Angewandte Physik (IAP) soll zum einen im FRANZ-Strahlbetrieb am Ende der Low Energy Beam Transport Section (LEBT) die zum Einschuss in den RFQ benötigten Strahleigenschaften wie Durchmesser, Form, Position, die Ausrichtung der Strahlachse und die Emittanz kontrollierbar machen, zum anderen auch flexibel genug sein um an Testständen eine detaillierte Untersuchung von Strahldynamiken zu unterstützen. Beide Anwendungssituationen sind auf eine einwirkungsfreie Diagnose angewiesen, da im FRANZ-Strahlbetrieb Energien bis 120 keV bei einem Strahlstrom bis 200 mA angestrebt werden und auf der anderen Seite für die Untersuchung von Strahldynamiken diese möglichst wenig bis gar nicht von der Messeinheit beeinflusst werden sollen. So bietet es sich in diesem Fall an, die Tomographie anhand von Projektionen des strahlinduzierten Restgasleuchtens durchzuführen, welches durch eine CCD-Kamera aufgenommen werden. Hierzu wurde kurz gezeigt, dass über die inverse Abeltransformation von der projizierten Leuchtintensität auf die Partikeldichteverteilung geschlossen werden kann. Dies ist wichtig, da in allen weiteren Untersuchungen die Partikeldichte durch die Leuchtintensität substituiert wird.

Die Bedingungen geben vor, welcher Raum und welche Zeit für die geplante Messung zur Verfügung steht, mit direktem Einfluss auf die Art der Tomographie, die später durchgeführt werden kann. Auf engem Raum ließen sich bisher nur wenige Profile durch die MP Technik messen und somit nur ART oder MEM als Rekonstruktionsalgorithmen anwenden. Da aber die Tomographie ebenfalls zur Analyse von Strahldynamik verwendet werden soll, ist eine hohe Anzahl von Profilen und eine Anwendung der FBP wünschenswert, nicht zuletzt da hierüber auch die Genauigkeit wesentlich besser gesteuert werden kann als bei ART und MEM<sup>2</sup>. Um sowohl dem geringen Platz, als auch der hohen Anzahl von Projektionen gerecht zu werden, wurde in Anlehnung an die medizinische Tomographie eine rotierbare Vakuumkammer entworfen, welche über einen Schrittmotor mit weit über 5000 Winkelschritte in einem Winkelbereich von 270° ansteuern kann. Dieser Turn-by-Turn (TbT) Ansatz wurde von Hancock [Han99] Ende der 90er Jahre diskutiert, jedoch nur an Simulationen getestet, da hierzu bisher die entsprechende Meßvorrichtung fehlte. Die in Fig.1 gezeigte rotierbare Vakuumkammer, die in Zusammenarbeit mit der *Neue Technologien GmbH* (NTG) entwickelt wurde, benötigt einen Platz von 351,2 mm entlang der Strahlstrecke und verfügt über eine Vakuumstabilität von mindestens  $10^{-7}$  mbar während der Rotation. Der Tank ist durch einen amorphen elektrolytischen Prozess tief geschwärzt, um auch kleine Reflexionen, welche die Bildaufnahme negativ beeinflussen könnten, zu unterdrücken. Im Anschluss an die Messung müssen die gemessenen Projektionen noch einen Aufbereitungsprozess durchlaufen, in dem die wahre Bildgröße auf die Bildpixel umgerechnet wird und der zusätzlich aufgenommene Hintergrund abgezogen wird. Hinzu kommt, dass mit zunehmendem Abstand der Kamera zum Aufnahmepunkt eine

---

<sup>2</sup>Diese beiden Algorithmen Weisen in der Anzahl der Profile ein Optimum auf. Ist dieses überschritten wird die Rückprojektion wieder zunehmend schlechter. Die Genauigkeit der FBP steigt jedoch mit der Anzahl der Projektionen stetig an, allein begrenzt durch die Bildauflösung.

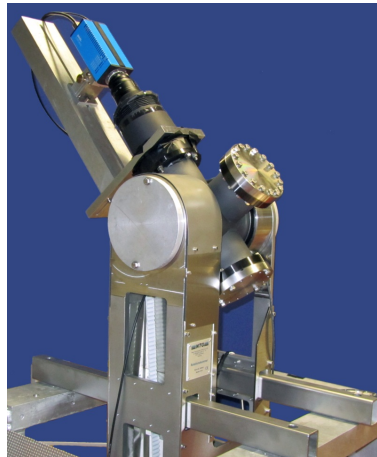


Figure 1: Die rotierbare Vakuumkammer für die Messung von Projektionen mit dem Turn-by-Turn Ansatz.

Vignettierung des Bildes entsteht: das Bild wird zu den Rändern hin abgeschattet<sup>3</sup>. Auf diese Weise wird das Meßergebnis verfälscht und die Zuordnung der Leuchtdichte zur Partikeldichte ist nicht mehr gültig. Die Vignettierung kann standardmäßig durch ein  $\cos^4$ -Filter entfernt werden. Zum Schluss wird die Intensität über das gesamte Bild auf  $[0,1]$  normiert (Fig.2). Durch die Art der Messung

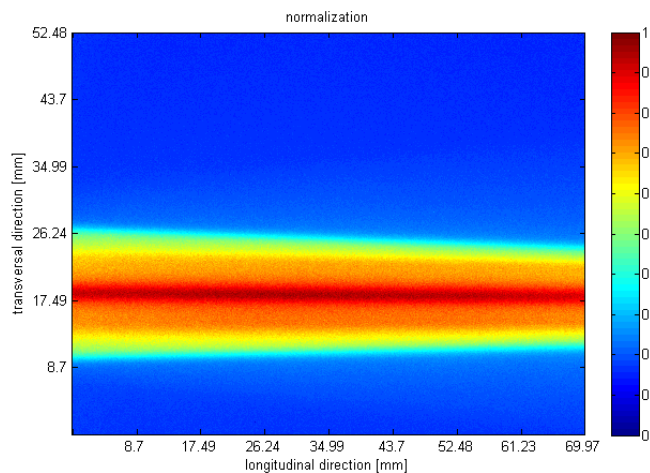


Figure 2: Aufbereitete Projektion einer Messung für die Verwendung in der Tomographie.

sind nun weitere Schritte in der Tomographie festgelegt. Die Tomographie selbst führt noch nicht zu den gewünschten Informationen. Sie ist eine Methode der Datenaufbereitung. Aus den aufbereiteten Daten können dann im weiteren jedoch die Informationen gewonnen werden. Die Art und Quantität

---

<sup>3</sup>Dies kommt dadurch zu stande, dass die Aufnahmesensoren des CCD-Camera-Chips in kleinen Vertiefungen liegen, so können sehr Flach eintreffende Lichtwellen den Sensor nur noch abgeschwächt erreichen



der Information ist dabei abhängig von dem benötigten a priori Wissen und der Wahl der Mikro- und Makroebene und den dazugehörigen Beschränkungen. Setzt man beispielsweise die Ebene der Partikel als Mikroebene ein und die Ebene des drei-dimensionalen Ortsraums als Makroebene, so lassen sich hier aufgrund des Zusammenhangs von Partikeldichte und Leuchtdichte die Parameter Strahldurchmesser und Strahlform bestimmen. Für die Rekonstruktion mittels Tomographie selbst ist kein a priori Wissen über die Partikel oder den drei-dimensionalen Ortsraum nötig. Im abschließenden Abschnitt dieses Kapitels wird zunächst die Diagnose-Pipeline eingeführt, welche den Weg von den gemessenen und aufbereiteten Daten zu den gewünschten Informationen aufzeigt. Dies ist besonders interessant beim Entwickeln neuer Algorithmen für nicht-Standard Parameter, da hier durch die systematische Vorgehensweise ein geeigneter Rahmen vorgegeben wird. Exemplarisch wird hierzu die Bestimmung der Hauptstrahlachse des Strahls gezeigt. Ebenfalls kann auf der Basis des Ebenen-Schemas gut abgeschätzt werden, ob eine Information überhaupt aus den Messdaten gewonnen werden kann. Wählt man beispielsweise die Ebene der Partikel als Mikroebene und die Ebene des drei-dimensionalen Impulsraumes als Makroebene, so lässt sich daraus allein zwar eine Information über die Strahlenveloppe gewinnen, nicht aber über einzelne Trajektorien. Der Grund hierfür ist, dass auf der Mikroebene der Partikel keine Daten über die einzelnen Partikel gegeben sind, sondern nur über Dichten von Partikelensembles. Die direkte Gewinnung ist daher nicht möglich.

Der Verlauf der Arbeit in ihrer Gesamtheit folgt der Diagnose-Pipeline. Zusätzlich wird am Ende ein Entscheidungsschema für die Einrichtung einer Strahltomografie aufgestellt, womit eine Grundlage für die routinemäßige Implementierung der Tomographie zur Strahldiagnose eingeführt wird. Im ersten Kapitel wurde die erste Station, die der Gewinnung und Aufbereitung der Messdaten dient, besprochen. In den folgenden beiden Kapiteln geht es um die zweite Station, in der die Daten zur Extraktion von Informationen durch Tomographie aufbereitet werden, und das nötige a priori Wissen für die Parameterbestimmung zusammen getragen wird. In den beiden letzten Kapiteln geht es um die dritte Station, in welcher die Evaluation und Analyse der Daten zu den gesuchten Informationen führt. Die letzte Station der Diagnose-Pipeline wird in den meisten Anwendungsfällen dann die Verwendung der Information entweder zur Kontrolle der Strahlparameter im Beschleunigerbetrieb oder aber zur Bildung von Modellen und Erkenntnissen zur Strahldynamik bedeuten. In dieser Arbeit wird sie dazu genutzt, die Erkenntnisse über die Anforderungen einer systematischen Prozedur für die Einrichtung und Verwendung der Tomographie für die Strahldiagnose zu evaluieren und zusammen zu fassen.

## 2 Tomographie

Im zweiten Kapitel wird die grundlegende Idee der Tomographie mittels der Herleitung der gefilterten Rückprojektion dargestellt. Diese ist dazu besonders geeignet, da sie unmittelbar die ursprüngliche Idee Radons [Ram71] implementiert. Der zentrale Angelpunkt dabei ist das Fourier-Scheiben-Theorem (Fig.3), welches bereits bei Radon eingeführt und bewiesen wird, jedoch erst viel später mit der Einführung tomografischer Techniken seinen Namen bekam. Die Tomographie ist eine Methode der Datenaufbereitung die eine weitergehende Analyse zur Gewinnung von Informationen darstellt und keine Methode zur Gewinnung von Informationen selbst. Jedoch hängt die Qualität und Quantität der Information die aus den durch die Tomographie aufbereiteten Daten gewonnen werden können erheblich von der Genauigkeit und Richtigkeit der Rücktransformation ab. Eines der wichtigsten zu lösenden Probleme für die gefilterte Rückprojektion ist das Lösen des Filterdilemmas. Durch einen

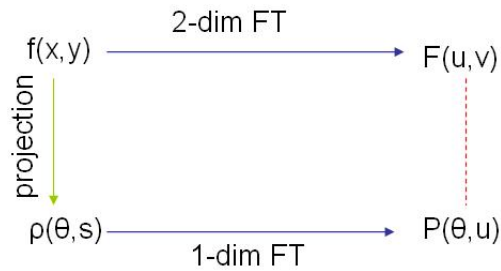


Figure 3: Die Grundlage für jede Form der Tomographie bildet das Fourier-Scheiben-Theorem.

Wechsel von Polarkoordinaten zu kartesischen Koordinaten kommt es zu einer Verzerrung. Diese bewirkt eine Überbetonung niedriger Frequenzen, welche im Fourierraum in der Mitte der Fouriertransformation liegen und große physikalische Abmessungen repräsentieren, und eine Unterbetonung hoher Frequenzen, welche im Fourierraum am Rand der Fouriertransformation liegen und kleine physikalische Abmessungen repräsentieren. Filtert man nun die Fouriertransformation mit einem mathematischen Filter, welches die niedrigen Frequenzen abschwächt und die hohen Frequenzen anhebt, so hebt man gleichzeitig das Rauschen an, welches im Fourierraum gerade im Bereich der hohen Frequenzen angesiedelt ist. Die Wahl des richtigen Filters ist daher sehr entscheidend für die Qualität und Verwendbarkeit des Rekonstruktionsergebnisses. Verschiedene Filter wurden diskutiert. Für die Strahltomografie stellte sich der RamLak-Filter mit Hamming-Fenster am brauchbarsten heraus. Bei einer Anwendung auf Simulations- und Messdaten zeigte sich für die Simulationsdaten kein Unterschied in den untersuchten Filtern, wohl aber bei den Messdaten, welche über ein gewisses Maß an Rauschen verfügen. Interessanter Weise zeigt sich, dass die Wahl des richtigen Filters noch entscheidender für das Rekonstruktionsergebnis ist, als das Entfernen des Hintergrundes (Fig.4). Unterschiedliche Bilddefekte

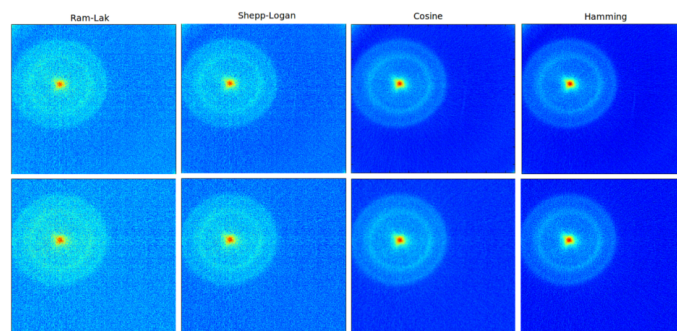


Figure 4: Auswirkungen der verschiedenen untersuchten Filter auf das Rekonstruktionsergebnis im Vergleich zur Entfernung des Hintergrundes.

wurden untersucht, wobei Fehler innerhalb einzelner Projektionen weitaus störendere Auswirkungen auf die Rekonstruktionsqualität zeigen, als das Fehlen ganzer Projektionen. Fehlende Projektionen führen zu Deformationen der Rekonstruktionsergebnisse, ähnlich dem Verwenden nicht äquidistan-

ter Projektionswinkel in der gefilterten Rückprojektion. In Kürze wurden dann sowohl die ART als auch die Methode der MEM der Idee nach eingeführt und die Anwendung der unterschiedlichen Algorithmen diskutiert. Prinzipiell lässt sich sagen, dass die gefilterte Rückprojektion ein hohes Maß an Rekonstruktionsgenauigkeit zulässt, welches über die Anzahl der verwendeten Projektionen gut gesteuert werden kann. Sie braucht eine vergleichsweise hohe Anzahl von Projektionen, jedoch verbessert sich ihr Ergebnis zunehmend mit jeder zusätzlichen Projektion. Sie ist jedoch anfällig für ein niedriges Signal-zu-Rauschverhältnis und benötigt, um Deformationen der Rückprojektion zu vermeiden, Projektionen aus äquidistanten Winkelschritten. ART und MEM kommen mit sehr wenigen Projektionen aus. Allerdings verfügen sie über ein Genauigkeitsoptimum an Projektionen. Ist die optimale Anzahl der Projektionen überschritten, wird das Projektionsergebnis zunehmend wieder schlechter. Ein großer Vorteil der maximalen Entropie Methode ist, dass sie keine äquidistanten Winkel benötigt. Dies ist besonders bei der Rekonstruktion von Phasenräumen nützlich, da hier berechnete Phasenraumrotationswinkel verwendet werden, deren Winkelabstand durch eine Arcustangens Funktion vorgegeben ist. So kann es in ungünstigen Fällen bei der FBP dazu kommen, dass die Werte nicht richtig im zurück transformierten Bild abgelegt werden und die Emittanz nicht mehr zuverlässig auf den rekonstruierten Phasenraumbildern berechnet werden kann. Indirekt liegt auch im Fall der MEM wie auch der ART das Problem der Verzerrung durch einen Wechsel von Polarkoordinaten (Profildaten mit Winkeln) und kartesischen Koordinaten (rekonstruiertes Bild) vor, kann aber nicht direkt durch einen Filterkern behoben werden. Da jedoch beide Algorithmen nur mit wenigen Projektionen arbeiten, ist die Verzerrung im Vergleich zur FBP gering. Vielmehr wirkt es sich im Fall der MEM insofern günstig aus, als kleine Intensitätseinsprengsel, die durch Rauschen in eigentlich intensitätsfreie Gebiete gelangen, durch ihre Unterbewertung verschwinden. Algebraische Rekonstruktion und maximale Entropie benötigen ungleich mehr Zeit und Speicherplatz als die gefilterte Rückprojektion. Welche der Methoden letztendlich umgesetzt werden hängt daher von den Gegebenheiten ab: Anzahl der verfügbaren Projektionen (Abhängig von Messmethode), Qualität der Projektionen, Signal-zu-Rausch Verhältnis, benötigte Genauigkeit und Steuerbarkeit der Genauigkeit für die auf die Tomographie folgende Analyse, sowie der Raumausschnitt (Phasenraum/Ortsraum), der rekonstruiert werden soll.

### 3 Strahltheorie und Analyse

Für die Ortsraumtomografie wird außer den Projektionen und den zugehörigen Projektionswinkeln kein a priori Wissen benötigt. Für die Rekonstruktion der Phasenräume, wird zusätzlich die Kenntnis der Transformationsmatrix benötigt, welche in die Tomographie involviert ist. Generell rekonstruiert die Phasenraumtomografie zwei-dimensionale Unterräume des sechs-dimensionalen Phasenraumes. Damit diese Aufteilung des gesamten Phasenraumes in die zwei-dimensionalen Unterräume gültig ist, muss gewährleistet sein, dass das Liouvill'sche Theorem für die zwei-dimensionalen Unterräume anwendbar ist. Nur in dem Fall, in dem die Impulse  $p_x, p_y, p_z$  voneinander unabhängig sind und keine transversale Kopplung zwischen ihnen wirkt, kann die Phasenraumtomografie mit einer  $2 \times 2$  Transformationsmatrix gültig durchgeführt werden. Ist diese Voraussetzung nicht gegeben, so kann die notwendige Transformationsmatrix nicht allein aus den Matrizen der ionenoptischen Elemente berechnet werden, sondern muss durch geeignete Methoden und mit in Kauf zu nehmender Ungenauigkeit geschätzt werden.

Danach wird genauer auf die Beschaffenheit der zwei-dimensionalen, transversalen Phasenräume eingegangen. Der ideale zwei-dimensionale Phasenraum wird durch eine Ellipse repräsentiert, welche

die zwei-dimensionale Projektion des sechs-dimensionalen Phasenraums darstellt. Die minimale Ellipse, die im Phasenraum die von Partikeln bedeckte Fläche umschließt, ist die effektive Emittanz. Des Weiteren werden drei verschiedene Ellipsenrepräsentationen eingeführt, welche für die weitere Vorgehensweise von Bedeutung sind. Aus der geometrischen Repräsentation der Phasenraumellipse lässt sich der Skalierungsfaktor und der Phasenraumrotationswinkel für die Phasenraumtomografie herleiten. Die Courant-Snyder Repräsentation wird für die Methode zur Bestimmung der effektiven Emittanz benötigt, sowie die Parameterdarstellung der Ellipse für die Methode der RMS-Emittanz. Abschließend werden die ionenoptischen Elemente für die Tomographie an FRANZ untersucht. Dabei stellt sich heraus, dass sowohl die einfache Drift als auch die dünne Linse für die Berechnung der Transportmatrix geeignet ist. Der Solenoid hingegen verletzt durch seine transversalen Kopplungseigenschaften die für die Phasenraumtomografie nötige Unabhängigkeit der transversalen Impulse. Um diesen in die tomografische Messung einzubeziehen, kann die Transfermatrix des Solenoids nicht direkt für die in der Tomographie berechnete Transportmatrix verwendet werden, sondern die gesamte Transportmatrix muss durch geeignete Methoden geschätzt werden. Wann immer ein zu bestimmender Strahlparameter durch einen Schwellwert anstatt durch einen statistischen RMS-Wert bestimmt wird stellt sich das Problem einer künstlich definierten Strahlgrenze. Dies gilt bis zu einem gewissen Grad auch für fraktionell bestimmte RMS-Werte. Der Schwellwert nimmt direkten Einfluss auf die Breite des Strahlprofils und hat ebenso Bedeutung, wenn er auf einen rekonstruierten Raum angewendet wird. Da die Information unterhalb des Schwellwertes verloren geht, ist es ratsam diesen erst so spät wie möglich anzuwenden, da sich der Verlust im Laufe weiterer Verarbeitung fortpflanzt. Gerade bei der Verwendung unregelmäßiger und verrauschter Projektionen, lässt sich keine eindeutige Strahlgrenze für einen festen Schwellenwert bestimmen. Eine mögliche Lösung besteht darin eine Strahlgrenze über eine lineare Regression über alle Werte der Projektion durchzuführen, welche im Bereich eines Konfidenzintervalls um den Schwellwert herum liegen. Günstig im Sinne einer künstlichen Strahlgrenze ist dabei, wenn die Werte in der Nachbarschaft um die Strahlgrenze herum möglichst wenig von dem gesuchten Schwellwert abweichen. So lässt sich als Gütekriterium für die gewählte Strahlgrenze der Fehler des Abstandes dieser Werte vom Schwellwert definieren. Sind die in Frage kommenden Werte durch Rauschen oder Artefakte weit und/oder ungünstig in der Projektion verstreut, so wird bei einer einfachen linearen Regression nicht die optimale Strahlgrenze gefunden. Der IRF-Algorithmus bestimmt zu einem gegebenen Schwellwert (Zielintensität) mit Konfidenzintervall eine Wahrscheinlichkeit dafür, dass die gesuchte Intensität in einen bestimmten Bereich der Projektion fällt. So ist die Wahrscheinlichkeit um so höher, je mehr Pixel mit der selben Intensität in den gleichen Bereich fallen. Pixel, welche außerhalb des definierten Wahrscheinlichkeitsbereiches fallen (in diesem Fall außerhalb des Bereiches der doppelten Standardabweichung) werden aus dem Bild entfernt. Die verbleibenden Werte werden an der Schwellwertintensität ausbalanciert, so dass die Verteilung der übrig gebliebenen Werte nahezu gaußförmig um die Strahlgrenze herum verläuft. Mit den so aufbereiteten Intensitätswerten wird dann die gewöhnliche lineare Regression ausgeführt.

## 4 Strahlprofilmessung, Emittanzbestimmung und ungewöhnliche Parameter

Die Datenbasis ist nun adäquat aufbereitet und das a priori Wissen zusammen getragen, so dass nun die gesuchten Informationen gewonnen werden können. Kapitel 4 widmet sich der Gewinnung

## 4 Strahlprofilmessung, Emittanzbestimmung und ungewöhnliche Parameter

von Ortsraumparametern. In transversaler Richtung ist dies die Bestimmung der Strahlprofile, in longitudinaler Richtung die Position des Strahlschwerpunkts und die Lage der Strahlschwerpunktsachse, gemessen an ihrer Abweichung zur longitudinalen  $z$ -Achse der Projektion, die im Idealfall mit der longitudinalen Achse des Strahlrohres deckungsgleich ist.

Bei der Bestimmung des Strahldurchmessers werden Standardmessverfahren üblicher Weise die Profile der Projektionen von zwei orthogonal zueinander verlaufenden Richtungen ausgemessen (gewöhnlich mit  $x$  und  $y$  bezeichnet). Daraufhin werden zur Gewinnung des gewünschten Strahldurchmessers die Profiltbreiten nach dem gewählten Maß (ABE oder RMS) bestimmt. Ist der Strahl annähernd rotations-symmetrisch, entspricht dieses Maß auch dem gesuchten Strahldurchmesser. Ist der Strahl jedoch nicht rotations-symmetrisch so wird auf diese Weise unter Umständen nicht der wahre Strahldurchmesser gefunden, welcher durch die größtmögliche Profiltbreite unter allen seinen Richtungen gekennzeichnet ist. In anderen Anwendungsfällen

Im nicht selten Fall ähnelt der Strahl einem Oval, welches im ungünstigsten Fall mit seiner Hauptachse gerade diagonal zu der durch die Profilmessung bestimmten  $x$ - und  $y$ - Richtung liegt. In diesem Fall sind die gemessenen Profile und ihre Profiltbreite für die  $x$ - und  $y$ - Richtung in etwa identisch. Es hat auf diese Weise den Anschein als wäre der Strahl rotations-symmetrisch.

Betrachtet man jedoch nach der hier vorgestellten Methode alle Profile in  $1^\circ$  Schritten um die rekonstruierte Ortsraumverteilung herum, kann dieser Irrtum schnell aufgedeckt werden und der tatsächliche maximale Strahldurchmesser bestimmt werden.

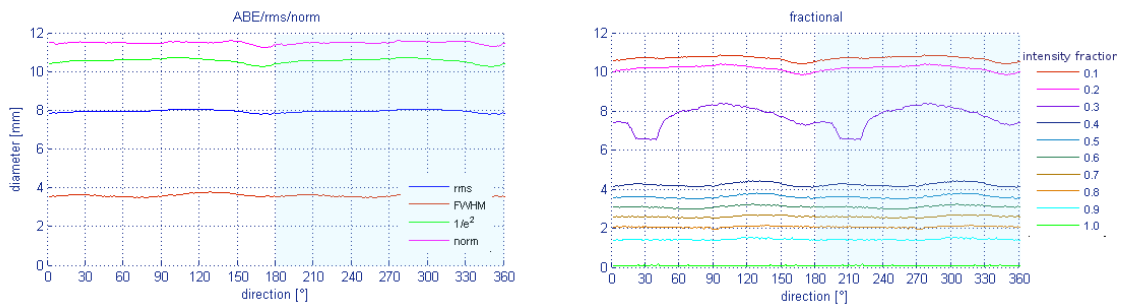


Figure 5: Bestimmung der Profiltbreiten für unterschiedliche Maße in verschiedenen Richtungen um den Strahl herum an einem gemessenen Strahl. Neben der Bestimmung des Strahldurchmessers (maximales Strahlprofil über alle Richtungen) lassen sich auch feinere Charakteristiken wie der Übergang des Strahlkerns in die Strahlaura untersuchen.

Auf einer tieferen Analyseebene lassen sich auch Übergangsbereiche innerhalb des Strahls feststellen. Betrachtet man das Verhalten der Strahldurchmesser über alle Winkel in unterschiedlichen Fraktionen, so lässt sich zum Beispiel feststellen, dass es sowohl in der Simulation, als auch in der Messung möglich ist, einen Strahlkern von seiner *Aura* zu differenzieren. Der Übergang ist in der Darstellung der Fraktionen durch eine größere Lücke gekennzeichnet. Die Übergangsintensität weist selbst bei nahezu Gaußförmigen Strahlen Unregelmäßigkeiten in der Profiltbreite um den Strahl herum auf. In Fig. 5 wurden für die Fraktionen 0.1 bis 1.0 eines gemessenen Strahls die Profiltbreiten für die Winkel  $0^\circ$  bis  $360^\circ$  aufgetragen, wobei es ausreicht, einen Winkel von  $1^\circ$  bis  $180^\circ$  zu betrachten. Der Übergang zwischen dem Strahlkern und seiner *Aura* lässt sich klar erkennen, obwohl der Strahl im Großen und Ganzen in

## Zusammenfassung

---

allen Fraktionen, außer der Übergangsfraction, rotationssymmetrisch ist.

Die Analyse ließe sich nun noch weiter verfeinern, indem beispielsweise der Abstand zwischen den Fraktionen 0.2 und 0.4 in feinere Fraktionen aufgeteilt würde, oder aber die Winkelschritte noch feiner gewählt würden. Dieses Beispiel soll verdeutlichen, welche Möglichkeiten der detaillierten Analyse gerade für die Strahldynamik über das Bestimmen der Standardparameter hinaus durch die tomografische Aufbereitung möglich ist. So ist beispielsweise auf der linken Seite von Fig. 5 beim Auftragen von Maßen wie dem oft gängigen RMS-Wert oder der Full-Width-Half-Maximum-Grenze (FWHM) von diesen Eigenschaften nichts zu sehen, ebenso wenig bei der Betrachtung von Profilen aus nur zwei Richtungen.

Ein weiterer Ortsraumparameter, der durch die Tomographie an Tiefe gewinnt, ist die Strahlposition. Generell wird dieser durch den transversalen Schwerpunkt bestimmt. Dieser Schwerpunkt wiederum ist zusammengesetzt aus dem Schwerpunkt der Profile in  $x$ - und  $y$ - Richtung, wie sie in der Regel gemessen werden. Prinzipiell ist dies derselbe Schwerpunkt, der auch aus der rekonstruierten Ortsverteilung berechnet werden kann. Dieser Schwerpunkt sagt lediglich etwas über die Position des Strahles an der eng umrissenen Meßstelle aus. Zur Position des Strahles gehört jedoch zusätzlich zum Schwerpunkt noch die Lage der Schwerpunktsachse, die durch diesen Schwerpunkt hindurch geht, so dass nicht nur festgestellt werden kann, ob sich der Strahl etwa mittig im Strahlrohr befindet, sondern auch ob seine Hauptachse parallel zur longitudinalen Achse des Strahlrohres verläuft. Dies lässt sich

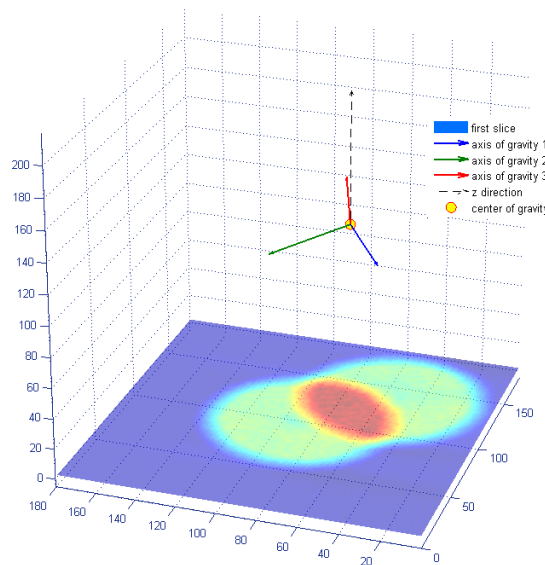


Figure 6: Berechnete Abweichung der Hauptstrahlachse von der longitudinalen Richtung des Ortsraumvolumens. Sind die Projektionen auf die Mitte des Strahlrohres justiert, gibt dieser Wert den Winkel an mit dem die Strahlhauptachse von der longitudinalen Richtung des Strahlrohres abweicht.

durch die Berechnung der Eigenvektoren des Trägheitstensors berechnen, indem man die Massen des Tensors durch die entsprechenden Intensitäten im rekonstruierten Volumen ersetzt. Die Abweichung der Schwerpunktsachse von der longitudinalen Richtung  $z$  des rekonstruierten Ortsraumvolumens kann

---

## 5 Grundlegende Schritte für die Implementierung einer Strahltomografie

dann durch das Skalarprodukt des Eigenvektors mit dem kleinsten Eigenwert (kleinstes Drehmoment auf der Hauptachse) und dem Richtungsvektor der  $z$ -Achse bestimmt werden (Fig.6).

Um von der Ortsraumtomografie zur Phasenraumtomografie zu gelangen, wird der eigentliche Tomographiealgorithmus nicht verändert. Der Unterschied ist, dass für die transversale Phasenraumtomografie nicht die Profile um den Strahl herum verwendet werden, sondern skalierte Profile in longitudinaler Richtung. Das heißt, der Phasenraum kann für jede Projektionsrichtung einzeln berechnet werden. Die für die Tomographie benötigten Winkel werden ebenso wie der Skalierungsfaktor aus der Transportmatrix bestimmt. Mit den rekonstruierten Phasenraumverteilungen kann dann die RMS-Emittanz berechnet werden. Ebenso ist es möglich die effektive Emittanz ohne tomografische Rückprojektion direkt für jede Projektionsrichtung zu bestimmen. Jedoch ergeben sich aus der Technik, die RMS sowie die effektive Emittanz aus jeder Projektionsrichtung zu bestimmen, ähnliche Möglichkeiten wie sie bereits für die Bestimmung von Ortsraumparametern aufgezeigt wurden, sowie die Möglichkeit die effektive Emittanz gegen die RMS-Emittanz zu vergleichen.

Der Fehler, der bei der Bestimmung des Divergenzwinkels im Rahmen der Emittanzberechnung auftreten kann, ist abhängig von der Distanz, über welche die Messung durchgeführt wird, von der Größe des zu messenden Winkels und von der räumlichen Auflösung der Projektionen. Es konnte gezeigt werden, dass die Messgenauigkeit des Divergenzwinkels mit zunehmender Distanz im gegebenen Meßbereich vorteilhaft verbessert werden kann. Ebenso verbessert sich der Fehler bei einer Vergrößerung des zu messenden Divergenzwinkels. Eine Erhöhung der Bildauflösung, mit der eine Projektion gemessen wird, wirkt sich im gegebenen Meßbereich nur schwach verbessernd auf den Fehler aus (Fig.7)

## 5 Grundlegende Schritte für die Implementierung einer Strahltomografie

Im letzten Schritt der Diagnosepipeline erfolgt dann die Verwendung der Informationen nach dem zu Beginn spezifizierten Ziel. Die Implementierung einer Strahldiagnose nach der Diagnosepipeline erfordert in jedem Schritt unterschiedliche Entscheidungen, die dann zur spezifischen Lösung führen. Im Folgenden werden diese Entscheidungen anhand der Strahltomografie für FRANZ diskutiert und in eine allgemeine Systematik für die Implementierung einer Tomographie zur Strahldiagnose eingeordnet.

Der Zweck, zu dem eine Strahltomografie eingeführt werden soll, bewegt sich in der Regel zwischen der Online-Bestimmung von Strahlparametern, um den Strahlbetrieb zu überwachen (Monitoring) und der detaillierten Analyse der Strahldynamik (Fig.8 linke Seite). Für das Monitoring werden in der Regel Standardparameter mit hinreichender Genauigkeit benötigt. Sehr wichtig ist hier vor allen Dingen die Mess- und Verarbeitungsgeschwindigkeit für den Online-Betrieb. Für die Analyse der Strahldynamik hingegen ist eine hohe Genauigkeit von Bedeutung, die Mess- und Verarbeitungsgeschwindigkeit hingegen zweitrangig. In dieser Arbeit wurde die Tomographie möglichst flexibel gestaltet. Zunächst wurde auf eine hohe Genauigkeit Wert gelegt. Die Genauigkeit der Rekonstruktion ergibt sich aus dem Signal-zu-Rausch-Verhältnis der gemessenen Daten und dem darauf verwendeten Rekonstruktionsalgorithmus (Diagram rechts oben). Die FBP ermöglicht bei einem hohen Signal-zu-Rauschverhältnis nicht nur die genaueste Rekonstruktion, sondern lässt sich durch die Anzahl der Projektionen gut kontrollieren. Zusätzlich ist sie die schnellste Möglichkeit der Rücktransformation mit den geringsten Speicherplatzanforderungen (oranger Kasten). Der für die Tomographie verfügbare Platz am Ende der LEBT von FRANZ ist sehr klein. So kam weder die MP Technik für die Aufnahme der Projektionen in Frage, da diese zu wenige Profile liefert, noch die Quad Technik, da diese weit über den verfügbaren

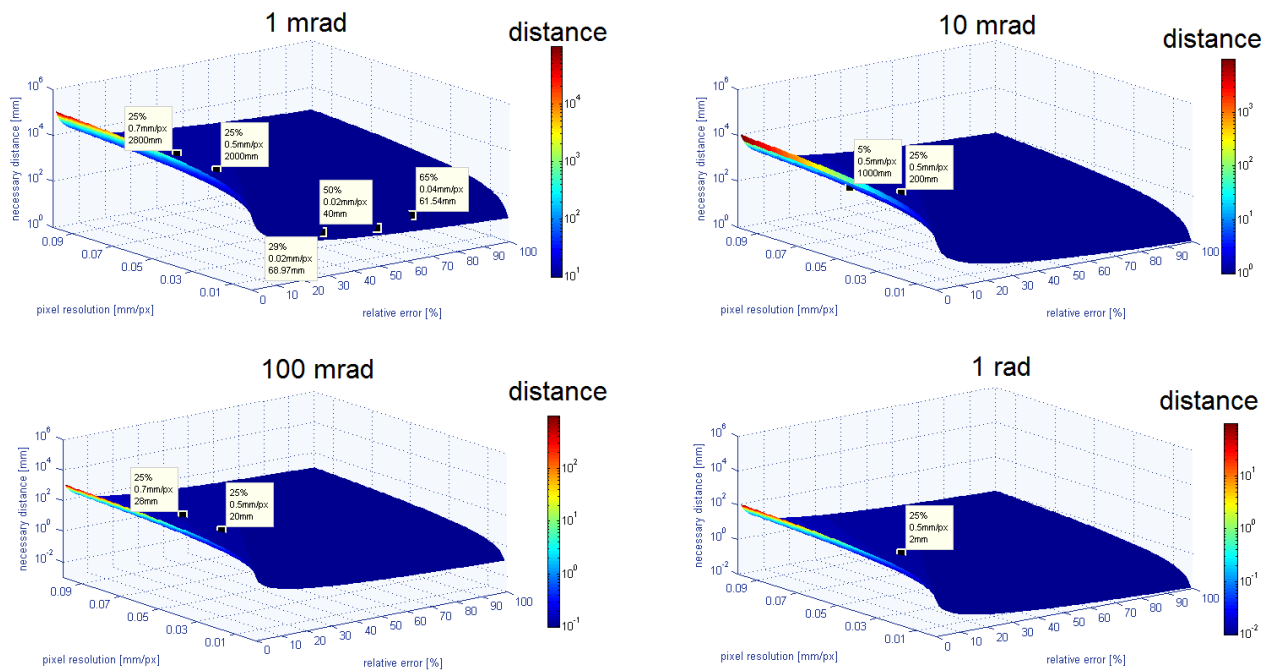


Figure 7: Die Relation zwischen Messlänge, Bildauflösung und Winkeldivergenz zum relativen Fehler im gegebenen Meßbereich zeigt, dass eine zunehmende Messlänge oder Winkeldivergenz sich wesentlich verbessernd auf den relativen Fehler auswirkt, die Erhöhung der Bildauflösung jedoch nur schwach.

Platz hinaus geht. Die entwickelte rotierbare Vakuumkammer schließt nun die Lücke der Diskrepanz zwischen geringem Platz und hoher Profilanzahl und erfüllt beide Anforderungen mit der TbT Technik auf weniger als 400 mm.

Allerdings sind die Meßmethoden für die Gewinnung einer großen Anzahl von Projektionen (TbT und Quad) bisher noch zu langsam für eine Online-Tomographie zum Zweck des Monitoring (grüner Kasten). Prinzipiell ist jedoch zumindest im Falle der TbT Messmethode eine wesentliche Steigerung der Geschwindigkeit möglich.

Eine weitere Frage, die es noch zu bedenken gilt, ist die, welcher Raum in der Tomographie rekonstruiert werden soll (unten rechts). Es gib einen qualitativen Unterschied des Zusammenwirkens von Messmethode und Rekonstruktionsmethode, je nachdem ob der Ortsraum oder der Phasenraum rekonstruiert werden soll. Im Ortsraum (blaue Pfeile) stellt sich bei akzeptablem Signal-zu-Rausch-Verhältnis und vielen Projektionen die durch die TbT-Technik gewonnen wurden, die FBP als weit aus beste Rekonstruktionsmethode heraus (durchgezogene Linie). Für die MP-Technik die nur wenige Profile liefert kommen für die Rekonstruktion nur MEM und ART in Frage. Die Quad-Methode liefert zwar auch viele Profile, da jedoch das Gewinnen der unterschiedlichen Projektionen durch die Veränderung der Spannung an Quadrupolen bewerkstelligt wird, sind die Winkelabstände unter Umständen nur sehr schwer äquidistant einzustellen. Daher ist hier die FBP zwar möglich (gestrichelte Linie) aber die MEM würde in diesem Fall unter Umständen doch die besseren Ergebnisse liefern, da sie als einzige Rekon-



## 5 Grundlegende Schritte für die Implementierung einer Strahltomografie

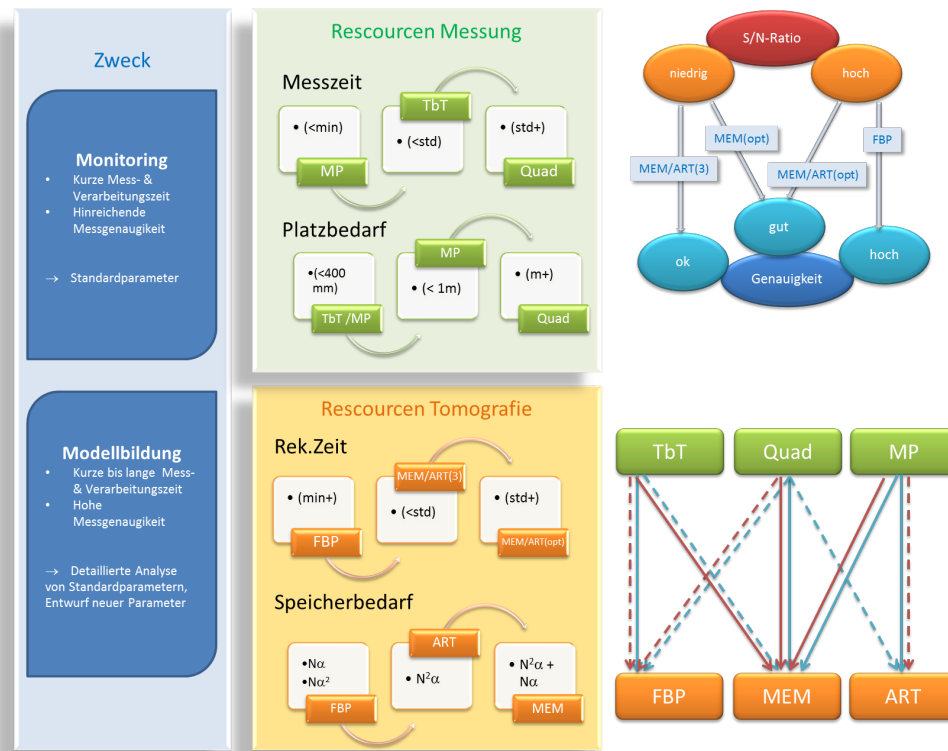


Figure 8: Allgemeines Schema von Entscheidungen die für eine spezifische Implementierung der Tomographie getroffen werden müssen.

struktionsmethode nicht auf die Äquidistanz der Winkel angewiesen ist. Im Phasenraum (rote Pfeile) ist die Situation für die FBP anders. Da die Phasenraumrotationswinkel, welche für die Rekonstruktion verwendet werden, aus der Transportmatrix mit einer Arcustangensfunktion berechnet werden, folgen die Winkelwerte dem Verlauf dieser Funktion und sind nicht äquidistant. Liefert die Phasenraumrekonstruktion mit der FBP nicht zufriedenstellende Ergebnisse, so kann ein Rückgriff auf die MEM die Rekonstruktion wesentlich verbessern auch wenn dadurch die Steuerbarkeit der Genauigkeit eingeschränkt wird.

Insgesamt wurde durch die Diagnosepipeline und das Entscheidungsschema die Grundlage für die routinemäßige Implementierung einer Strahltomografie entwickelt und an FRANZ exemplarisch demonstriert. Mit der Entwicklung der rotierbaren Vakuumkammer wurde eine wichtige Lücke zwischen der Verfügbarkeit vieler Projektionen und damit der Anwendbarkeit des FBP auf engem Raum geschlossen. Für den späteren Strahlbetrieb ist es im weiteren wichtig die Mess- und Verarbeitungsgeschwindigkeit wesentlich zu erhöhen. Für den geplanten, gepulsten Strahlbetrieb ist die Rekonstruktion des longitudinalen Phasenraums und seine Einordnung in das Entscheidungsschema von Bedeutung. Ein großer Gewinn wäre die Entwicklung einer Methode oder Vorgehensweise die der FBP ermöglicht, mit den nicht äquidistanten aber arcustangensförmigen Winkelabständen für die Phasenraumrekonstruktion umzugehen.



# 1 Preparations for Beam Diagnostics using Tomography

## Contents

---

<b>1.1</b>	<b>Review of Tomography for Beam Diagnostics and Outline of Thesis</b>	<b>2</b>
<b>1.2</b>	<b>The Frankfurt Neutron Source (FRANZ)</b>	<b>4</b>
<b>1.3</b>	<b>Diagnostic Device</b>	<b>6</b>
1.3.1	Preliminary Specification of Tomography Environment at FRANZ	7
1.3.2	Rotatable Vacuum Chamber	8
<b>1.4</b>	<b>Object of Measurements</b>	<b>14</b>
<b>1.5</b>	<b>Data Recording and Preprocessing</b>	<b>17</b>
<b>1.6</b>	<b>Diagnostic Pipeline</b>	<b>22</b>

---

Etymologically the word diagnosis (Greek: *διάγνωση*) is derived from the two words *διά* meaning *per* or *by* and the word *γνωση* which means *insight* and *judgement*. In a broader sense diagnosis is the correlation of a phenomenon to a category. For example, visiting a doctor the phenomenon of distinct discomfort is correlated with a specific disease. In beam diagnostics measurement results will be used to gain information about beam characteristics which are correlated with a special state of the beam, reflecting the quality of it in matters of predefined requirements. This predefined requirements essentially influence the result and reliability of beam diagnosis. In the following these requirements will be defined in more detail by discussing the process of data acquisition and the gain of information. Section 1.1 gives a short historical overview of the investigations in tomography for beam diagnostics over the last thirty years. It is analyzed why tomography is not a standard diagnostic method up to now, although it exhibits a wide range of very different information on the beam. In section 1.2 an overview of the new Frankfurt Neutron Source (FRANZ) is given. This is the environment in which the tomography will be implemented for beam diagnostics. Sections 1.3 to 1.5 deal with the first step of the diagnostic pipeline answering questions about the nature of the data dealing with the questions how the measurements are performed (1.3), the object of measurement viz what is measured (section 1.4) and how the resulting raw data have to be preprocessed to be useful for the following steps of the diagnostic pipeline (section 1.5). Since the tomography approach is a very general method to derive information from the measured data, the diagnostic pipeline is introduced to show a way to develop particular methods for gaining particular information from this general method (section 1.6). The basic steps from measurement to information in beam diagnostics are depicted.

### 1.1 Review of Tomography for Beam Diagnostics and Outline of Thesis

Tomography was first applied in the late 70s as a method for particle beam diagnostics by Minerbo [Min77], five years after the first commercial implementation of tomography for medical application. The essential difference in these times was the significant smaller number of projections which were used in beam diagnosis. The method of filtered backprojection (FBP)(2.2) that directly transcripts the basic idea of Radon [Rad17], the mental father of tomography<sup>1</sup>, relies on the use of much more profiles. Therefore Minerbo used the iterative method of maximum entropy (MEM) to implement the reconstruction. One year later Fraser [Fra78] also introduced the method of algebraic reconstruction (ART), which also is an iterative method, which can be used for the reconstruction of a distribution with just a few projections. In the appendix of his work a proof can be found that the reconstruction of the transverse ordinary space and the phase space of a particle beam can adequately be reconstructed by three projections. Both proofs make an assumption, which should not be underestimated. The assumption for the ordinary space distribution was that the beam has approximately a bivariate Gaussian distribution of particles. For the phase space he supposed the particle distribution of the beam to be contained within a circle of radius  $\sqrt{\epsilon\pi}$  (where  $\epsilon$  is the emittance), citing Metzger [Met73]. Although these assumption are quite common up to now, because they are criteria for the ideal beam, they do not hold in the problematic and interesting cases. Additionally, by making these assumptions, significant information contents will be erased with the consequence that perhaps an analysis cannot be performed or leads to misinterpretations. Nevertheless, the reconstruction was feasible and used for the purpose of beam diagnostics [Fra79, Min79, Mot85]. This was a major step forward. Soon the reconstruction of the four-dimensional transverse phase-space was invented [Min81]. The reconstruction of the longitudinal phase space was introduced by Jackson [Jac87] in 1987. He intended to develop an online-tomography by a phase space tomography monitor (PST Monitor) to gain detailed information about the bunch dynamics by reconstructing the longitudinal phase space. In 1993 he presented the first implementation and measurements of the PST-Monitor at the Fermi Lab main ring [Jac93]. In 1997 the idea of longitudinal phase space reconstruction was uptaken by Hancock and Mane [Han97, Man97]. In 2001, Hancock et. al. implemented the PST for the longitudinal online-tomography in the PS complex of Cern. In the years 2000 to 2009 tomography was introduced in different places for the reconstruction of the transverse and also of the longitudinal phase space [Kos01, Hue02, Yak03, Hon05, Hol06, SD06, SD07]. The collection of projections was performed by a set of fixed CCD-cameras along the beam line (Multi-Port-Technique (MP)) or the new invented Quad-Scan-Technique(Quad). The Quad-Scan-Technique uses a set of quadrupoles or an even number of solenoids to rotate the beam by applying different currents. Thereby it was possible to obtain a large number of profiles along the beam line, but also around the beam, to improve the reconstruction quality of position and phase space. It had become possible to use the FBP effectively. The main interest of developments in these times was dedicated to the investigation of nonlinear effects caused by space charge, and also transverse coupling when using solenoids. This was very important, because phase space tomography is dependent on the use of the transport matrix that can be computed from the matrices of the different ion optical devices in the beam line. In the presence of space charge the trajectories of the particles differ from the ideal path that is given by the transport matrix, therefore the projections measuring the real distribution does not

---

<sup>1</sup>Radon did not have anything in mind about tomography, but his historical talk was motivated by the solution of a problem, that he has discussed with a friend, which was interested in mathematical topography

## 1.1 Review of Tomography for Beam Diagnostics and Outline of Thesis

---

sufficiently fit the ideal distribution at every longitudinal position, which is predefined by the transport matrix and used by the reconstruction algorithm. In the case of transverse coupling by a solenoid there is the problem, that the transport matrix is valid for the four-dimensional transverse phase space but not for both of the two-dimensional subspaces. Unfortunately phase space tomography computes the two-dimensional subspaces. The problem also arises by the reconstruction of the four-dimensional transverse phase space since this is determined by the use of the two reconstructed subspaces and optionally by the use of the transverse ordinary space. For all these problems, special solutions have been proposed in the referred literature.

In spite of all achievements of the last thirty years, tomography still is not a standard application for beam diagnostics. There are two main reasons.

On the one hand the techniques used to obtain the projections required too much effort for a routined utilization or one had to accept a very small number of projections (Quad versus MP). Additionally the set up of a tomography covers a broad spectrum of techniques from mathematics, computer science, ion optics and particle physics, which supposes a great expenditure of resources.

On the other hand the real possibilities of tomography have not been exhausted by far. Most efforts have been made to successfully develop a non-invasive method for emittance determination. But as it was already adumbrated by Jackson [Jac87], tomography is able to allow a deeper insight into beam dynamics than any other technique that is available at the moment, since it is non-interceptive such that beam dynamics can be observed without disruptive or disturbing influence. The accuracy of measurement is manageable and depending on the aim of the investigator. The method is general and flexible enough to serve as a basis for investigations beyond the determination of standard beam parameters (which are also possible).

But also for monitoring beam parameters in online accelerator operation, tomography is going to become an applicable non-interceptive method to observe beam parameters in transverse or longitudinal position and phase space.

What is missing up to now, is a systematic concept to set up the right configuration of tomography for a given environment and investigation aim to allow a routined utilization of tomography in ion beam diagnostics.

In chapter 1 the basic requirements of data acquisition for the tomography at FRANZ are discussed. Since space is very narrow because the tomography is placed in the last section of the LEBT, the Quad technique was no option. On the other hand, a high accuracy for beam dynamic investigations was needed, so the MP technique also did not fulfill the requirements. Therefore a new device was developed in dependence on medical tomography, where the measurement data are taken by a rotatable device around the beam (Turn-by-Turn technique (TbT)) allowing a very high and scalable angle resolution. After this, the object of measurements, residual gas radiation, briefly is discussed. Using residual gas radiation in visible spectrum one has to consider that the final results of the diagnosis are depending on factors like residual gas pressure, shutter speed of the camera, vacuum pressure and the used residual gas. In the next section the steps of necessary preprocessing of the data before applying it to tomography is shown. In the last section the coherencies between the conditioned data from the previous steps and the information that has to be obtained from it are discussed.

In chapter 2 at first the fundamental ideas of tomography are discussed and shown in detail by deriving the algorithm of FBP. This algorithm is a direct implementation of the fundamental ideas that had made tomography possible. The FBP algorithm then is analyzed with respect to its behavior

## 1 Preparations for Beam Diagnostics using Tomography

---

on noise, distortions, and artifacts. After this, the two other reconstruction algorithms, which are often used for beam tomography, ART and MEM, are introduced in a nutshell. At the end there will be a discussion about the criteria that have to be taken into consideration to choose the right algorithm for particular tomography set ups.

Tomography in three-dimensional ordinary space needs no a priori knowledge about the beam. For a phase space reconstruction the transport matrix has to be known, which is derived from the different ion optical devices in the beam line which are involved in the tomography process. In chapter 3 the a priori knowledge which is needed for a phase space tomography at FRANZ and the analysis of its results to obtain information on the emittance of the beam is discussed.

In chapter 4 the enhanced possibilities of beam profiling and beam size measurements when using tomography in ordinary space is demonstrated. Additionally an algorithm was investigated to determine the aberration of the beam axis from the longitudinal direction. This is an example, how tomography supports the investigation of non standard parameters.

Finally chapter 5 shows the application of tomography for determining the RMS- as well as the effective-emittance. Transverse phase space tomography does not change the used tomography algorithm but modifies the projections and their angles. Firstly, the necessary scaling of the profiles and the computation of the phase space rotation angles, which are used for phase space tomography are derived. After that, the RMS-emittance is introduced and it is shown how it can be determined on the reconstructed phase space. Effective emittance can be obtained by a projection from one projection angle, which is also possible for the method with phase space tomography. But both methods take great advantages in their accuracy when using projections from many angles. Therefore the determination of effective emittance, although it has no obvious relation to tomography at the first sight, is introduced. Finally, the use of RMS- and effective- emittance is demonstrated by some examples.

### 1.2 The Frankfurt Neutron Source (FRANZ)

The Frankfurt Neutron Source (FRANZ) based at the new science campus of the Goethe University in Frankfurt on the Main will consist of a proton driver linear accelerator (LINAC) providing energies up to 2.2 MeV, which are needed for neutron production using the  ${}^7\text{Li}(p,n){}^7\text{Be}$  reaction[Meu08]. The main application for FRANZ will be the investigation of astrophysical nucleosynthetic processes. Besides that, also experiments in the field of materials research and detector design will be possible because of a high neutron flux density of up to  $10^{10}\text{cm}^{-2}\text{s}^{-1}$  within an energy range of 1 to 500 keV. A high energy proton beam with a challenging time structure is demanded. This efforts to enhance existing accelerator concepts, which will be realized in FRANZ [Wie10]. Two different modes will be available:

The activation mode is at the expected neutron fluxes allows an interesting experimental program. By a cw proton beam of up to 5 mA a continuous high average neutron flux will be created. The compressor mode facilitates energy-dependent measurements of neutron capture cross-sections. A precise measurement of neutron capture reactions also for isotopes with small cross-sections or which are only available in very small samples, need a very high intensity of single pulses and a high repetition rate. In compressor mode FRANZ produces a 1 ns long neutron pulse, which is formed with a repetition rate of up to 250 kHz.

The design of FRANZ is shown in Fig. 1.1. A high current proton source with a pentode extraction system can be seen on the left. A 200 mA  $\text{H}^+$ -beam at an energy of 120 keV can be provided.

## 1.2 The Frankfurt Neutron Source (FRANZ)

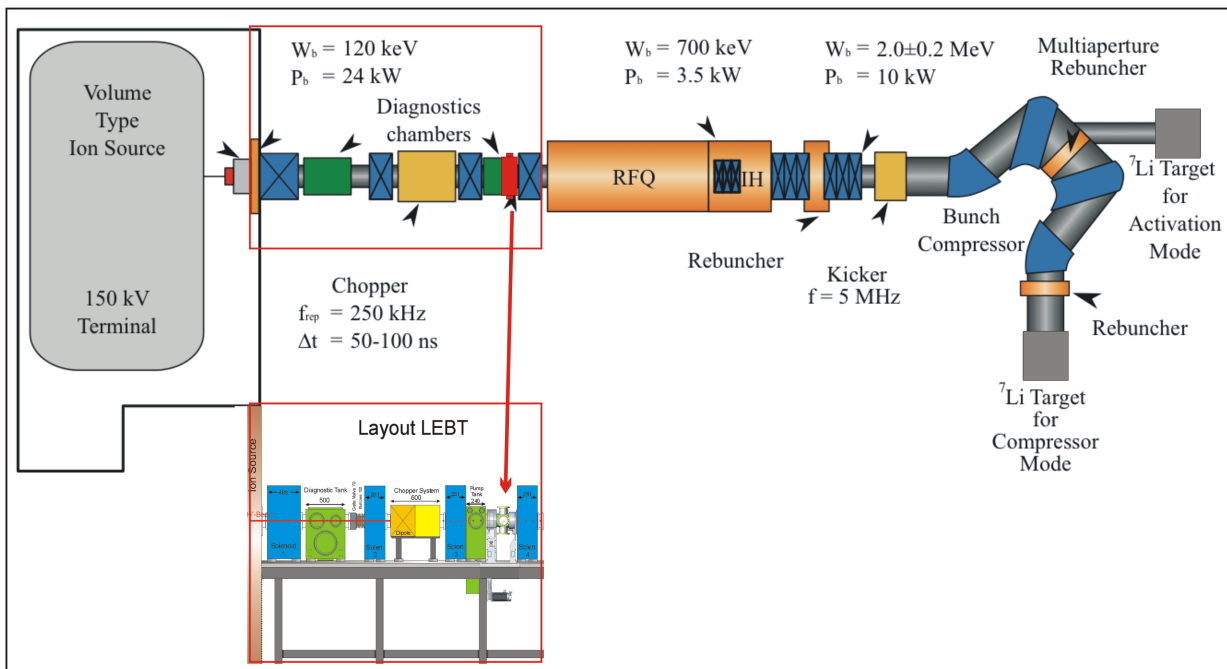


Figure 1.1: The planned FRANZ and the position of the diagnostic device in the LEBT section.

The pentode extraction system makes it possible to influence the beam formation without changing the beam energy. After the first focussing solenoid, an diagnostic chamber and a second focussing solenoid a  $E \times B$ -Chopper system will provide pre-pulses of 100 ns every  $4 \mu\text{s}$  with a beam free pulse interception of more than  $3 \mu\text{s}$ . After the third solenoid, just in front of the last solenoid of the Low-Energy-Beam-Transport (LEBT) section the rotatable vacuum chamber (section 1.3) will be placed to provide tomographic beam diagnostics as described in this thesis. In the linear accelerator section a four-rod Radio-frequency Quadrupole (RFQ) and an interdigital H-type drift tube linac (IH-DTL) will be placed. Then a 5-cell CH-rebuncher with a 12 kW transmitter will provide a longitudinal focussing in compressor mode. In activation mode the rebuncher will be used to vary the output energy between 1.8 MeV and 2.2 MeV. After the rebuncher the Arc Magnetic Dipole System for Longitudinal Compression (ARMADILLO) serves as a bunch compressor for mono-energetic proton beams [Chau08]. In the bunch compressor nine of the subsequently incoming microbunches from the RFQ will be deflected on individual tracks to arrive at the same time at the target. At the end two lithium-7 targets, one for each mode, will be installed. In activation mode a neutron flux of  $10^{10} \text{cm}^{-2} \text{s}^{-1}$  and in compressor mode  $10^7 \text{cm}^{-2} \text{s}^{-1}$  at a distance of 0.8 m form the target are expected.

The design of FRANZ provides a wide range of astrophysical measurements, detector development and material research. It also serves as test bench for new accelerator concepts and high power neutron production targets.

## 1.3 Diagnostic Device

The choice or development of an appropriate measurement device for a given set of specifications is an important factor for the success of the aspired diagnosis. These specification can be grouped into three fields: the required parameters that shall be extracted, the allowed degree of influence on the beam and the claims of environment.

### 1. required parameters

The kind and functionality of the measurement device depends on the parameters that have to be measured and the raw data which could be gained from. For example, one would determine the position, size, shape, intensity of the beam. The raw data for the determination of such parameters can be taken from a Faraday cup, a scintillator screen, the observance of residual gas radiation, a wire scanner, and many others. Most of the devices support more than one parameter determination. Additionally, to measure a whole set of parameters, often more than one device will be needed.

### 2. degree of influence

The degree of influence estimates the affect of a diagnostic device on the beam. For some applications this is a very critical factor. In relation to the application of the diagnosis the diagnostic device can be rated as:

- *destructive*: the beam will be destroyed or stopped by the diagnostic device. One example is the use of a Faraday Cup.
- *objectionable*: the beam will be disturbed and modified, such that beam qualities, represented by the parameters that have to be marked, may change during the measurement of the diagnostic device. This, for example, will be the case by the use of some scintillator screens, a wire scanner or a ionization chamber.
- *negligible*: the beam will be influenced in a way that does disturb the application or the measurement of beam parameters in an acceptable way. As for the point before, the question “What is acceptable?” depends on the given circumstances. A scintillator screen, for example, also could be a measurement device with a negligible effect of the beam.
- *none*: The beam will not be affected at all by the diagnostic device. This is the case for some settings of optical measurements. Taking the residual gas radiation by an optical sensor (e.g. a CCD-camera) has no effect on the beam, if the energy is high enough to compensate the interaction between the residual gas and the beam particles.

At least the question is not, if the beam is principally disturbed, but if it is influenced in a way that contradicts the defined diagnostic goal.

### 3. claims of environment

The possibility to use a diagnostic device depends on the given environment where it will be used. Using a wire scanner in combination with a high energy beam will almost certainly lead to a destroyed measurement device instead of proper data for the determination of beam parameters. The other way round, if the beam is needed after the diagnosis section one could not use a Faraday Cup as online diagnostic device, since this will just dump the beam. Beside these extremes is a



transverse parameter specification	
parameter	expectation
beam size	< 50 mm
beam shape	nearly rotational symmetric
beam position	centered in the beam hole
main beam axis	parallel to the beam hole
emittance	[0.0...30.0]mrad

Table 1.1: Specification of beam parameters that have to be determined by the diagnostic device at the end of the LEBT section.

brought area of consideration that have to be taken as far as the environment is concerned. In the field of tomography, for example, a special discrepancy made it quite awkward to use beam tomography. For many years one had the choice in using tomography: using techniques with a very low number of projections (accepting the limited possibilities and arising problems), since they could be measured in one place by a couple of optical detectors or to build up a very long beam line with up to four quadrupoles to rotate the beam in ordinary space, to gain an adequate number of projections. Before setting up a diagnostic device, the determination of the claims of environment has to be one of the first steps. A question that will arise in different places in this work for example is, if a solenoid can be used for the determination of parameters which can be influenced sensitively by the transverse coupling, caused by this optical devices. If yes, how can this influence be limited to an acceptable degree? This also is a question how to deal with the given claims of environment.

In [Koz01] it states:

*When setting out to describe a large number of diagnostic devices, one first tries to establish a systematic order. [...] However, none of that makes much sense.*

The argument in [Koz01] for this statement is that there are many devices measuring more than one parameter, or that they differ in the groups of specification named above. Of course this is the case, nevertheless the understanding of a systematic order for beam diagnostic devices, although most devices will share different subsets of it, will help to find and construct the most optimal diagnostic device for the designated application and to use it in an information sensitive way.

### 1.3.1 Preliminary Specification of Tomography Environment at FRANZ

The diagnostic device will be placed at the end of the LEBT section of FRANZ (Fig. 1.1). The available space for a diagnostic device in this place is very narrow. Before entering the RFQ, the beam has to be matched as optimally as possible to grant an undisturbed acceleration. Therefore several transverse beam-parameters have to be determined in this place (Table 1.1).

Additionally to the determination of those parameters during experimentation, it has to be analyzed what influences the newly designed chopper and the adjustment of the source will have on the beam.

## 1 Preparations for Beam Diagnostics using Tomography

---

FRANZ will be operated in activation mode mode as well as in compressor mode. For the latter the longitudinal emittance will matter<sup>2</sup>. In summary the following specifications can be fixed:

- available space for device: < 400 mm
- no effect on the beam
- non-destructive also for the equipment (high energies)
- beam parameters for the fitting into the RFQ
- possibility to analyze the effects of the chopper and the adjustment of the source
- allowing continuous and pulsed mode

The diagnostic device therefore serves two aims: to monitor the operation in the LEBT during an experiment and to enable an analysis of the operation of newly invented parts of the accelerator. In the light of this specification, it was decided to introduce a tomography based diagnostic system consisting of a very compact rotatable vacuum chamber, which allows to perform tomography with a high number of projections for position and phase space, and a set of parameter determining algorithms. In addition the possibilities will be kept as flexible as possible, meaning that the system has to be expandable as far as the measurement possibilities and as well as the algorithms will be concerned.

### 1.3.2 Rotatable Vacuum Chamber

The rotatable vacuum chamber was developed in cooperation with the *Neue Technologien GmbH* (NTG). It has to fulfill the space requirements of less than 400 mm and a vacuum stability of at least  $10^{-7}$  mbar during rotation. The angle resolution has to be in a range of at least  $180^\circ$  with a step width of  $1^\circ$ . The final solution can be seen in Fig. 1.2

The length along the beam line amounts to 351,2 mm. There are two beam line flanges with a size of 150 mm that integrate the vacuum chamber into the drift. Orthogonal to this flanges there are four pairwise opposed adapter flanges with a size of 100 mm, to plug measurement devices. The vacuum chamber is propelled by drive belts and a strong pecking motor. Fig.1.3 depicts the constituent parts in more detail.

---

<sup>2</sup>There also is a possibility to determine this by tomography. In this work that will be marked only in the outlook.

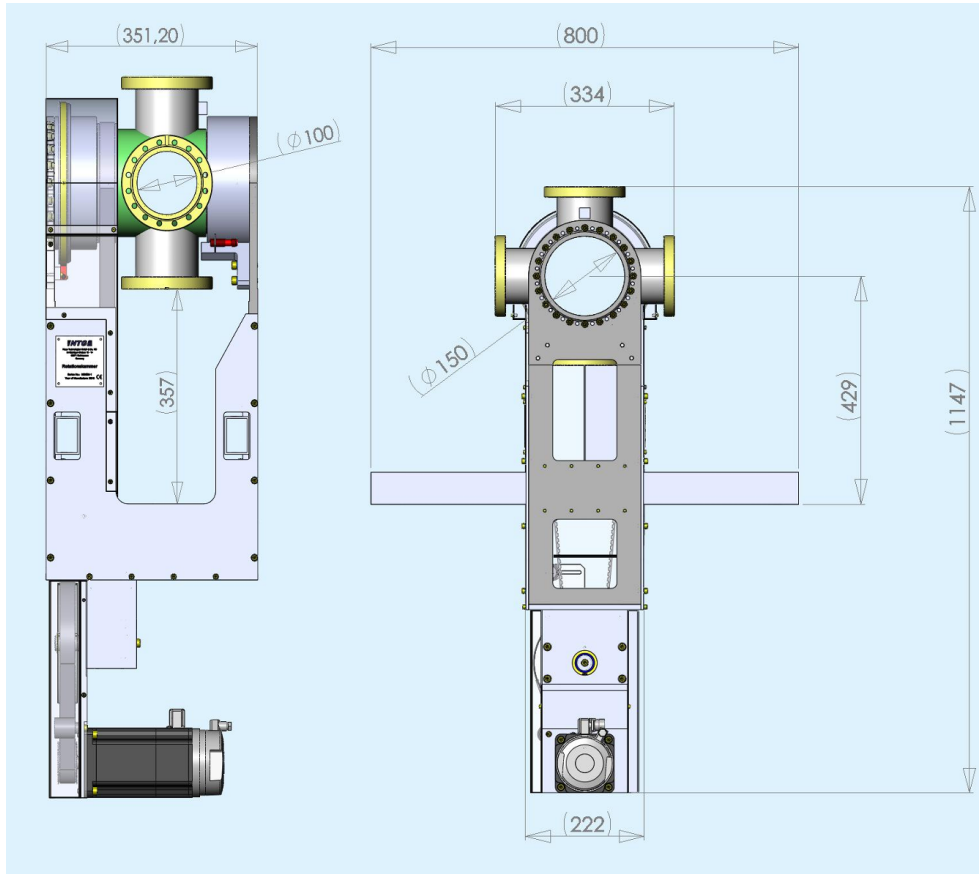


Figure 1.2: Final solution of the rotatable vacuum chamber. Left: side view. The beam passes the chamber from left to right. The 100 mm flange in top view is one of four adapter flanges for measurement devices. Along the beam line the chamber only takes 351,2 mm length. Right: beam line view. The beam passes through the 150 mm flange in top view. The width of 800 mm is due to the fixing at the LEPT base frame.

## 1 Preparations for Beam Diagnostics using Tomography

---

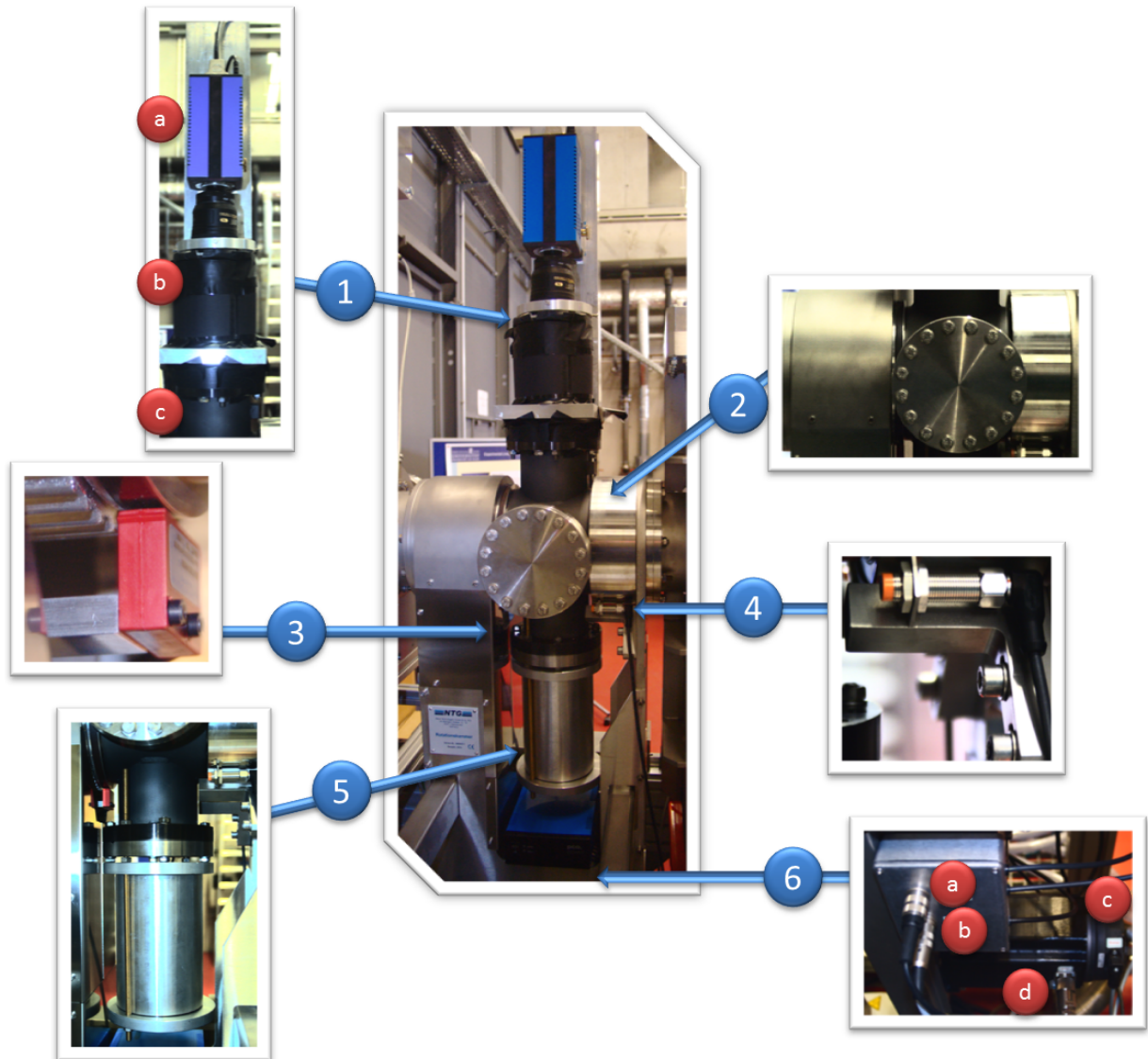


Figure 1.3: Overview of the constituent parts of the rotatable vacuum chamber with adapted CCD-camera.

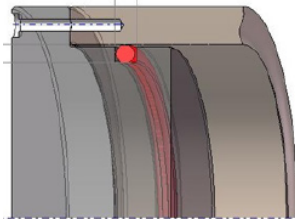
Explanation of parts in Fig. 1.3:

1. *camera assembly*: A CCD-camera was mounted on a fixing frame allowing to regulate the distance of the camera from the beam line center. In the shown distance of about 30 cm it captures a longitudinal distance of 69.97 mm of the beam, which is a resolution of 0.0437 mm per pixel.
  - a. A PCO 1600s CCD-Camera is used presently. The resolution of the camera is  $1600 \times 1200$  px for 14 bit grey scale, with a  $5\mu\text{s} - 60\mu\text{s}$  shutter speed and a wavelength sensibility of 320 nm-1000 nm. It is featured with a peltier cooling and a quantum efficiency of 55%. The object lens is a AF-S Micro NIKKOR 60mm f/2.8G ED.



Used CCD-camera: PCO 1600s

- b. An opaque flexible protection was inserted between the camera and the adapter flange to enable a regulation of the camera distance on the one hand, and a complete dim out of light on the other hand.
  - c. Adapter flange of the vacuum chamber.
2. *vacuum chamber with vacuum seal*: To avoid a debasement of the image quality by reflections the vacuum chamber was sandblasted to roughen the surface and then blackened by an amorphous electrolytic process. The vacuum seal is a tripartite Viton seal on each side.

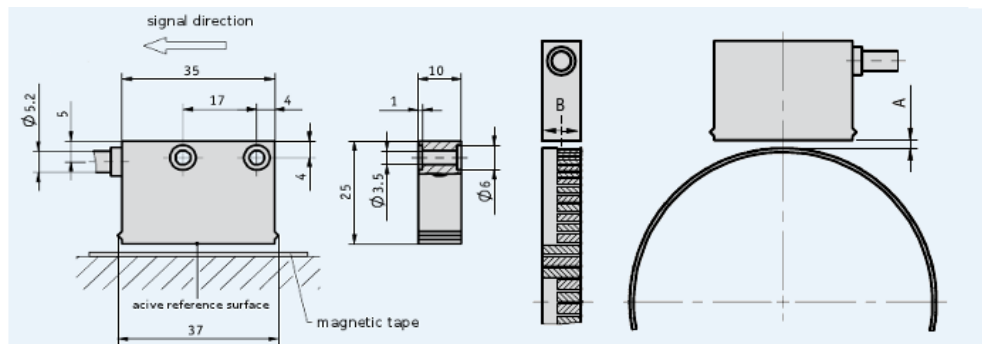


A single embedded viton seal.

It is released of friction by an intern ball bearing. In general a viton seal grants a vacuum stability of about  $10^{-7}$  mbar at a throughput of 2000 l of the vacuum pump. A 72 hour physical performance test of the rotatable vacuum chamber showed a vacuum stability of  $3 \cdot 10^{-8}$  mbar at a throughput of 56 l. On the left hand side the seal cover is larger because it also hides the anchor of the drive belt for the rotation.

3. *angle encoder*: The angle encoder serves two aims. The first is to control the rotation of the pecking motor (as can be seen in 6.). The second is that it feeds back the effective angle in which the chamber was rotated, by reading the actual position from a magnetic tape fixed at the body of the chamber.

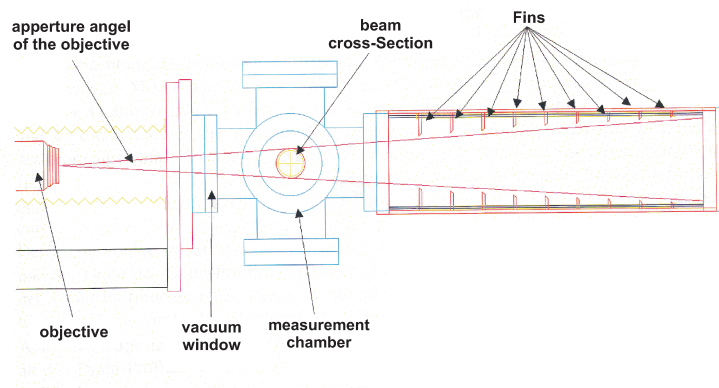
## 1 Preparations for Beam Diagnostics using Tomography



**Angle encoder reading actual angle position from magnetic tape.**

That way it can easily be ascertained, if there was a slip in the drive belt or if there are other influences causing a disturbance in equidistant angle resolution. The encoder itself allows an angle resolution of more than 6000 steps within  $360^\circ$ . The chamber has a possible rotation angle of about  $272^\circ$ .

4. *final position switch*: To calibrate the rotation chamber at the beginning of a measurement to one fixed  $0^\circ$  point the final position switch is attached. Without this switch the chamber is able to turn around  $360^\circ$ . To avoid problems with assembly and cables at the adapter flanges this angle range is constricted to  $270^\circ$ . To perform a tomography, a rotation of exactly  $180^\circ$  is necessary.
5. *light absorber and balance weight*: This weight is added at the opposite flange of the CCD-camera flange to grant a balanced statics during rotation. The camera assembly in 1. is massive and causes irregularities when rotating from one side of the zenith to the other. Inside it is populated additionally with light absorbing fins, granting a completely anechoic image recording.



**Camera and light absorber.**

6. *pecking motor*: A three-phase stepper motor (d) with holding break (c) and connections to the sensor of the angle encoder (b) and the final position switch (a).

The rotatable vacuum chamber was integrated into a test stand to conduct several measurements and tests. Fig. 1.4 shows the assembly with a source behind a protection cover (1) delivering a 10 keV  $\text{He}^+$ -beam. A focussing lens in form of a solenoid (2) used with a focussing field of 0.21 Tesla.

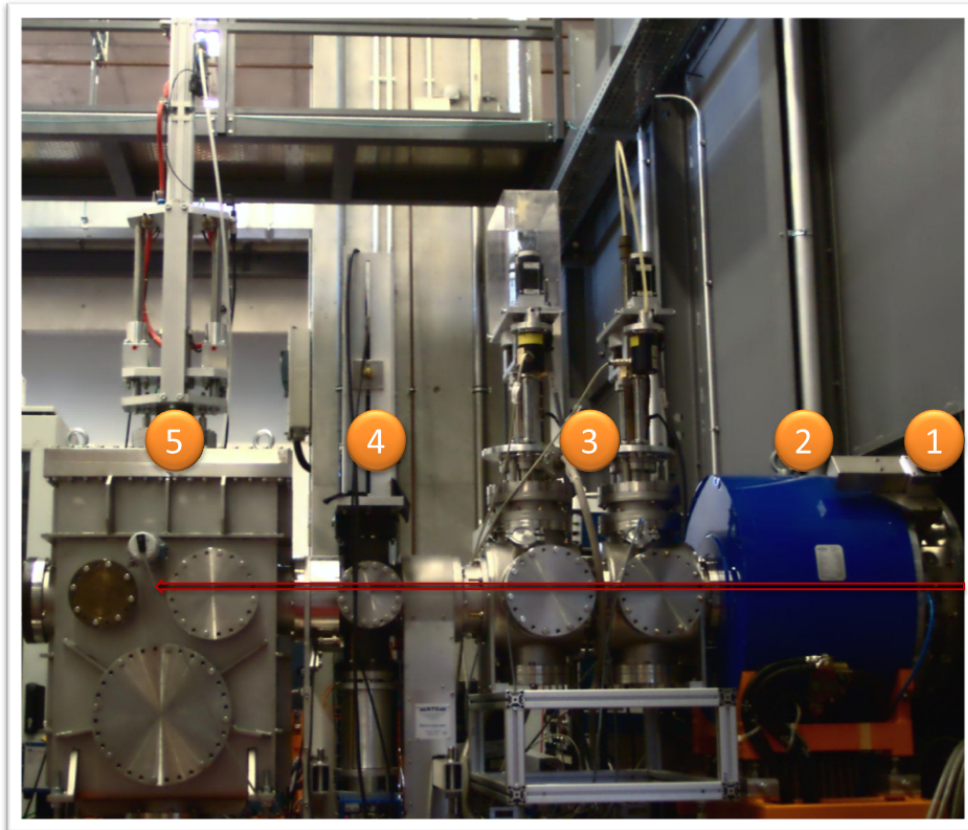


Figure 1.4: The actual test stand. (1) source, (2) focussing solenoid, (3) slit-grid measurement device, (4) rotatable vacuum chamber, (5) Faraday cup for beam dump

A slit-grid measurement device (3) to compare the results of two independent emittance measurement methods. The rotatable vacuum chamber (4) with the plugged CCD-camera as described before. The used residual gas for the radiation is nitrogen at a vacuum pressure of  $10^{-6}$  mbar. A Faraday Cup serving as beam dump (5).

The activation piloting (Fig. 1.5) supports the control of the rotatable vacuum chamber in manual and computer-aided mode. Beside the power button (1 red) there are controls for the motor (2 red) at the front side to activate/deactivate, rotate/fix the motor and to handle the direction of the rotation. The interface for the motor control can be seen at the back side (2 red). The speed of rotation is controlled by (3 red). At the front there are two indicator lamps for the end positions of the final position switch (1 green), which is connected at the back side. If the final position of one direction has been reached, the motor deactivates automatically also in manual operation. The trigger for the angle encoder (1 blue) in the front is connected by a RS232 adapter in the back. The PS2 connector chains the angle encoder sensor with the chamber. For a computer-aided operation mode the activation piloting can be connected via LAN (2 green). This mode is displayed by the indicator lamp in the front.

## 1 Preparations for Beam Diagnostics using Tomography

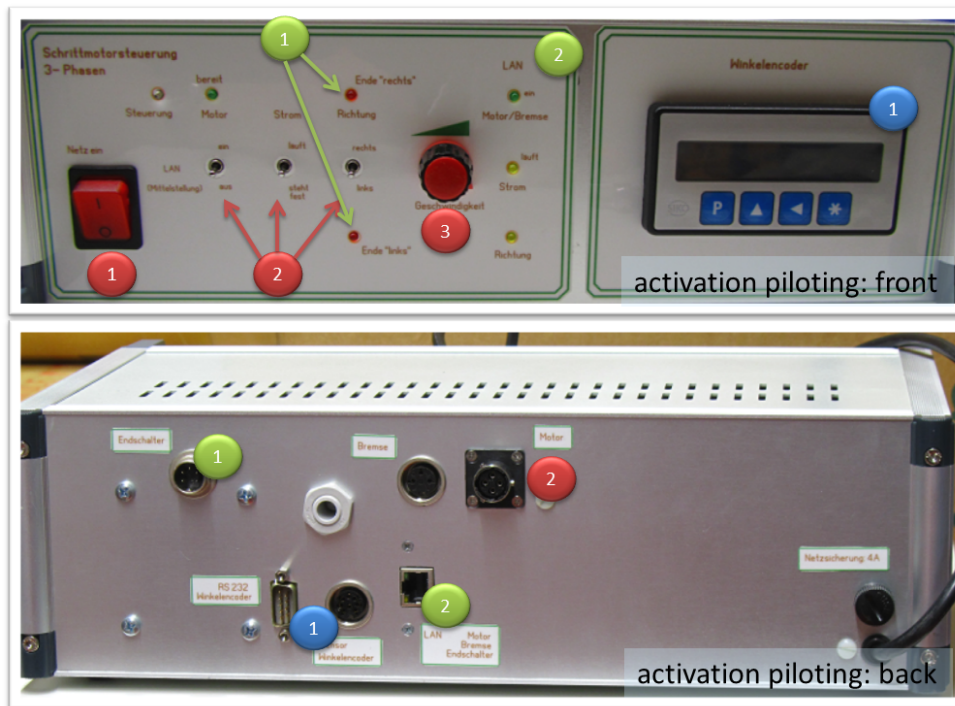


Figure 1.5: Activation piloting for the rotatable vacuum chamber to realize an automated online control for the diagnosis.

### 1.4 Object of Measurements

Most of the methods in this work deal with data represented by *profiles*. A profile is an array of intensity values projecting a set of line integrals along a given direction on a single line. In beam tomography a profile is called Radon transform, and is back transformed to the original intensity distribution that was given before integrating over the given directions. Although the intensity profiles in many cases are integrals of visible light intensity, this is not compulsory. It is, for example, also possible using optical intensities beyond visible light or even current strength profiles.

Optical diagnostics supports a wide range of applications, and its use was rapidly increased by the fast progress in the development of optoelectronic measurement components. Reconstruction techniques were applied firstly in the fields of medical radiology and radio-astronomy using X-ray radiation. The first experiments on beam tomography were performed by holographic interferometry which was “*used to measure the plasma beta in the beam*” [Min77]. Later on, X-ray cameras were applied. Today a wide scope of optoelectronic measurement techniques are available. The choice of a device is depending on the wavelength of the radiation that has to be observed. Fig.1.6 shows the broad bandwidth of possibilities for optical diagnosis. At the left hand side of the wavelength scale one will find measurement techniques based on X-ray radiation, often used to extract information from synchrotron radiation. This can be measured for example by a pinhole design, where an X-ray image from a pinhole is taken by a CCD-camera with a capable converter screen[SJ96, Cai96]. At the right hand side of the wavelength scale,



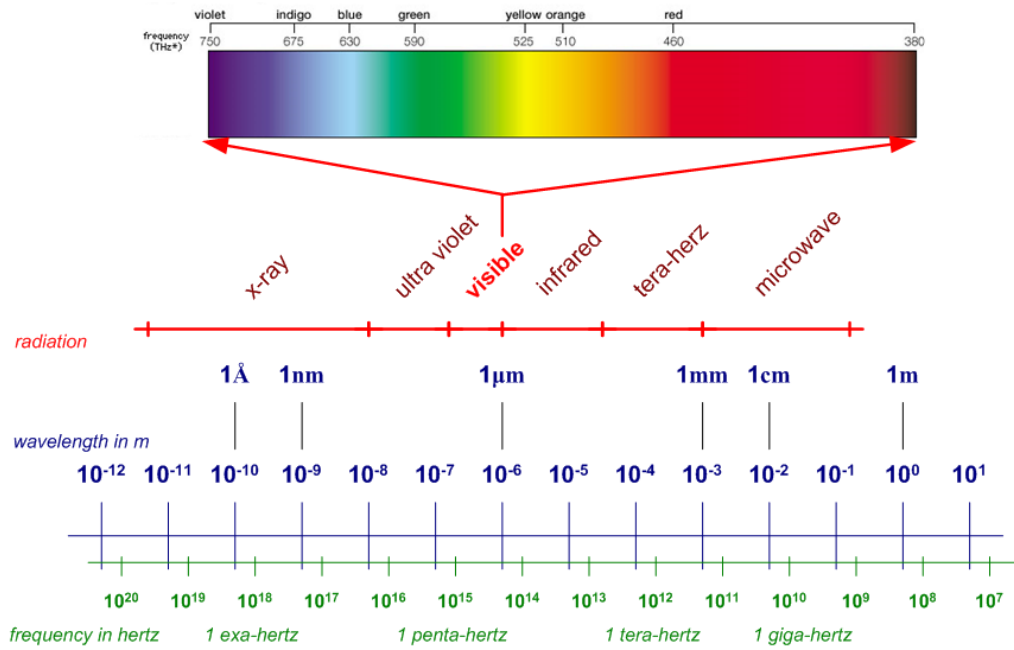


Figure 1.6: The choice of an optoelectronic measurement technique is depending on the wavelength of the radiation that has to be observed. The scope of devices nowadays is very broad.

methods interpreting microwave radiation are used for optical diagnostics in plasma physics [Nie97], but more often in medical applications for the early diagnosis of osteoporosis or cancer. Tomographic techniques are also applicable at this wave range (e.g. see [Pas10] for an introduction). Visible light with a wavelength of about  $1 \mu\text{m}$  covering frequencies from about 750 to 380 THz is subject to the investigations in this work, but the methods are also applicable for other wave ranges as far as they can be measured with adequate accuracy.

Interactions between beam particles and residual gas occur very frequent under the given relative densities in the LEBT. Two factors for a radiation ejection causing light in visible wavelength are crucial. There is on the one hand the loss of energy of a colliding charged beam particle transferring its energy and on the other hand the subsequent excitation or ionization of the residual gas atoms. Other interactions<sup>3</sup> are just marginal, because of their much smaller effective cross sections. In a collision the charged particle of the beam transfers energy to the residual gas atom causing the excitations:



where  $X$  is a beam particle and  $Y$  is a residual gas atom, resulting in the emission of a light quantum.

<sup>3</sup>e.g. elastic scattering of ions by residual gas, ionization of the residual gas by electrons, additional, secondary ionization of the beam ion by residual gas

# 1 Preparations for Beam Diagnostics using Tomography

---

By the Bohr frequency condition<sup>4</sup> the relation between the excitation energy  $\Delta\mathcal{E}$  and the emission of a spectral line with wavelength  $\lambda$  is given by

$$\Delta\mathcal{E} = \hbar c \tilde{\nu} = \frac{\hbar c}{\lambda}, \quad (1.2)$$

where  $\hbar$  is the Planck constant,  $c$  is the light velocity and  $\tilde{\nu} = \frac{\nu}{c} = \frac{1}{\lambda}$  with  $\nu$  as the frequency of the emitted spectral line. The intensity of this excitation radiation is given by the number of emitted light quanta per time and volume. This number depends on the density and composition of the residual gas, the energy of beam ions, the kind of ions, and beam current as well as on the effective cross sections. Another not negligible fraction influencing the intensity, results from the recombination of ionized residual gas atoms with captured electrons:



and the process of charge reversal



More details and a focussed analysis of the effective cross-sections and influences can be found in [Sit95]. The changeover from optical projection of the intensity distribution of the emitted light  $I(y)$  to the particle density distribution in a three-dimensional space  $\rho(r)$  is well known as inverse Abel transformation, which is a preliminary stage of tomography. Based on the measurement of one projection and the assumption of a radial, cylindric geometry one can describe the relation between  $I$  and  $\rho$  by (also see Fig. 1.7)

$$I(y) = 2 \int_0^{x_R} dx \rho(r(x)), \quad (1.5)$$

where  $x_R$  is the length of  $x$  at a maximum radius  $R$ .

With  $x^2 + y^2 = r^2$  and  $y$  a parameter, it follows from (1.5)

$$dx = \frac{r \, dr}{\sqrt{r^2 - y^2}}. \quad (1.6)$$

Applying (1.6) to (1.5) it follows the relation between  $I(y)$  and  $\rho(r)$

$$I(y) = 2 \int_y^R dr \rho(r) \frac{r}{\sqrt{r^2 - y^2}}. \quad (1.7)$$

Equation (1.7) is referred to as Abel integral equation [Hac89] or Abel transformation. It has to be noticed that the Abel transform in Eq. (1.7) only is valid for plasma which is optical permeable. A derivation of the Abel transform of optically dense plasma can be found in [Neu67]. The analytic

---

<sup>4</sup>well known from the historical Franck-Hertz experiment

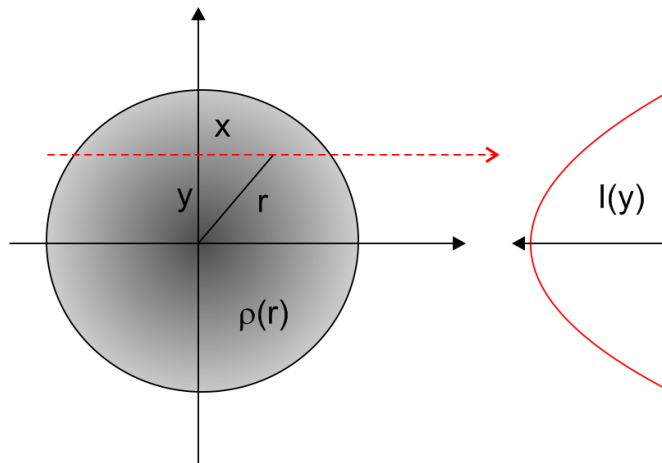


Figure 1.7: The inverse Abel transformation on a light intensity profile  $I(y)$  under the assumption of a radial, cylinder geometry of the density distribution  $\rho(r)$ , where  $r$  is the radius of the cylinder coordinates

reconstruction of the unknown distribution  $\rho(r)$  from the measured profile  $I(y)$  can be described by the inverse Abel transformation

$$\rho(r) = -\frac{1}{\pi} \int_r^R \frac{d I(y)}{dy} \frac{dy}{\sqrt{y^2 - r^2}}. \quad (1.8)$$

$I(x)$  could not be described analytically, but is given by a finite number of data points. As a consequence the integration in Eq. (1.8) can not be performed directly but has to be determined by numerical methods (e.g. [Tho94]). Optical methods, which are based on the determination of visible light have to take into consideration that the *profile width* is depending on several influences that have to be clarified before information can be obtained and interpreted. Additionally to the points mentioned above the luminous sensitivity of the optical measurement system has to be taken into consideration<sup>5</sup>. It is possible to conclude from the light intensity distribution to the particle density distribution by the inverse Abel transform in combination of some numerical methods, but the profile width can only be approximated.

## 1.5 Data Recording and Preprocessing

First measurements at the test stand were realized manually. In the future this will be taken on by an activation piloting.

Performing the tomography algorithm on the first measured datasets, the result was a twisted set of lines. To analyze and correct this deformation a thin twine was clamped exactly parallel through the

---

<sup>5</sup>e.g. it has been experienced that the measurement of uniform distributed beams also show a decay of light sensitivity from the center to the edge of the beam

## 1 Preparations for Beam Diagnostics using Tomography

---

beam hole in beam direction and a measurement with tomography was performed. The result was the same deformation as was noticed at the beam data before and can be seen in Fig. 1.8 (left) The reason

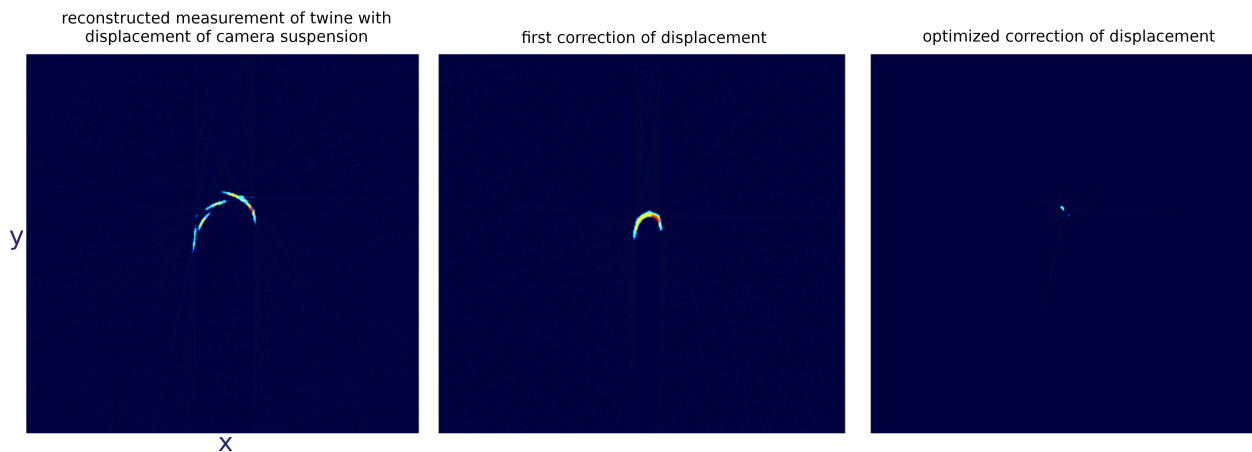


Figure 1.8: The distortion discovered at the first measurements were analyzed and corrected by using a thin twine which was clamped through the beam hole. Colors are inverted for a better visibility of differences.

for this very characteristic distortion of the measurement is a displacement of the camera suspension. It results from the fact that two opposed projections are not congruent but shifted against each other, which contradicts the basic requirement of the Radon transformation. The middle and right hand side of the figure shows the correcting adjustment steps. After this mechanical correction, the focus of all projections is the middle of the image, which is a good approximation, since the twine was centered in the beam hole. Nevertheless, the projections do not meet all in the same point, although they are close to it. To accomplish a congruence, one can determine the centroid for every projection in the Radon plot and shift it to the center of the projection by enlarging the profile by zeros. As can be seen by a comparison to the optimally adjusted camera suspension, performing the centroid correction on a not optimized measurement causes differences not negligible in the back projected distribution. The center of the beam with high intensities is significantly enlarged. Details of strategies to optimize profile adjustment can be found in [Wag11].

It also has to be noticed that the assumption of a beam that is centered in the beam hole, as it is done by the centroid shift method, has to be paid with the loss of information about beam position. In Fig. 1.9 this can be seen by the centering of the back projected beam on the right hand side. If an adjustment of the camera suspension can be carried out with sufficient accuracy, the centroid shift better is avoided. If the information of beam position is not important, the centroid shift can enhance the accuracy of the back projected distribution.

In the given assembly the rotatable vacuum chamber is driven to predefined angles. In the example measurement the angle steps have been set from  $0^\circ$  to  $179^\circ$  in steps of  $1^\circ$ . Having reached the actual position the driver unit feeds back the real value of the angle, from which the projection has been taken. Because of static reasons there are small deviations from the predefined angles, which range in many cases at an angle accuracy of  $\pm 0.1^\circ$  but sometimes raise to aberrations of  $\pm 0.9^\circ$  (Fig. 1.10) A

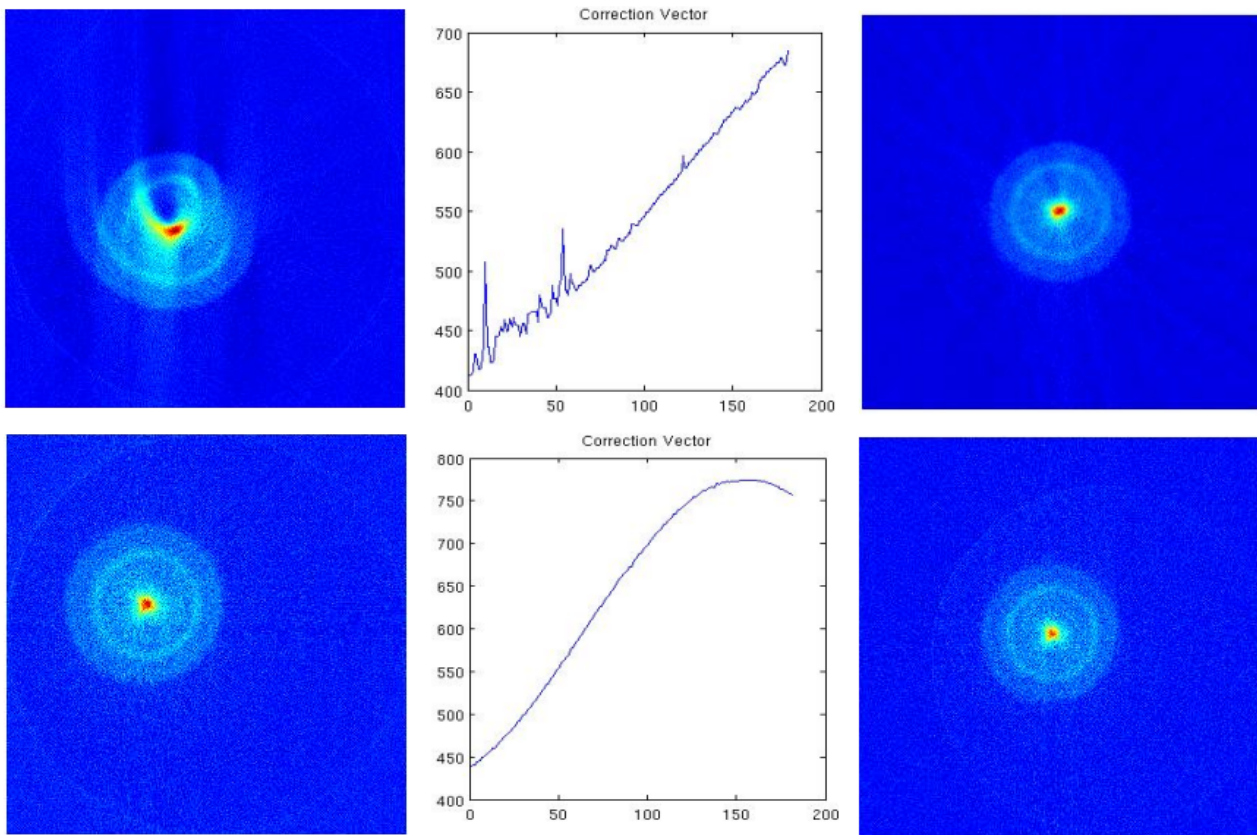


Figure 1.9: The correction by centroid shift for a beam with not optimally adjusted camera suspension (top) and optimated camera suspension (bottom). The correction vector shows the amount of corrections necessary for every projection angle in the Radon plot.

general aberration can be estimated by a mean square error of  $0.07^\circ$  for the introduced measurement device<sup>6</sup>. The influence of this aberration to the tomography result for ordinary space tomography is comparable with the effect shown in section 2.3.4, especially Fig. 2.25. Considering this, the influence of an aberration of  $< 1^\circ$  is definitely negligible.

The data acquisition is divided into two subtasks. The first is the data recording. The second is the data preprocessing. The images were taken as 14-bit grey scale pictures at a shutter speed of 5s. The choice of the residual gas and shutter speed has influence on the result of the processed data. In the following, only the generally necessary data preparation by preprocessing will be described.

1. *raw data* The data of a single measurement is a  $1200 \times 1600$  px image storing the intensity distribution of the beam along the longitudinal direction and one transverse direction from one angle of sight in a matrix.

<sup>6</sup>based on different measurement cycles

# 1 Preparations for Beam Diagnostics using Tomography

---

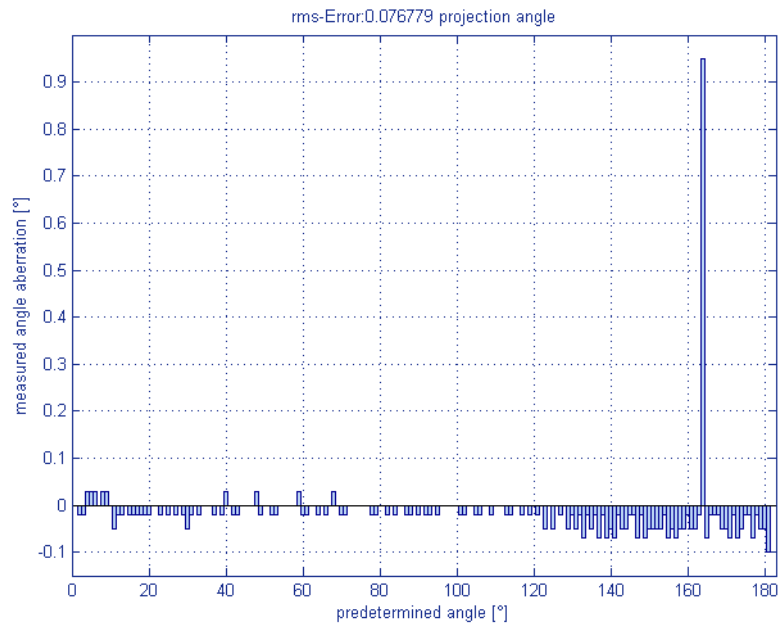
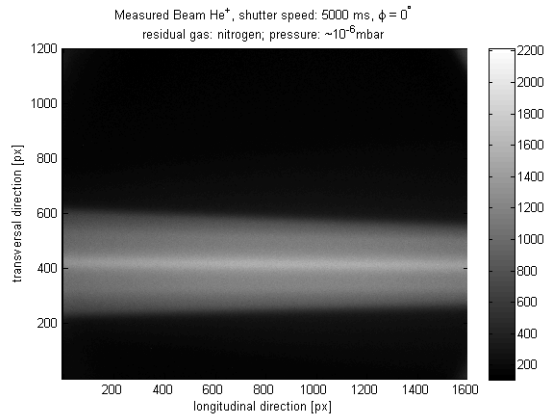
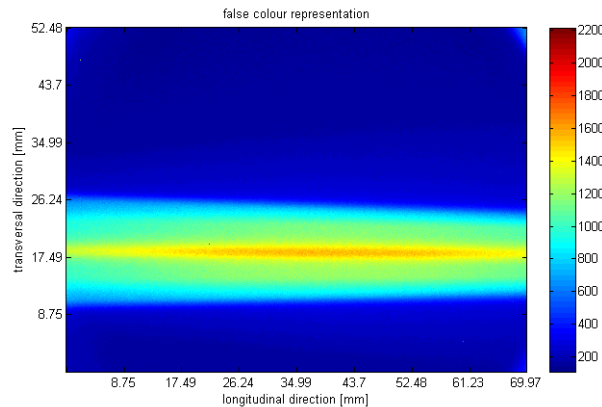


Figure 1.10: Aberration of real projection angles from predefined projection angles for the introduced measurement device.



raw data

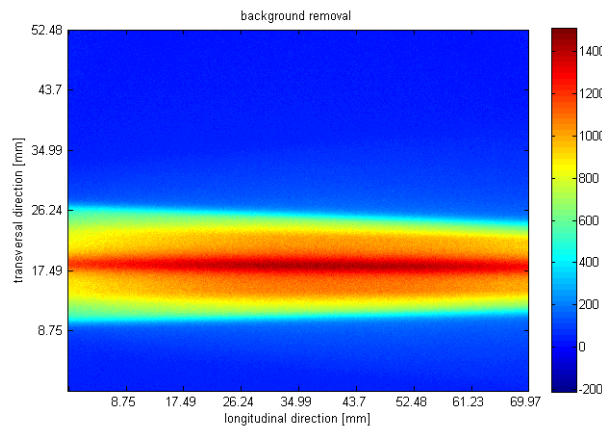
2. *false color and size* The real size of the image is determined by the analytic computation of the sensor diagonal and the opening angle of the objective. From that the size of the object at a given distance can be determined. Additionally the grey scale representation is displayed in a false color scale for a better differentiation of intensities.



**size and false color representation**

In this representation two problems become obvious. The first are the intensity artifacts at the image edges. The second is the deformation on both sides of the beam caused by a vignetting of the camera.

3. *background removal* The background is subtracted. The background was taken during the measurement by taking an image without beam. In the manual operation of the measurement, a background for every angle of sight was taken, what makes sense, since there may be different background artifacts depending on the amount of reflection. In online mode this will not be possible. In this case the background has to be taken once at the beginning of the measurement to remove background noise.



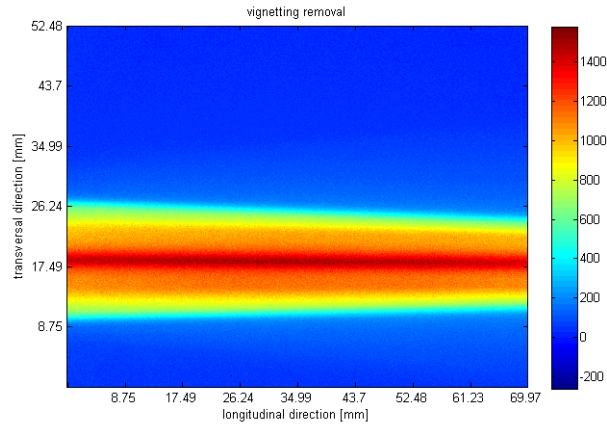
**background removal**

The intensity artifacts at the image edges disappeared. The intensity range was shrunk from  $[0..2200]$  to  $[-200..1400]$ . The deformation of the vignetting is more distinct. The focussed character of the beam now could be seen very clearly.

4. *vignetting removal* The vignetting is removed by a  $\cos^4$ -filtering.

# 1 Preparations for Beam Diagnostics using Tomography

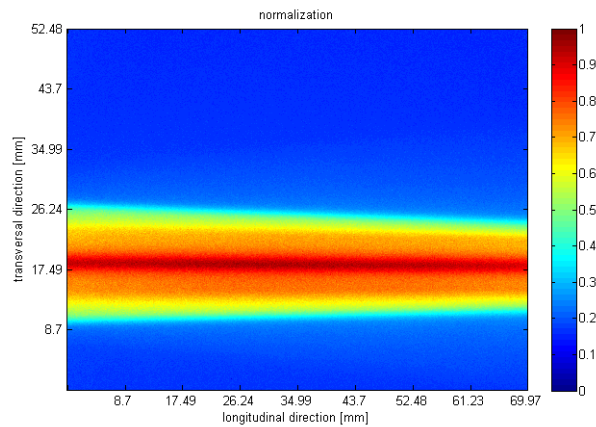
---



**vignetting removal**

The deformation now clearly is repaired.

5. *normalization* The image intensities are normalized to values of [0..1].



**normalization**

The data now are prepared for further processing by tomography and analysis algorithms.

## 1.6 Diagnostic Pipeline

The procedure of beam diagnostics is a complex task that consists of subtasks like acquisition, conditioning by preprocessing, reduction to information and analysis of the information to evaluate if the diagnostic aim is fulfilled. Diagnostics follows a fixed order of steps that can be represented in a general diagnosis pipeline as shown in Fig. 1.11.

At the beginning of the diagnostic procedure data has to be gained from a measurement or a simulation (step one Fig. 1.11). A measurement or simulation just leads to *datasets* (or better *raw datasets* to



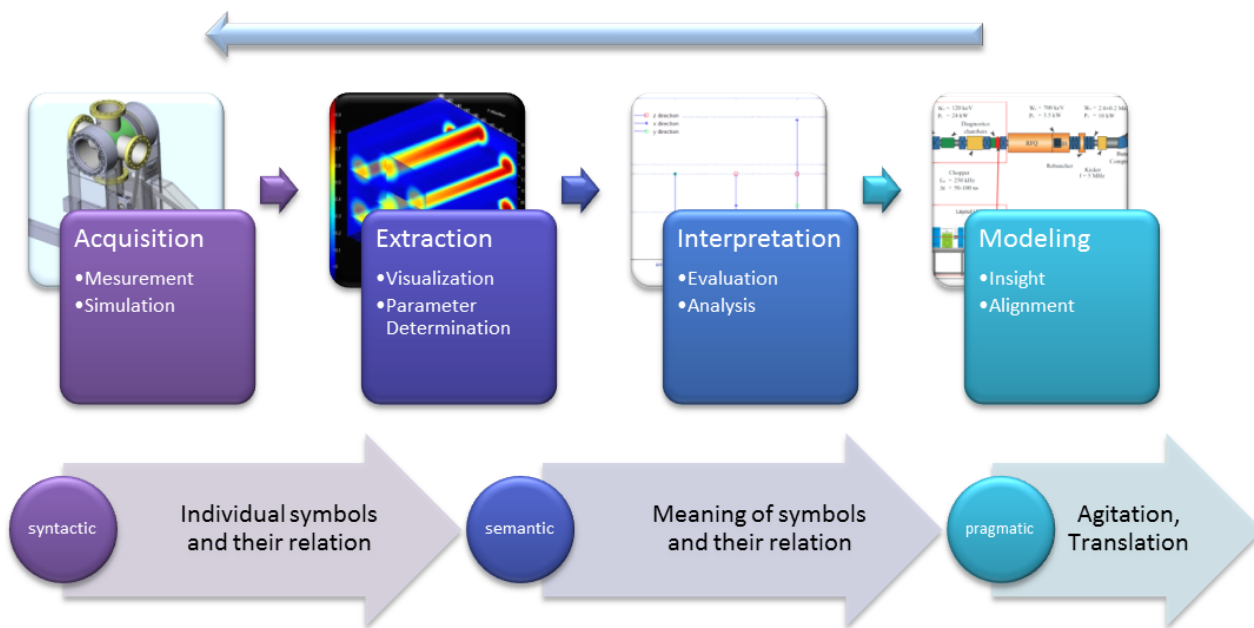


Figure 1.11: A general diagnosis pipeline with the corresponding three dimensions of information.

distinguish them from processing data). Obtaining data from a measurement or simulation already includes knowledge about the information that has to be gained from it. On the other hand, information requires a defined amount of a priori knowledge. A fact that will be discussed in the next paragraphs. At this point it will only be noticed that this has to be considered when designing a measurement device in section 1.3. Because of measurement artifacts and noise, raw data have to be conditioned by a preprocessing as shown in section 1.5. Preprocessed datasets are still raw datasets. In the strict sense they are just a large amount of numbers. Therefore in a next step there is a need to extract processing data from it. Processing data are obtained by visualization and parameter determination (step two Fig. 1.11). Processing data still are not information but they are the primary stage to gain it. In [Ham73] R.W.Hamming cites

*The Purpose of Computing Is Insight, Not Numbers.*

This *implies a purpose behind the computing* such that the mathematical processes mirror real-world situations<sup>7</sup>. Information can be gained by analysis and evaluation of processing data (step three Fig. 1.11). This information is not independent. It depends on the questions asked, and again on the a priori knowledge that is brought along to understand the answers. The result of this stage is information that can be used to have insight into major coherencies, real world situations or thesis building on the one hand, or to help to operate larger structures, and to serve necessary alignment

<sup>7</sup>There was a decades lasting discussion about the statistical measure of the *RMS-emittance* and the question if there really exists a correspond of it in real world. As discussed in section 5 one can find a real world derivation from the harmonic oscillator, that elevates the RMS-emittance from the state of a pure numerical concept to a real world representation.

## 1 Preparations for Beam Diagnostics using Tomography

---

procedures (step four Fig. 1.11). It is possible to draw back an arrow to the acquisition again, since the diagnostic pipeline will be iterated in most cases repeatedly to get satisfying results.

As mentioned there is a reciprocal coherency between a priori knowledge and newness of information that influences the quantity of information that can be obtained by a method. The more assumptions a method needs to be performed, the less the output of the method will be something new. But newness is one of the basic requirements for information [Sha49]. A priori knowledge is needed to set

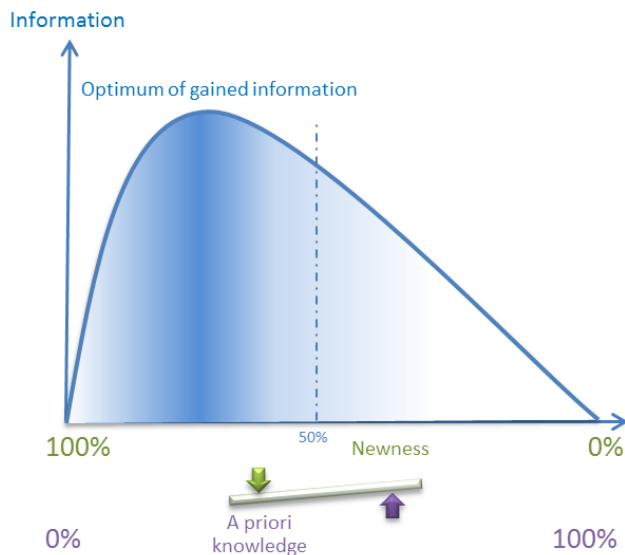


Figure 1.12: Reciprocal coherency between a priori knowledge and newness which influences the quantity of information to be obtained.

up an experiment and analyze and interpret resulting data, otherwise the data are meaningless. The optimum of information gain is not placed in the middle between a priori knowledge and newness of information but is placed at minimum a priori knowledge that is necessary and maximum newness that is possible, as shown in Fig. 1.12. One example of this principle related to this work is the determination of emittance. Determining the RMS-emittance out of a reconstructed phase space image includes the a priori knowledge of the beam transport matrix. Neglecting effects of noisy data<sup>8</sup>, the RMS-value mirrors a statistical approximation of the actually occupied phase space area. Determining the effective emittance value includes the additional assumption of a beam edge<sup>9</sup>, which leads to the surface area of an encircling phase space ellipse that is equal or larger than the actual emittance value. The additional assumption in a method using the surface area of the ellipse excludes all beams where nonlinear effects cause a distortion of the elliptical area by treating them the same way as beams without aberrations (see Fig. 5.6). The result is a less reliable information about the real beam emittance. On the other hand,

---

<sup>8</sup>In many cases a 80% RMS-value is regarded since the influence of noise in the lower 20% leads to aberrations not negligible. For this example one can imagine to compare this 80% RMS-value with the 80% effective value, to disregard this circumstance.

<sup>9</sup>this is where the signal to noise ratio is approximately 1, which is an extremely unreliable criterion.

if it is assured that there are no (or negligible) effects on the beam, such that the elliptical area is not expected to be distorted, the assumption is a fact that rises out of the nature of the particle ensemble, acting as one particle that is *blurred* over the phase space area, which is elliptical for reasons explained in section 3.2 and Fig. 3.2. This is equivalent to a determination of RMS-emittance (Eq. (5.12) to Eq. (5.20)) since it also represents the description of a harmonic oscillator. Many of these assumptions have been made to handle problems that otherwise could not be solved efficiently. Two of them are the assumptions that the beam has nearly rotational symmetry and that the particle distribution of it is Gaussian-like.

It has been shown that information is dependent on the problem it is related to and the a priori knowledge. This is a requirement of Shannon's [Sha49] basic mathematical theory of information. The information content is based on a probability that a message transfers *nothing new* to the receiver. From this, Shannon derives the definition of entropy as a measure for the expectation of newness of an information. In the context of an experiment or diagnosis the abstract concept of a message can be described by the potential information, which is the information that can be gained by observation, expressed in the change of entropy between two or more observations<sup>1011</sup>. The principles of Shannon's information theory are the first dimension of information, called syntactic dimension. It deals with the relation between different, individual symbols of a message or observations. Having a look on Fig. 1.11 this dimension of information is used by translating raw data gained by the measurement device into processing data which in this case show the relation between different intensity levels in form of an intensity distribution with a set of characteristics. The syntactic dimension is a subset of the semantic dimension of information [Kue90]. The second dimension additionally contains the meaning of the relations between symbols. The syntactic dimension just contains observations. The semantic dimension contains the context of a priori knowledge. In this dimension there are two reference layers. The micro layer contains all possible configurations that can be observed. The macro layer contains the potential information, which is the maximum information that can be derived by the complete knowledge about the micro layer. Semantic stages are hierarchic and are depending on the context. The symbols of every stage are restricted by constraints. This means that there will be no information if the macro layer is set to a hierarchically lower and the micro layer to a hierarchically upper stage, only the other way round. The a priori knowledge is stored in the semantic stages and the constraints between them. In the following this will be vividly explained the way it was used for optical diagnostics in this work.

The observed system is the beam, which can be separated into different semantic stages storing information which can be obtained by setting the micro and the macro layer and following the given constraints. In this work the semantic stages given in Fig. 1.13 have been defined to serve as basis for the optical diagnosis using tomography at the end of the LEBT of FRANZ. The definition of the

---

<sup>10</sup>The disadvantage of this definition in terms of the Shannon entropy is, that the difference between the entropy of two different observations can become negative. Therefore Alfred Renyi developed a generalized theory of the Shannon entropy [Ren70]

<sup>11</sup>One has to be careful to *not* connect the principle of entropy in Shannon's and Renyi's probability theory with the entropy used in statistical mechanics e.g. [Bri62, Bri53, Pet01]. The function of entropy in the context of phase space, which is a thermodynamic probability space is based on the Boltzmann constant, energy, and momentum. On the other hand the concept of entropy in probability theory is just based on an abstract definition of information without mechanical dimension. This is important to know when using techniques determining the entropy of projections (e.g. Tomography using Maximum Entropy), this entropy is *not* an entropy in a thermodynamic sense.

# 1 Preparations for Beam Diagnostics using Tomography

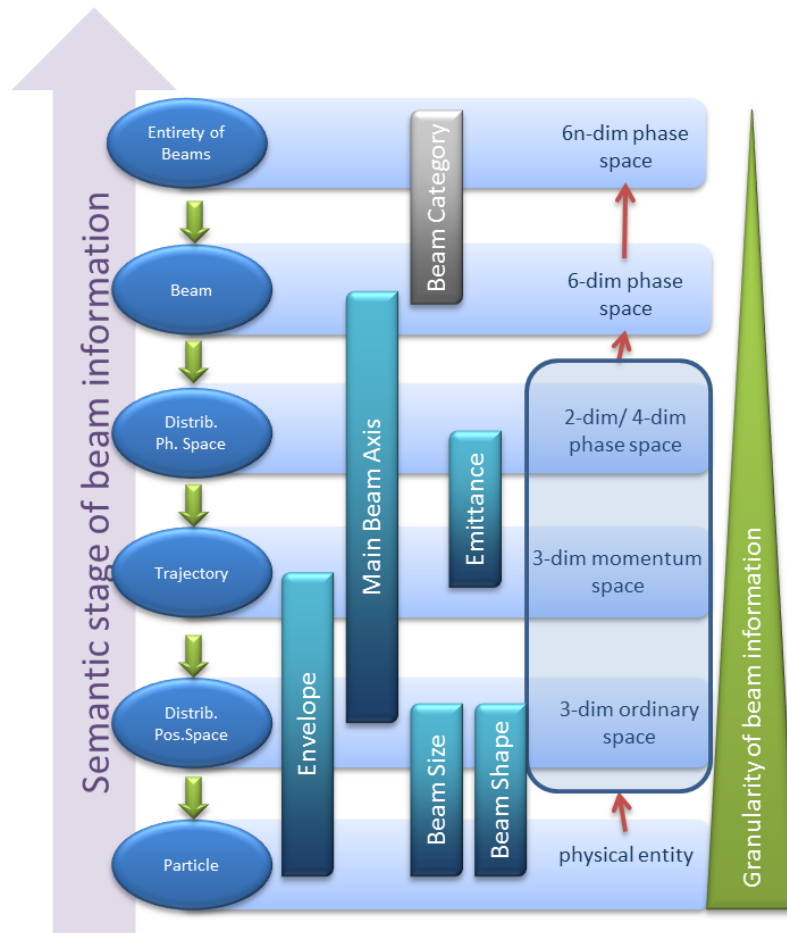


Figure 1.13: Semantic stages of an ion beam and the micro-macro relations containing information determined in this work.

semantic stages is depending on the application, therefore in another context they may be defined in a different way. The lowest stage is given by the physical entity of particles of the beam. Using optical diagnostics they could not be measured directly but their behavior can indirectly be determined by the recording of the residual gas radiation with a CCD-camera as described in the proceeding sections. The residual gas radiation is not a semantic stage on its own in this case<sup>12</sup>.

Observing one single point of time and the position of each particle at this point in a Cartesian coordinate system with two transverse directions  $x$  and  $y$  and a longitudinal direction  $z$  leads to the definition of the second semantic stage, the three-dimensional ordinary space. Performing a tomography as described in chapter 2 on the complete observed area leads to a three-dimensional map in form of a volume. This volume stores in every slice, representing a step in  $z$  direction, the density distribution

<sup>12</sup>There may be other situations where this is indicated. Over here the stage is reduced to the physical entity of the particles. The relation to the residual gas radiation is given by the constraints explained in 1.4.

of particles in the transverse  $xy$ -plane. Setting the physical entity of all particles as a micro layer and the distribution in ordinary space as macro layer, the possible distributions result from all possible configurations of particles under the effective constraints. These constraints are explained in detail in chapter 3. From this setting of the micro and the macro layer the information of beam size and beam shape can be obtained as shown in section 4.1.

Regarding the fact that a beam is the result of moving particles, which each on its own traces a trajectory. The next semantic stage is the three-dimensional momentum space reflecting the collectivity of all moving directions of the particles as shown in Fig. 1.14. Since it is not possible to distinguish

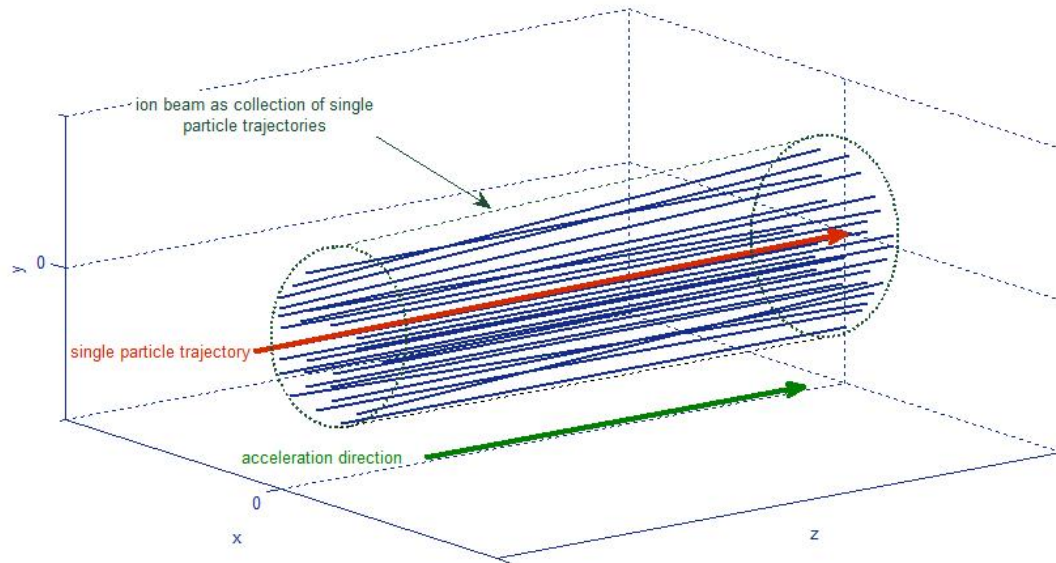


Figure 1.14: The beam as a collection of moving particles, each tracing its own trajectory.

single particles on the first stage, setting the momentum space stage as macro layer and the physical entity stage as the micro layer can *not* lead to an information concerning single trajectories<sup>13</sup>. The information, which can be obtained over here is that of the beam envelope mapping the behavior of the collectivity of particles which are given at the micro layer to an information about the global character of all trajectory paths in the macro layer, this can be measured as the change of beam size over the longitudinal direction.

The next semantic stage maps every dimension of ordinary space to its corresponding dimension of momentum space. The result are two- or four-dimensional phase spaces (see section 3.1), which are subspaces of the six-dimensional phase space representing the beam in the superior stage. Setting the micro layer to the two three-dimensional stages of impulse and ordinary space and the macro layer to the chosen phase space the information that can be obtained is the transverse and longitudinal emittance. The extraction of the transverse emittance is discussed in detail in chapter 5. Since the measured projection of one viewing angle contains the requirements for one of the two-dimensional subspaces

<sup>13</sup>This is a consequence of the reduction that had to be made in the first stage, when mapping the observation of particles to the observation of residual gas radiation. At this point the single trajectory information got lost.

## 1 Preparations for Beam Diagnostics using Tomography

---

viz a ordinary space dimension with its corresponding momentum space dimension like  $x$  and  $x'$ , the emittance can be obtained without performing a tomography in this dimension. For this technique, some a priori presumptions have to be made, which means to increase the a priori knowledge. With a modification of the tomography input, the two- dimensional subspaces can be reconstructed without this presumptions too, and the emittance can be computed from the reconstructed phase space.

As already mentioned, the six-dimensional phase space characterizing a beam in a distinct state is the next semantic stage. The three-dimensional position and momentum spaces as well as the two- or four-dimensional phase spaces are subspaces of this six-dimensional space. At this semantic stage the beam entirely is characterized. Setting the micro layer to the three-dimensional ordinary space and the macro layer to the six-dimensional phase space the relation between particle distributions in ordinary space, can be used to determine the centroid of the reconstructed volume and the main beam axis, which is an information about the beam position, discussed in section 4.2.

As said before, the six-dimensional phase space is the characterization of one distinct beam. As explained in section 3.1 this beam can be interpreted as one single super-particle which is blurred over the full phase space, in the sense of its behavior. This *super-particle* is one point in the six- $n$ -dimensional phase space which contains all possible beams with  $n$  sub-particles. This allows to compare beams in different states and to evaluate their quality. With this, the beam diagnosis has reached its aim. Finally, it has to be mentioned, that the use of some optical devices (e.g a solenoid) may cause a violation of constraints between some micro- and macro-layers (e.g. it changes the validity to separate the six-dimensional phase space in two-dimensional phase spaces which is necessary for phase space tomography).

# 2 Tomography

## Contents

---

<b>2.1</b>	<b>Properties and Conditions of the Dataset <math>M_p</math></b>	<b>30</b>
<b>2.2</b>	<b>Tomography with Filtered Backprojection</b>	<b>30</b>
2.2.1	Derivation of Algorithm	31
2.2.2	Examples and Representations	36
<b>2.3</b>	<b>Artefacts and Noise</b>	<b>41</b>
2.3.1	Distortions in Fourier Space	42
2.3.2	Filter Performance for Measurement and Simulation	45
2.3.3	Ghost Particles	47
2.3.4	Image Defects	50
<b>2.4</b>	<b>Other Tomography Algorithms in a Nutshell</b>	<b>51</b>
2.4.1	Algebraic Reconstruction Technique	52
2.4.2	Maximum Entropy Method	54
<b>2.5</b>	<b>Comparison of Algorithms</b>	<b>57</b>
2.5.1	Space and Time Requirements	57
2.5.2	Projections	58
2.5.3	Noise and Image Defects	58
2.5.4	Choosing a Reconstruction Algorithm	59

---

In general tomography deals with the task of reconstructing a 3-dimensional volume out of two-dimensional measurement representations of an object. Unfortunately a descent to a lower dimension layer always is associated with loss of information. Whenever one maps a  $n$ -dimensional object with a  $(n - 1)$ -dimensional representation there is a lack of information when trying to backtransform the object again into  $n$ -dimensional space. In 1917 the Austrian mathematician Johann Radon showed in his cutting-edge talk [Rad17] that a two-dimensional object property can be exactly and without loss of information described by an infinite number of line integrals.<sup>1</sup> In case of ion beam tomography this two-dimensional object property can be the particle density in a two-dimensional Cartesian space  $(x,y)$  at a defined position  $z_i$  of the longitudinal direction  $z$ , which is the acceleration direction. The problem for the ion beam tomography algorithm can be defined as follows:

---

<sup>1</sup>Originally Radon states, which he owes the idea for his proofs out of a question that arose from the theory of Newtonian Potential.

## 2 Tomography

---

Given a set of two-dimensional optical measurements  $M_p$ , determine the distribution of particle density  $\mathcal{F}(x, y)$  inside the beam.

The general form of the Radon-Transformation denotes: If for all angles  $\varphi$  in the interval  $\varphi \in [0^\circ, 180^\circ]$  and an infinite number of line integrals  $s_i$  for each projection all associated Radon transforms  $\rho(\varphi, s)$  can be determined, no information of the object property  $\mathcal{F}(x, y)$  will be lost

$$R(\mathcal{F})(\gamma) := \int_{\gamma} \mathcal{F}(x, y) dx = \int_{-\infty}^{+\infty} \mathcal{F}(x, mx + b) dx, \quad (2.1)$$

where  $\gamma : \{(x, y) \in \mathbb{R}^2 | y = mx + b, x \in \mathbb{R}\}$ . In the following it will be investigated how this can be adapted to the special case of ion beam tomography. In section 2.1 the properties and conditions which are necessary to perform a beam tomography are determined. The tomography algorithm using filtered backprojection, which predominantly is used in this work, is derived in section 2.2, and results with different possibilities for the visualization of the backprojected volumes are shown in section 2.2.2. In 2.3 problems with noise and artefacts are discussed. The filtered backprojection method contains a filter dilemma, which is introduced and analyzed to find the best fitting filter for the application in beam tomography. The effect of the analyzed filters then are demonstrated by the reconstruction of a simulated and a measured beam in section 2.3.1. Other occurring artefacts and defects like ghost particles and the influence of image defects are investigated in sections 2.3.4 and 2.3.3. Two other generally used tomography algorithms are introduced shortly and evaluated with their assets and drawbacks in section 2.4.

### 2.1 Properties and Conditions of the Dataset $M_p$

The classical area of application of the tomography algorithms is medical diagnostics with X-radiation. Out of a source X-rays are forwarded through a collimator, that lets pass only rays in the intended direction. Those rays permeate the parts of the body that have to be examined. On the opposite side a detector measures the incoming rays. This data will be converted to a negative profile that contains the information of transmissibility of the X-rayed tissue to gain  $M_p$  (see Fig. 2.1 a). Although there exist optical techniques in beam diagnostics that extract beam information from radiations in frequency spectra of X-ray, visible, infrared and micro-wave, only the projections in visible frequencies will be considered, since the used measurement device in this case will be a CCD-camera. However, if one derives the necessary parameters for a tomography, viz necessary matrices with adequate intensity values with the corresponding angles, tomography also will work in other frequencies. Taking data with a CCD-camera by making a picture of visible residual gas radiation will directly lead to  $M_p$  (see Fig. 2.1 b). Also structures inside the beam are visible, presupposed that the residual gas radiation is not optical dense. One also can compute a 3-dimensional tomography representation of an optical dens beam. The result will be the outer shape of the beam, without inside information.

### 2.2 Tomography with Filtered Backprojection

To understand, what tomography means in terms of an ion beam environment, firstly a look at the initial geometrical situation of equation (2.1) will be taken (see Fig. 2.2). A CCD-camera picture, taken



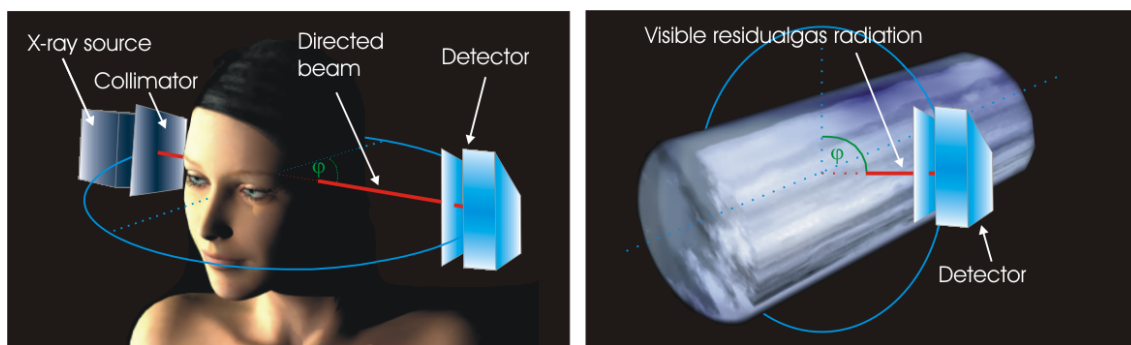


Figure 2.1: a) Medical tomography (left). Detector measures incoming X-rays which have permeated tissue.  $M_p$  is computed by the difference of original X-ray intensity and incoming intensity into a negative profile that contains information about the transmissibility of the X-rayed parts of the body. b) Beam tomography (right). Detector measures the intensity of residual gas radiation in visible spectrum, which can be used directly as  $M_p$

from outside of the beam is a matrix of intensity values in transverse direction  $y_{ccd}$  and longitudinal direction  $z$ . Additionally fixed Cartesian coordinates  $(x, y)$  will be added to define the angle of view  $\varphi$ . In relation to the beam-slice always  $(x, y)$  will stay the same. This is necessary because the rotation of the angle of view changes for every CCD-camera picture the  $y_{ccd}$  and  $x_{ccd}$ . In every location  $z$ ,  $y_{ccd}$  projects all intensities along a line in  $x_{ccd}$  direction to one single intensity value. This is what, in terms of Radon, called line integral (in Fig. 2.2 these integrals are shown as green lines in the  $(x, y)$ -plane of the beam-slice in location  $z$ ). All line integrals at one single projection angle  $\varphi$  form an intensity profile  $s$  called the Radon transform  $\rho(\varphi, s)$  of angle  $\varphi$ . If the profile of one angle only is considered, this can be denoted as  $\rho_\varphi(s)$ .

### 2.2.1 Derivation of Algorithm

The first requirement to be determined is the linear equation of  $s$  (red line in Fig. 2.2). The general form of a linear equation is given by  $y = m \cdot x + b$ . The linear equation for a line through origin (see Fig. 2.2 : red dashed line) can be derived as follows. The slope is defined by  $m_1 = \frac{\sin(\varphi)}{\cos(\varphi)}$  and the ordinate axis intercept by  $b=0$ . Therefore, the linear equation is defined by  $l = \frac{\sin(\varphi)}{\cos(\varphi)} \cdot x$ . Now it holds

$$\begin{aligned}
 m_1 \perp m_2 &\rightarrow m_1 \cdot m_2 = -1 \\
 &\rightarrow \frac{\sin(\varphi)}{\cos(\varphi)} m_2 = -1 \\
 &\rightarrow \sin(\varphi) \cdot m_2 = -\cos(\varphi) \\
 &\rightarrow m_2 = -\frac{\cos(\varphi)}{\sin(\varphi)}.
 \end{aligned} \tag{2.2}$$

$m_2$  is the slope of the orthogonal line (see Fig. 2.2: red dashed line). The linear equation of  $s$ , then turns out if the polar coordinates are defined and applied as follows:

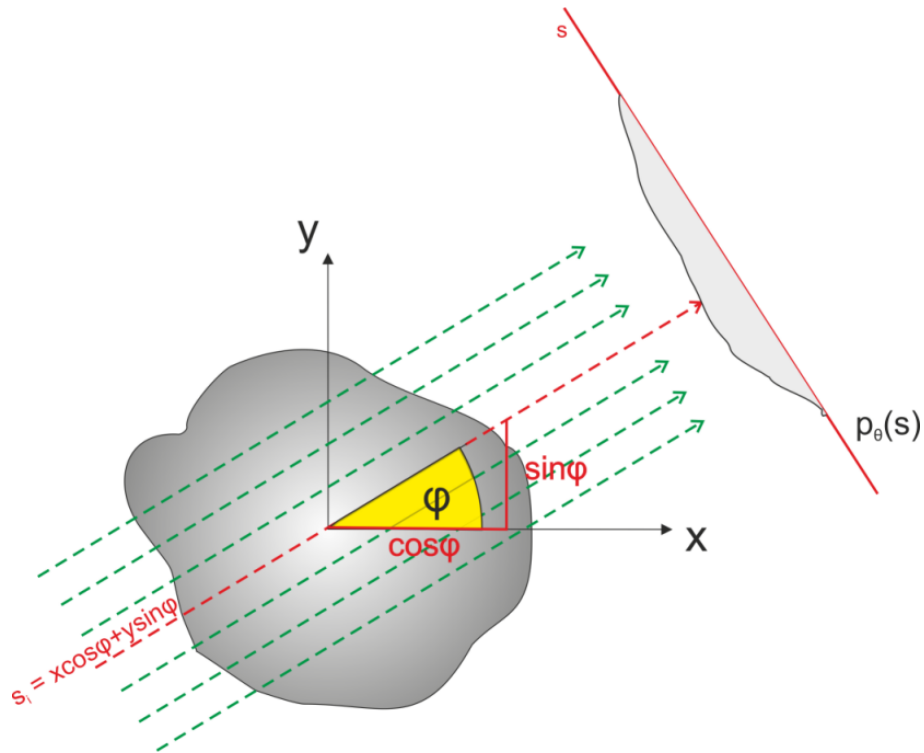


Figure 2.2: Initial geometrical situation of ion beam tomography. In a Cartesian plane  $(x, y)$  exists an unknown distribution of particles  $\mathcal{F}(x, y)$ . With equation (2.1) it is possible to approximate  $(x, y)$  by considering all line integrals along a projection  $s$  for all possible angles  $\varphi$ . For an exact reconstruction of  $\mathcal{F}(x, y)$  an infinite number of line integrals and angles would be necessary.

linear equation of orthogonal line  $s$ :  $y = -\frac{\cos(\varphi)}{\sin(\varphi)} \cdot x + b$   
 polar coordinates

$$\begin{aligned} y &= s_i \cdot \sin(\varphi) \\ x &= s_i \cdot \cos(\varphi) \\ \Rightarrow b &= \frac{s_i}{\sin(\varphi)}, \end{aligned} \tag{2.3}$$

it follows

$$y = -\frac{\cos(\varphi)}{\sin(\varphi)} \cdot x + \frac{s_i}{\sin(\varphi)} \tag{2.4}$$

$$\Rightarrow s_i = x \cdot \cos(\varphi) + y \cdot \sin(\varphi). \tag{2.5}$$

## 2.2 Tomography with Filtered Backprojection

In the following it is referred only to a single slice of the beam, seen from all projection angles. Given a set of pairs  $\langle M_p, \varphi_a \rangle$  of pictures  $M_p$  taken from the angle  $\varphi_a$ , exemplarily one slice  $s_j$ , viz one  $z$  position  $j$  is fixed, without loss of generality. All Radon transforms  $\rho_\varphi(s)$  of slice  $s_j$  for all angles  $\varphi$  will be added to the Radon plot (see Fig. (2.3)). The values of the Radon plot correspond to the

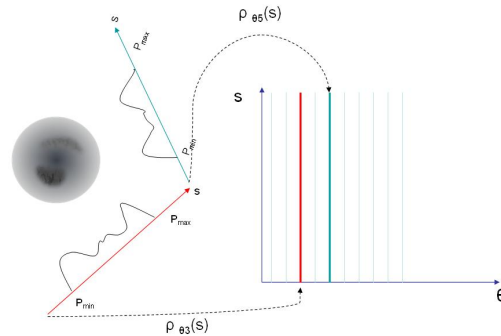


Figure 2.3: The Radon plot of one single slice  $s_j$  is created by adding all Radon transforms  $\rho_\varphi(s)$  of  $s_j$  for all angles  $\varphi$  to one single representation.

two-dimensional Fourier transform of the original density function  $\mathcal{F}(x, y)$ . Radon shows this in part A of [Rad17], later on it became usual to call the argumentation the Fourier Slice Theorem, which states:

*Given a function  $\mathcal{F}(x, y)$  with its two-dimensional Fourier transform  $F(u, v)$ . Let  $P(\varphi, w)$  be the 1-dimensional Fourier transform of the Radon transform  $\rho(\varphi, s)$ . Then  $P(\varphi, w)$  describes the values of  $F(u, v)$  along a radial line at angle  $\varphi$*

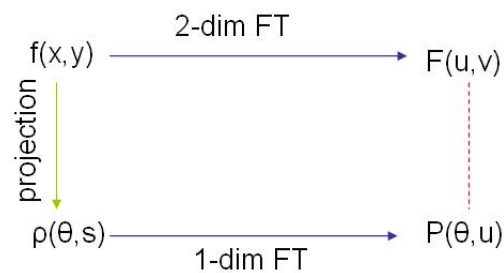


Figure 2.4: The Fourier slice theorem states, that the 1-dimensional Fourier transform of the projection of the original function  $\mathcal{F}(x, y)$  corresponds to the values of the two-dimensional Fourier transform of  $\mathcal{F}(x, y)$

<sup>2</sup>It has to be ensured that the pictures all project the same part of the beam

## 2 Tomography

---

Without loss of generality now the Radon transform for  $\varphi=0$  is considered by  $p(\varphi, s) \rightarrow p(0^\circ, x)$ . Following Radon, one can denote

$$\begin{aligned}
 p(0^\circ, x) &= \int_{-\infty}^{+\infty} \mathcal{F}(x, y) dy \\
 \overset{1\text{-dim FT}}{\rightarrow} P(0^\circ, u) &= \int_{-\infty}^{+\infty} p(0^\circ, x) \cdot e^{-2i\pi ux} dx \\
 p(0^\circ, x) \overset{\int_{-\infty}^{+\infty} \mathcal{F}(x, y) dy}{\rightarrow} P(0^\circ, u) &= \int_{-\infty}^{+\infty} \left[ \int_{-\infty}^{+\infty} \mathcal{F}(x, y) dy \right] \cdot e^{-2i\pi ux} dx \\
 \Rightarrow P(0^\circ, u) &= \int_{-\infty}^{+\infty} \int_{-\infty}^{+\infty} \mathcal{F}(x, y) \cdot e^{-2i\pi(ux+0y)} dx dy. \tag{2.6}
 \end{aligned}$$

Eq. 2.6 is the two-dimensional Fourier transform  $F(u, 0)$ . To gain the original, up to now unknown, distribution  $\mathcal{F}(x, y)$ , one only has to back project  $P(\varphi, u)$  by the inverse two-dimensional Fourier transformation, which is denoted by

$$\mathcal{F}(x, y) = \int_{-\infty}^{+\infty} \int_{-\infty}^{+\infty} F(u, v) \cdot e^{2i\pi(ux+vy)} dudv. \tag{2.7}$$

To apply (2.7), first the planar polar coordinates have to be defined by

$$\begin{aligned}
 u &= w \cdot \cos(\varphi) \\
 v &= w \cdot \sin(\varphi) \\
 dudv &= w \cdot dw d\varphi.
 \end{aligned} \tag{2.8}$$

Eq. (2.8) are applied to Eq. (2.7) which proceeds to

$$\begin{aligned}
 \mathcal{F}(x, y) &= \int_0^{2\pi} \int_{-\infty}^{+\infty} F(w, \varphi) \cdot e^{2i\pi(w \cdot \cos(\varphi)x + w \cdot \sin(\varphi)y)} w dw d\varphi \\
 \mathcal{F}(x, y) &= \int_0^{2\pi} \int_{-\infty}^{+\infty} F(w, \varphi) \cdot e^{2i\pi w(\cos(\varphi)x + \sin(\varphi)y)} w dw d\varphi.
 \end{aligned} \tag{2.9}$$

Applying  $\varphi \in [0, 180^\circ]$  and (2.5), equation (2.9) can be rewritten as

$$\mathcal{F}(x, y) = \int_0^\pi \int_{-\infty}^{+\infty} F(w, \varphi) \cdot e^{2i\pi ws} |w| dw d\varphi. \tag{2.10}$$

## 2.2 Tomography with Filtered Backprojection

By the Fourier slice theorem it is known that  $F(w, \varphi) = P(\varphi, w)$ , according (2.6) in the second step, it follows

$$\begin{aligned} \mathcal{F}(x, y) &= \int_0^\pi \left[ \int_{-\infty}^{+\infty} P(\varphi, w) \cdot e^{2i\pi w s |w|} dw \right] d\varphi \\ \Rightarrow \mathcal{F}(x, y) &= \int_0^\pi \tilde{p}(\varphi, s) d\varphi, \end{aligned} \tag{2.11}$$

where  $\tilde{p}(\varphi, s)$  is approximating  $P(\varphi, s)$ .

$\tilde{p}$  has to be introduced, since the infinite integral can not be calculated in practice. It is limited by the size and number of pictures in  $M_p$ . This implies that the quality of approximation, as far as image defect and noise are not concerned, *only* depends on the resolution of the pictures and the number of angles. The algorithm itself is not constrained by the size of the measurement data. Now the last thing to do is to care for the mysterious  $|w|$  that has slipped into the algorithm, when the polar coordinates were introduced, which was necessary to follow the two-dimensional Fourier transform from the Cartesian coordinate space to the polar coordinate space. For small  $w$  the values lie closer in the polar coordinate space because of the radial nature of this space (see Fig. 2.5). The consequence

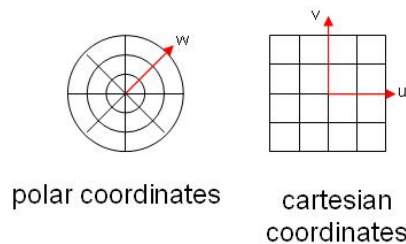


Figure 2.5: Because of the radial structure of the polar coordinates, values for small  $w$  lie more close to each other, than values for large  $w$ . This leads to a contortion of structures in Cartesian space.

for the backprojection will be, that low frequencies are over emphasized, with the result that large structures will be accentuated to much, while high frequencies, related to small detail structures, will be attenuated. A solution for this problem is to use a filter to equalize this effect. The accentuation of the low frequencies also have the undesirable effect that image noise will be intensified, which is located in this frequency domain.

There are two possible ways of application for a filter. The first will be to multiply the result of the 1-dimensional Fourier transform with  $|w|$ , such that  $F(w, \varphi) = P(\varphi, w) \cdot |w|$ , the second possibility is a convolution of the measured projection  $\rho(\varphi, s)$  with a kernel  $h(s)$ . The convolution in ordinary space or the filtering in Fourier space, both will correct the projection error: high frequencies will be

## 2 Tomography

emphasized, while low frequencies will be attenuated. The representation of details in the tomographic image of the beam will be improved.

Noise in Fourier space is located in high frequency domain. That implies that the filtering after the 1-dimensional Fourier transform with the mathematical filter  $|w|$ , will increase this noise. Therefore a practical filter with low pass characteristics is needed. Different filters will be discussed in section (2.3.1). For the main algorithm, just the filter kernel denoted by  $h(s)$  is mentioned and convoluted with the measured projection

$$p(\varphi, s) \rightarrow p(\varphi, s) \otimes h(s). \quad (2.12)$$

The algorithm is graphically explained in Fig. 2.6.

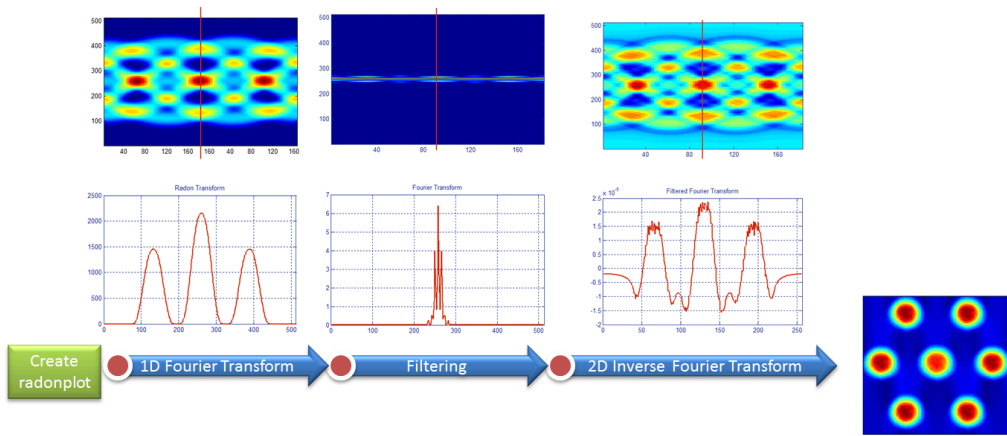


Figure 2.6: After the creation of the Radon plot a one-dimensional Fourier transform is performed on every Radon transform in the Radon plot. Then all Fourier transforms are then filtered by the selected filter kernel  $h(s)$ . A two-dimensional inverse Fourier transform then is performed on the complete result to obtain a single slice. For a complete volume all slices have to be determined and collected.

### 2.2.2 Examples and Representations

In the following the backprojection of a single slice of the simulated dataset S1 (see appendix) is shown exemplarily by the progress at  $0^\circ$  to  $180^\circ$ , in steps of  $30^\circ$ . A typical image of this dataset can be seen in Fig. 2.7. From these images, always the second profile is taken to backproject the second slice of the volume. First the Radon plot for the slice has to be created by arranging all second slices in a Radon plot as shown in Fig. 2.8. In this example always two columns are interpolated by an averaging to reduce computational requirements and the angle step-width was 2. The computational cost for a complete volume is high. If the number of discrete data-points in a Radon transform is  $n_{px}$  pixel (vertical length of the Radon plot) and  $\alpha_{px}$  pixel (horizontal length of the Radon plot) is the number of angles that have to be taken into consideration, for a single slice one has to compute  $n_{px}^2 \cdot \alpha_{px}$  values. If an image is about  $s_{px}$  in length (number of possible slices) the complete volume then can be computed

## 2.2 Tomography with Filtered Backprojection

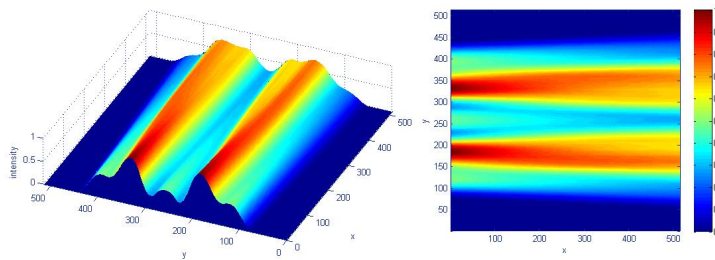


Figure 2.7: Basic image of data set A, showing a side projection from  $0^\circ$  angle of 511 slices. For the example slice 2 of all such projections is used.

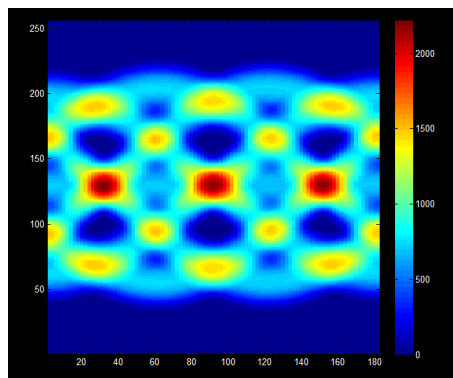


Figure 2.8: Radon plot of all second slices. To reduce computational cost, only 90 angles from  $0^\circ$  to  $180^\circ$  are taken with step-width 2, every Radon transform is interpolated to unite always two adjacent values.

by determining  $n_{px}^2 \cdot \alpha_{px} \cdot s_{px}$  values. For the simulated data sets with an image size of  $511 \times 511$  pixel and an angle step of 1 using 180 angles, this will be  $511^2 \cdot 180 \cdot 511 = 24.017.909.580$  values to be computed. As far as a measurement is concerned with an image size of  $1200 \times 1600$  pixel, this will be  $1200^2 \cdot 180 \cdot 1600 = 414.720.000.000$  values. Therefore strategies to downsizing computational cost are very important. Depending on what kinds of parameters have to be determined, one may only backproject selected slices. If the complete volume is needed (e.g. for beam position in section 4.2) one may prefer interpolation strategies in the different dimensions to reduce cost. Every computation for the update of a value is composed by obtaining the Fourier transform of a Radon transform, filtering the Fourier transform, computing the value of the actual pixel, and adding it to the image storing the over all progress of the backprojection. In Fig. 2.9 all these steps are shown for selected angles.

## 2 Tomography

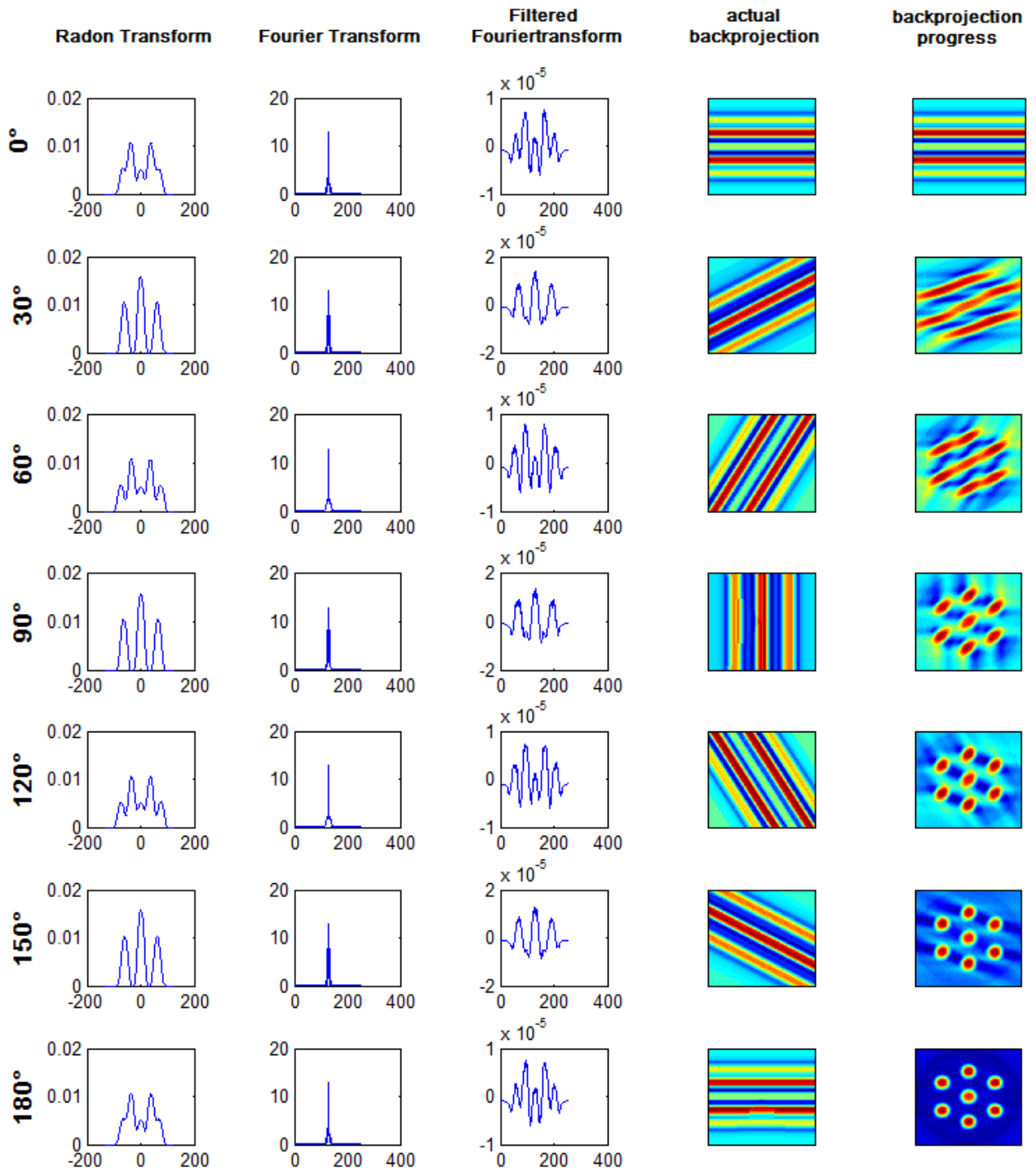


Figure 2.9: Computational steps for filtered backprojection shown at selected stages for the second slice of data set A.



## 2.2 Tomography with Filtered Backprojection

Having determined the Radon plot in Fig. 2.8. and the corresponding angles for every Radon transform in it, the backprojection can discretely be computed as shown in detail in [Kak88]. Another possibility is, to use the predefined matlab function *iRadon*, if working in this environment. This is useful for a quick look at single slices. Since the overall computational performance of matlab is quite more restricted than the implementation in other programming languages, for a permanent implementation the discrete algorithm is much more useful<sup>3</sup>. The result of the matlab function is quite as good as the discrete realization of the algorithm. There are some differences between the two possibilities that have to be known to interpret the result of the filtered backprojections in the right way. The first is, that the resulting slice is rotated clockwise by  $90^\circ$  using the discrete algorithm as can be seen by Fig. 2.10. The backprojection with *iRadon* is compressed in one dimension causing contortions. Re-

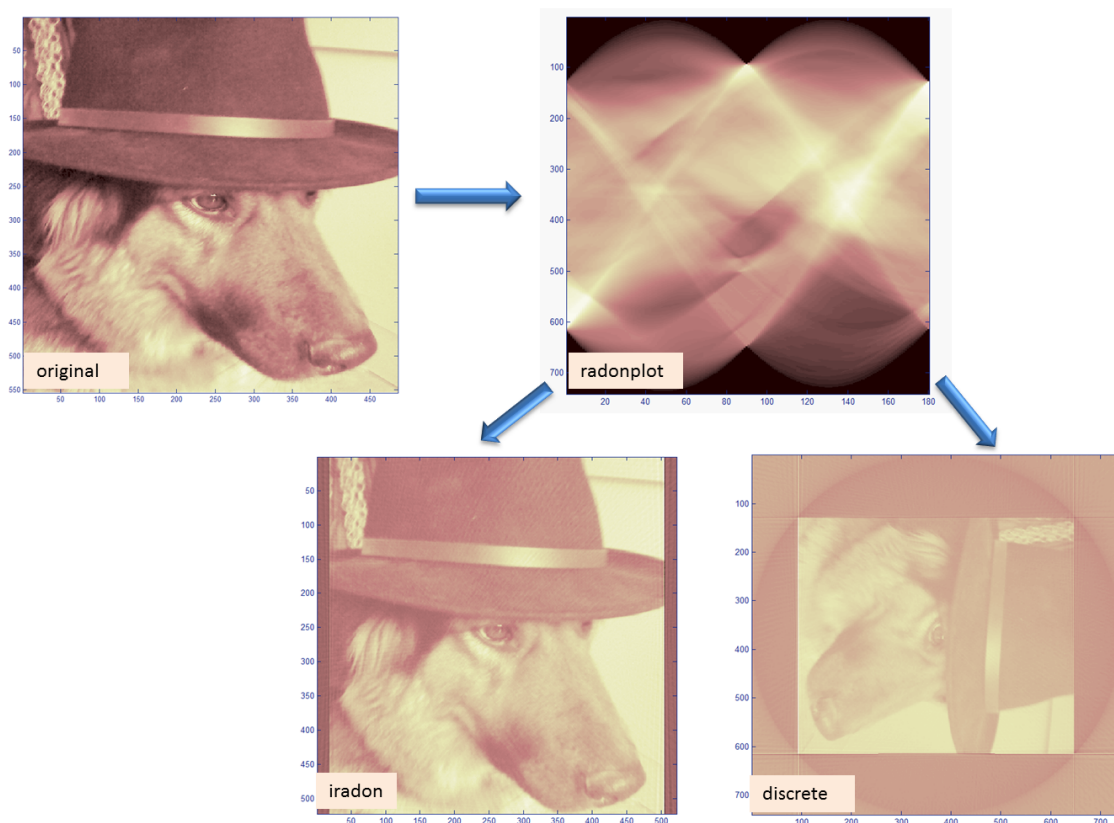


Figure 2.10: The image of Detective Emma has been backprojected by the matlab function *iRadon* and the discrete backprojection algorithm described in [Kak88]. Although the quality of the backprojection is nearly comparable, there are some points that have to be noticed, to interpret the image in the right way.

garding the backprojection with [Kak88] this effect is less distinctive (this is very obvious if comparing

<sup>3</sup>If dealing with problems of time performance a good way is, to implement the algorithm on a modern graphic board, which allows a massive parallel computing.

## 2 Tomography

the end of the nose and its distance to the bottom edge). On the first sight, the image of the discrete algorithm seems to have changed size. This is not the case, but one has to clip the frame that results from the rotation of the single backprojection angles. Having a look at the units, it turns out that the inner image corresponds in size with the image of the iRadon backprojection. This clipping has to be considered before determining real measurement units. Having a look back at the picture of the right bottom edge of Fig. 2.9 the circle caused by the rotation also could be identified. The true size of the image is the square that fits in this circle, as could better be seen in the example shown in Fig. 2.10 for the discrete case. Having backprojected one or more slices there are different possibilities to visualize and use the result corresponding to the information that has to be gained (Fig. 1.11 stage two on page 23). The whole volume can be characterized by showing the first and the last slice (representing the evolution of the beam in the observed sector) and to sum up all slices to one slice (representing cumulative characteristics) as shown in Fig. 2.11. The divergent characteristics of the beam, for example,

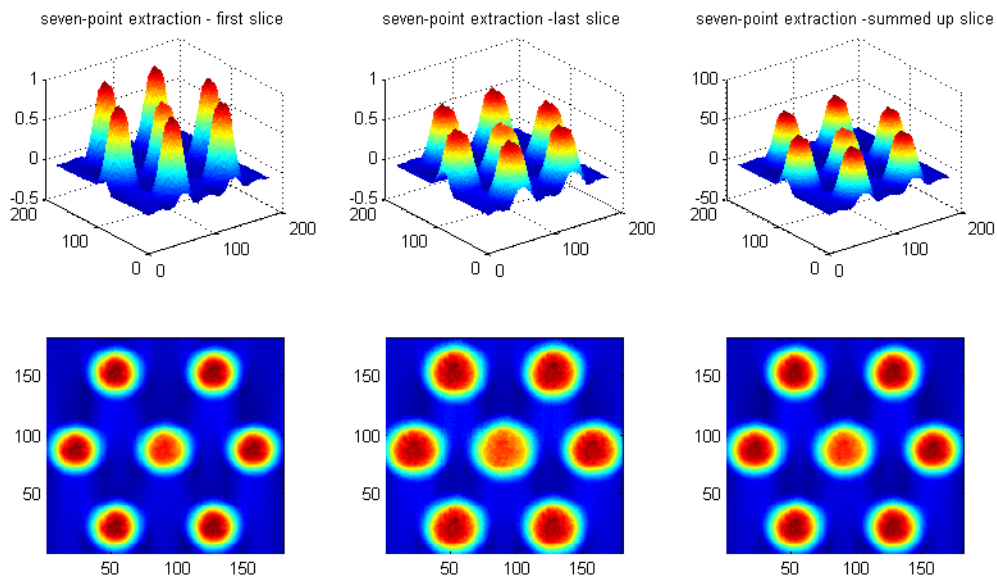


Figure 2.11: Visualization of a volume by the first slice, the last slice and a sum up over all slices.

can be recognized by the expansion which can be seen by a comparison of the first and the last slice. The beam size in the section which is covered by the volume, on the other hand, can be determined by the summed up slice, since this quantity is related to the total section. Being interested in the general behavior of the beam edges, one can have a look on the iso-surface areas in the volume. Fig. 2.12 (left) shows that the intensity fraction of 0.9 decreases very fast for the outer beamlets. The inner beamlet even do not have an intensity level of 0.9. In the representation of Fig. 2.11 one can guess that the intensity level of the inner beamlet is not equal to the outer ones, this fact is more obvious in the representation of iso-surfaces. Also the fast decay of this selected intensity can be analyzed in more detail. The characteristics of the iso-surface at an intensity level of 0.5 (Fig. 2.12) (right) shows irregularities especially in the second part of the volume. Such differences may give valuable hints for

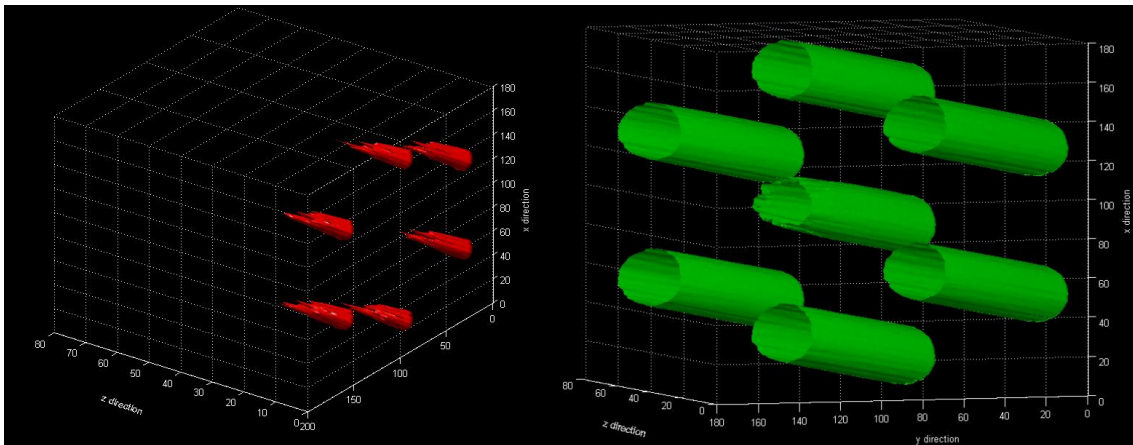


Figure 2.12: Iso-surface at an intensity of 0.9(left) and Iso-surface at an intensity of 0.5 (right)

an advanced analysis of the beam behavior beyond standard parameter determination. Finally the representation in three-dimensional ordinary space will be introduced. In many cases it is not useful to visualize the complete volume, since this blocks the view on interesting sections of the volume, as can be seen in Fig. 2.13 (left). The transparency of the data points had to be raised to see structures inside

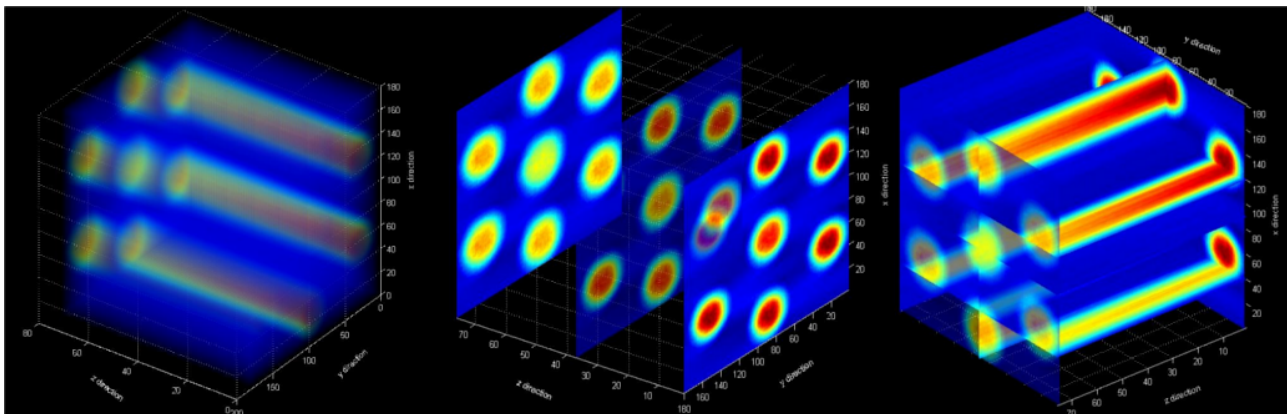


Figure 2.13: Possibilities to visualize the computed beam volume by 3d-representations.

the beam, but still the display is very diffuse and less informative. A solution is to just show selected slices. This can be done in the longitudinal direction Fig. 2.13 (middle) and then fulfills the same aim as the representation in Fig. 2.11 or vertically and even diagonally as shown in Fig. 2.13 (right).

## 2.3 Artefacts and Noise

The reconstruction of defective image data leads to ambivalent mapping and artifacts. Systematic errors impede the analysis of the measured data. Therefore it is necessary to detect and understand

## 2 Tomography

---

the impact of this influences and, if possible, to compensate it. In the following, first a look at the above mentioned problem of distortions in Fourier space and its compensation is investigated. Second, the well known phenomenon of ghost particles that arise out of tomography tasks on particle fields will be analyzed. Third the impact of image defects on the tomography result will be examined.

### 2.3.1 Distortions in Fourier Space

As already denoted in Fig. (2.5) the transformation from polar Cartesian space to Fourier space is attended by a contortion of the projection result. In polar space points related to small radii  $w$  lie closer to each other than those for large  $w$ . Having a look at the tomography algorithm the values of the 1D-FT are applied to the two-dimensional function  $F(u, v)$  (see Eq. (2.7) to (2.10)). To gain the point  $(u, v)$  all values of all Fourier transformed projections that contact this point, have to be summed up. Noting that this means all intensity values on a radial line around this point are taken into consideration, a pixel that is located near the center point of this radial lines is contacted more often than a pixel that is located farther away. Therefore the amplitudes in Fourier space are weighted unsymmetrically in favor of small distances from the rotation center. Regarding the frequency allocation of the Fourier space, low frequencies are located in the center of the Fourier transform, while high frequencies are located more outwards. Applying this in words of image processing, low frequencies representing large

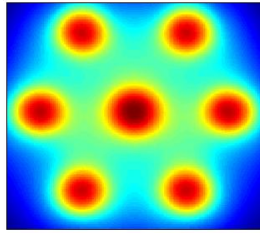


Figure 2.14: Backprojected slice of the seven point extraction beam (see appendix) without Fourier filtering. Because of an asymmetric weighting of the amplitudes in Fourier space, low frequencies are overemphasized, while high frequencies are attenuated. Therefore the back-projection has to be filtered to straighten the distribution for a correct reconstruction.

physical dimensions are overemphasized and high frequencies representing details are underemphasized. As shown in Fig. 2.14, this contortion leads to a haziness in the reconstruction, which blurs details and distorts a correct backprojection. This problem is solved commonly by applying a Ram-Lak filter introduced by Ramachandran and Lakshminarayan in 1971 [Ram71]. The Ram-Lak filter kernel is given by

$$h(s) = \frac{1}{2 \cdot a^2} \cdot \left\{ \frac{\sin(\pi \cdot \frac{s}{a})}{\pi \cdot \frac{s}{a}} + \frac{\cos(\pi \cdot \frac{s}{a}) - 1}{(\pi \cdot \frac{s}{a})^2} \right\} \quad (2.13)$$

to allow every intensity level. The intensity step-size  $a$  is set to 1, therefore the kernel can be rewritten as

$$h(s) = \frac{1}{2} \cdot \left\{ \frac{\sin(\pi \cdot s)}{\pi \cdot s} + \frac{\cos(\pi \cdot s) - 1}{(\pi \cdot s)^2} \right\}. \quad (2.14)$$

The idea of this approach is that in equation (2.10) the inverse two-dimensional Fourier transform does not converge for  $|w|$  because of the infinite bounds. That means theoretically, that there will be no possible windowing for all samples in the local frequency space. Therefore [Ram71] proposed to limit the frequency band by an adequate filter, as denoted in (2.14). Although the Ram-Lak filter provides the best local resolution, it tends to increase noise which is always present in real data. The choice of a filter leads always to a compromise between the necessary resolution of the result and the noise sensitiveness. Therefore, Shepp and Logan in [LB74] proposed an improvement of the Ram-Lak filter which is near to the main maximum of the ideal filter of Ramachandran and Lakshminarayan but reduces undesirable side lobes. This can be implemented by multiplying the Ram-Lak filter by a sinc-function<sup>4</sup>, with  $\text{sinc}(x) = \frac{\sin(\pi x)}{\pi x}$ . The proposed filter kernel of Shepp and Logan is given by

$$h(s) = -\frac{2}{\pi^2} \cdot \frac{1 - 2s \cdot \sin(\pi s)}{4s^2 - 1}. \quad (2.15)$$

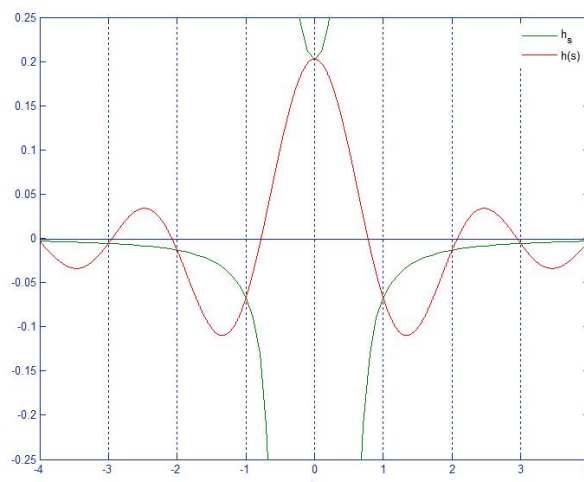


Figure 2.15: The original Shepp-Logan filter kernel  $h(s)$  can be replaced by an alternative function  $h_s$  in order to reduce computational intense, if there is a discrete data set with  $s \in \mathbb{Z}$ , as in the case of image data sets

In medical imaging this filter is used mostly, because it provides a good compromise between resolution and a smoother looking reconstruction. For special clinical applications there exists a data base assigning anatomic groups of the body to the accordant filters. In beam tomography this distinction

<sup>4</sup>Note, that a multiplication in the original space is a convolution of the transform in Fourier space, which is called the spectrum. The sinc-function is the transform of the rectangular window, which is the form of the ideal band-pass filter wanted.

## 2 Tomography

---

is not necessary because up to now, the composition of the beam can be seen as homogeneous as far as the imaging of the origin of visible residual gas radiation is concerned. Anyhow, the reduction of background noise in combination with a good resolution of the particle distribution in the beam is desirable. The Shepp-Logan filter denoted by (2.15) is known to be computationally intense.

Since in practice, all data sets are discrete, this filter can be replaced very well by an alternative function (see Fig. 2.15). The modified kernel is given as

$$h_{\mathbb{Z}}(s) = -\frac{2}{\pi^2} \cdot \frac{1}{4s^2 - 1}. \quad (2.16)$$

This filter is adopted widely in beam tomography as it provides good results within an appropriate time. In the following another possibility will be discussed: Having a look at the series expansion of a Fourier approximation, it is well known [Hes93, Kam06] that breaking off the expansion after a defined term means a weighting of the pulse response by the square function in time domain, as already denoted above. This weighting shows quite awkward characteristics, because of the convolution of the requested, spectral function and the strictly bounded function. In signal processing this problem is dealt with by applying adjusted window functions which balance the width of the major lobe and the amplitude of the highest sub-maximum<sup>5</sup>. The choice of the window function then is depending on the character of the signal. Going back to the problems which arise out of the filtered back projection, one can recapitulating see: the one-dimensional Fourier transformation overemphasizes low frequencies and attenuates high frequencies. Convolution in ordinary space or filtering in Fourier space corrects this distortion by accentuating high frequencies and attenuating low frequencies. The dilemma is, that in Fourier space noise is located in the high-frequency range and is also accentuated by trying to correct the distortion of the Fourier transformation. The idea is nearby to find a window function that can be used with the well working Ram-Lak filter that fulfills the demand of a bandpass filter additionally to the necessary Fourier filtering. Having a look at the filter characteristics in Fig. 2.16 the hamming window seems to fit quite well to these demands.

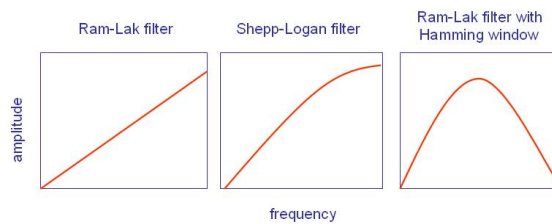


Figure 2.16: Comparison of the characteristics of the ideal Ram-Lak filter, the modified often used Shepp-Logan filter, and the Ram-Lak filter with hamming window. The third one shows a characteristic that is adjusted to the demands of the filter dilemma arising out of the filtered backprojection

The hamming window is defined by the function

---

<sup>5</sup>in general this is the first sub-maximum

$$w(n) = 0.54 - 0.46 \cdot \cos\left(\frac{2\pi n}{N-1}\right), \quad (2.17)$$

and optimized to minimize the maximum side-lobe. This happens by cancellation of strong side lobes and doubling the width of the main lobe. At a closer look, the hamming window consists of three sinc-functions, that are shifted against each other.

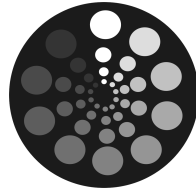


Figure 2.17: Test picture with a full range of intensity levels

Fig. 2.17 shows a test picture which consists of a full range of intensity levels from 0 to 1 which can occur in a beam image. Performing the tomography algorithm on this picture with different filtering methods shows the effect of the different filters introduced above (Fig. 2.18)

The tomography algorithm without filtering shows a blurred backprojection result. The Ram-Lak and Shepp-Logan filter both show similar, quite good results. The over all structure and all dimensions are reconstructed correctly. Also the different intensity levels are depicted distinctively. The Ram-Lak filter with hamming window additionally presents better intensity level dynamics, approaching closest to the original test picture before application of the tomography algorithm.

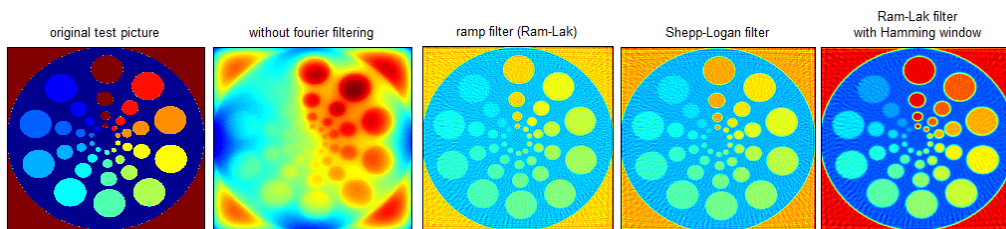


Figure 2.18: Performing the tomography algorithm on the test picture. From left to right: original test picture in false color representation; Test picture after performing filtered back projection - with no Fourier filtering, with Ram-Lak filtering, with Shepp-Logan filtering, with Ram-Lak filtering and hamming window

### 2.3.2 Filter Performance for Measurement and Simulation

For medical applications different filters are used depending on the tissue which has to be analyzed. All of these filters are distinct to each other in the way they solve the filter dilemma based on the interference

## 2 Tomography

---

of Fourier space distortion and noise. If noise is absent totally, as in the case for the simulated seven-beamlet-composition, which is shown unfiltered in Fig. 2.14, all filters solve the problem of Fourier space distortion equally well, as can be seen in Fig. 2.19.

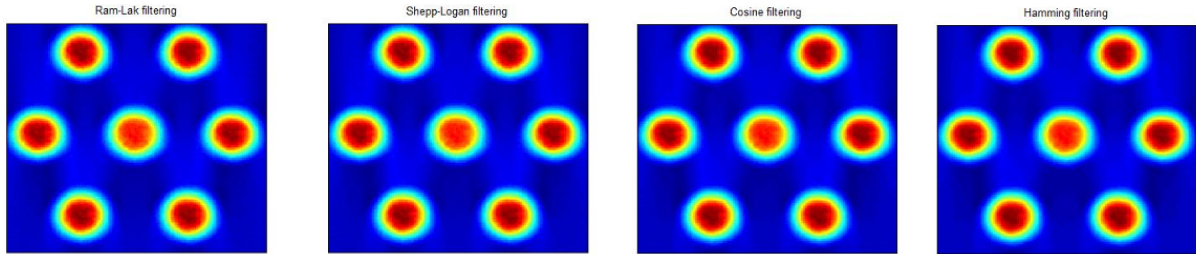


Figure 2.19: Under absence of noise, all tested filters solve the problem of Fourier space distortion equally well.

The differences occur under the appearance of noise. The filters then will show different dynamics corresponding to the peculiarity and strength of noise. In Fig. 2.20 the behavior of the Shepp-Logan filter is demonstrated applying white noise with different strength (scaled by the standard deviation) to the test image. The results bare why tomographic methods using filtered backprojection also are used

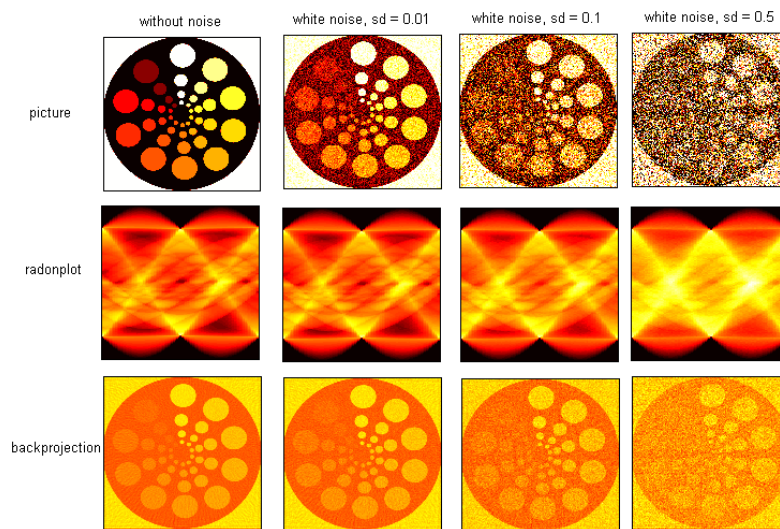


Figure 2.20: Application of white noise with different standard deviations (strength of noise) and its influence on the backprojection result using a Shepp-Logan filter.

to clarify noisy images. Having a look on the images with superimposed white noise at an standard deviation of 0.1 or 0.5, the backprojection discloses structures which seem to be lost or hidden in the original noisy picture. Applying the different types of filters on measured dataset M2-A (see Appendix for detailed information on the different datasets) it can be seen, that using the right filter enhances the



backprojection quality much more than just the removal of background noise (Fig. 2.21). Background

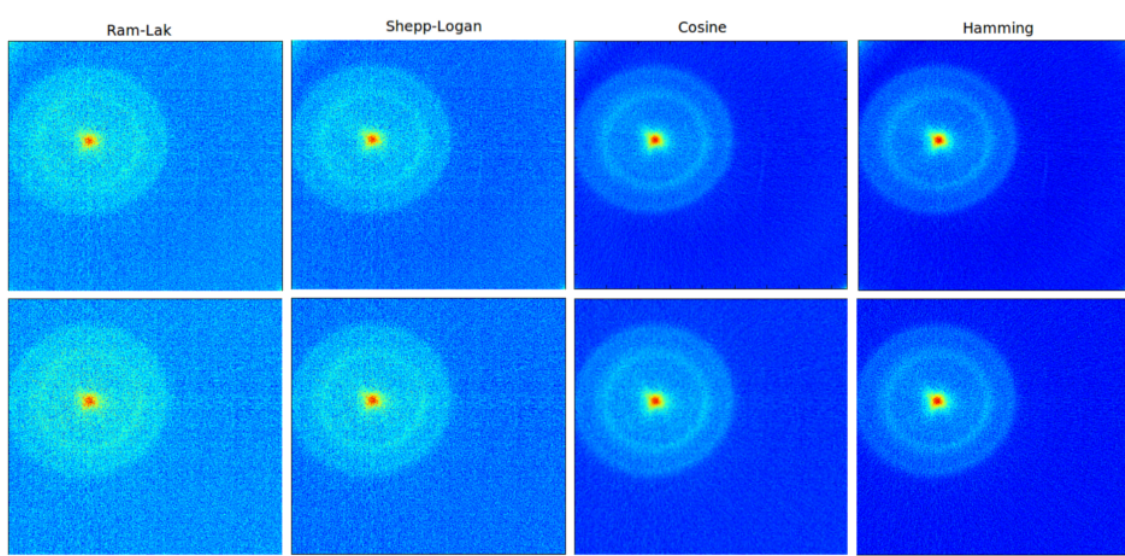


Figure 2.21: Measured Dataset I back projected without background subtraction (top) and with background subtraction (bottom). The effect of the use of different filters has much more influence on the backprojection quality, than background removal.

subtraction is very useful to remove residual reflection effects as can be seen in the top row as compared the bottom row in the left top edge of every image. For beam tomography the Ram-Lak filter with Hamming window still will be the best choice, as already analyzed. Also the cosine filter may work fine. In special cases the decision has to be proofed if the Hamming or cosine filter will give more advantage.

### 2.3.3 Ghost Particles

In [AC07] it was shown that for tomographic reconstruction of a particle field, the problem of ambiguous information of particles is quite common. The consequence of this ambiguity is that the backprojection includes typical intensity artifacts, which are not related to real particle positions. Therefore, they are called ghost-particles. Based on the assumption that non-zero intensity value on the line of sight on a projection is related to the location of a particle, the camera observes the particle in possible locations on this line of sight. Considering two projections observing the same particle, the location of it explicitly will be there where the two lines of sight cross. If there are two particles observed by two projections, there will be four possible locations for the two particles, as there exist four cross-sections of the lines of sight, as can be seen in Fig. 2.22.

Three particles will lead to nine possible locations, as far as two projections are concerned, and so on. Given a large set of particles, the reconstruction noise, consisting of the set of ghost particles, will create structures in the tomography output, which are unfound in the real particle distribution. This noise can be reduced by choosing a sufficient number of projections. Every projection reduces the number of possible locations for real particles by excluding positions, which are not observed by a projection.

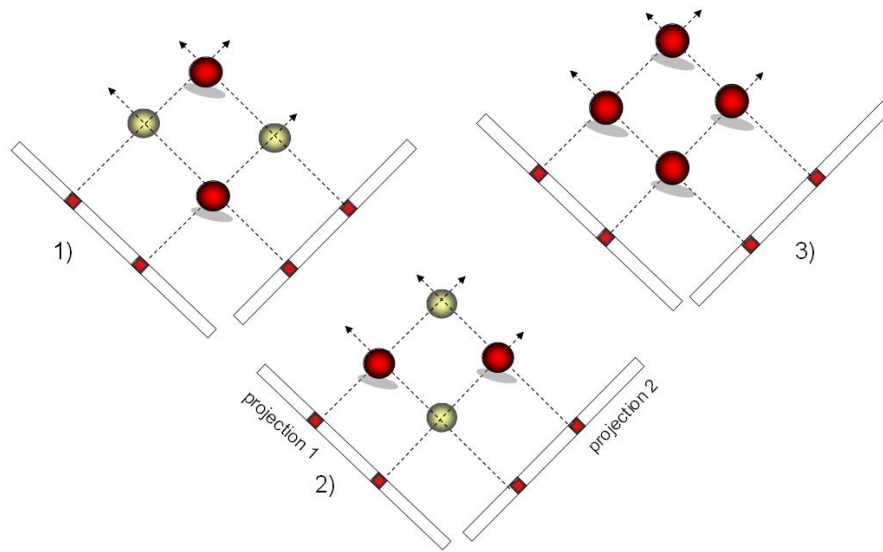


Figure 2.22: Ambiguous location information in reconstruction artefacts result from multiple possibilities for the real location of particles (red marbles: real particles, yellow marbles: ghost particles)

Reconstruction noise can be characterized by a set of lines in the direction of used projection angles, featuring the same intensity level. With an increasing number of projections these lines are conflating first to star-like then to cloud-like structures, ending at least in a diffuse background noise (see Fig. 2.23).

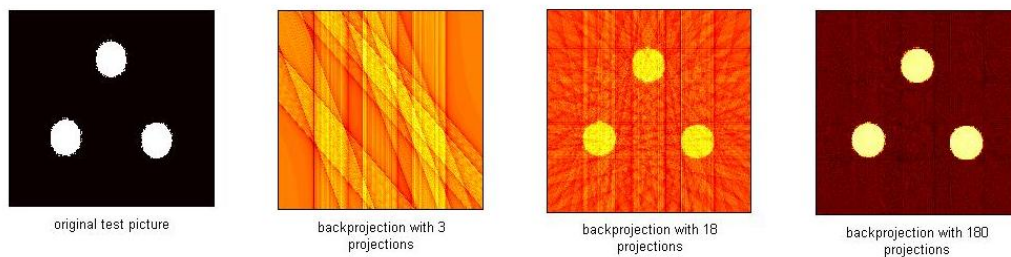


Figure 2.23: Typical behavior of reconstruction noise demonstrated by means of a simple test picture. With an increasing number of projections, ghost particles create line structures, star structures, cloud structures up to diffuse background noise

As mentioned, the ambiguity of location information is increased by the number of particles in a given particle distribution of an ion beam that is to be reconstructed by beam tomography. A very large number of particles as given in an ion beam, combined with a very small amount of projections for the reconstruction, can lead to double images of characteristic structures of the beam. It is possible that such ghost images in the backprojection seem to be related to real distribution locations, because they

are very concise, while other structures step into the background. Increasing the number of projections then shows that this was a misapprehension.

In Fig. 2.24 the simulated test distribution of 10000 particles is reconstructed using two, six and ninety projections. The backprojection with two projections convey, that there are two highly occupied particle clouds at the left and right side near the middle. In the top and bottom row there are three additional particle clouds, respectively. The columns exhibit additional particle clouds at a medium intensity level. Increasing the number of projections just to six projections, will eliminate quite a lot of ghost particles of the backprojection. A ring-like cloud of ghost particles remains. Line structures are still visible and cause a contortion of the dense particle clouds of the real distribution. The main characteristic of this idiosyncratic beam distribution now clearly has come out. Executing the tomography algorithm with 90 projections reduces the projection noise already very reliable.

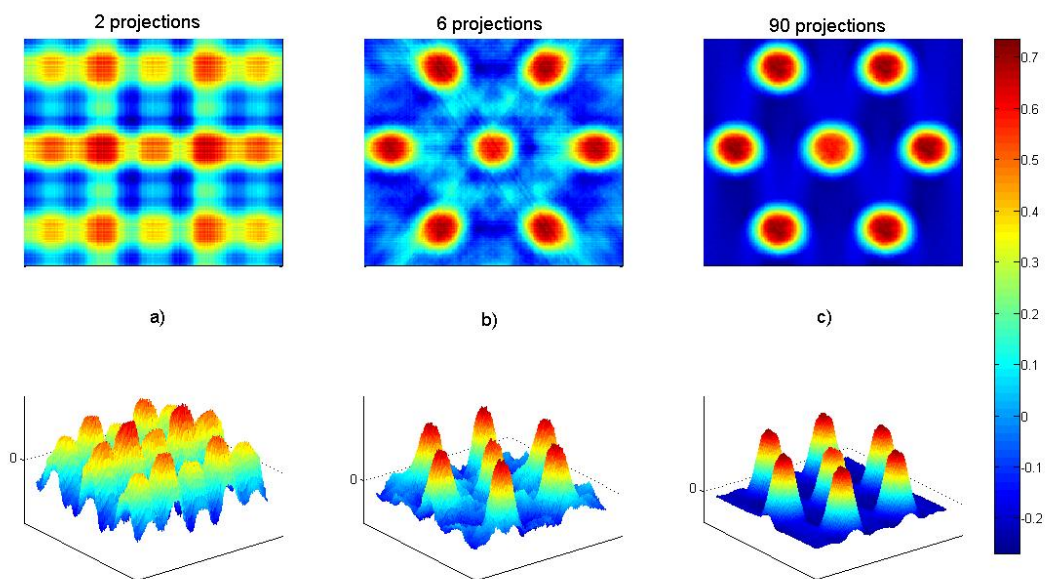


Figure 2.24: The evolution of reconstruction noise in an application of the tomography algorithm on a particle distribution with 10000 particles. (a) Increasing the number of projections, leads to an elimination of a high number of ghost particles. (b) Ghost images fade to low intensity ghost particle clouds. (c) Performing the tomography algorithm with 90 projections already shows very good results. The characteristic beam shape is clarified, ghost particles are present only in form of a rare background noise.

### 2.3.4 Image Defects

Besides distortion caused by data processing and measurement noise there might occur image defects. These effects can arise out of a read-out error from the CCD-camera chip, a loss of data in the memory or while transferring it. In simulated beams there may be computational deficits causing data losses. The following demonstrates, how defects will influence the result of the tomography.

One imaginable defect is, the successive loss of a series of projections. One may expect that the result of these losses will only manifest in an empty or at least alleviated line along the defect projection angles, but this is not the case. The loss will cause an apparent distortion of the original distribution when using filtered back projection. The distribution only is distorted apparently since this effect is caused by a misinterpretation of the intensity distribution in  $\tilde{p}(\phi_{defect}, \vec{s} = \vec{0})$  while performing the two-dimensional inverse Fourier transformation, and this is not comparable with the distortion caused by the mis-mapping during the one-dimensional Fourier transformation as seen before.

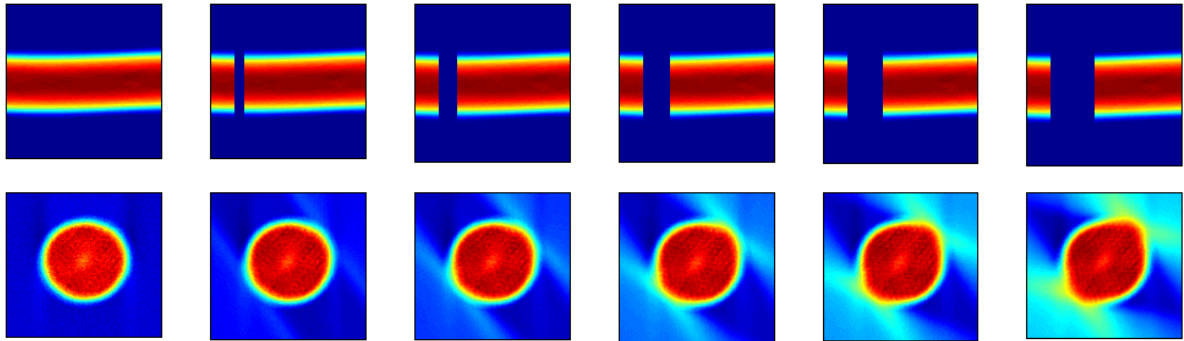


Figure 2.25: Distortion of the back projected beam distribution, when projections at different successive angles are lost. Above the Radon plot, with all projections from every angle is seen. Beneath every corresponding back projected density distribution is shown. From left to right: No loss. Loss of 10, 20, 30, 40 and 50 projections. The missing projections will not cause an empty or alleviated line along the projection angle, but lead to an apparent distortion by misinterpreting the intensity distribution in the two-dimensional inverse Fourier transformation.

In Fig. 2.25 one can see in the upper row the Radon plot of six different situations. In the first situation all projections available. The back projected distribution is a nearly complete radial symmetrical Gaussian beam. In the second situation 10 projections of the angles  $30^\circ$  to  $40^\circ$  are consecutively lost. Since the projection is computed using 180 angles with an angle step of  $1^\circ$  this means a loss of  $\approx 5\% - 6\%$ . What can be observed is a slight shift of intensity at two opposite locations of the distribution, appearing in form of very diffuse tangential branches. In situation three 20 projections ( $\approx 11\%$  loss) along the angles  $30^\circ$  to  $50^\circ$  are lost. The effect is, besides the increasing characteristic of the two branches, a distortion in the entire distribution back projection in form of an expansion in the two directions of the branches. The increase of this behavior can also be observed regarding a loss of 16% (30 projections) and 22% (40 projections) and so on. The worst case will occur if all projections corresponding to one slice are lost, then the Radon plot and also its back projection will

---

## 2.4 Other Tomography Algorithms in a Nutshell

lead to an empty slice. These distortions or total loss will affect single slices, if the corresponding projection angles are involved. Much more profound will be the impact of another kind of image defect that affects only parts of slices but therefore a range of slices consecutively. An example of a horizontal loss of data in every slice can be seen in Fig. 2.26. The left picture shows an example image exhibiting a horizontal read-out error. On the first look one can assume that such a defect, in comparison to a loss of whole projections (even more if they amount to 20% and more) might be of much less impact, since the projections are partly taken into account. The Radon plot in the second image of Fig. 2.26 reveals that the same ‘little’ error can be found in all projections. But unlike to this assumption it turns out that the back projection, given in the third image, exhibits large deficits.

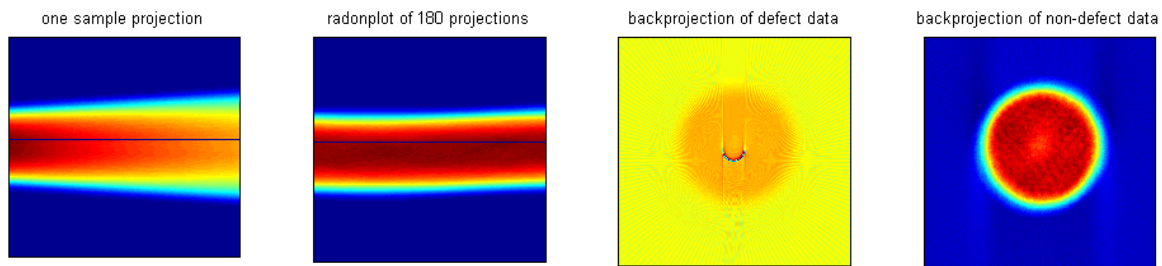


Figure 2.26: A partial - but in all slices present - defect shows a much more disturbing impact on the whole beam tomography, so that it might not be possible to use the result in a meaningful way anymore.

Such a horizontal read-out error will disable the whole volume, since every slice is impacted. Every projection itself represents a distribution that can be mapped to its spectrum by the Fourier transform. If whole projections are lost, as in the case in Fig. 2.25, this means that full spectra are not taken into consideration, while the existent spectra remain unchanged. A hole in one single projection, means to alter the spectrum of the intensity profile in such a way that spectrum components are lost, the inverse Fourier transformation then shows the lack of information in form of a degenerated back projection throughout the whole slice. Although the CCD-camera always reads out the data line-wise, it would happen more frequently that some pixel locations will fail. If this dead pixel is part of every projection, the distortion, which can be seen in Fig. 2.26 will affect only the slices concerned. This slice can automatically be identified and rejected if necessary.

## 2.4 Other Tomography Algorithms in a Nutshell

The filtered backprojection algorithm discussed in the previous sections is that one closest to the original idea and proofs of Radon [Rad17]. According to Eq. (2.1) it also supports the best approximation for the original density distribution, since it can handle a large number of projections from different angles. When beam tomography firstly was established in the late 70s the filtered backprojection method was not applicable, because of the very restricted amount of projections, being available at these times. Therefore, the two methods of Algebraic Reconstruction (ART) and Maximum Entropy (MENT) to implement the idea of Radon were lent from electron microscopy, astronomy, and radiology. Fraser showed [Fra78] that three profiles in the use of ART will give quite good results for the backprojection

## 2 Tomography

---

in ordinary space and phase space. He presupposed a bivariate Gaussian distribution, with a defined major-to-minor axis ratio for the ordinary space. In the phase space case he cited Metzger [Met73] who presupposed that the beam in a normalized transverse phase space “is contained within a circle of radius  $\sqrt{\epsilon\pi}$ ”. One has to be careful in using such presuppositions, because in every case they entail loss of information as described in section 1.6. That beams are sometimes far away from this ideal kind of beam is impressively demonstrated by the humming bird picture of P.Evtushenko shown on the title page of this work. Nevertheless, the use of a very small number of projections is warrantable ensured the beam is close to an ideal beam, or if no other possibility is given to perform a reconstruction, or if the resulting accuracy is proved to be sufficient for the inherent question to be answered by the diagnosis. The method of maximum entropy is a quite different approach to the implementation of Radon’s idea. According to its nature, on the one hand a larger number of projections is quite helpful to find the maximum entropy, on the other hand it is very prone to a poor noise-to-signal ratio of the dataset when using a large set of projections. In the following, both methods will be introduced in short with their main idea. The numerous modifications developed for different applications and problems are left beside.

### 2.4.1 Algebraic Reconstruction Technique

in the late seventies the algebraic reconstruction technique (ART) and the maximum entropy method (MEM) have been introduced nearly contemporaneously for an application in beam tomography. While Minerbo [Min77] preferably discussed the reconstruction with very view projections using MEM, Fraser [Fra78] investigated the use of ART for beam tomography. The ART approach is a very direct method to obtain the reconstruction from a set of projections. The main idea is that every projection can be described by a set of linear equations [Kak88]. The distribution  $f(x, y)$  which has to be reconstructed can be mapped to a grid of  $N$  cells, each representing an unknown variable  $f_i$  for an intensity value in the cell. The  $f_i$  are defined in the grid as shown in Fig. 2.27 on the left side. Now given a projection  $p(s)$  with  $M$  values  $s_j$  one can define a set of linear equations of the form

$$Fw = p, \tag{2.18}$$

where  $F = f_1, f_2, \dots, f_N$  are the unknown values of the distribution ordered in the the grid,  $w = w_{ji}$  with  $j = 1 \dots M$  and  $i = 1 \dots N$  are weights for the influence of a cell on the projection and  $p = s_1 \dots s_M$  is the projection with  $M$  intensity values. This set of equations can be obtained by assuming that each intensity value  $s_j$  in a projection  $p(s)$  is determined by a ray sum. A ray is a line  $s_j$  that runs orthogonal to the projection across the grid of all  $f_i$ . If this ray crosses a cell with intensity value  $f_i$  this value will be added up, multiplied with a weight  $w_{ji}$  indicating the length of the path that the ray needs to pass the cell. If the ray and the cell width are very small (this may be the case if using the resolution of 1 px) one can simplify the situation by setting a weight  $w_{ji}$  to 1 if the ray passes the pixel in the grid and 0 otherwise. The ray-sum of an intensity value  $s_j$  in a profile then can be written by

$$s_j = \sum_{i=1}^N w_{ji} f_i \quad j = 1, \dots, M. \tag{2.19}$$

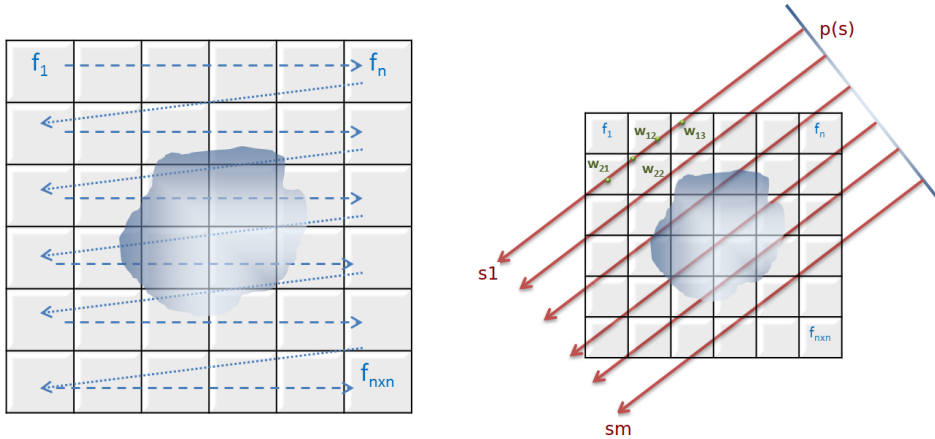


Figure 2.27: Left: The algebraic reconstruction technique acts on the assumption that one can arrange a set of linear equations with  $N$  unknown variables  $f_i$ , given by the number of cells. Right: Each value in a projection is a sum over a ray from the value position across the density distribution with corresponding weights.

For all intensity values  $s_j$  of one projection  $p(s)$  the set of equations can be given in matrix form following Eq. (2.18)

$$\begin{pmatrix} w_{11} & \cdots & w_{1N} \\ \vdots & \ddots & \vdots \\ w_{M1} & \cdots & w_{MN} \end{pmatrix} \begin{pmatrix} f_1 \\ \vdots \\ f_N \end{pmatrix} = \begin{pmatrix} p(s_1) \\ \cdots \\ p(s_M) \end{pmatrix}. \quad (2.20)$$

Having a look on Fig. 2.27 on the right side, for ray  $s_1$  only the weights  $w_{21}, w_{22}, w_{12}$  and  $w_{13}$  will be set to one in the matrix  $W$ . Every ray passes a comparatively small number of cells and the matrix  $W$  will be occupied sparsely. The  $p(s)$  are given by the measured projections. Now the task is to determine the reconstruction given by the  $f_1, \dots, f_n$ . If  $N = M$  there are as many equations as unknown variables  $f_i$  and the equation system is solvable unambiguously for every projection by a matrix inversion. If the data are noisy or if  $N \neq M$  a simple inversion can not be performed. In these cases least square methods<sup>6</sup> may provide an acceptable result. For large  $M$  and  $N$  the computational cost of least square methods may become very high. The classical ART uses the *method of projections* firstly was introduced by [Kac37] and investigated in more detail by [Tan71]. The iteration starts with an initial guess about the unknown variables  $f_i$  which are given as a vector  $\vec{f}^{(0)}$ . In most cases all  $f_i$  are initialized with 0, such that  $\vec{f}^{(0)} = \vec{0}$ . The number of iteration steps  $j$  is given by the number of rays in the profile. The iteration step for one ray now is performed by

$$\vec{f}^{(j)} = \vec{f}^{(j-1)} - \frac{\vec{f}^{(j-1)} \cdot \vec{w}_j - p_j}{\vec{w}_j \cdot \vec{w}_j} \cdot \vec{w}_j, \quad (2.21)$$

where  $\vec{w}_j$  is the  $j$ -th row of the sparse matrix  $W$ . Obtaining these results in the first approximation of  $f(x, y)$ , which is  $\vec{f}^{(M)}$  on the basis of the first profile. For the second profile, the initial guess is

<sup>6</sup>Using a least square method to solve an over-determined equation system is shown in other context in section 5.5.3

## 2 Tomography

---

$\vec{f}^{(M)}$ . Repeating the iteration steps with the second profile leads to  $\vec{f}^{(2M)}$  and so forth. If there are  $k$  profiles available for the reconstruction, the iteration ends with  $\vec{f}^{(kM)}$ . As shown by [Kak88, Tan71] an existing unique solution  $\vec{f}_u$  for the system of equations can be found by

$$\lim_{k \rightarrow \infty} \vec{f}^{(kM)} = \vec{f}_u. \quad (2.22)$$

Due to the geometrical derivation of this iteration method [Kak88] the number of necessary iterations to obtain the correct image is depending on the angle between the projections. The smaller the angles between the single projections, the more iterations are necessary. The best case is given in a situation where two profiles are perpendicular to each other. If a unique solution  $f_u$  exists will depend on the constrained  $M = N$  and the absence of noise. If the  $s_j$  are disturbed by noise or if there are more equations than variables that have to be determined, not an unique solution exists but a set of solutions. In this case the iterative method can also be performed yielding an approximative  $\vec{f}'_u$ . If from the set of possible solutions for the over determined equation system those solutions are chosen which minimize the distance  $|\vec{f}^{(0)} - \vec{f}'_u|$  between the initial guess and the resulting image after the iterations, a solution can be approximated.

### 2.4.2 Maximum Entropy Method

The most popular illustration to explain the main principle of maximum entropy is the apes argument [Siv06]. A group of apes are throwing  $N$  bananas in a square arrangement of  $M$  baskets. After a while they are stopped and all bananas in every basket are counted giving a random distribution (Fig. 2.28). Since the apes have no preferences for special baskets, they represent best the status of knowledge at the beginning, corresponding with all possible distributions that can be produced in this way. Fixing a once given distribution (e.g. the one in the figure), this distribution can be obtained in many different ways, since each two of the bananas can change their basket without influence on the total of the distribution. Setting  $n_1$  to the number of bananas in in basket 1,  $n_2$  to the number of bananas in basket 2 and so forth. Then the number of all bananas in all baskets then is given by

$$N = \sum_{i=1}^M n_i. \quad (2.23)$$

In how many ways can  $n_1$  bananas be chosen for basket 1 out of  $N$  bananas? This is given by the binomial coefficient  $\binom{N}{n_1}$ . For basket two there are  $\binom{N-n_1}{n_2}$  possibilities and so forth. Therefore the number of ways  $\mathcal{W}$  yielding a fixed distribution  $\{n_i\}$  for all baskets can be obtained as

$$\mathcal{W} = \binom{N}{n_1} \cdot \binom{N-n_1}{n_2} \cdot \dots \cdot \binom{n_M}{n_M} = \frac{N!}{n_1! \cdot n_2! \cdot \dots \cdot n_M!} = \frac{N!}{\prod_{i=1}^M n_i!}. \quad (2.24)$$

The entropy  $H$  of a two-dimensional function  $f$  is a unique measurement of the manifold of all micro states of a given distribution [Mot85], denoted by

$$H(f) = - \iint f(x, y) \ln f(x, y) dx dy. \quad (2.25)$$



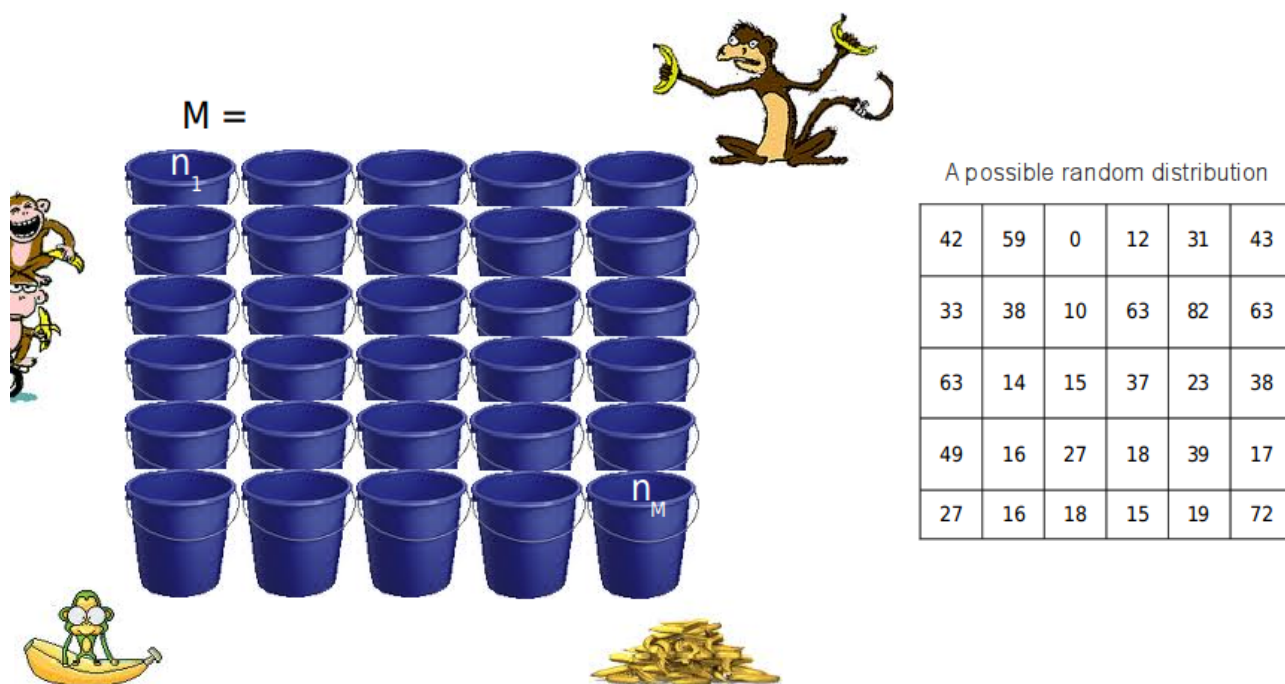


Figure 2.28: A group of apes throwing  $N$  bananas into  $M$  baskets thus generating a random distribution. This is the most popular illustration of distributing  $N$  equal intensities into  $M$  pixel of an image. The maximum entropy method finds the most uniform image that can be validated by the data.

To determine this function  $f$  the number of bananas in every basket  $n_i$  has to be made unique by setting

$$n_i = N \cdot f_i, \quad (2.26)$$

where  $f_i$  is the fraction of bananas in basket  $i$ , then  $f_i$  follows as

$$f_i = \frac{n_i}{N}. \quad (2.27)$$

Ignoring terms of order  $1/N$ , by a Sterling approximation it can be written

$$\ln \mathcal{W} \approx -N \sum_{i=1}^M f_i \ln f_i. \quad (2.28)$$

This sum is the discretisation of entropy  $H$  in Eq. (2.25). Rearranging Eq. (2.28) to obtain the manifold  $\mathcal{W}$  of all distributions with entropy  $H$  containing  $N$  bananas leads to

$$\mathcal{W} = e^{NH}. \quad (2.29)$$

Now if the entropy of a distribution is increased by 1 the number of possible ways to gain this distribution by a random experiment will be increased by  $e^N$ . Of course the baskets can be replaced by the pixels

## 2 Tomography

---

in an image. In this case the bananas will be replaced by equal intensity values. The essential idea of the maximum entropy approach of tomography then is the following: Considering all available data but nothing more (in this case: only profiles at different angles) find the most uniform image that is maximally non-committal. This image might not cover the true density distribution that has to be reconstructed, but under the given conditions it is the most probable one. Constructing the image with the maximum entropy is the solution with the highest number of possible micro states if only comprising only the given data but also not less. Noise will influence the maximum entropy and therefore the chosen image of the solution.

The mathematical task to find the image with maximum entropy can be defined as an optimization problem where one finds the maximum entropy solution of an intensity distribution  $f(x, y)$ , considering a set of constraints. In [Mot85] this problem is solved by using Lagrange Multipliers. The transformation of a point  $(x, y)$  to a rotated point  $(s, t)$  is done by a simple rotation matrix

$$\begin{pmatrix} s \\ t \end{pmatrix} = \begin{pmatrix} \cos(\phi) & \sin(\phi) \\ -\sin(\phi) & \cos(\phi) \end{pmatrix} \begin{pmatrix} x \\ y \end{pmatrix}, \quad (2.30)$$

where  $\phi$  is the angle of rotation, from which a projection of a distribution  $f(x, y)$  is taken. To maximize the entropy of the function  $f(x, y)$  the Lagrange function has to be defined as

$$\Lambda(f, \lambda) = H(f) + \sum_{n=1}^N \lambda_n(s) \cdot \left[ \int f(x_n, y_n) - p_n(t, s) dt \right] ds, \quad (2.31)$$

where  $H(f) = -\iint f(x, y) \ln f(x, y) dx dy$  is the entropy,  $\lambda_n(s)$  are constant Lagrange multipliers,  $p_n(t, s)$  is a point of the projection in the sense of a Radon transform in Eq. (2.11). The complete sum is the sum of constraints for the entropy function  $H(f)$ . The Lagrange multipliers  $\lambda_n(s)$  and the function  $f(x, y)$  are unknown but  $\Lambda(f, \lambda)$  is stationary in relation to this two unknown dimensions. Now the critical points have to be found. First having a look at the partial derivative with respect to the Lagrange multiplier

$$\frac{\partial \Lambda}{\partial \lambda_n} = 0. \quad (2.32)$$

The variation of the Lagrange multipliers with  $\lambda_n(s) \rightarrow \lambda_n(s) + \delta \lambda_n(s)$  corresponds according to the construction for all  $\lambda_n(s)$  with the initial entropy, since the partial derivation of  $\Lambda$  with respect to the Lagrange multipliers always results in the constraint function [Min79]. The more interesting case is the derivation with respect to the function  $f$ . The difference of entropies in this case is given by

$$\delta H = - \iint [1 + \ln f(x, y)] \delta f(x, y) dx dy. \quad (2.33)$$

To find the condition by that  $\Lambda$  remains stationary for the variation of the function  $f$ , all coefficients of  $\delta f(x, y)$  have to be collected. Let  $s_n(x, y)$  be a function that stores the values according to a point  $(x, y)$ . This function already has been found in Eq. (2.5), and now can be written as

$$s_n(x, y) = x \cdot \cos(\phi) + y \cdot \sin(\phi). \quad (2.34)$$

Now the constraints for the entropy function, represented by the sum in Eq. (2.31), can be rewritten like

$$\sum_{n=1}^N \iint \lambda_n(s_n(x, y)) \delta f(x, y) J_n dx dy, \quad (2.35)$$

where  $J_n$  denotes the Jacobi matrix of the transformation. In the case of performing a ordinary space tomography  $J_n$  is given by the unity matrix. In the case of performing a phase space tomography  $J_n$  contains the information about the phase space scaling. Using filtered backprojection, this scaling directly is applied to the projections as will be discussed later in section 5.1 (page 107). The geometrical interpretation of this phase space scaling is illustrated in Fig. 5.4. The condition under which the Lagrange function in Eq. (2.31) is stationary can now be formulated by

$$\ln f(x, y) = \sum_{n=1}^N \lambda_n(s_n(x, y)) \cdot J_n - 1. \quad (2.36)$$

With this condition, the unknown Lagrange multipliers  $\lambda_n(s)$  can be replaced by rearranging Eq. (2.36)

$$h_n(s) = e^{\lambda_n(s) \cdot J_n - 1/N}. \quad (2.37)$$

The maximum entropy of the distribution now can be expressed as product over all Lagrange multipliers

$$f(x, y) = \prod_{n=1}^N h_n[s_n(x, y)]. \quad (2.38)$$

This can be mapped to the set of  $N$  different projections, resulting in  $N$  non-linear equations with  $N$  unknown variables. Finally this equation system can be solved by using conventional methods.

## 2.5 Comparison of Algorithms

There exists no *best* reconstruction algorithm. The choice of the right algorithm depends on the particular case. Crucial indications will be the available computational space and time requirements as well as the number of projections, and the equidistance of their projection angles, and signal to noise ratio of the data.

### 2.5.1 Space and Time Requirements

The filtered backprojection (FBP) is a time and space efficient algorithm. It is nearly a direct inversion of the projection and a straight forward implementation of the Fourier-slice-theorem. A Radon plot of each projection angle has to be arranged. Since this means just a rearranging of the original measurement data, the required space is as large as the measurement data themselves. For the algebraic reconstruction (ART) large matrices have to be allocated. The number of values is quadratic in relation to the number of values of the profile for every projection angle. This also holds for the maximum entropy method (MEM). Additional to ART, MEM has to determine and store the corresponding Lagrange multipliers in each iteration step. FBP by far is the fastest algorithm. The time performance

## 2 Tomography

---

of ART is depending on the version of ART that has been implemented. There is a large set of algorithms for ART each dealing with different problems. Speed enhancement for ART can be managed by simultaneous iterative reconstruction (SIRT). The computational time requirements of MEM are comparable with ART.

### 2.5.2 Projections

Using FBP, a small number of projections increases the number of ghost particles and their superstructures, which have no correspondence to the real distribution. On the other hand, using a large number of projections with the right filtering method and with equidistant angles leads to very high accuracy of relative intensities in the reconstructed image is very high, and increases with additional projections. Also with a very small number of two or three projections ART and MEM do *not* show the problem of ghost particles, since they both are solving equations for each cell of the projection range on its own. Whereas the FBP needs an equidistant set of projection angles to avoid distortions, MEM is not dependent on them. For ART a set of equidistant angles is recommended to get a more consistent result. For MEM and ART one finds an optimal number of profiles for the reconstruction. At a specific iteration, depending on the quality of the projections, the reconstruction becomes worse again. This includes that the accuracy is bound to this optimal number of iterations and can not be increased by more projections as it is possible in the FBP.

### 2.5.3 Noise and Image Defects

As shown in section 2.3.4, small imperfections in the projections are able to cause disadvantageous impact on the whole reconstruction when using FBP, because they effect the spectrum of the used Fourier transform. MEM and ART are relatively robust against such image defects. If the projection data exhibit a low signal to noise ratio, the FBP performs worse than MEM. Noise that is non-uniformly scattered within the data increases the noise in the reconstructed image. This effect can be seen with its consequence for example in Fig. 4.9. MEM underestimates weak intensity peaks. The advantage of this is that in low intensity regions the noise of the reconstructed image is less or absent. On the other hand, in regions where high intensities superimposed with noise, this noise is more overemphasized then within the FBP. This is a subliminal effect of the dilemma explained in section 2.3.1. Although there is no explicit Fourier transform, the projections by nature build up a sinusoidal function around an object, which are transformed from a polar coordinate system of the projections to a Cartesian coordinate system of the reconstructed image. For ART the dilemma is appreciable due to the fact that when computing the difference between the reconstructed image and the original image, the error in the middle of the reconstructed image becomes worst and decreases in direction to the edges. Since there is no or only insufficient Fourier filtering for those algorithms, this is one reason that the reconstruction becomes worse when the number of profiles exceeded the optimal number of iterations. There is a second effect also responsible for that behavior. It can be observed that the reconstruction image is pixilated increasingly for iterations exceeding the optimal number of profiles. This effect also appears using noise free data. The reason is that the discretisation, which is inherent in the methods themselves, evokes little aberrations for every projection. These aberrations are very small but they constantly mount up with every new iteration. For ART there are corrective modification algorithms that take into account those aberrations.

### 2.5.4 Choosing a Reconstruction Algorithm

In general one can conclude that the FBP is a good choice, if many projections are available and the signal to noise ratio lying within a tolerable range. The result can be enhanced by using a representation where all slices of a volume are summed up to one slice (as an example see Fig. 4.9 in comparison to Fig. 4.10 on page 96). This is possible, when the following analysis methods are not using successive slices (e.g. beam profiling (Sec. 4.1.3) or emittance measurements (Sec. 5.6). The use of an adequate Fourier filter kernel is very crucial for this method (more crucial than background removal for example (see. Fig. 2.21)). MEM or ART will be a good choice when there are only a few projections. To find the optimal number of projections for particular data several test iterations have to be performed for a noise free image. For every reconstruction the error between the original image and the reconstructed image has to be computed. The error will decrease for the first iterations. The optimal number of iterations is given at the last projection that shows a decreasing error. After this projection, the error will increase. MEM and ART are also a good choice if the signal to noise ratio gives no sufficient results with the FBP. In this case, the accuracy will hardly increase with the number of projections using the FBP. Furthermore MEM is a good choice if the projection angles are not sufficiently equidistant. This is for example indicated, when using phase space tomography, since the projection angles are computed phase space rotation angles from the transport matrix. When determining profiles by grid measurements, ART will be a good choice since it takes the width of the wires into consideration by using correspondent weights.



# 3 Beam Theory and Analysis

## Contents

---

<b>3.1</b>	<b>Spaces and Subspaces of six-dimensional Phase Space</b>	<b>62</b>
<b>3.2</b>	<b>Phase Space Ellipse</b>	<b>65</b>
<b>3.3</b>	<b>Ellipse Representations</b>	<b>66</b>
3.3.1	Geometric Representation	66
3.3.2	Courant-Snyder and Parametric Notation	67
<b>3.4</b>	<b>Ellipse Transformations</b>	<b>70</b>
3.4.1	Simple Drift	71
3.4.2	Thin Lens	73
3.4.3	Solenoid	74
<b>3.5</b>	<b>Artificial Beam Edges</b>	<b>78</b>
3.5.1	Fixed ABE's	79
3.5.2	Fractional ABE's	79
3.5.3	IRF-Method	83

---

In this chapter the prerequisites for the interpretation of measurement and analysis results will be introduced. In terms of the discussion about information in section 1.6, this is the a priori knowledge, which in general is necessary to gain information. In section 3.5 the definition and derivation of artificial beam edges is discussed, that can be used to determine profile widths and beam size. This approach characterizes the state of the beam by the behavior of its edges, as is needed for a treatment of effective emittance for example. In section 3.1 the concept of the six dimensional phase space, and the conditions under which it can be divided into three two-dimensional subspaces, will be discussed. Later on it has to be ensured that these conditions are fulfilled, to validly perform tomography in the subspaces or to determine the emittance using the profile method with a focal lens. In section 3.2 it will be explained why the phase space can be approximated by an ellipse, since this is later on relevant for determining of the effective emittance. In a way this is connected strongly with the assumption of artificial beam edges and the reason, how it can be valid to describe a beam just by its edge behavior. Section 3.3 introduces three different possibilities of representations for the phase space ellipse that will be useful to understand the technique of phase space tomography or will help to derive characteristics of the phase space ellipse for other methods. In section 3.4 a closer look, on the ellipse transformation in different ion optic entities, namely drift, thin lens and solenoid will be taken. It will be proved, if they are suitable to use methods presupposing a two-dimensional phase space and the requirement that the theorem of Liouville is valid for it.

#### 3.1 Spaces and Subspaces of six-dimensional Phase Space

A completely different approach to the determination of ABE's is to use an a priori knowledge about ion optics and beam transport to reconstruct the phase space, and then calculating the wanted parameters from it by determining RMS-values. The state of a single mass point can be described by its position vector  $q = (x, y, z)$  in a three-dimensional ordinary space and its impulse components  $p = (p_x, p_y, p_z)$  in momentum space. The trajectory of a particle moving along an ion optic system is given by its position, angle, and impulse aberration. Many methods use the concept of tracing single particles along individual paths that are influenced by magnetic and electric devices along a beam line. The corresponding matrix formalisms deal with the influence of induced electric and magnetic fields of these devices on the path of individual particles. A particle beam can be seen as a collection of a very large number of particle trajectories. The beam then is defined completely, if the density distribution of all particles along their different longitudinal positions  $\mathcal{F}(x, p_x, y, p_y, z, p_z)$  is determined. The volume of the beam then can be understood as the integral over all particles

$$V^{\mathcal{F},t} = \iiint \iiint \iiint \mathcal{F}(x, p_x, y, p_y, z, p_z) dx dp_x dy dp_y dz dp_z. \quad (3.1)$$

This six-dimensional volume is placed in phase space, which is subject to general constraints allowing a perspective, where it is possible to talk about the characteristic dynamics of the whole beam in the nomenclature of single particle behavior. This is possible because of the assumption that the particle ensemble acts like one single particle which is blurred over the full phase space. That also includes that there is no interdependence of particles, that means in a way every particle has its own phase space. From this perspective, the six- $n$ -dimensional phase space can be understood in a deeper way, since it is occupied by those *blurred* particles, which in effect are collectively behaving particles in different ensembles. This is the maximum stage of diagnosis, referring from single particle behavior to the categorization of the beam by its position in six- $n$ -dimensional space. One has to take a careful look on these constraints since the conclusion from single particle behavior to beam behavior is not given in all cases. The state of a single particle can be captured by knowing where it is and where it is moving, as stated above. For describing the state of a particle beam one has to consult Liouville's theorem, which originates from statistical mechanics. With Banford [Ban66] the theorem states:

*Under the action of forces which can be derived from a Hamiltonian, the motion of a group of particles is such that the local density of the representative points in the appropriate phase space remains everywhere constant.*

The Hamilton equation  $\mathcal{H}(q, p, t)$  is considered in respect of classical particle motion [Bel87, Hin08], where  $p$  is called "the momentum conjugate to coordinate  $q$ ". In the six-dimensional phase space a particle is moving along the three directions  $q_1, q_2, q_3$  with the corresponding momenta  $p_1, p_2, p_3$  that are all parameterized in terms of the physical time  $t$ . It will be shown that for a Hamiltonian system the equation of continuity of the smooth density function  $\mathcal{F}(x, p_x, y, p_y, z, p_z, t)$  yields Liouville's Theorem in six-dim phase space. The current density distribution in phase space is given by

$$\vec{j}_6 = \mathcal{F}(x, p_x, y, p_y, z, p_z, t) \vec{v}_6, \quad (3.2)$$



### 3.1 Spaces and Subspaces of six-dimensional Phase Space

---

where  $\vec{v}_6$  is the velocity vector in phase space. Note that  $\mathcal{F}$  is depending explicitly on time, as could be seen by the last parameter  $t$ . Applying  $\vec{\nabla}_6$  to  $\vec{j}_6$

$$\begin{aligned} \frac{\partial \mathcal{F}}{\partial t} + \vec{\nabla}_6 \cdot \vec{j}_6 &= 0 \\ \frac{\partial \mathcal{F}}{\partial t} + \sum_{i=1}^3 \left[ \frac{\partial}{\partial q_i} (\mathcal{F} \dot{q}_i) + \frac{\partial}{\partial p_i} (\mathcal{F} \dot{p}_i) \right] &= 0 \\ \frac{\partial \mathcal{F}}{\partial t} + \sum_{i=1}^3 \left[ \dot{q}_i \frac{\partial \mathcal{F}}{\partial q_i} + \dot{p}_i \frac{\partial \mathcal{F}}{\partial p_i} + \mathcal{F} \frac{\partial \dot{q}_i}{\partial q_i} + \mathcal{F} \frac{\partial \dot{p}_i}{\partial p_i} \right] &= 0. \end{aligned} \quad (3.3)$$

From the Hamilton function, the equations of motion can be derived

$$\begin{aligned} \dot{p}_i &= -\frac{\partial \mathcal{H}}{\partial q_i} \\ \dot{q}_i &= \frac{\partial \mathcal{H}}{\partial p_i}. \end{aligned} \quad (3.4)$$

The last two terms in the sum of Eq. (3.3) then cancel

$$\frac{\partial \dot{q}_i}{\partial q_i} = \frac{\partial^2 \mathcal{H}}{\partial q_i \partial p_i} = -\frac{\partial \dot{p}_i}{\partial p_i}. \quad (3.5)$$

For a Hamiltonian system the continuity equation (3.3) then simplifies to

$$\frac{\partial \mathcal{F}}{\partial t} + \sum_{i=1}^3 \left[ \frac{\partial \mathcal{F}}{\partial q_i} \frac{dq_i}{dt} + \frac{\partial \mathcal{F}}{\partial p_i} \frac{dp_i}{dt} \right] = 0, \quad (3.6)$$

which is just the total time derivative of  $\mathcal{F}$

$$\frac{d\mathcal{F}}{dt} = 0. \quad (3.7)$$

If the system can be described by a Hamiltonian, this means, that the phase space volume  $V^{\mathcal{F},t}$  remains constant, and only the shape of the distribution may change. A system of conservative forces that takes influence on a beam exhibits a Hamiltonian. If the components of motion  $p_x, p_y, p_z$  are independent, such that there is no coupling between axial and transverse motions, Liouville's theorem also is applicable, supposed the six-dimensional volume is parted into longitudinal and transverse spaces [Sto06]. Under this condition it can be written

$$V_6^{\mathcal{F},t} = \iiint \mathcal{F}(x, p_x, y, p_y) dx dy dp_x dp_y \cdot \iint \mathcal{F}(z, p_z) dz dp_z = V_{4,tr}^{\mathcal{F},t} \cdot V_{2,lo}^{\mathcal{F},t}. \quad (3.8)$$

The longitudinal sub-volume  $V_{2,lo}^{\mathcal{F},t}$  is determined by the axial position of the particles and their variation in time. It therefore is depending on the beam current measured as a function of time related to a specified location.

### 3 Beam Theory and Analysis

Again, if the two transverse directions are not coupled, the four-dimensional sub-volume  $V_{4,tr}^{\mathcal{F},t}$  can be separated into two two-dimensional subspaces

$$V_{4,tr}^{\mathcal{F},t} = V_{2,x}^{\mathcal{F},t} \cdot V_{2,y}^{\mathcal{F},t}, \quad (3.9)$$

where

$$V_{2,x}^{\mathcal{F},t} = \iint \mathcal{F}(x, p_x) dx dp_x \quad V_{2,y}^{\mathcal{F},t} = \iint \mathcal{F}(y, p_y) dy dp_y. \quad (3.10)$$

If the particle energy does not change along the  $z$  direction, it is possible to factor out the momentum  $p_z$ . One now can define Cartesian trajectory angles  $x'$  and  $y'$ , in form of the slope of the trajectory, as is shown in Fig. 3.1

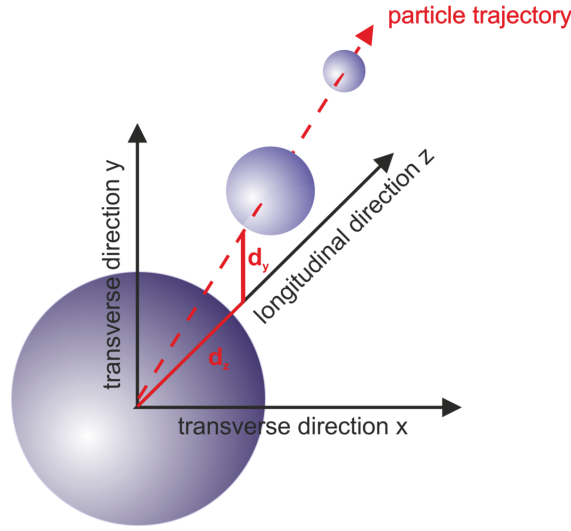


Figure 3.1: The slope of the trajectory angle can be used to substitute the momentum  $p$ , if the energy along the longitudinal  $z$  direction does not change.

$$x' = \arctan\left(\frac{dx}{dz}\right) \quad y' = \arctan\left(\frac{dy}{dz}\right) \quad (3.11)$$

$$V_{4,tr}^{\mathcal{F},t} = \iiint \mathcal{F}(x, p_x, y, p_y) dx dp_x dy dp_y = \vec{p}_z^2 V_{2,x}^{\mathcal{F},t} V_{2,y}^{\mathcal{F},t}, \quad (3.12)$$

and with (3.10)

$$V_{2,x}^{\mathcal{F},t} = \iint \mathcal{F}(x, x') dx dx' \quad V_{2,y}^{\mathcal{F},t} = \iint \mathcal{F}(y, y') dy dy'. \quad (3.13)$$

In further considerations, the density distribution of the sub-volumes  $(x, x')$  and  $(y, y')$  will be referred to as

$$V_{2,x}^{\mathcal{F},t} \hat{=} \mathcal{F}(x, x') \quad V_{2,y}^{\mathcal{F},t} \hat{=} \mathcal{F}(y, y'). \quad (3.14)$$

### 3.2 Phase Space Ellipse

The phase space area occupied by particles can be represented generally by an ellipse. Under the influence of restoring forces particles moving along the longitudinal axis underlie a harmonic radial motion, which is projected as a sinusoidal oscillation in ordinary space.

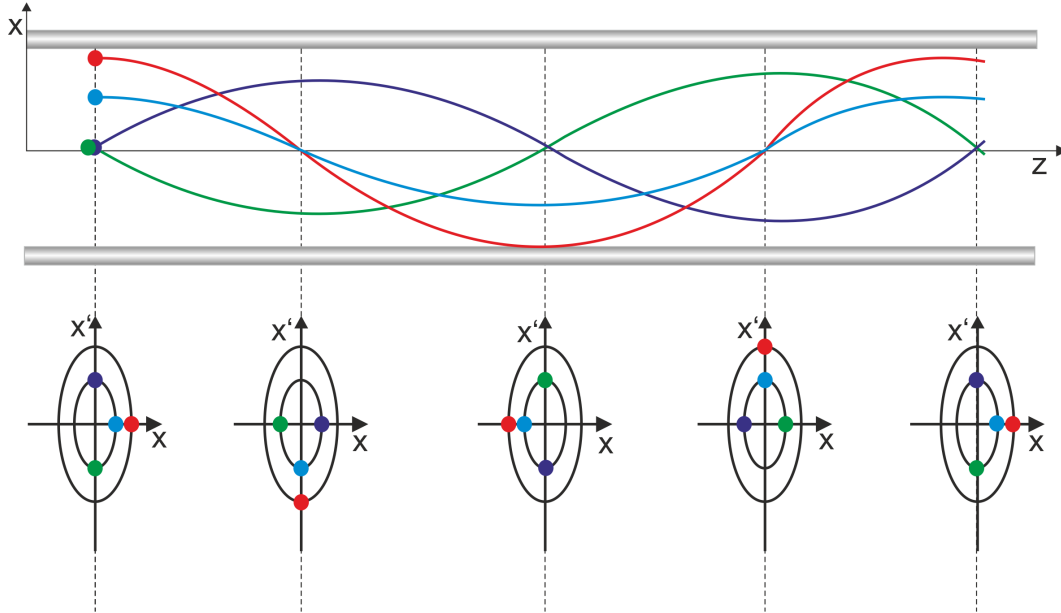


Figure 3.2: Particles moving under restoring forces in a harmonic oscillation, prescribe a trajectory ellipse in phase space (picture in dependence on [Ban66]). Particles with same phase but different amplitude share the same radial motion in different orbits. Particles with the same amplitude but different phases keep their relative position to each other while moving.

This motion is transformed in a two-dimensional transverse subspace to the representation of an ellipse. According to [Ban66] the equation of motion can be written as

$$x'' = -x \left( \frac{2\pi}{\lambda} \right)^2, \quad (3.15)$$

where  $\lambda$  describes the wavelength corresponding to the restoring force. The harmonic motion about the  $z$ -axis then turns out to be

$$x = a \cdot \sin \left( \frac{2\pi z}{\lambda} + \phi \right). \quad (3.16)$$

where  $\phi$  is the phase and  $a$  the amplitude of the sinusoidal characteristics of every particle trajectory shown at the top of Fig. 3.2. From Eq. (3.16) it can be obtained

$$x' = a \left( \frac{2\pi}{\lambda} \right) \cdot \cos \left( \frac{2\pi z}{\lambda} + \phi \right), \quad (3.17)$$

Now the equation for the ellipse in phase space can be derived from Eqs. (3.16) and (3.17)

$$\begin{aligned}
 & \begin{cases} x &= a \cdot \sin\left(\frac{2\pi z}{\lambda} + \phi\right) & | : a \cdot \left(\frac{2\pi}{\lambda}\right) \\ x' &= a \left(\frac{2\pi}{\lambda}\right) \cdot \cos\left(\frac{2\pi z}{\lambda} + \phi\right) & | : a \end{cases} \\
 & \begin{cases} \frac{x'\lambda}{2\pi a} &= \cos\left(\frac{2\pi z}{\lambda} + \phi\right) & | ()^2 \\ \frac{x}{a} &= \sin\left(\frac{2\pi z}{\lambda} + \phi\right) & | ()^2 \end{cases} \\
 & \begin{cases} \left(\frac{x'\lambda}{2\pi a}\right)^2 &= \cos^2\left(\frac{2\pi z}{\lambda} + \phi\right) \\ \left(\frac{x}{a}\right)^2 &= \sin^2\left(\frac{2\pi z}{\lambda} + \phi\right) \end{cases} \\
 & \Rightarrow \left(\frac{x'\lambda}{2\pi a}\right)^2 + \left(\frac{x}{a}\right)^2 = \cos^2\left(\frac{2\pi z}{\lambda} + \phi\right) + \sin^2\left(\frac{2\pi z}{\lambda} + \phi\right) \\
 & \Rightarrow \left(\frac{x'\lambda}{2\pi a}\right)^2 + \left(\frac{x}{a}\right)^2 = 1. \tag{3.18}
 \end{aligned}$$

As already mentioned, by moving on a sinusoidal trace in ordinary space, the particle prescribes an elliptic path in phase space. The location of the particle is depending on the phase  $\phi$  and the amplitude  $a$ . Having a look on the purple and green particle and their path in Fig. 3.2 at the top, it can be seen that they are in a different phase  $\phi$  (here: reverse phase). While moving along  $z$  in ordinary space, both particles are also moving in phase space, but they always keep their relative position to each other (phase space picture in the lower row: green and purple points). Having a look on the red and blue particles and their path, both particles have the same phase  $\phi$  but they are moving along with different amplitudes. In phase space it can be seen that they share a corresponding circular motion but, since the red particle starts with a higher amplitude it describes a larger elliptic path than the blue one.

### 3.3 Ellipse Representations

The phase space ellipse as a two-dimensional projection of the six-dimensional ellipsoid can be represented by different notations depending on the task to be solved. At this point, the ellipse will be explained in the notation of a projection which is useful to create transforms for the phase space reconstruction in section 5.1 and in the two useful representations Courant-Snyder notation and parametric notation, which are needed to deal with emittance in section 5.

#### 3.3.1 Geometric Representation

For the tomographic reconstruction of the phase space a geometrical representation has to be found. The tomography for ordinary space reconstructs the function  $\mathcal{F}(x, y)$  of the intensity distribution. This later on turns out to be a special case of the phase space reconstruction, since for backprojecting the ordinary space at a position  $z$ , the distance in the computation of all transforms of the radon plot is set to 0 (section 5.1).

In Fig. 3.3 this special situation is given by a centered, horizontal ellipse. The distances  $A$  and  $B$  denote the principal axes. A projection  $p_\varphi(s)$  of the ellipse is taken at an angle  $\varphi$  on a line  $s$ , by computing all line integrals from the zero point of the coordinate system to a distance  $a(\varphi)$  at both

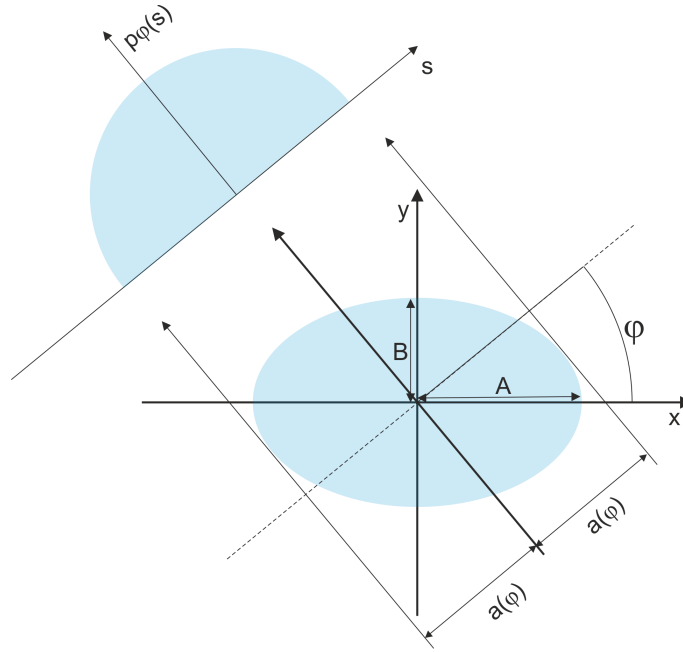


Figure 3.3: The geometrical situation for a centered ellipse lying horizontal with its principal axes on the coordinate system in ordinary space.

sides. Since the function  $\mathcal{F}(x, y)$  inside the ellipse has to be found, a distinction of the following two cases is defined with regard to Eq.(3.18)

$$\iota = \begin{cases} 1 & \text{for } \frac{x^2}{A^2} + \frac{y^2}{B^2} \leq 1 \\ 0 & \text{otherwise.} \end{cases} \quad (3.19)$$

The projection  $p_\varphi(s)$  now can be written in terms of the geometrical situation of the ellipse [Kak88]

$$p_\varphi(s) = \frac{2\iota AB}{a^2(\varphi)} \cdot \sqrt{a^2(\varphi) - s^2}, \quad (3.20)$$

where

$$a^2(\varphi) = A^2 \cdot \cos^2(\varphi) + B^2 \cdot \sin^2(\varphi). \quad (3.21)$$

Eq. (3.21) is explained in more detail in section 2.2. Eq. (3.20) arises out of the geometrical situation in Fig. 3.3. Eq. (3.20) becomes zero if a point  $(x_i, y_i)$  is not element of  $\mathcal{F}(x, y)$ , because of the parameter  $\iota$ , which in this case sets everything to 0 in this case.

#### 3.3.2 Courant-Snyder and Parametric Notation

In dependence on the discussion in section 3.1 it can be assumed that with the knowledge of the transformation of one particle under given conditions and with linearity, also the transformation of the particle ensemble is known.

### 3 Beam Theory and Analysis

With [Hin08] a radial phase space ellipse can be written as

$$\sigma_x = \begin{pmatrix} \sigma_{11} & \sigma_{12} \\ \sigma_{12} & \sigma_{22} \end{pmatrix}. \quad (3.22)$$

Given a point  $(x, x')$  on the ellipse, the equation of the phase space ellipse will be

$$(x, x')\sigma_x^{-1} \begin{pmatrix} x \\ x' \end{pmatrix} = 1, \quad (3.23)$$

where  $\sigma_x^{-1}$  is the inverse of  $\sigma_x$

$$\sigma_x^{-1} = \frac{1}{\det(\sigma_x)} \begin{pmatrix} \sigma_{22} & -\sigma_{12} \\ -\sigma_{12} & \sigma_{11} \end{pmatrix}. \quad (3.24)$$

Now solving Eq. (3.23) leads to

$$\sigma_{22}x^2 - 2\sigma_{12}xx' + \sigma_{11}x'^2 = \det(\sigma_x) = \epsilon_x^2. \quad (3.25)$$

Where  $\epsilon_x$  is the emittance. Having a look on an ellipse in the  $(x, x')$ -space there are four distinct points determining its shape.

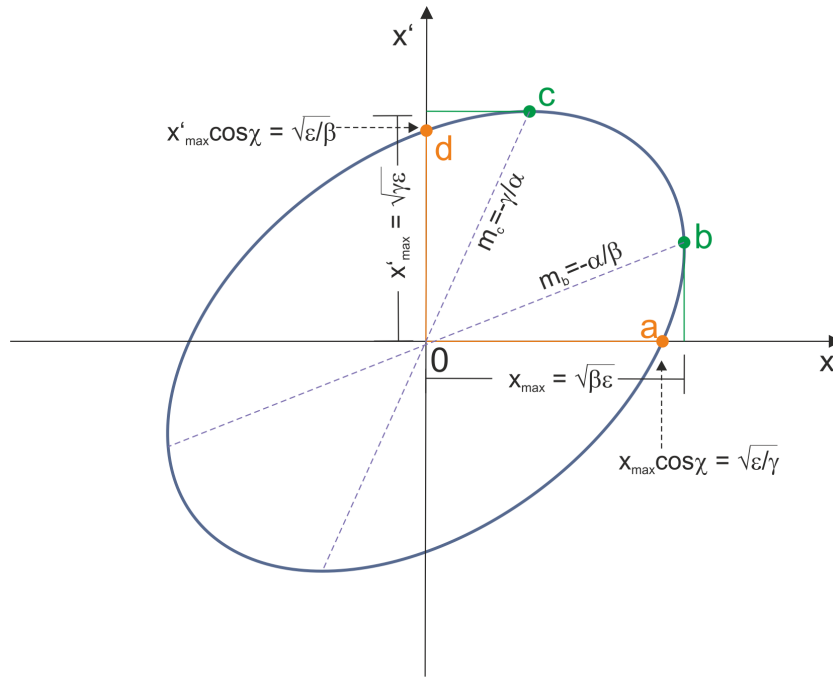


Figure 3.4: Four points which determine the characteristics of the ellipse in phase space.  $a$  and  $d$  are the axis intercepts.  $c$  and  $b$  are the maximum spreads of the two dimensions.  $m_c$  and  $m_b$  are the slopes of the lines connecting the maximum and minimum spreads of the  $x$  and  $x'$  dimension.

notations overview			
point/distance	sigma	cour-sny	parametric
$(0,0)(b,0)$	$\sqrt{\sigma_{11}}$	$\sqrt{\epsilon \cdot \beta}$	$x_{\max}$
$(0,0)(0,c)$	$\sqrt{\sigma_{22}}$	$\sqrt{\epsilon \cdot \gamma}$	$x'_{\max}$
a	$\sqrt{\sigma_{11}(1 - r_{12}^2)}$	$\sqrt{\frac{\epsilon}{\gamma}}$	$x_{\max} \cos \chi$
b	$r_{12}\sqrt{\sigma_{22}}$	$-\alpha\sqrt{\frac{\epsilon}{\beta}}$	$x'_{\max} \sin \chi$
c	$r_{12}\sqrt{\sigma_{11}}$	$-\alpha\sqrt{\frac{\epsilon}{\gamma}}$	$x_{\max} \sin \chi$
d	$\sqrt{\sigma_{22}(1 - r_{12}^2)}$	$\sqrt{\frac{\epsilon}{\beta}}$	$x'_{\max} \cos \chi$

Table 3.1: The four important points of a phase space ellipse, can be represented by different notations, depending on the task, that have to be solved.

The  $x'$ -axis intercept at point d is related to the beam temperature (Fig. 3.4). The maximum spread in  $x$  direction at point b is related to the beam envelope. Courant and Snyder [Sny57] introduced a notation by Twiss-parameters  $\alpha, \beta, \gamma$ , where  $\sqrt{\beta}$  defines the rooted mean square of the divergence of the beam envelope and  $\sqrt{\gamma}$  the rooted mean square of the beam divergence.  $\alpha$  is proportional to the correlation between  $x$  and  $x'$  and is linked to the orientation of the ellipse. If  $\alpha$  is negative the beam is divergent and the ellipse has an orientation to the right. If it is positive the beam is convergent and the ellipse orientation turns to the left (see Fig. 3.5 including explanations for more details). Eq. (3.25) now can be given in Courant-Snyder notation by

$$\gamma x^2 + 2\alpha x x' + \beta x'^2 = \epsilon^2, \quad (3.26)$$

where  $\epsilon$  is the effective beam emittance, which will be discussed more detailed in section 5.4. Here it is only relevant to know that the effective emittance is given by the area of the ellipse

$$\epsilon = \frac{A}{\pi}, \quad (3.27)$$

where  $A$  is the surface area of the ellipse.

The correlation parameter  $r_{12}$  with  $-1 \leq r_{12} \leq 1$  is a dimensionless measure for the correlation between  $x$  and  $x'$ . It can be described by

$$r_{12} = \frac{\sigma_{12}}{\sqrt{\sigma_{11}\sigma_{22}}}. \quad (3.28)$$

Usually the twiss-parameters are defined to satisfy the normalization condition  $\beta\gamma - \alpha^2 = 1$ .

### 3 Beam Theory and Analysis

---

The most apparent possibility to describe the four distinct points [Joh80] is to define the distance from the zero point to the maximum value of  $x$  with parameter  $x_{\max}$  and the maximum value of  $x'$  with  $x'_{\max}$ . To include the correlation between  $x$  and  $x'$  for the orientation of the ellipse the parameter  $\chi$  is introduced. The above mentioned dimensionless correlation parameter can be written in parametric notation by  $r_{12} = \sin(\chi)$ . Then a point  $(x, x')$  in parametric notation can be denoted as

$$\begin{pmatrix} x \\ x' \end{pmatrix} = \begin{pmatrix} x_{\max} \cos(\delta) \\ x'_{\max} \sin(\delta + \chi) \end{pmatrix}, \quad (3.29)$$

where  $0 \leq \delta \leq 2\pi$  is a radial running parameter.

To define the ellipse for any given distribution of particles, the following statistical parameters are introduced with Eq. (3.14) and the normalization  $\iint \mathcal{F}(x, x') dx dx' = 1$  like

$$\begin{aligned} \overline{x^2} &= \sigma_x^2 = \iint x^2 \mathcal{F}(x, x') dx dx' \\ \overline{x'^2} &= \sigma_{x'}^2 = \iint x'^2 \mathcal{F}(x, x') dx dx' \\ \overline{xx'} &= \iint xx' \mathcal{F}(x, x') dx dx'. \end{aligned} \quad (3.30)$$

### 3.4 Ellipse Transformations

A particle travelling along a drift underlies different transformations of its position in phase space, depending on the configuration of the beam guide system. Given a phase space ellipse in sigma notation Eq. (3.22), for a particle position  $(x, x')$  of this ellipse, according to (3.23) can be written

$$\begin{aligned} (x, x') \sigma_x^{-1} \begin{pmatrix} x \\ x' \end{pmatrix} &= 1 \\ \Rightarrow \mathbf{x}^T \sigma_x^{-1} \mathbf{x} &= 1. \end{aligned} \quad (3.31)$$

Assuming a transfer matrix  $\mathcal{A}$  along  $z$ , the mapping of a particle from a position  $z_0$  to a position  $z_1$  and inversely, can be described by

$$\begin{aligned} \mathbf{x}_1 &= \mathcal{A} \mathbf{x}_0 \\ \mathbf{x}_0 &= \mathcal{A}^{-1} \mathbf{x}_1. \end{aligned} \quad (3.32)$$

Applying this to (3.31) leads to

$$\begin{aligned} (\mathbf{x}_1 \mathcal{A}^{-1})^T \sigma_{x_{z_0}}^{-1} (\mathbf{x}_1 \mathcal{A}^{-1}) &= 1 \\ \mathbf{x}_1^T (\mathcal{A}^T)^{-1} \sigma_{x_{z_0}}^{-1} \mathcal{A}^{-1} \mathbf{x}_1 &= 1 \\ \mathbf{x}_1^T \underbrace{(\mathcal{A} \sigma_{x_{z_0}} \mathcal{A}^T)^{-1}}_{\sigma_{x_{z_1}}^{-1}} \mathbf{x}_1 &= 1 \\ \Rightarrow \mathbf{x}_1^T \sigma_{x_{z_1}}^{-1} \mathbf{x}_1 &= 1. \end{aligned} \quad (3.33)$$



Now this can be expressed for a particle at position  $z_0$  with the coordinates  $(x_{z_0}, x'_{z_0})$  travelling to a position  $z_1$  with coordinates  $(x_{z_1}, x'_{z_1})$  by

$$\sigma_{x_{z_1}} = A\sigma_{x_{z_0}}A^T. \quad (3.34)$$

Regarding two-dimensional subspaces of the six-dimensional phase space volume, it has to be ensured that the transformation performed by  $\mathcal{A}$  do not establish a correlation between the two transverse directions as shown in Eq. (3.9).

In the following, three realizations of a transfer matrix  $\mathcal{A}$  will be discussed, and it will be analyzed to what extent they are correct for application in phase space tomography.

#### 3.4.1 Simple Drift

The simple drift bridges the distance between two ion optic elements. Without space charge, this means that the particles follow their way on their trajectories without influence. The only factor that has to be considered then is the drift length  $d$ . The transformation matrix  $\mathcal{A}_d$  of a simple drift will be

$$\mathcal{A}_d = \begin{pmatrix} 1 & d \\ 0 & 1 \end{pmatrix}. \quad (3.35)$$

Now consider a phase space ellipse at position  $z_0$ , such that for a particle at  $(x_0, x'_0)$  the parameters  $x_{\max}$  and  $x'_{\max}$  are the maximum displacement and divergence at position  $z_0$ . The ellipse ([Ban66]) then can then be denoted in a parametric notation by

$$\left(\frac{x_0}{x_{\max}}\right)^2 + \left(\frac{x'_0}{x'_{\max}}\right)^2 = 1. \quad (3.36)$$

Noting that a particle at a position  $z_0$  with divergence  $x'$  and displacement  $x$  has the same divergence  $x'$  at position  $z_1$  (since the drift does not influence the divergence angle) but the displacement  $x + dx'$  (which means that the particle is travelling along its trajectory with divergence  $x'$  for a distance  $d$ ) with Eq. (3.29) the divergence and displacement at position  $z_1$  with distance  $d_1$  can be written

$$\begin{aligned} x_1 &= x_{\max} \cos(\varphi) + d_1 x'_{\max} \sin(\varphi) \\ x'_1 &= x'_{\max} \sin(\varphi). \end{aligned} \quad (3.37)$$

With

$$x_{\max} \cos(\varphi) + d_1 x'_{\max} \sin(\varphi) = (x_{\max}^2 + (d_1 x'_{\max})^2)^{\frac{1}{2}} \cos\left(\varphi - \arctan\left(\frac{d_1 x'_{\max}}{x_{\max}}\right)\right), \quad (3.38)$$

the ellipse equation given by Eq. (3.36) at position  $z_1$  turns out to become

$$\left(\frac{x_0}{x_{\max}}\right)^2 - 2d_1 \left(\frac{x_1 x'_1}{x_{\max}^2}\right) + \left(\frac{x'_0}{x'_{\max}}\right)^2 \left(\frac{1 + d_1^2 x_{\max}^2}{x_{\max}^2}\right) = 1. \quad (3.39)$$

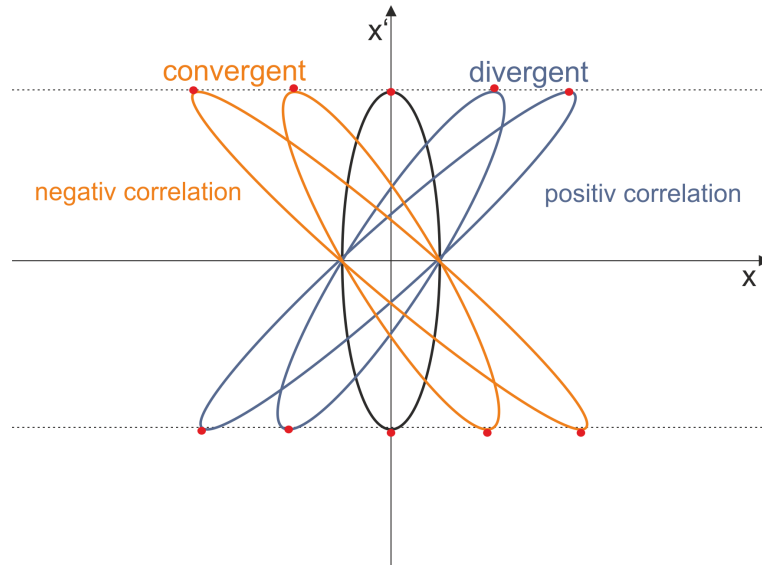


Figure 3.5: Transforming the phase space ellipse by a drift distance leads to a shearing. If the correlation of  $x$  and  $x'$  is positive the beam is divergent and the ellipse is tilting to the right, into the positive quadrant of the phase space coordinate system. If the correlation is negative the beam is convergent and the ellipse tilts to the left.

Having a look on the ellipse before and after transformation by the drift in Fig. 3.5 it turns out that the drift causes a shearing of the phase space ellipse. The length of the major axis of this transformed ellipse is given by  $x_{\max}(1 - d_1 \tan(\theta))^{-\frac{1}{2}}$ , where  $\theta$  is the angle between the major axis and the  $x$ -axis. Therefore, the length of the minor axis of the ellipse now is  $x_{\max}(1 + d_1 \cot(\theta))^{-\frac{1}{2}}$ . It is important to see, that now  $x_{\max}$  and  $x'_{\max}$  are only denoting distances in the graph.  $d_1$  then turns out to be just a scaling factor, that influences the degree of the shearing. This coherency will be discussed in more detail when dealing with phase space tomography in section 5.1, where it will be shown that the crossover from ordinary space tomography to phase space tomography can be performed by applying a scaling factor on the radon transforms and defining a phase space angle for the backprojection. It is important also for the direct determination of the effective emittance.

The shearing mirrors the position of the ellipse in relation to a given beam waist. A phase space ellipse tilted to the left, points to a position in front of a beam waist, indicating a convergent beam characteristic (Fig. 3.5 orange ellipses). At the beam waist, the ellipse will be upright (black ellipse) and behind the beam waist it will be a right tilted ellipse indicating a divergent beam (blue ellipses). The shearing is not a rotation. There are two fixed points given at the intersection of the ellipse with the  $x$ -axis given at  $x_{\max} \cos(\chi)$  or accordingly in Twiss-parameter form at  $\sqrt{\frac{\epsilon}{\gamma}}$  (Fig. 3.4 point a) and at  $-x_{\max} \cos(\chi)$  or  $-\sqrt{\frac{\epsilon}{\gamma}}$  respectively. Only the extrema  $\pm x_{\max} \sin(\chi)$  are shifted. This can be seen better in Courant-Snyder notation with  $-\alpha \left( \pm \sqrt{\frac{\epsilon}{\gamma}} \right)$ , since  $\alpha$  is linked to the orientation of the ellipse as explained before. The area of the ellipse is conserved as required by Liouville. Concluding it can be said that the simple drift influences the displacement of a particle and the correlation factor of

the phase space ellipse. It has no effect on the divergence of the particles or the surface area of the two-dimensional ellipse projection of the six-dimensional phase space volume. The drift is a suitable transformation matrix for phase space tomography and also works for the direct determination of effective emittance.

### 3.4.2 Thin Lens

In contrast to the drift, a linear thin lens performs a change  $\Delta\alpha'$  of the slope of the trajectory of a particle. Given a thin lens with focal distance  $f$  the refraction power is  $f^{-1}$ . For a displacement  $\alpha$ , the change turns out to be [Hin08]

$$\Delta\alpha' = \frac{\alpha}{f}. \quad (3.40)$$

Fig. 3.6 illustrates the connection between  $\Delta\alpha'$  and the type of lens.

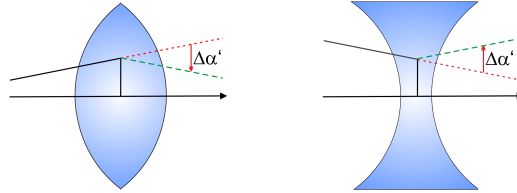


Figure 3.6: Within a focussing lens with a positive focal distance,  $\Delta\alpha'$  changes the slope of a particle trajectory as shown in the left picture. The influence of a dispersing lens with a negative focal distance is shown on the right.

The transformation matrix for a thin lens is given by

$$\mathcal{A}_l = \begin{pmatrix} 1 & 0 \\ -f^{-1} & 1 \end{pmatrix}. \quad (3.41)$$

Although this assignment holds for both transverse directions, the focal distances and refraction powers may be different. Applying a thin lens to a beam with an upright ellipse will also lead to a shearing but on the contrary to the shearing of the simple drift the two fixed points are now given by the intersection points of the ellipse with the  $x'$ -axis. Namely  $\pm x'_{\max} \cos(\chi)$  (or  $\pm \sqrt{\frac{\epsilon}{\beta}}$ ) (see Fig. 3.7). The direction of the shearing depends on the algebraic sign of the focal distance of the lens. If the focal distance is positive, so the refraction power will be, then the lens is a collecting lens. In this case the ellipse will be tilted to the left upwards and to the right downwards indicating that the beam will become convergent. If the focal distance and refraction power is negative, the lens will be a dispersing lens, such that the beam will become divergent and the phase space ellipse is accordingly tilted to the right upwards and to the left downwards.

The degree of shearing depends on the refraction power. Concluding it can be said that the thin lens has influence on the divergence of a particle and the correlation factor of the phase space ellipse but not on the displacement or the surface area. According to the drift, the area of the ellipse is conserved as

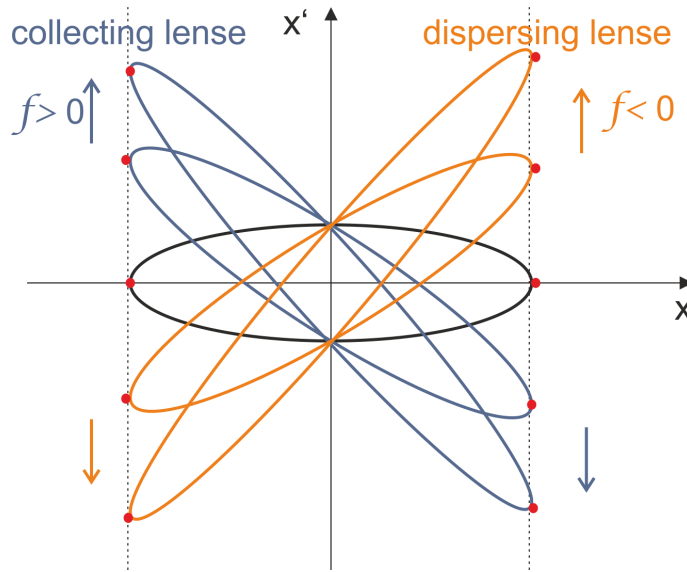


Figure 3.7: Transforming the phase space ellipse by a thin lens leads to a shearing in the  $x'$  direction of the ellipse. If the focal distance of the lens is positive, the lens will be sheared upwards (blue), if it is negative it will be tilted downwards (orange).

required by Liouville . The only difference between simple drift and thin lens in terms of the influence of the phase space ellipse is the direction of shearing.

#### 3.4.3 Solenoid

Solenoids are symmetrically focussing magnetic elements. Particles travelling parallel to the homogeneous magnetic field, will unaffectedly pass the solenoid. Particles that exhibit transverse velocity components will be exposed to a deflective force, causing them to travel on a circular path around the magnetic field lines. Unfortunately, this fact establishes a coupling between the transverse components. This, on a first view, contradicts the use of solenoids to perform a phase space tomography for a two-dimensional subspace and also the use of a solenoid instead of a thin lens for the direct determination of effective emittance. The separation of the six-dimensional phase space into three two-dimensional subspaces is allowed under the condition that the components of motion are independent, viz uncoupled (section 3.1). Otherwise, the conditions for the preservation of emittance in the subspaces will not be fulfilled. The tomographic computation of a subspace essentially requires the conditions for Liouville's theorem to be kept valid for the computed subspace (see Eq. (5.4) on page 108) throughout the whole transformation described by a matrix  $\mathcal{A}$ . Nevertheless, there will be a way out [Hin08, Ban66].

Having a look on the circular motion in ordinary space (Fig. 3.8), radius  $r$  can be determined from

$$\mathcal{B}er = mv_T, \quad (3.42)$$

since a particle experiences a force  $\mathbf{F}$  in a field  $\mathcal{B}$  that is given by  $\mathbf{F} = \mathcal{B} \cdot e \cdot v$ , where  $v$  is a velocity vertical to  $\mathcal{B}$ , and  $e$  the charge of the particle. With Newton's second law and the centripetal acceleration  $\frac{v^2}{r}$ ,

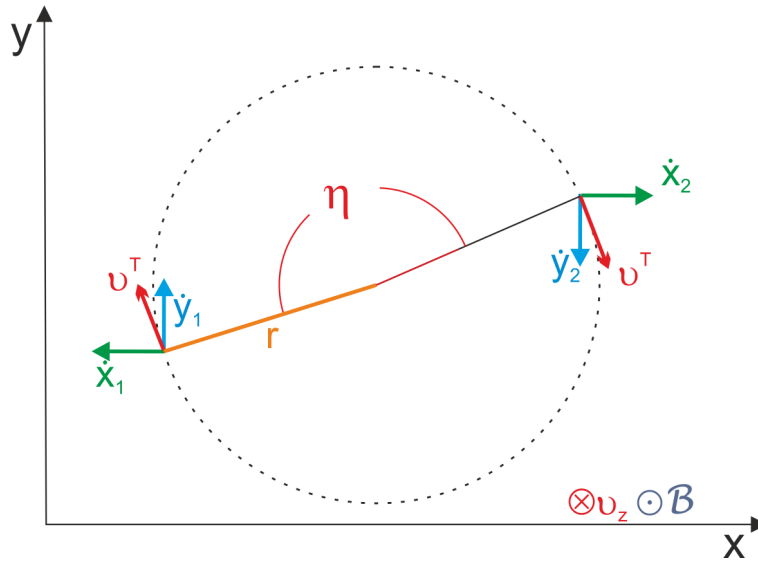


Figure 3.8: Particles leaving the end of a solenoid experience a force causing a helical motion, seen in three-dimensional ordinary space. Projected on a top view seen from the longitudinal direction, this motion can be described by a circle. A particle at position  $x_1, y_1$  with transverse velocity  $v_T$  will be influenced by an angle of deflection  $\eta$ , such that it travels along a circle, ending up in position  $x_2, y_2$ . The axial velocity  $v_z$  and the magnetic field  $\mathcal{B}$  are pointing to the drawing plane.

Eq. (3.42) can be derived. Given the effective length  $L$  of the solenoid, the angle  $\eta$  of deflection can be denoted by

$$\eta = \frac{v_T L}{v_z r}. \quad (3.43)$$

Out of this circular geometry, one can derive the transformation matrix for the relation between the starting point and end point of the solenoid by dividing the velocity components by the axial velocity, since this leads to the angular difference relative to the axis. The transformation matrix for the four-dimensional subspace  $(x, x', y, y')$  now can be given by

$$\begin{pmatrix} x_1 \\ x'_1 \\ y_1 \\ y'_1 \end{pmatrix} = \begin{pmatrix} 1 & \frac{L \sin(\eta)}{\eta} & 0 & -L \frac{1 - \cos(\eta)}{\eta} \\ 0 & \cos(\eta) & 0 & -\sin(\eta) \\ 0 & L \frac{1 - \cos(\eta)}{\eta} & 1 & L \frac{\sin(\eta)}{\eta} \\ 0 & \sin(\eta) & 0 & \cos(\eta) \end{pmatrix} \begin{pmatrix} x_0 \\ x'_0 \\ y_0 \\ y'_0 \end{pmatrix}. \quad (3.44)$$

The red entries are responsible for the coupling of the transverse components. If a complete circle is described by  $\eta = 2\pi$ , then the transformation matrix becomes the unity matrix, where every entry becomes 0, except the entries on the main diagonal which become 1. In this case, the initial- and end-coordinates of a particle are equal, as also can be seen from Fig. 3.8.

According to [Ros60] at the end of the solenoid there is an interaction of the radial magnetic field component  $\mathcal{B}_r$  and the axial velocity component of the particles, which leads to an azimuthal acceleration

### 3 Beam Theory and Analysis

as can be seen from Fig. 3.9. Since a charged particle is moving with longitudinal velocity  $v_z$  in a radial

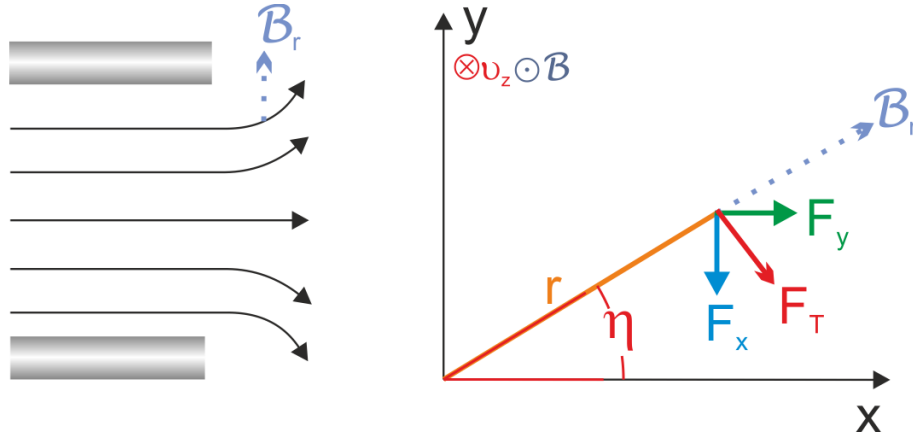


Figure 3.9: Left: a particle at the end of a solenoid experiences an azimuthal acceleration, since the radial magnetic field component influences the axial velocity of the particle. Right: axial representation of the forces that are affected by the radial magnetic field component  $B_r$ . The magnetic field  $B$  and the axial velocity  $v_z$  again are pointing to the drawing plane.

magnetic field component  $B_r$  it is affected by a Lorentz force, which is the reason for the additional angular velocity  $\eta$ . Assuming a rotational symmetry which is given by a radial field component that is linear with radius  $r$ , then with Maxwell's Equation  $\text{div}B = 0$  it follows in linear approximation

$$B_r = -\frac{r}{2} \frac{\partial B_z}{\partial z}. \quad (3.45)$$

From Fig. 3.9 on the left, it can be seen that the force  $F_x$  in  $x$  direction is

$$F_x = F_y \cdot \sin(\eta). \quad (3.46)$$

The field component  $B_x$  (accordingly  $B_y$ ) affecting the  $x$  (resp.  $y$ ) position of a particle under consideration of the deflective radial magnetic field component, then can be expressed by

$$\begin{aligned} B_x &= \frac{x}{r} B_r = -\frac{x}{2} \frac{\partial B_z}{\partial z} \\ B_y &= \frac{y}{r} B_r = -\frac{y}{2} \frac{\partial B_z}{\partial z}. \end{aligned} \quad (3.47)$$

Neglecting any change of the displacements  $x$  and  $y$  at the boundary field, one can obtain the change of direction  $\Delta x'$  and  $\Delta y'$  by integrating over the boundary field

$$\begin{aligned} \Delta x' &= \int B_y dz = \pm y \cdot \frac{1}{2} \eta L \\ \Delta y' &= \int B_x dz = \mp x \cdot \frac{1}{2} \eta L. \end{aligned} \quad (3.48)$$

Therefore, the relation between the initial and final displacements of a particle travelling along the field of length  $L$ , can be described by

$$\begin{aligned}x'_1 &= x'_0 \pm y_0 \frac{1}{2} \eta L \\y'_1 &= y'_0 \mp x_0 \frac{1}{2} \eta L.\end{aligned}\tag{3.49}$$

In this representation the coupling is very obvious. The leading sign distinguishes the entrance (upper) and the exit(lower) of the solenoid. For reasons of clarity some abbreviations

$$\begin{aligned}\kappa &= \frac{1}{2} \eta L \\C &= \cos\left(\frac{\eta}{2}\right) \\S &= \sin\left(\frac{\eta}{2}\right).\end{aligned}$$

are introduced. Now Eq. (3.49) now is written in matrix notation by

$$\begin{pmatrix} x_1 \\ x'_1 \\ y_1 \\ y'_1 \end{pmatrix} = \begin{pmatrix} 1 & 0 & 0 & 0 \\ 0 & 1 & \pm\kappa & 0 \\ 0 & 0 & 1 & 0 \\ \mp\kappa & 0 & 0 & 1 \end{pmatrix} \begin{pmatrix} x_0 \\ x'_0 \\ y_0 \\ y'_0 \end{pmatrix}.\tag{3.50}$$

Rewriting the transformation matrix from Eq. (3.44) by multiplying it with the matrix from Eq. (3.50), the complete transformation matrix for the solenoid in the transverse plane yields

$$\mathcal{A}_s^* = \begin{pmatrix} C^2 & \frac{SC}{\kappa} & SC & \frac{S^2}{\kappa} \\ -SC\kappa & C^2 & -S^2\kappa & SC \\ -SC & -\frac{S^2}{\kappa} & C^2 & \frac{SC}{\kappa} \\ S^2\kappa & -SC & -SC\kappa & C^2 \end{pmatrix}.\tag{3.51}$$

As a beam is travelling through the solenoid, its particle distribution is rotated as a consequence of the azimuthal force affecting transverse velocity components of the particles. The change of displacement is a function of distance  $z$ , which can be seen from the composition of  $\kappa$  in Eq. (3.50).  $\mathcal{A}_s^*$  is not the final transformation matrix, useful for phase space tomography, since it contains still the transverse coupling.

As stated above, particles travelling parallel to the magnetic field will pass the solenoid without being rotated. Given a cylinder symmetric system, the particles will pass completely unaffected through the lens. This is equivalent to Busch's theorem. [Rei08]<sup>1</sup>

The radially oscillating motion of the particles take place in a plane rotating with Larmor frequency  $\omega_t$ .

---

<sup>1</sup>This is another conservation theorem, obtained by considering systems in which the Hamiltonian does not depend on the space coordinates, as it is given in cylinder symmetric systems. This conservation law is used to describe particle dynamics in axis-symmetrical fields, e.g the magnetic field of a solenoid. It is this conservation law that is equivalent to Busch's theorem, stating, that in a cylinder symmetrical system, the canonical angular momentum is a constant of particle motion.

### 3 Beam Theory and Analysis

---

If now the space charge is zero, the particle trajectories in the transverse plane are off-centered circles as described before. There are two extreme situations. The first is, the particles are launched with zero angular velocity behaving like particles in a cylinder symmetric system according to Busch's theorem, which means that they form a helix touching the  $z$ -axis but without crossing it. The second is the particles completely are dominated by space-charge fields, leading to centered circles in the transverse plane, where the particles are rotating around the center with Larmor frequency. In between these two extremes the trajectory pattern depends on the ratio of plasma frequency to Larmor frequency, and is much more complicated to describe.

Particles with zero angular velocity at a starting point without magnetic field, get harmonic oscillation in the transverse plane because of the transverse particle motion in the Larmor frame. The complete transformation matrix, given in Eq. (3.51) can be decomposed in its rotational component and its focussing component

$$\mathcal{A}_s^* = \mathcal{A}_f \mathcal{R}. \quad (3.52)$$

The rotation matrix  $\mathcal{R}$  represents a rotation around the axis about an angle  $\frac{\eta}{2}$ , and is given by

$$\mathcal{R} = \begin{pmatrix} C & 0 & S & 0 \\ 0 & C & 0 & S \\ -S & 0 & C & 0 \\ 0 & -S & 0 & C \end{pmatrix}. \quad (3.53)$$

The focussing part of the transformation matrix, the rotation matrix  $\mathcal{R}$ , now remains to

$$\mathcal{A}_f = \begin{pmatrix} C & \frac{S}{\kappa} & 0 & 0 \\ -S\kappa & C & 0 & 0 \\ 0 & 0 & C & \frac{S}{\kappa} \\ 0 & 0 & -S\kappa & C \end{pmatrix}. \quad (3.54)$$

The transformation matrix  $\mathcal{A}_s^*$  can be used for phase space tomography assuming no space charge, as discussed before. With a predominating influence of space charge, one has to rotate the density distribution in ordinary space with the angle that is obtained by the Larmor frequency. For every beam moving between these two extrema, one has to estimate iteratively the initial conditions to obtain the real characteristics of the rotation matrix  $\mathcal{R}$ . As said before, the deflection angle affecting the particle trajectories are then described by a not known ratio of the plasma and the Larmor frequency. This estimation can be done by accomplishing adjusting measurements that determine  $\mathcal{R}$  with respect to measured profile sizes, by trial and error. [Str08] proposes an adjustment until the error fall below 10%. Another way is to use  $m$  profiles to perform the estimation for a place of determination  $z_0$  by the method described later in section 5.5.

### 3.5 Artificial Beam Edges

Several methods to derive beam parameters such as emittance or beam size by means of optical measurements deal with the assumption of a beam edge that is defined in quite different terms. This artificially defined beam edge (ABE) is an auxiliary construction and therefore in some cases might not



fit the proper theoretical beam dynamics, then giving non-interpretable results. Another possibility is to use RMS-values for the parameters to be determined. Both approaches have their advantages and disadvantages. RMS-values derived from optical measurements are used quite commonly and are robust. But they are prone to contortions, if there is a critical amount of noise within low intensities, as it is usual for real image data. This trouble is then handled by cutting off the first 20% in the intensity range of a given optical profile. Therefore, the RMS-value always is a parameter estimated smaller than the real value. The great advantage of this approach is, that no assumption on the particle distribution or beam shape has to be made, which could falsify the measurement for the underlying theory. One has to take only an equitable error-estimation into consideration to interpret the result of RMS-values in the right way.

If the data base consists of optical beam measurements that represent the particle distribution in the beam by different intensity values, techniques that make the assumption of ABEs are an obvious approach. Such methods are often easy to use and fast in their algorithmic performance. They allow to derive the wanted parameters directly out of the images. As already mentioned there might be some problems by using such techniques in practice, since the error-proneness could be very high and the ABE has to be defined very carefully. There are two main reasons for this discrepancy. The first is an imprecision in the definition of what the term profile width means in an image that correspond to an underlying real existing beam dynamics and how to measure it, because the beam has no sharp edges. The second is, that therefore the profile width depends on the method it is measured with. The result of a pair of methods could be quite different.

### 3.5.1 Fixed ABE's

First of all there are methods, which fix a certain intensity level due to the area of application. Regarding such measurement techniques, one method commonly used is the full width half maximum (FWHM) method: two diametral lying points of a beam profile specifying  $\frac{1}{2}$  fraction of the maximum intensity are chosen. The profile width then is defined as the distance of these two points. Another often used threshold is an intensity value of  $\frac{1}{e^2} = 0.135$ . The reason for this is that at an optical intensity of  $1/e^2$  the strength of the electric field attains a value of  $\frac{1}{e}$  of the maximum under the assumption of a "fundamental beam"<sup>2</sup>[KH66]. Methods determining the profile width under the assumption of such a parameter work quite good for stigmatically Gaussian distributed beams (see [ISO] Part 1).

Having a look on Fig. 3.10 the blue and red distributions both have the same FWHM value and a clear Gaussian like shape. The wings of the red distribution show a slower decay of intensity in the lower part. This is a meaningful difference, since the beam width with respect to low intensities then will differ significantly. For example, the  $1/e^2$  cut-off level, will be quite different for the blue and red distribution. The information of this distinctive characteristic between both profiles will be lost, if using a fixed threshold only.

### 3.5.2 Fractional ABE's

Another group of methods do determine the profile width by an ABE are fractional methods. Instead of fixing one single intensity threshold a set of intensity fractions is considered. One can on the one hand

---

<sup>2</sup>"fundamental beam" denotes a Gaussian distributed beam

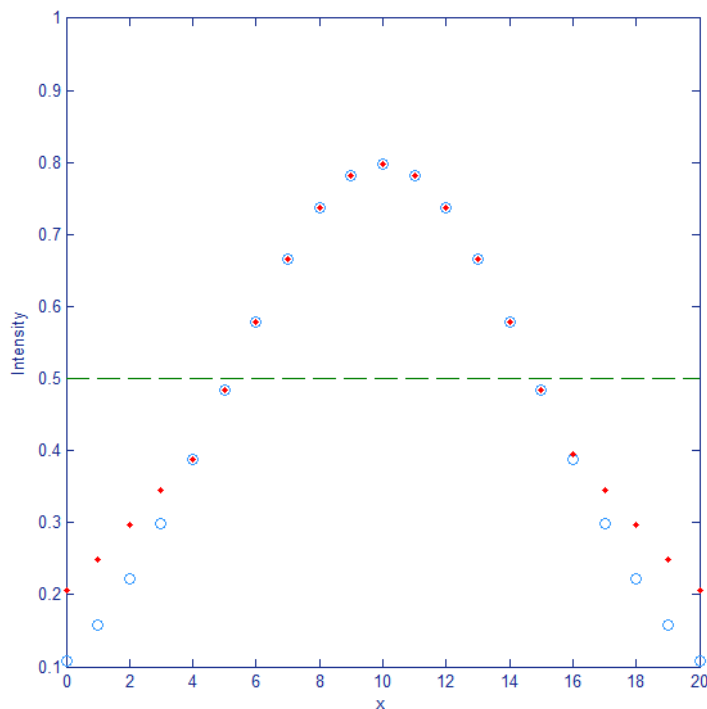


Figure 3.10: The profile width determination with a single cutt-off parameter (here FWHM) leads to the problem that the information of the distribution below the cutt-off level is lost, although there may be meaningful differences

observe every single transverse profile in  $z$ -direction (slice) or on the other hand assume the ABE in form of an isolumen<sup>3</sup>, along the different intensity levels of the picture. The latter is shown in Fig. 3.11

The reason for computing isolumen instead of using intensity values of every single slice is, that there may occur two problems. The first problem is, that for the intensity level chosen, although one might fix a confidence interval<sup>4</sup>  $\Delta x$ , there could be a hole in the profile at this intensity level(Fig. 3.12 Problem 1).

The second problem is that there might be several positions in one profile which could lead to ambiguous positions of the ABE as could be seen in Fig. 3.12 (Problem 2) and Fig. 3.13.

The smallest profile width of the situation in Fig. 3.13 is 25.36 mm and the broadest is 29.83 mm, which is a difference of 4.47 mm thus causing a variation of 11% of the entire transverse profile width. This will yield to impreciseness in the determination of the beam diameter and will influence the usability of methods to derive the emittance out of optical measurements by ABE's (section 5.4 on page 114). In this case taking the innermost or the outermost data points will be a usual strategy to dissolve the ambiguity. Other strategies are to smoothing the chosen beam edge with Gaussian filters

<sup>3</sup>Isolumen here are lines of equal light intensity in an image. For a more formal definition see Def. 3.5.1.

<sup>4</sup>Fixing one single intensity level is not very useful since there are always little aberrations. Therefore it is useful to define a confidence interval.

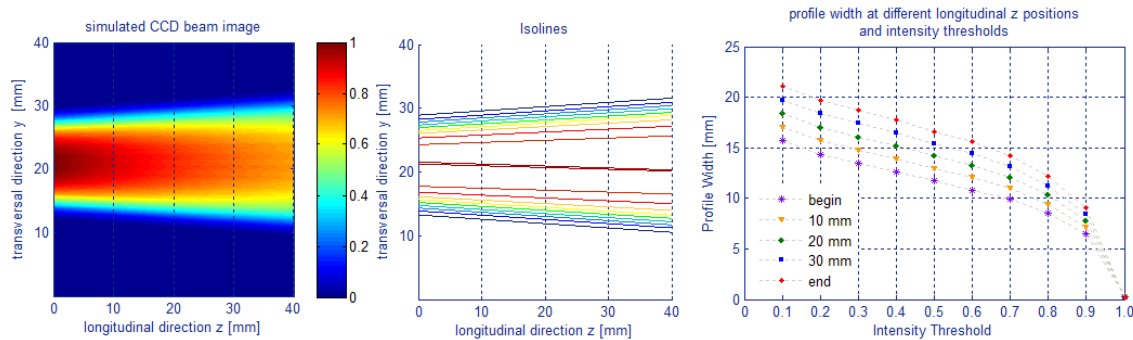


Figure 3.11: Isolines of a given simulated beam image and corresponding beam widths at different longitudinal positions

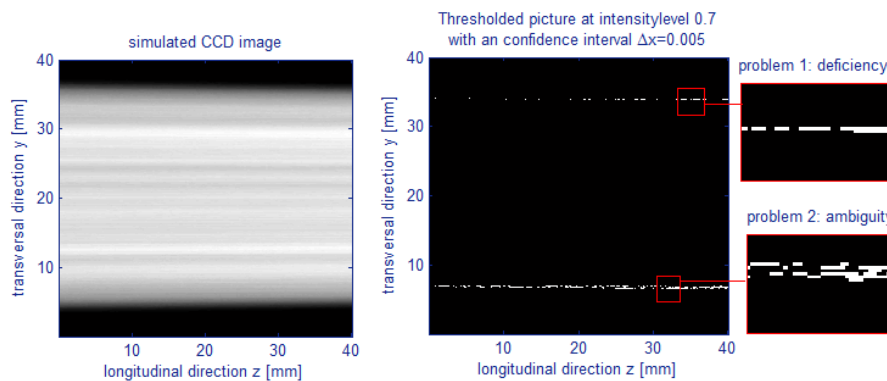


Figure 3.12: Two problems if single slices of an image are analyzed to find corresponding intensity levels. Problem 1: there may be a lack of such an intensity level. Problem 2: there are ambiguous possibilities.

until the ambiguity disappears or to applying methods that compute averages, such as the already mentioned implementation of isolines computed by linear regression on all relevant intensity points for each fraction. Several optical methods for the determination of emittance use the parameter of profile width, e.g. [Poz00, Sit95, Str06]. The error propagation of this methods is influenced seriously by the possible accuracy of specifying the profile width. For instance, the determination of emittance from beam profile measurements makes evident that an aberration of 1% from the exact profile width leads to a maximal error in the range of 12%-14% for a determination of emittance out of three profile widths. An aberration of 5% even causes a maximal error of about 25% [Sit95]. Therefore, an optimal calculation of profile width will be essential for the accuracy of methods using optical beam profile measurements to determine the emittance. Initially a definition of profile length will be developed, that enables to define an error estimation for the precision of a profile length.

### 3 Beam Theory and Analysis

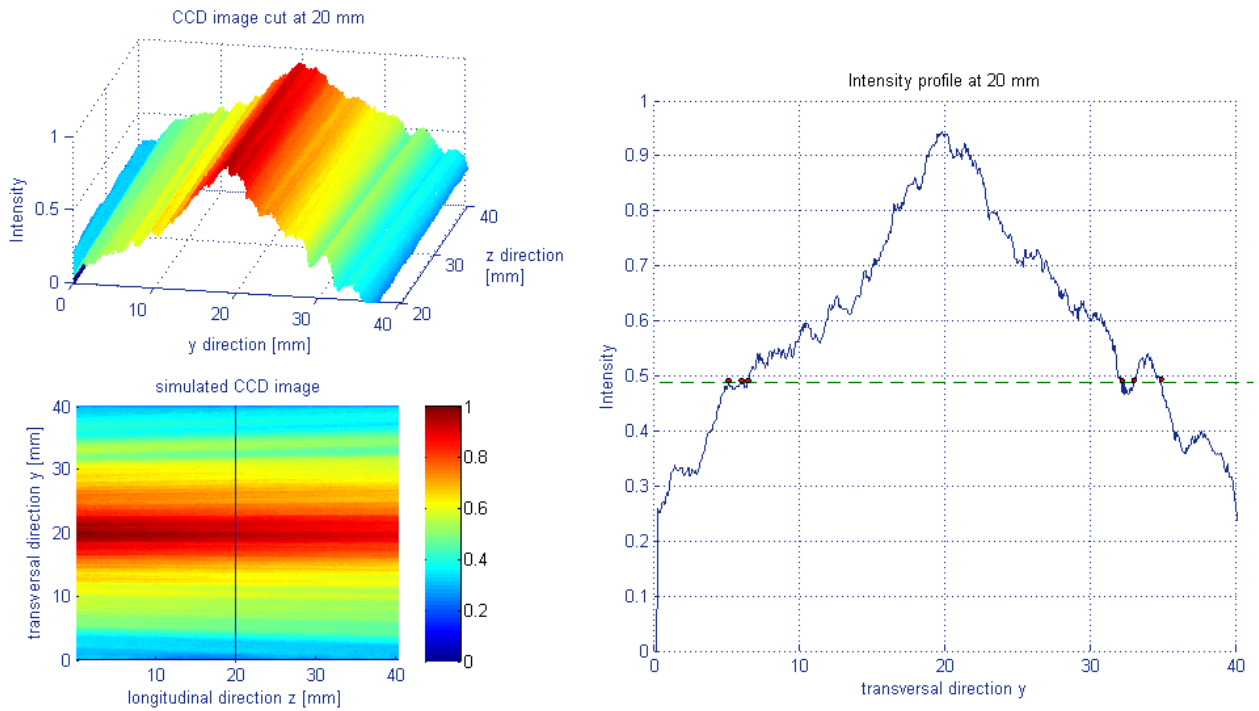


Figure 3.13: The problem of more than one possibility for the ABE. For intensity level 0.48 there exists at the left and right side of the maximum three possible points that come into consideration to be a beam edge. Depending on which possibilities are chosen, the profile width will differ in a non-negligible amount of 11% of the transverse profile width.

**Definition 3.5.1 (Isolumen)** .....

Two lines  $g_1^{I_l}, g_2^{I_l}$  with

$$g_{1,2}^{I_l}(x) = m_{1,2}^{I_l} \cdot x + b_{1,2}^{I_l}, \tag{3.55}$$

are called *isolumen* for intensity  $I_l$ , iff<sup>5</sup>

$$\max_P \{p^{(i,j)} \in N_r \mid \min\{|I_p^{(i,j)}(x) - I_l|\}\}, \tag{3.56}$$

where  $P$  is the optical beam measurement, e.g. a CCD-camera picture,  $I_p^{(0,0)}(x)$  is the intensity of pixel  $p_x^{(0,0)}$  at the position  $(x, g_{1,2}^{I_l}(x))$  of  $P$ ,  $N_r$  is the neighborhood of  $p_x^{(0,0)}$  of size  $r$ , such that

$$N_r = \begin{pmatrix} p_x^{(-r,-r)} & \dots & p_x^{(-r,-0)} & \dots & p_x^{(-r,r)} \\ \vdots & & \vdots & & \vdots \\ p_x^{(0,-r)} & \dots & p_x^{(0,0)} & \dots & p_x^{(0,-r)} \\ \vdots & & \vdots & & \vdots \\ p_x^{(r,-r)} & \dots & p_x^{(r,0)} & \dots & p_x^{(r,r)} \end{pmatrix}, \tag{3.57}$$

---

<sup>5</sup>iff := if and only if

$I_p^{(i,j)}(x)$  then is the intensity of  $p_x^{(i,j)}$  at the position  $(x + j, g_{1,2}^{I_l}(x) + i)$  for  $i, j = -r, \dots, 0, \dots + r$ .

Two lines thus are called isolumen for an intensity  $I_l$ , iff they fit in the area along an optical beam measurement, where the maximum number of pixels with a minimal distance to  $I_l$  in a defined neighborhood is located. From Def. 3.5.1 one could specify

**Definition 3.5.2 (Profile Width)** .....

The profile width  $x_{prof}(x)$  at the position  $x$  of  $P$ , determined by using ABEs, in an optical beam measurement is defined as

$$x_{prof}(x) := |g_1^{I_l}(x) - g_2^{I_l}(x)| \cdot \frac{l}{N}, \tag{3.58}$$

where  $l$  is the width of  $P$  in [mm] and  $N$  the width of  $P$  in pixels.

Next, an error quantity will be introduced, that helps to compare isolumen found by different algorithms, to get a quality criterion relating to the precision of profile length. For all algorithms that take a given optical measurement as input, size and quantification has to be the same for comparing. Without loss of generality the optical measurement is a picture from a CCD-camera taken along the drift. Size  $l$  will be the width of picture  $P$  in [mm] and the quantification  $N$  is the number of pixels along  $l$ . Therefore only the distance between two isolumen could be consulted to implement an error quantity for profile width viz the error is depending on the accuracy of determination of the isolumen. To prove how exact an isolumen is found, the deviation of the proximity of the line from the exact intensity value  $I_l$  has to be computed. The mean  $x_k$  over all  $p_x^{(i,j)}$  and its aberration from  $I_l$  has to be considered

$$x_k = \frac{1}{(2 \cdot r + 1)^2} \sum_{j=-r}^r \sum_{i=-r}^r I_p^{(i,j)}(x). \tag{3.59}$$

Then the error could be calculated by a RMS-error between all  $x_k$  and  $I_l$  as follows

$$e_{RMS} = \sqrt{\frac{1}{N} \sum_{k=1}^N (x_k - I_l)^2}. \tag{3.60}$$

**3.5.3 IRF-Method**

In [Rei10] an information sensitive algorithm based on the previous considerations has been introduced. Simply smoothing of the whole data by filtering, e.g. with a Gaussian filter, included information will be erased or blurred. Therefore an information sensitive filter will be introduced. The intensity range filter (IRF) takes an intensity  $I_l$  and a confidence interval  $\pm \Delta x$  to separate relevant information from irrelevant information. An overview of the IRF-Method is illustrated in Fig. 3.14.

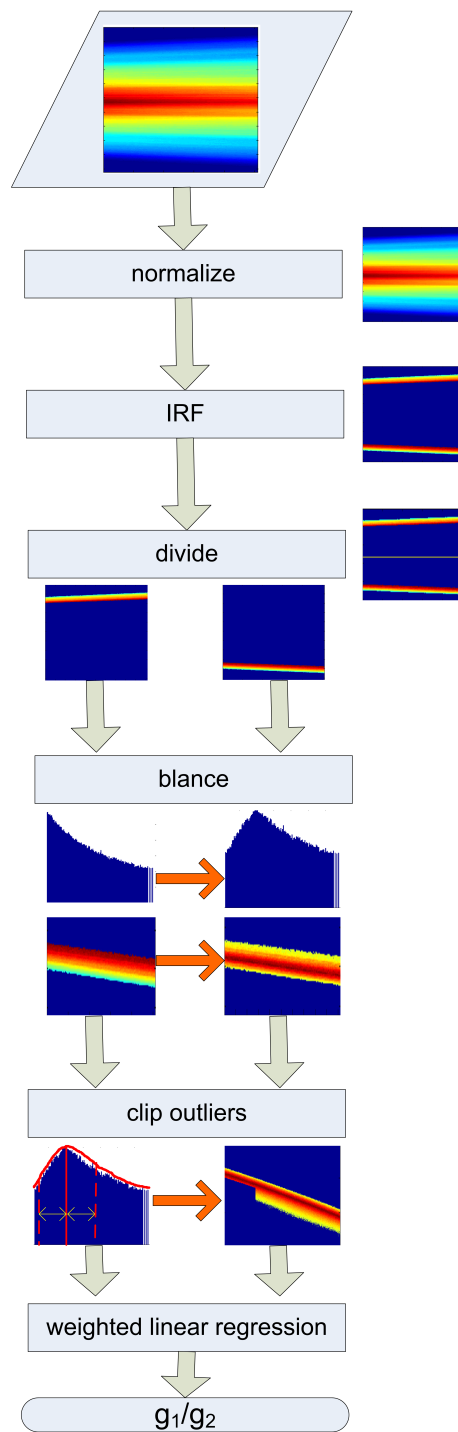


Figure 3.14: The IRF-method determines isolumen sensitive to information

The algorithm works as follows:

The input for the algorithm is a picture taken from a CCD-camera, the desired intensity level  $I_l$  and the confidence interval  $\Delta x$

1. *Normalization*: The original picture  $P$  is normalized column-wise to value 1. Thus intensity levels  $I_l$  could be implemented as percentage values. Result of this step is  $P^1$
2. *IRF*: all values not lying in the defined confidence interval will be set to zero

$$\{\forall p_x \in P^1 | I_l - \Delta x > p_x \vee I_l + \Delta x < p_x\} = 0. \quad (3.61)$$

The result of this step is  $P_{IRF}^1$ .

3. *Divide*: The centroid line of  $P_{IRF}^1$  is computed. Along this line the picture is divided in two pictures  $P_{IRF}^{1,T}$  and  $P_{IRF}^{1,B}$ , where in  $P_{IRF}^{1,T}$  ( $P_{IRF}^{1,B}$ ) all values under (above) the centroid line will be set to zero. With  $P_{IRF}^{1,T}$  ( $P_{IRF}^{1,B}$ ) the top (bottom) isolumen is computed.
4. *Balance*: The intensity distribution within the intensity range will be balanced around  $I_l$  by their distance. Consequently of this the distribution will become approximated to a Gaussian distribution. This balancing is done by:

$$\forall I_p(x) \in P_{IRF}^{1,T/B} : I_p(x) = I_l - |I_p(x) - I_l|. \quad (3.62)$$

The result of this step are the two pictures  $P_{bal}^{1,T}$  and  $P_{bal}^{1,B}$

5. *Clip outliers*: All relevant data for a proper determination of the desired information viz all values that are part of the chosen confidence interval are untouched up to now. If desired, one can skip to the next step. In case of a beam where isolated intensity points are widespread within the picture, outliers could adversely influence the determination of the isolumen. This might be the case with data having a bad signal to noise ratio. The accuracy of the isolumen also in these cases could be increased by clipping outliers. Therefore, in a defined window the expectancy  $\mu$  of the position of intensities in the confidence interval and the standard deviation  $\sigma$  is computed. The vertical distribution then is clipped (Fig. 3.15) with  $n \cdot \sigma$  to both sides (top and bottom). The results of this step are  $P_{cut}^{1,T}$  and  $P_{cut}^{1,B}$

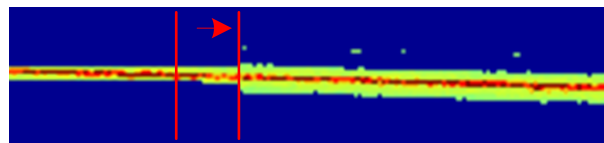


Figure 3.15: Clipping outliers in step 5 of the IRF-Method. Outliers are pixels which lie in the confidence interval but not in the expected position in the picture

The IRF-method determines isolumen with a fair approximation as far as numerical effects as well as noise effects could be suppressed. To determine the profile width on the basis of isolumen, one has to make sure that always only two isolumen are determined for one intensity fraction. The error

### 3 Beam Theory and Analysis

---

estimation provides a possibility of comparison for isolumen computed by different algorithms, but does not prove if the two isolumen are minimal for a picture, as is claimed in the definition for an isolumen. This constraint has to be ensured by the used algorithms.

Furthermore, the profile width also is depending on the choice of the residual gas, the shutter speed of the camera, and the vacuum pressure. The reason is that these factors influence the radiation intensity of the residual gas. To compare different measurement results the conditions approximately have to be the same. Fig. 3.16 demonstrates two measurement results taken under nearly equal conditions but with different residual gases.

Both measurements were performed at a vacuum pressure of  $5 \cdot 10^{-6}$  mbar and a shutter speed of 10 seconds. The residual gases were helium and air. The measurement with helium gas visibly shows a broader beam. Having a look on the detailed characteristics of the different intensity levels of both measurements in Fig. 3.17 one can see that lower intensity levels are much more influenced by the choice of the residual gas than the higher intensity levels.

This differences in the characteristics of beam profile width are not only interesting for the application of profile methods as shown in section 5.4 (page 114). They also have noticeable influence on the tomographic reconstruction. The influence of different residual gases, residual gas pressure, vacuum pressure, and shutter speed are discussed in more detail in [Sit95, Wag11].



### 3.5 Artificial Beam Edges

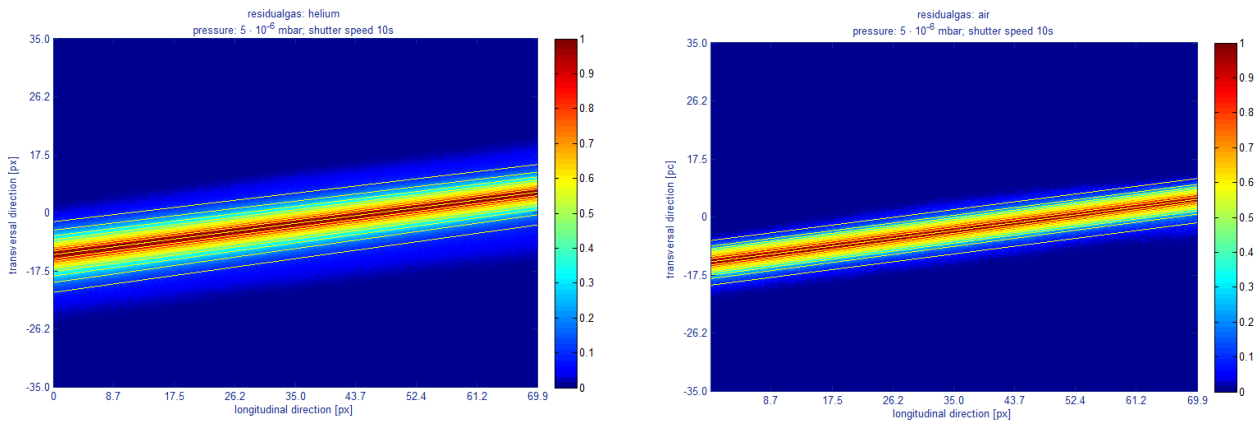


Figure 3.16: Comparison of ABEs of beams under quite equal conditions but with different residual gases.

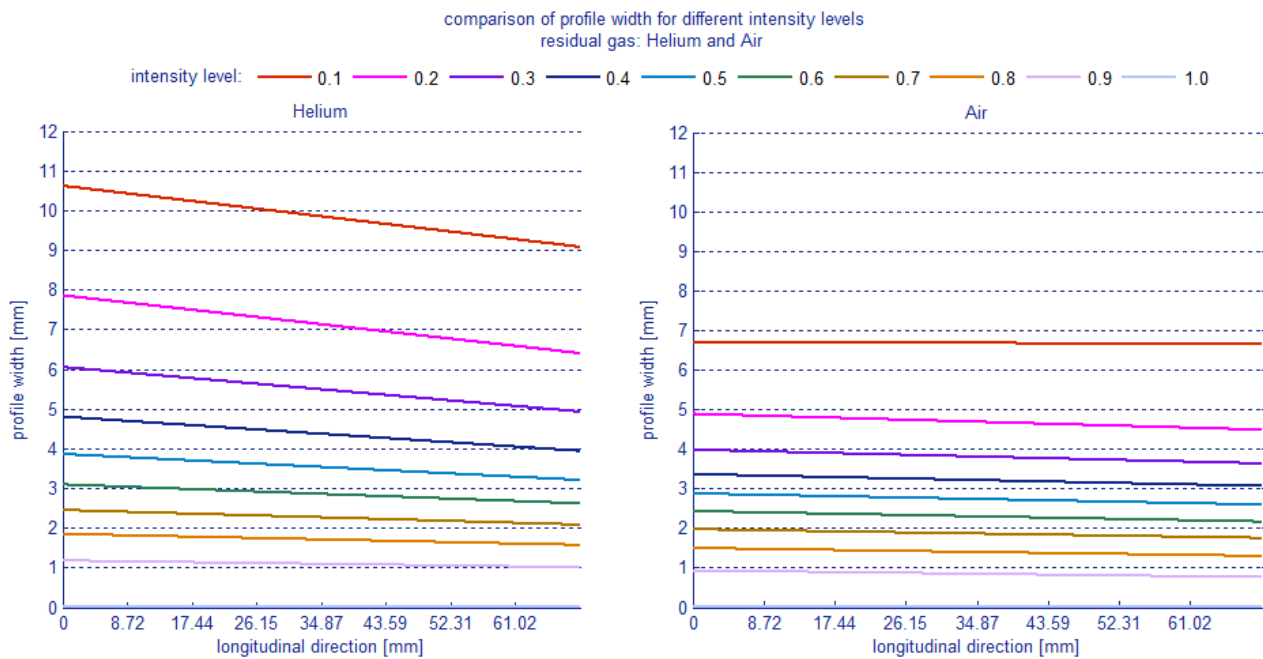


Figure 3.17: Fractional profile widths for the situation of Fig. 3.16. Helium as residual gas causes a higher excitation.



# 4 Beam Profiling

## Contents

---

<b>4.1</b>	<b>Beam Width</b>	<b>89</b>
4.1.1	Profile Width and Beam Diameter	90
4.1.2	Maximal and Minimal Beam Diameter	91
4.1.3	Diameter Determination for Measurement Data	96
<b>4.2</b>	<b>Beam Position</b>	<b>99</b>
4.2.1	Center of Gravity	99
4.2.2	Direction of Main Axis	100
4.2.3	The Two-Beam Example and the Limits of Optical Diagnosis	103

---

Beam profile measurements tend to gain information on the spatial distribution of power intensities. If spatial beam characteristics like intensity distribution, size, shape, and intensity maximum change with time, they can cause negative impact of the behavior of the beam in the beam line. Precise measurements of those parameters allow to react on these changes for a better control of the beam. In this chapter techniques of beam profiling with ion beam tomography will be shown. From the backprojected intensity distribution in ordinary space the spatial beam characteristics can be determined. The determination of beam size is depending on the predefined beam edge leading to a determination of profile width, which can be defined as a fixed or fractional ABE or RMS-value. Methods to determine the width of a profile in different cases have been explained in section 3.5. The beam size is related to the shape of the beam, and the direction of the measurement, if the beam is not rotational symmetric (section 4.1). Knowing the shape of the beam helps to apply several methods. The shape directly is given by the backprojected ordinary space slices. Nevertheless it is not always possible to decide to which amount the beam is symmetric. The determination of beam position comprises the computation of the centroid of the transverse beam position and the direction of the main beam axis that runs through it. The method is tested and illustrated by an example of a set of different data, showing two beams moving apart in section 4.2.

## 4.1 Beam Width

The beam width measured on the basis of a two-dimensional spatial distribution of intensities can be defined as the diameter along a line of sight that perpendicularly intersects the beam axis.

Here, it is assumed that the beam axis is parallel to the longitudinal axis of the beam hole. Only then, a line across the two-dimensional slice, containing the spatial intensity distribution is perpendicular to the beam axis. If there is an aberration of the beam axis from the longitudinal direction of the beam

## 4 Beam Profiling

hole, which can be proved by the method in section 4.2, the beam has to be aligned to the longitudinal direction to avoid an error propagation in beam width determination. If necessary, one also can align only the reconstructed representation of the beam by multiplying the resulting eigenvector matrix of the beam position with the three-dimensional volume tensor. This means to shift the aberrant main axis of the reconstructed distribution to the internal longitudinal axis.

### 4.1.1 Profile Width and Beam Diameter

Beam profile measurements by Beam Profile Monitors (BPM) in general support measurements of two transverse directions that are orthogonal to each other. In Fig. 4.1 on the left the reconstructed volume was summed up to one slice as explained in section 2.2.2 and its intensities  $i$  were normalized to  $i \in [0, 1]$ . In the middle, differences in determining the beam diameter using different intensity

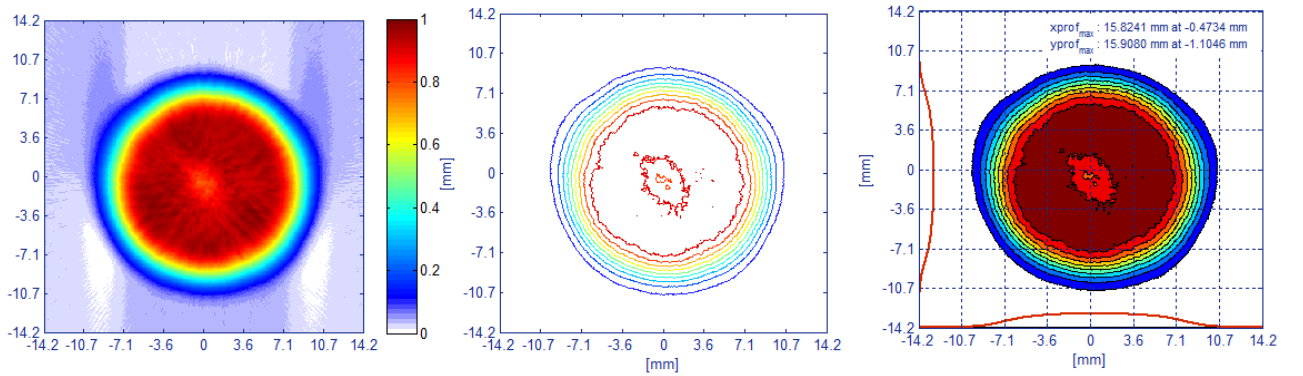


Figure 4.1: Left: the normalized, summed up slice of a reconstructed beam volume. Middle: fractional intensity thresholds from 0.1 to 1.0 of the slice. Right: fractional intensity areas and two transverse profiles in  $x$  and  $y$  direction.

fractions is represented by the use of ABEs. Fractions from 0.1 to 1.0 by steps of 0.1 are shown, but also fixed ABEs as FWHM and  $1/e^2$  are possible (section 3.5). On the right hand the profiles of the two directions  $x$  and  $y$  are obtained as normalized profile by:

$$\begin{aligned} x_k &= res_{px} \cdot \sum_j I_{jk} \\ y_j &= res_{py} \cdot \sum_k I_{jk} \end{aligned} \quad (4.1)$$

where  $I_{jk}$  is the intensity contained in the  $j$ th row and  $k$ th column pixel of the spatial distribution image, and  $res_{px}$  is the pixel resolution of the image according to Eq. (5.65) (page 122).  $x_k$  and  $y_j$  are vectors containing the information on the two beam profiles. The beam diameter in the form of a normalized value then is given by the maximum of  $x_k$  and  $y_j$ . Now the beam diameter can be evaluated for both directions and different diameter definitions as illustrated in Fig. 4.2. The diameters using ABEs differ according to the chosen threshold. While the RMS, the normalized, and the FWHM diameter exhibits comparatively smooth characteristics, the  $1/e^2$  threshold is irregular. The reason

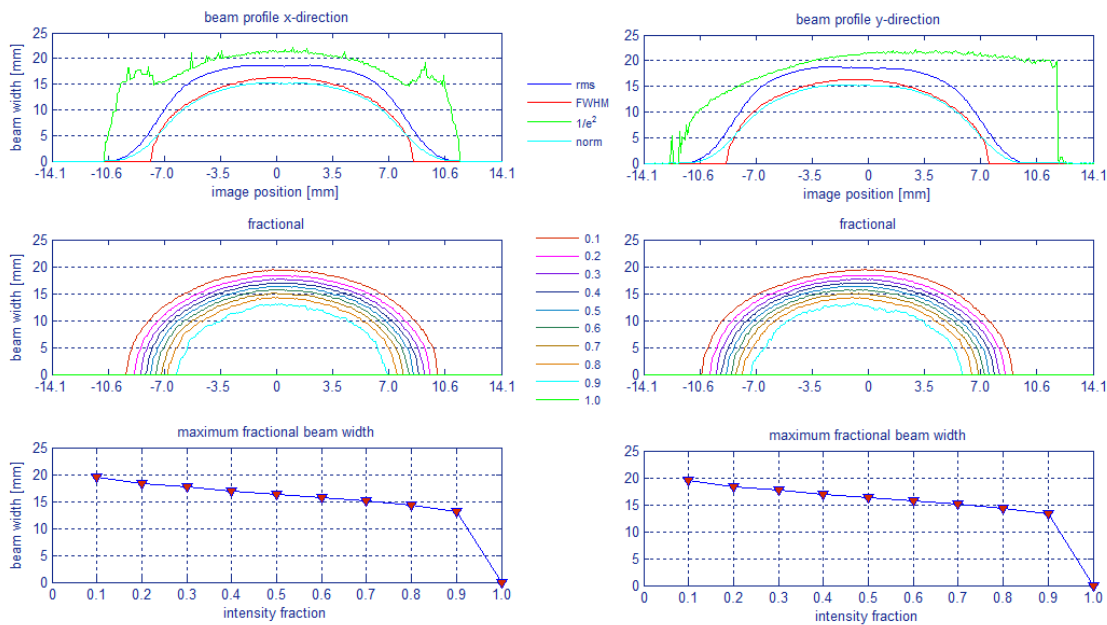


Figure 4.2: Evaluation of beam diameters using different ABEs and fractions.

can be found having a look on Fig. 4.1(left) again. This threshold is placed at a low intensity fraction where the spatial distribution exhibits apparent inconstancy.

In Fig. 3.10 in section 3.5 it has been shown that the FWHM profile width depends on the maximum of the profile, from which the half maximum is taken. If using this measure in determining the beam profile, this will lead to an incorrect effect, when applying the half maximum of every  $x_k$  or  $y_j$ , respectively. In the example in Fig. 4.1 at the edges the maximum of each row and column will be very small, as consequence also the ABE threshold value will be very small. The effect is that the profile width then will be very large. Compared to a row or column in the middle of the image, where the maximum of the profile will be very high, and also the FWHM threshold is, the profile width will be much smaller. The result of using the maximum of every column or row profile is shown in Fig. 4.3 by the red line. Therefore, the FWHM value has to be computed using the *maximum of the complete slice*. Using the maximum of each column leads to a profile width that meets the width of the complete image, what in this example obviously could not be true. Using the maximum of the complete slice results in a profile width of 16.3601 mm in terms of the above defined normalized beam width.

#### 4.1.2 Maximal and Minimal Beam Diameter

The profile width also is depending on the point of view viz the direction in which the projection is observed. In many applications, the beam is assumed to be nearly Gaussian like, which means that every beam projection has a Gaussian intensity profile, which is the case, if the beam is nearly or completely radially symmetric. This assumption has to be made if the beam profile is taken from one or two directions, as shown in the examples above. Unfortunately, there are no perfect Gaussian beams or beam profiles are only approximations of it. Good approximations are often common. Nevertheless,

## 4 Beam Profiling

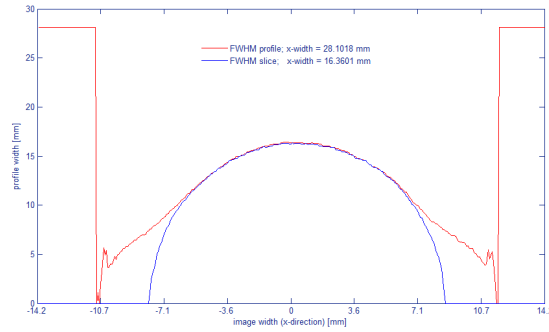


Figure 4.3: Difference in profile determination using the maximum of each row or the maximum of the complete slice to define the FWHM threshold.

there are also many situations in which the beam is not Gaussian like. In these cases it is a great advantage, if the beam width can be determined from every point of view. This is possible by using the reconstructed two-dimensional density distribution. It can be rotated, such that the profile width can be determined from every viewing angle. In Fig. 4.4 the beam diameter, defined by the maximum of the determined beam profiles is observed for different thresholds. Again the beam diameter for the  $1/e^2$ -

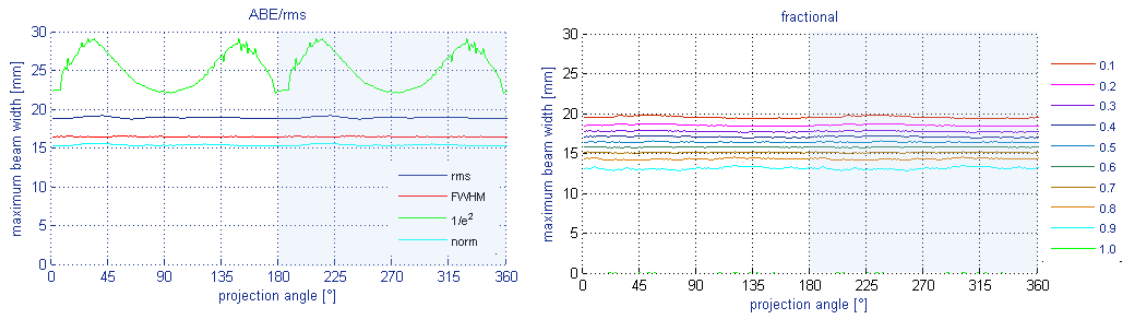


Figure 4.4: The beam width according to different characteristics is observed from all 360 angles of view around the reconstructed density distribution.

beam width shows the irregularities already explained for low intensities. All other thresholds again lead to a very smooth characteristics, which is expected, because the distribution is nearly rotational symmetric. Using reconstructed distributions, in general only the computation of the beam width from viewing angles between  $0^\circ$  and  $180^\circ$  are necessary, angles from  $180^\circ$  to  $360^\circ$  repeat the diameter values from their opposite viewing angles.

If the beam is not Gaussian, determining the diameter from an arbitrary direction may lead to a beam width smaller than the real diameter, because the beam has not been observed at its widest extent. In the worst case, the beam is projected at its smallest side. Computing the width of the beam in Fig. 4.5 on the left side, with the according directions  $x$  (horizontal) and  $y$  (vertical) the results for the different beam diameters with respect to the chosen threshold are shown in Tab. 4.1 The values of

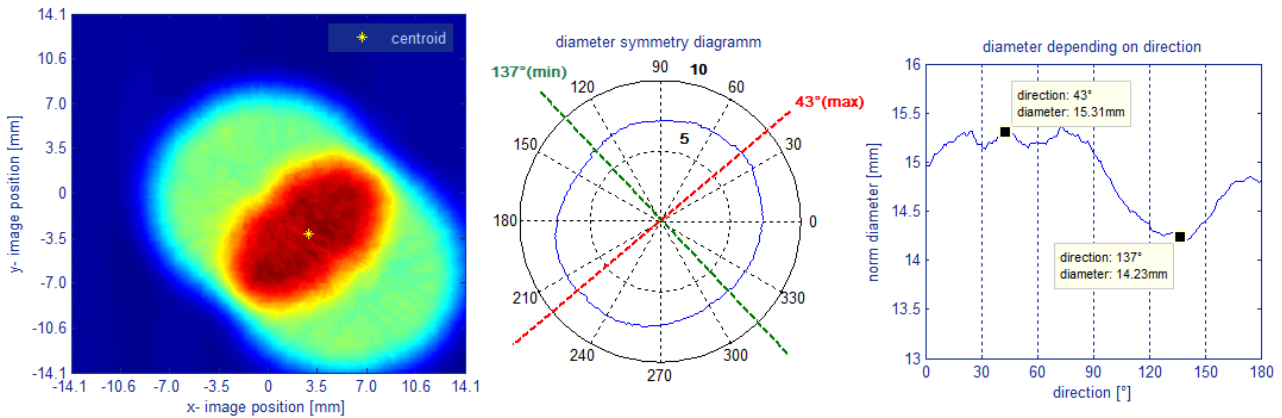


Figure 4.5: In the case of a not rotational symmetric beam the diameter will differ according to the direction the beam profile was taken from.

diameter determination $x$ and $y$					
direction	norm[mm]	FWHM[mm]	$1/e^2$ [mm]	RMS[mm]	fract <sub>max</sub> [mm]
$x(0^\circ)$	14,9596	12,3283	14,8216	11,9330	14,8584
$y(90^\circ)$	15,1502	12,7736	14,9863	11,9786	15,0214

Table 4.1: Beam width of beam in Fig. 4.5, determined in the two transverse directions  $x$  at  $0^\circ$  and  $y$  at  $90^\circ$ .

both directions differ less than 0.6 mm. Having a look on the characteristic profiles in Fig. 4.6 they are almost symmetric but seem to be mirrored. The reason is that the beam is axially symmetric. The longest axis of the beam is tilted in a way that profiles from the  $x$ - and  $y$ -directions are close to be equal. If only considering these profiles in a measurement, the interpretation might be that the beam has a quite good approximation to a Gaussian beam. But this is not correct. Having obtained the complete transverse distribution, it is possible to determine the point of view with the maximal (minimal) beam width, and compute the diameter from this angle to obtain the real diameter, which is the maximal diameter of the beam seen from any transverse direction. First the centroid has to be calculated according to section 4.2.1. The centroid of the example beam is shown in Fig. 4.5 on the left side. Then the normalized radius is computed from the centroid to the edge of the image in every direction. In Fig. 4.5 in the middle this is done by a series of steps of  $1^\circ$  of the viewing angle around the centroid. On the right side the radii of opposite viewing angles are added to find the maximal and minimal diameter of every direction from  $0^\circ$  to  $180^\circ$ . In this example the maximal diameter is given at a viewing angle of  $43^\circ$  and the minimal diameter at an angle of  $137^\circ$  applying the normalized diameter of Eq. (4.1).

Regarding the characteristic of the diameter for different thresholds and fractions these two directions are nearly common for each of them as can be seen in Fig. 4.7. The differences between the viewing angles for the minimal and maximal diameter are quite small for the set of measures that take weak

## 4 Beam Profiling

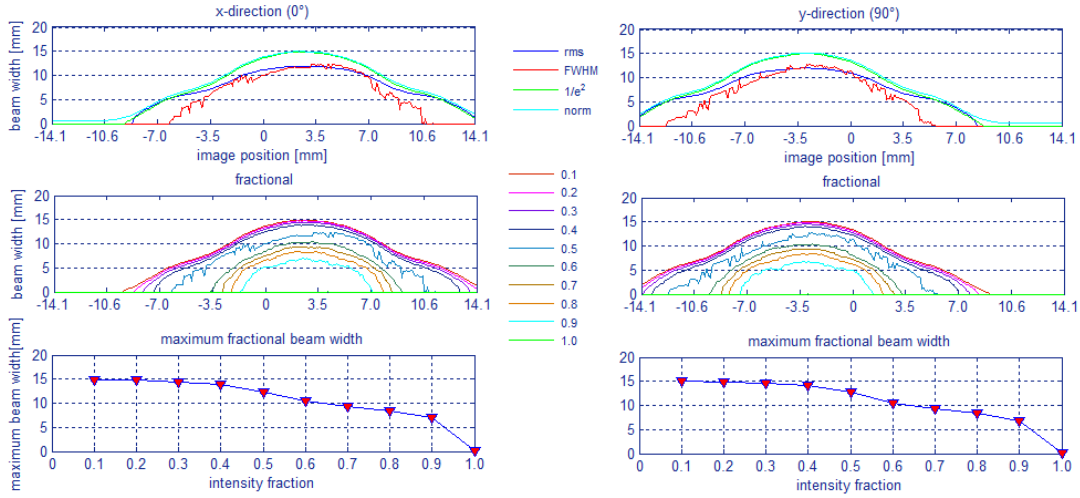


Figure 4.6: Characteristic profiles of the beam shown in Fig. 4.5, taken at an viewing angle of  $0^\circ$  (x-direction) and the orthogonal angle  $90^\circ$  (y-direction)

comparing diameter $x/y$ and min/max						
direction	norm[mm]	FWHM[mm]	$1/e^2$ [mm]	RMS[mm]	fract <sub>0.1</sub> [mm]	fract <sub>0.6</sub> [mm]
$0^\circ(x)$	14,9596	12,3283	14,8216	11,9330	14,8584	10,3678
$90^\circ(y)$	15,1502	12,7736	14,9863	11,9786	15,0214	10,4136
$43^\circ(\text{max})$	15,3068	13,6988	15,1794	11,7492	15,2254	8.6111
$137^\circ(\text{min})$	14.2330	12,9991	13,9347	12,4352	13,9817	12.5993

Table 4.2: Diameter (maximal beam width) of the beam in Fig. 4.5, determined in the two transverse directions  $x$  at  $0^\circ$  and  $y$  at  $90^\circ$  in comparison with the viewing angles for the minimum ( $137^\circ$ ) and maximal diameter ( $43^\circ$ ) with respect to the normalized diameter

intensities into consideration. For the  $1/e^2$  measure the maximal diameter is at  $32^\circ$  and the minimum at  $137^\circ$ . Very close to it is the normalized diameter with a maximum at  $43^\circ$  and a minimum at  $137^\circ$ . Diameters based on fractional intensities from 0.1 to 0.4 also exhibit the maximal diameter at a viewing angle of  $40^\circ$  and their minimum at  $134^\circ$ . Since the maximal intensity of the normalized distribution in the image is 1.0 the FWHM measure is 0.5. Therefore it is common with the fractional intensity 0.5. For the represented beam this is an inflection point. For high intensities the directions of the maximal and minimal diameters are approximately orthogonal to those for low intensities, which indicates that the beam exhibits an axial symmetry. The directions for the minimal and maximal diameter are interchanged. This effect clearly is visible having a look on the characteristics of the beam diameter for intensity fractions from 0.6 to 1.0, where the directions of the minimal and maximal diameter are interchanged. As a statistical measure using the second moment, the RMS-measure for the beam diameter is influenced considerably by high intensities. Therefore the characteristic of the RMS-measure exhibits its maximum at an angle of  $136^\circ$  and its minimum at  $46^\circ$ .



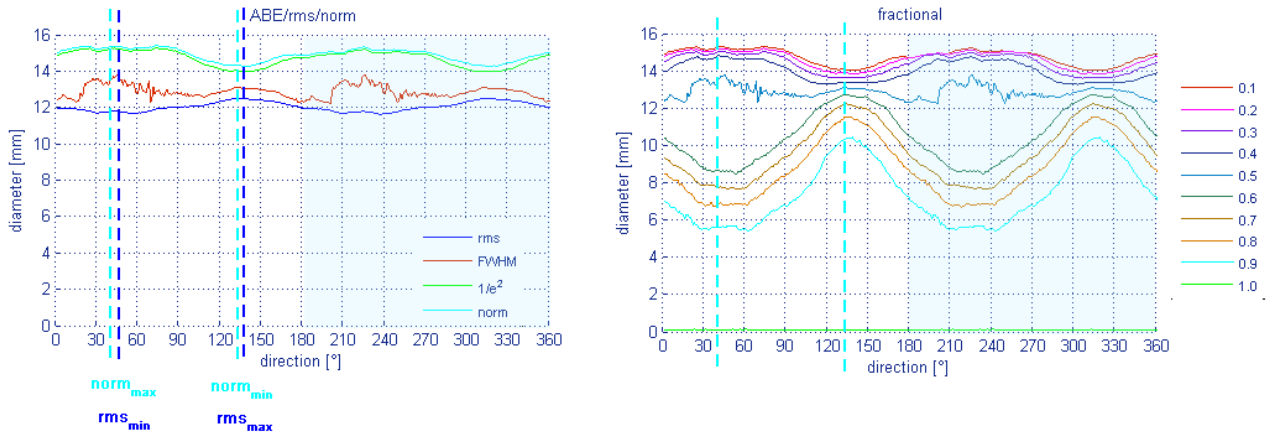


Figure 4.7: Characteristic profiles of the beam shown in Fig. 4.5, taken at viewing angles in a series of steps of  $1^\circ$ . There are two directions that fit for several thresholds and fractions as far as low intensities are concerned. For high intensities above a fraction of 0.5 the direction changes.

Comparing the projections in Fig. 4.6 with the profiles of these two viewing angles in Fig. 4.8 shows, how the point of view influences (crossing of fractional diameters in the lower diagram) the result for the beam diameter. The exact values are given in table 4.2.

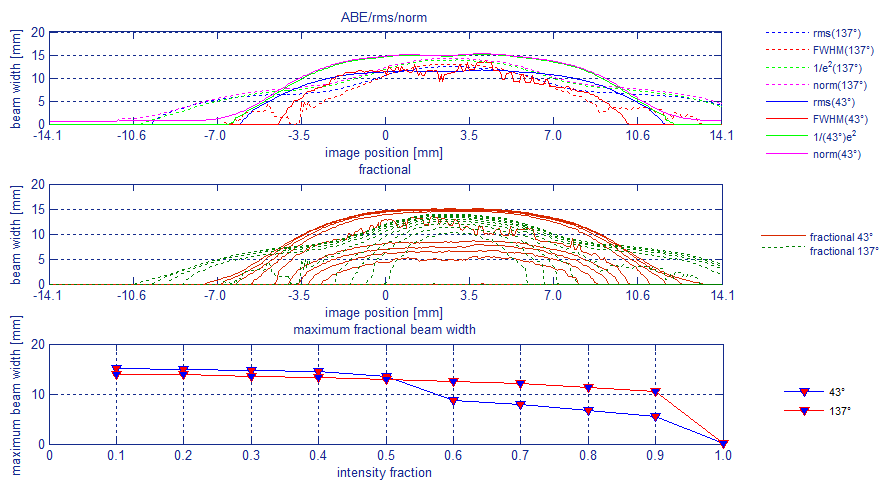


Figure 4.8: Comparison of profiles in direction  $42^\circ$  and  $137^\circ$ .

## 4 Beam Profiling

### 4.1.3 Diameter Determination for Measurement Data

The accuracy of the diameter determination is influenced by noise and irregularities in the image. Reasons for that have been discussed already in section 3.5. If the intensities are scattered irregularly, the fractional intensity thresholds are not clearly cut. In Fig. 4.9 the reconstruction of one measured

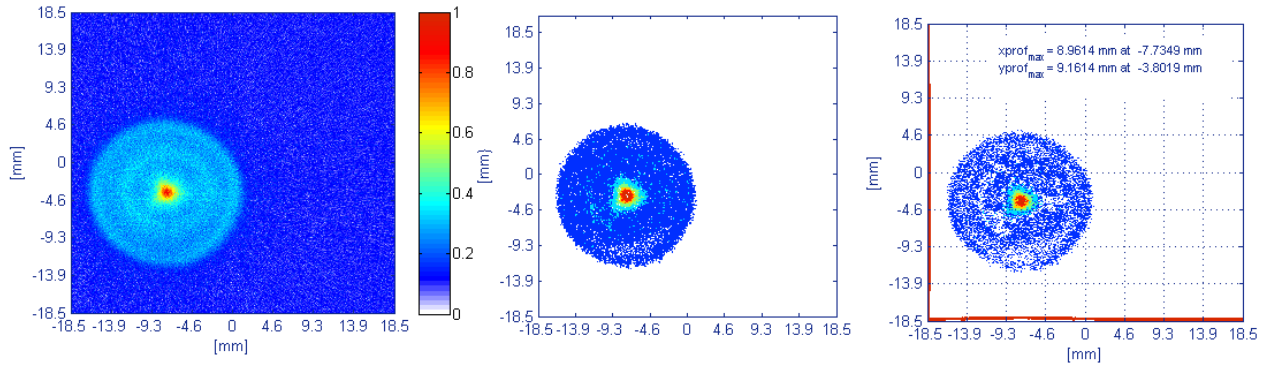


Figure 4.9: Reconstruction of one slice from measurement projections. Irregularly scattered intensities impede a distinct separation to the different intensity fractions.

beam slice is given at the left side. In the middle and at the right side it can be seen that no distinct separation of intensity fractions can be determined, as it is shown for the simulated beam in Fig. 4.1. A solution is, to use a representation that has been summed up over all slices as shown in Fig. 2.11. Performing the determination of intensity thresholds for the summed up slice in Fig. 4.10 shows a useful improvement. The following results have been obtained by the use of a slice summed up over 1600

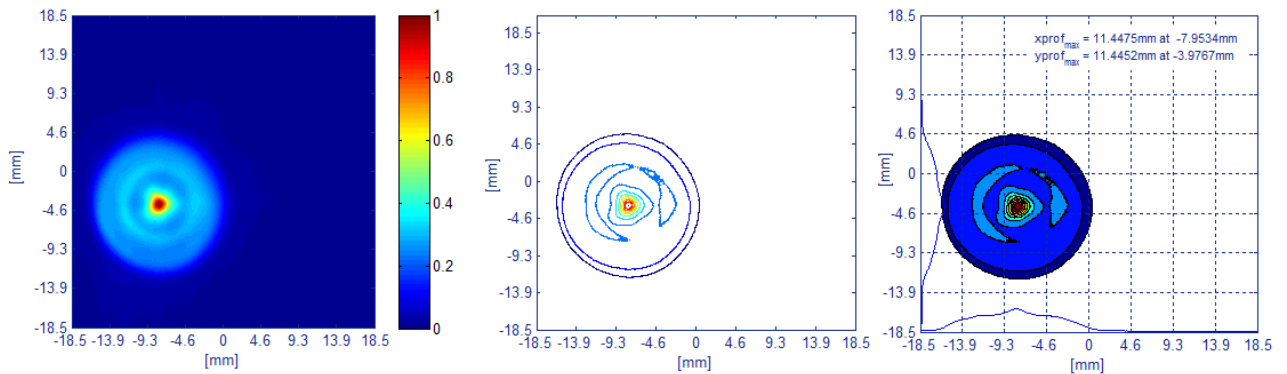


Figure 4.10: Improvement of determination of fractional intensity thresholds by using a representation of summed up slices.

reconstructed slices of the measurement of a  $H^+$ -Beam<sup>1</sup>. First, the different maximal profile widths

<sup>1</sup>see appendix for more information on the dataset

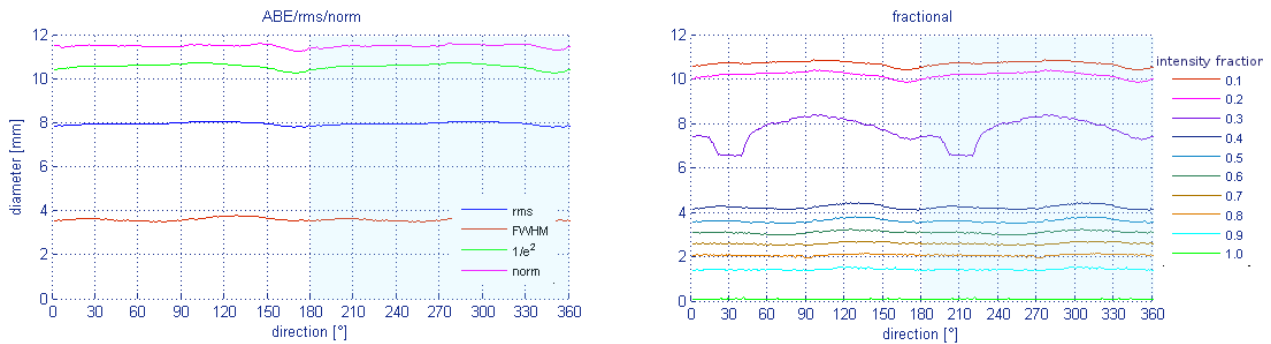


Figure 4.11: Diameters obtained from viewing angles by step-width  $1^\circ$ .

from all directions taken with a step-width of  $1^\circ$  of the given distribution are obtained (Fig. 4.11). For the given beam the diameters are quite equal from each direction. There are no larger peculiarities. The only conspicuous aberration is the gap between intensity fraction 0.2 and 0.4, with an irregularity in the characteristics of intensity fraction 0.3. The minimal and maximal diameter therefore are not expected to differ in a broader range. In the next step one can determine the direction of the maximal and minimal diameter as shown in Fig. 4.12. As expected the difference is quite small. The maximal

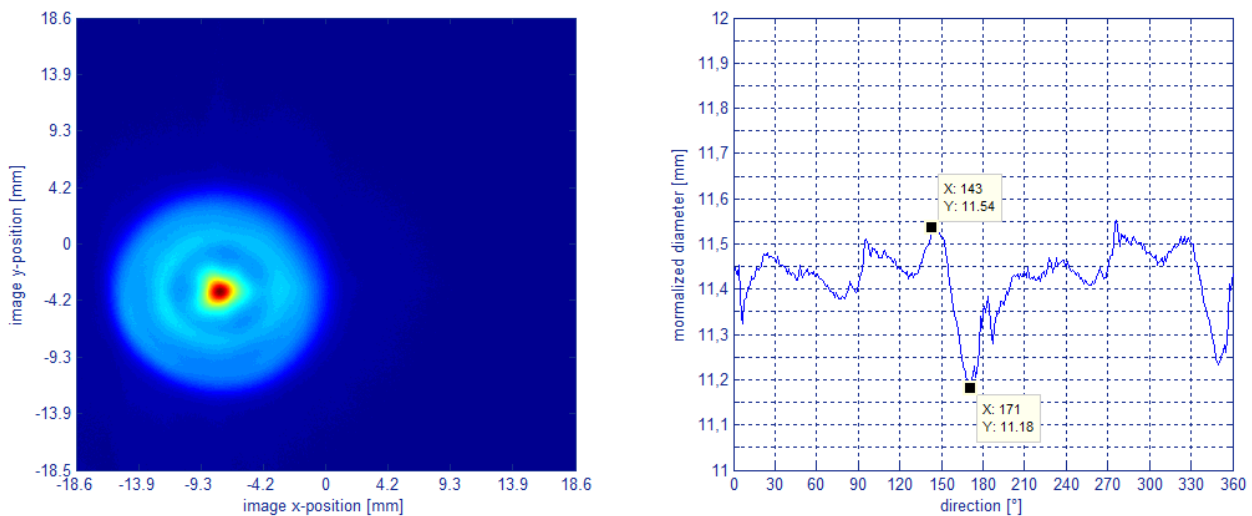


Figure 4.12: Determining the minimal and maximal diameter for the measured reconstructed distribution.

normalized diameter is found at an viewing angle of  $143^\circ$ , the minimum at an angle of  $171^\circ$ . The exact values are given in Tab. 4.3. This also is visible by the difference between the maximal diameter of fraction 0.1 and 0.4. This marks, metaphorically speaking, the crossover from the outer “ring” to the kernel of the beam. The aberrations in intensity fraction 0.3 can clearly be seen at this border in

## 4 Beam Profiling

diameter $x/y$ and min/max for measured data						
direction	norm[mm]	FWHM[mm]	$1/e^2$ [mm]	RMS[mm]	fract <sub>0.1</sub> [mm]	fract <sub>0.4</sub> [mm]
$0^\circ(x)$	11,4475	3,5191	10,3534	7,8076	10,5057	4,1123
$90^\circ(y)$	11,4452	3,5622	10,6069	7,9644	10,7392	4,1493
$143^\circ(\text{max})$	11,5476	3,6869	10,9455	7,9455	10,6352	4,3127
$171^\circ(\text{min})$	11,2039	3,5791	10,2586	7,7893	10,3961	4,0985

Table 4.3: diameters of  $x$ ,  $y$ , min and max direction of a measured beam.

Fig. 4.11 at the left side. At this intensity level the beam is not circular but exhibits contortions. Over all, the aberrations in the profiles are quite marginally and the beam is nearly rotational symmetric.

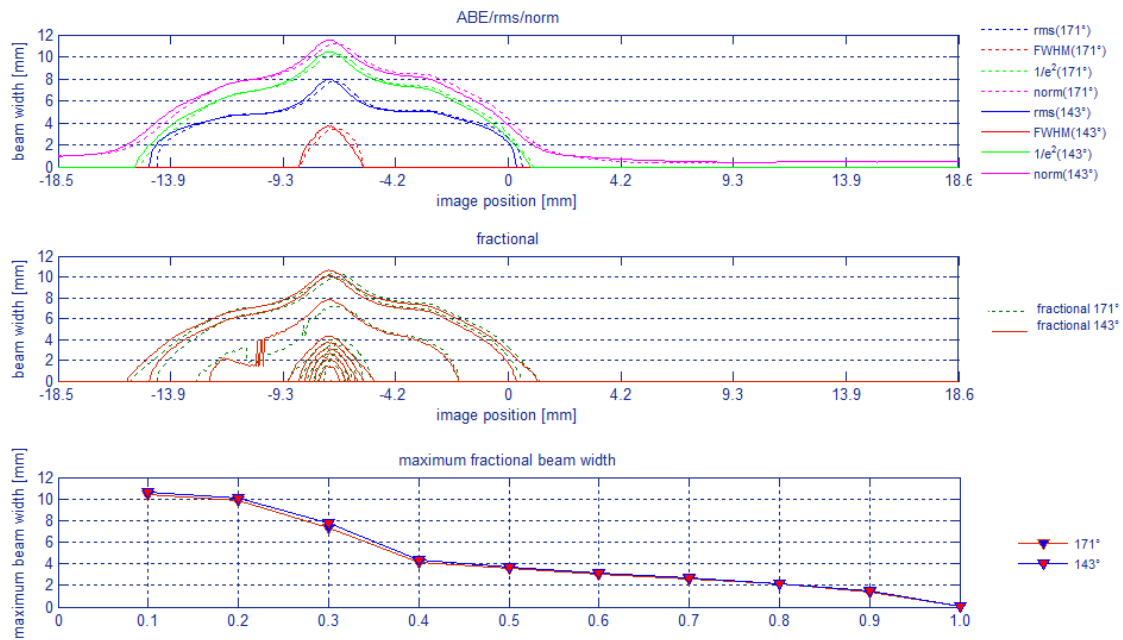


Figure 4.13: Comparison of minimal and maximal diameter. The differences are marginal.

## 4.2 Beam Position

The determination of beam position can be separated into two tasks. The first task is to find the center of gravity, the second task is to determine the axis of gravity that specifies the direction of the beam movement, which can be measured by an angle that gives the aberration from the  $z$  direction.

### 4.2.1 Center of Gravity

The first task can be accomplished by calculating the center of gravity in each of the three dimensions (Fig. 4.14)

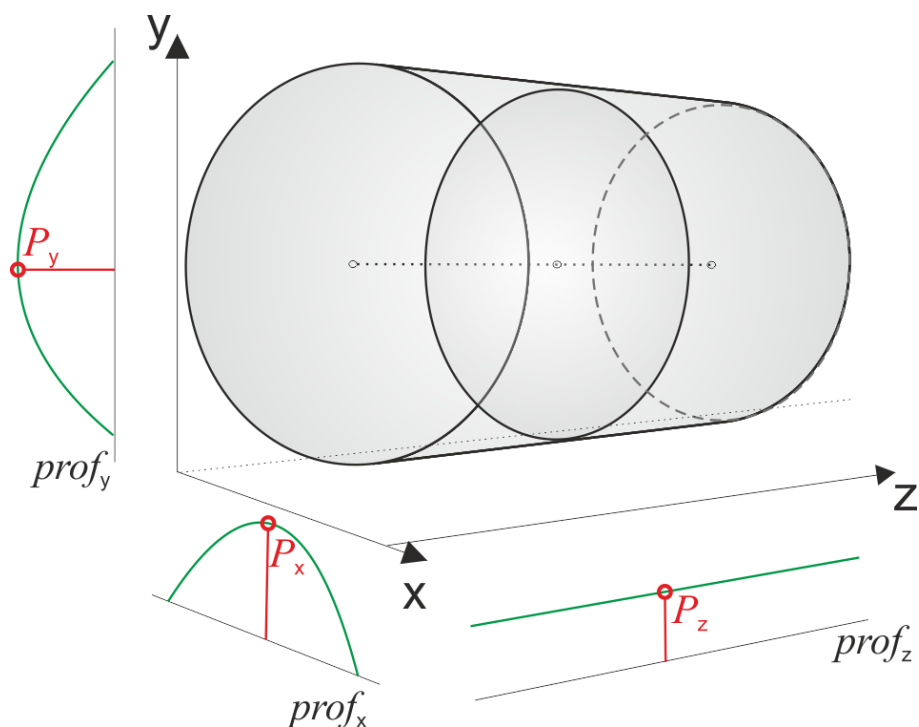


Figure 4.14: To calculate the center of gravity of the backprojected beam, one has to determine the center of each dimension. On the left the cumulated intensity distribution of all slices can be used to compute the  $x$ - and  $y$ -center. The  $z$ -center considers the  $z$ - $y$ -plane with cumulated  $x$  values.

To determine the  $x$ - and  $y$ -coordinates of the center all slices in  $z$  direction are summed up to one  $xy$ -slice

$$I_{xy} = \sum_{k=1}^n [i_{xy}]_k. \quad (4.2)$$

## 4 Beam Profiling

---

Then the intensity profiles  $prof_x$  in x-direction and  $prof_y$  in y-direction are given by

$$prof_x = \sum_{y=1}^m I_{xy} = \vec{I}_x \quad (4.3)$$

$$prof_y = \sum_{x=1}^l I_{xy} = \vec{I}_y. \quad (4.4)$$

To calculate  $prof_z$  all  $prof_y$  in  $z$  direction have to be computed firstly, which results in the Matrix  $I_{yk_j}$

$$I_{yk_j} = \sum_{j=1}^n I_{zk_j} \cdot y_{zk_j}. \quad (4.5)$$

The profile in  $z$  direction then follows as

$$prof_z = \sum_{i=1}^n I_{yk_i} \cdot y_{zk_j}. \quad (4.6)$$

Then the coordinates of the center of gravity can then be calculated by

$$P_x = \sum_{i=1}^n i \cdot \frac{I_{x_i}}{\sum_i x_i} \quad P_y = \sum_{j=1}^m j \cdot \frac{I_{y_j}}{\sum_j y_j} \quad P_z = \sum_{k=1}^l k \cdot \frac{I_{z_k}}{\sum_k z_k}. \quad (4.7)$$

In general, the center of gravity in  $z$  direction has to be in the middle of the  $z$  plane. The reason for this is that the intensity distribution also gives the number of particles in each direction. Since this number remains constant for every slice, the center of gravity has to be in the middle, where on both sides of the center are the same number of slices (or particles). But there is an exception, if the beam moves out of the image. For the calculation this is equivalent to a loss of particles and the center will be shifted in  $z$  direction.

### 4.2.2 Direction of Main Axis

The center of gravity itself does not determine the position of the beam unambiguously. One also has to know in which direction the beam runs through this point. This direction can be defined by an angle that measures the divergence from the pure  $z$  direction, where  $x$  and  $y$  are set to zero. Note that the origin of this direction is not generally the middle of the image or the middle of the beam, but the center of gravity.

An often applied method in statistical data analysis to find relevant components in multivariate datasets is the principal component analysis (PCA). The main question of the PCA is, how to transform partly correlated data in a way that only uncorrelated components remain. By an alteration of the basis of description to preferably problem optimized variables, a formulation of the observed correlation, which is independent from the measurement method, is to be achieved. In the following this approach will be very useful. The back projected volume is a three-variate dataset of intensity values that are partly correlated, since the intensities can be mapped to particle accumulations of different depth

influencing each other. Anyhow, the directions of the axes of gravity are uncorrelated. They only depend on the actual intensity (or indirectly particle) distribution of the available back projection. The determination of the direction vectors of a distribution is known as eigenvalue problem, which usually is solved by PCA. All resulting vectors, which are the eigenvectors of the covariance matrix, are the directions demanded. A conventional PCA in summary is performed as follows:

First the data has to be whitened. This means, the expectancy of the distribution along each dimension is calculated and subtracted from the dataset. The expectancy is used because the input of the PCA is seen as random variable with an empirical mean value that can be derived from the dataset. After that the covariance matrix is set up and out of it the eigenvalues and eigenvectors are computed. For most applications, the eigenvectors will be ordered in the sequence of their descending eigenvalues. All eigenvectors will be combined to one transformation matrix, containing the eigenvector with the largest eigenvalue as first column and the eigenvector with the smallest eigenvalue as last column. In the last step, the original dataset will be multiplied with the transformation matrix to rotate the whole dataset in the direction of the main components. Now, this approach will be used to find the axes of gravity, mainly the one corresponding to the  $z$  direction. The empirical mean of the back projected beam volume is the center of gravity, represented by its components  $P_x$ ,  $P_y$  and  $P_z$  for every direction. For every point  $P_i(x_i, y_i, z_i)$  the particular center of gravity direction has to be subtracted

$$\forall P_i(x_i, y_i, z_i) : \tilde{x}_i = x_i - P_x, \quad \tilde{y}_i = y_i - P_y, \quad \tilde{z}_i = z_i - P_z. \rightarrow \tilde{P}_i \quad (4.8)$$

In the conventional PCA now the covariance matrix  $C = \frac{1}{n}DD^T$  is derived from the whitened data matrix  $D$  which is positive definite and symmetric because it holds that  $C_{ij} = C_{ji}$ . The problem is that the intensity value of every data point of the volume is not taken into consideration by the normal covariance matrix. It is possible to reduce this problem to the definition of the moment of inertia of a three-dimensional solid body. This moment of inertia can be described by the covariance matrix of a three-variate random vector. The probability density distribution of this vector then has to be proportional to the point-wise density of the solid body, or in this case, to the point-wise intensity of the back projected volume. Due to this argumentation it is allowed to use the inertia tensor instead of the covariance matrix in this next step. Given the mass  $m_i$  of a mass point  $i$  (here represented by an intensity) and the whitened data points  $\tilde{P}_i$ , the inertia tensor  $T$  is given by

$$T = \sum_i m_i \begin{pmatrix} \tilde{y}_i^2 + \tilde{z}_i^2 & -\tilde{x}_i\tilde{y}_i & -\tilde{x}_i\tilde{z}_i \\ -\tilde{y}_i\tilde{x}_i & \tilde{x}_i^2 + \tilde{z}_i^2 & -\tilde{y}_i\tilde{z}_i \\ -\tilde{z}_i\tilde{x}_i & -\tilde{z}_i\tilde{y}_i & \tilde{x}_i^2 + \tilde{y}_i^2 \end{pmatrix}. \quad (4.9)$$

This tensor is a bilinear representation of the torsional moment of the body concerned. In the next step a decomposition of  $T$  into its eigenvectors and eigenvalues is performed, such that it holds

$$T = \sum_{i=1}^n \lambda_i \nu_i \nu_i^T, \quad (4.10)$$

where  $\lambda_i$  is the corresponding eigenvalue to eigenvector  $\nu_i$ . In general the  $\nu_i$  are sorted in descending order of their  $\lambda_i$ . But over here, mainly the component corresponding to the  $z$  direction is demanded.

In case of a directed beam this is the direction of the strongest axis of gravity, and therefore the direction with the smallest torsional moment. Given that  $T$  is a representation of this moment, here,

## 4 Beam Profiling

the eigenvectors have to be increasingly ordered by their eigenvalues. Since the eigenvector with the smallest eigenvalue is correlated to the strongest axis of gravity.

For the purpose of determining the angle  $\phi$  of aberration from the  $z$  direction (Fig. 4.15), the PCA can now be aborted, since the volume is not to be rotated by a multiplication of the found transform matrix. For further processing, the three eigenvectors  $e_1$  (smallest eigenvalue),  $e_2$  and  $e_3$  (largest eigenvalue) are of interest.

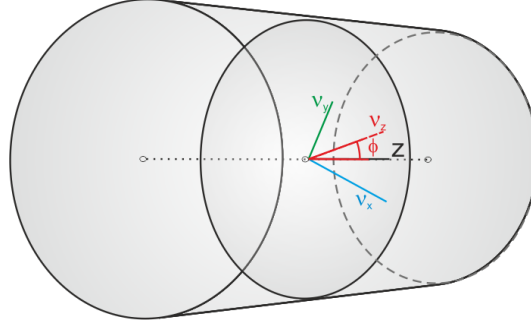


Figure 4.15: Axes of gravity for all three dimension of beam 1. Usually, the length of an axis mirrors the torsional moment, which is smallest at the strongest axis of gravity. In this figure, the axes do not have the original length, because in general the length of the  $z$ -axis will be nearly 0. Instead it is demonstrated, that the beam as a whole can have a course through the center of gravity, which differs from the  $z$  direction by an angle  $\phi$

The eigenvectors are multiplied by their eigenvalues, such that the length of the axes mirror the fraction of torsional moment. The torsional moment in  $z$  direction is smallest. The last thing that has to be done is to determine the angle of this aberration. First the directions of  $x$ ,  $y$ , and  $z$  direction are defined by

$$\vec{x} = (P_x, 0, 0), \quad \vec{y} = (0, P_y, 0), \quad \vec{z} = (0, 0, P_z) \quad . \quad (4.11)$$

The angle between two vectors is given by their scalar product

$$\vec{a} \cdot \vec{b} = |\vec{a}| \cdot |\vec{b}| \cdot \cos \phi. \quad (4.12)$$

Which can be rewritten for the smallest eigenvector as

$$\cos \phi = \frac{\vec{z} \cdot \vec{e}_1}{|\vec{z}| \cdot |\vec{e}_1|} \quad (4.13)$$

$$= \frac{\vec{z} \cdot \vec{e}_1}{P_z \cdot \sqrt{e_{1,1}^2 + e_{1,2}^2 + e_{1,3}^2}}. \quad (4.14)$$

For  $e_2$  and  $e_3$  this works accordingly. In most cases it is not unambiguously clear which of the second and third eigenvector belongs to the  $x$  and  $y$ -direction respectively.

The first component is the eigenvector with the smallest eigenvalue, and is related to the direction with the strongest axis of gravity, which is the  $z$  direction.



### 4.2.3 The Two-Beam Example and the Limits of Optical Diagnosis

The simulated dataset B is a series of 10 volumes, each consisting of two beams simulated with 10.000 particles. In every volume the second beam progressively moves from the center to the border of the beam hole. The very strong longitudinal impulses in the center are increasingly influenced by transverse impulses and space charge effects the more the beam has moved to the border. The consequence should be the movement of the transverse centroid and a deflection effect on the main beam axis. The centroid of the longitudinal direction should not change, since for every slice of the volume the number of particles has to be preserved. In Fig. 4.16 the center of gravity and the main beam axes are exemplarily shown. In general the length of the main beam axes is nearly zero. The reason for this is, that eigenvector

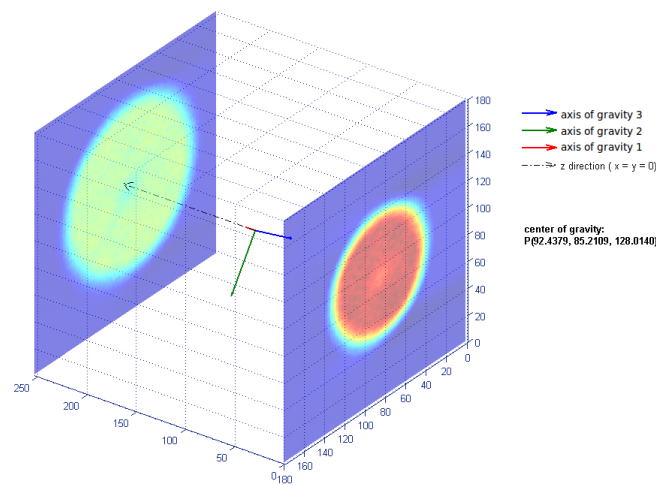


Figure 4.16: The center of gravity and the main beam axes are computed for Beam 1 of dataset B. The main axes are prolonged, since otherwise the main beam axis in longitudinal direction will not be visible, because it is near to zero.

of this axes mirrors the torsional moment of the volume around the longitudinal axes. Therefore the axis in Fig. 4.16 have been scaled for a better illustration. Fig. 4.17 shows the directions of the eigenvectors in relation to the two transverse directions  $x$  and  $y$  and the longitudinal direction  $z$  and their corresponding eigenvalues. The axis of gravity 1, which is the axis with the smallest eigenvector do not have any aberrations from the longitudinal  $z$  direction, but an aberration of  $90^\circ$  from the two transverse directions. On the other hand the two other eigenvectors have an aberration of  $90^\circ$  from the  $z$  direction. The axis of gravity 1 stands perpendicular to both transverse directions, while the same is valid for the axes 2 and 3 in relation to the longitudinal direction. Note, that the main axes of gravity in longitudinal direction is unambiguous, while the two other axes can be identified as transverse axes but they do not identify the  $x$  or the  $y$  direction unambiguously. Their aberration from the  $x$  and  $y$  depend on the distribution of the slice at the position of the longitudinal centroid  $P_z$ . The center of gravity has been computed for all ten volumes of dataset B. Since one beam moves to the border in a transverse direction, also the transverse center of gravity is moved, as can be seen in Fig. 4.18. It has been explained that the center of gravity in the longitudinal direction do not have to change. Nevertheless it moves to the front of the volume in beam 5 to 10. Having a look on the representation of

## 4 Beam Profiling

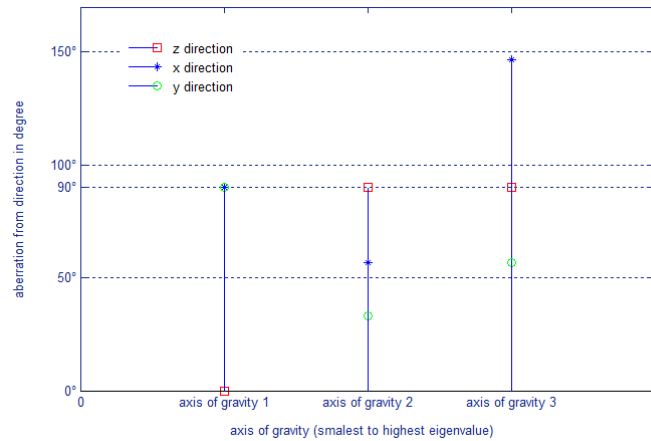


Figure 4.17: The relation between the direction of the eigenvectors and their corresponding eigenvalues.

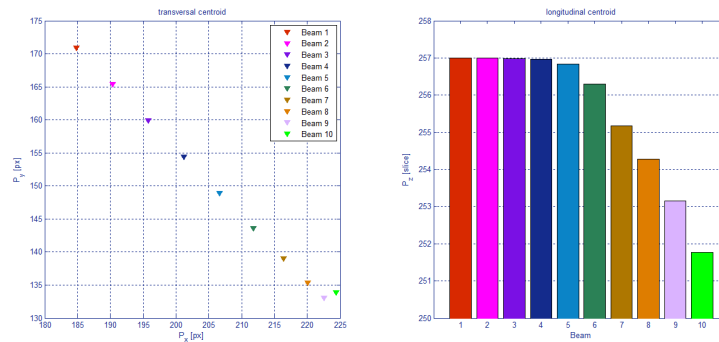


Figure 4.18: Movement of the centroid in transverse direction. The center of gravity in  $z$  direction also is moved for beam 5 to 10. The reason is, that the representation of the beam crosses the image edge. For the algorithm this corresponds to a loss of particles.

these datasets, one can see that the beam in this volumes crosses the image border. For the algorithm this is equal to a loss of particles. Because of the diverging characteristics of this particle ensembles, at the back end of the volume more particles seem to be “lost”. This shifts the centroid in front direction of the volume. Next the aberration of the main axis from the longitudinal  $z$  direction was computed for every volume (Fig. 4.19). Again, the particle ensemble behaves as expected for beam 1 to beam 4. At beam 5 a little aberration from the longitudinal direction can be identified, which increases very fast for beam 6 to 9. Beam 5 seems not to have the problem, that the beam crosses the image edge, but this is deceptive. The representation shows the sum up of all slices. The last slices of this volume already cross this edge as can be seen in the appendix by the summary for dataset B. Beam 10 seems to be something special. Having a look on the transverse centroid in 4.18 of beam 10, represented by the light green triangle, the movement of the transverse centroid of this volume experiences a back movement in  $y$  direction different to the beams 1 to 9, where the centroid has moved quite consistent in

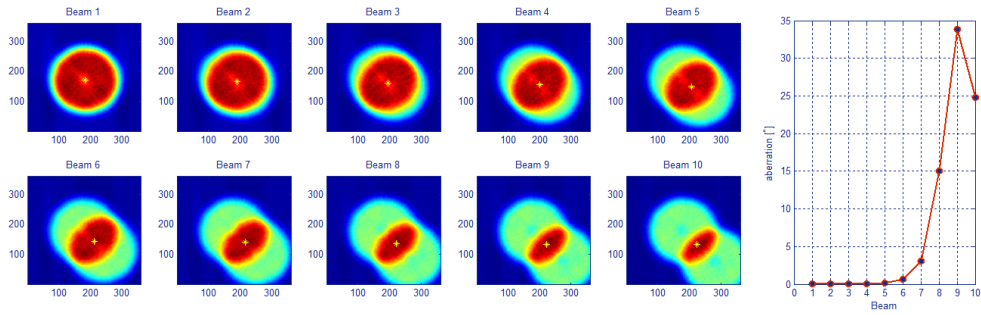


Figure 4.19: All volumes of dataset B, given by their summed up slice representation and their transverse centroid. On the right the aberration of the main beam axis of each volume from the longitudinal direction is shown.

increasing  $x$  direction and decreasing  $y$ -direction. In beam 10 the “loss” of particles on the bottom edge has reached a point, where the influence of this “loss” becomes larger than the influence of the shift of emphasis of the beam. The consequence is a back shifting in  $y$  direction. The same effect also can be seen in the aberration of the main beam axis for beam 10. One can also interpret this as the point where the strong connection of the two particle ensembles of 10.000 particles each, which consists in a coordinated behavior between them, gets lost. If the moving particle ensemble continues on its way, the beam characteristics will rapidly distribute to the properties of the fixed particle ensemble, which means that it will again arrive at the characteristics of beam 1, when the moving particle ensemble has totally left the image. Fig.4.20 exemplarily shows the aberration of the main beam axis from the  $z$  direction for beam 7, where the aberration starts to increase rapidly.

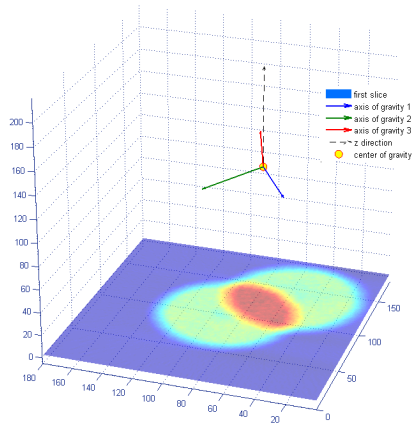


Figure 4.20: Aberration of main beam axis from longitudinal direction of beam 7.

This example was not only designed to show, how the algorithm for the determination of the beam direction works, but also to show the limits of optical diagnosis. If the projection of the beam do not cover the distribution of all involved particles this is interpreted as a loss of particles. That is a not negligible source of errors. For example, the maximal expected beam size at the end of the LEBT is

## 4 Beam Profiling

---

according to table 1.1 50 mm. In table 5.1 it can be seen that the size of the vertical image section covers 52.44 mm. To avoid the effect of apparent particle loss by not gathering the complete beam, the camera assembly and the beam have to be coordinated very exactly, since the range of adjustment is very small in this extreme case. Both, the beam and the camera assembly have to be centered as good as possible to the beam hole center to fit the beam completely to the image section. Otherwise the algorithms for the optical diagnosis will rapidly increase errors, since they are all dependent on the proper projection of the intensity distribution.

# 5 Emittance Determination

## Contents

---

<b>5.1</b>	<b>Tomography in Phase Space</b>	<b>107</b>
<b>5.2</b>	<b>RMS-Emittance</b>	<b>111</b>
<b>5.3</b>	<b>Discretisation of the RMS-Emittance for Phase Space Tomography</b>	<b>113</b>
<b>5.4</b>	<b>Effective Emittance</b>	<b>114</b>
<b>5.5</b>	<b>Direct Determination of Effective Emittance</b>	<b>115</b>
5.5.1	Effective Emittance with Three Profiles in Longitudinal Direction	118
5.5.2	Effective Emittance with Three Different Focal Lengths of a Thin Lens	119
5.5.3	Effective Emittance with More than Three Profiles	120
5.5.4	Estimation of Expected Angle Resolutions	122
<b>5.6</b>	<b>Determining Effective and RMS-Emittance</b>	<b>130</b>

---

Emittance measurement means to determine the volume of a particle ensemble in phase space. Regarding a two-dimensional subspace, it appears as the surface area of the phase space ellipse, discussed in section 3.2. This emittance in general can be represented by a rooted mean square function (RMS-emittance) of the second moments of the phase space distribution or by the area of a real ellipse including the corpus of the occupied phase space area (effective emittance). RMS-emittance as well as effective emittance can be given in form of fractional emittances by increasingly considering a fraction of the whole density distribution. In the following the emittance will be discussed in more detail.

## 5.1 Tomography in Phase Space

To determine the emittance later on, it will be very useful to not only reconstruct the spacial density distribution in the  $(x, y)$ -plane along  $z$ , but also the phase space with tomographic methods. Fortunately this task can be accomplished by using the Fourier slice theorem as done before. The difference is that the Radon plot for the two-dimensional inverted Fourier transform, has to be modified, such that it backprojects the  $\mathcal{F}(x, x')$  (accordingly  $\mathcal{F}(y, y')$ ) phase space density distribution instead of the spacial density distribution of  $(x, y)$ . For the purpose of simplicity only the  $(x, x')$  phase space now will be applied without loss of generality. The method is equivalent for the  $(y, y')$  phase space. Assuming the phase space density distribution given by equation (3.14) the spacial projection of this phase space distribution at a position  $z$  is given by (following [Mot85, McK95, SD06])

$$p(x, z) = \int \mathcal{F}(x, x', z) dx'. \quad (5.1)$$

## 5 Emittance Determination

This integration is equivalent to the beam profile along  $x$  at a given position  $z$  (Fig. 5.1). W.l.o.g it is

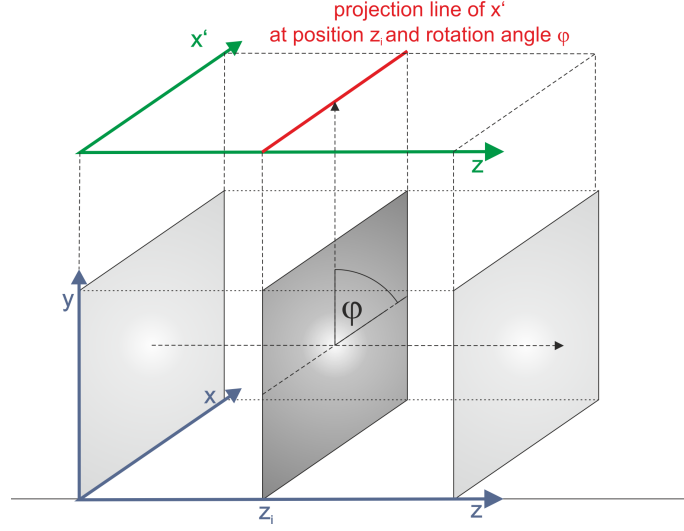


Figure 5.1: Integrating  $x'$  over the phase space distribution  $\mathcal{F}(x, x')$  leads to the projection  $p(x)$  in a given location  $z_i$ .

possible to multiply a delta-function since this is equivalent to a multiplication with 1<sup>1</sup>.

$$p(\xi, z) = \iint \mathcal{F}(x, x', z) \cdot \delta(x - \xi) dx dx'. \quad (5.2)$$

A particle traveling along  $z$  passes through a transformation whose characteristic is determined by the composition of the drift matrix. The transformation of a particle in  $z_0$  moving to  $z_1$  can in general be denoted with Eq. (3.34) by

$$\begin{pmatrix} x_{z_1} \\ x'_{z_1} \end{pmatrix} = \mathcal{A} \begin{pmatrix} x_{z_0} \\ x'_{z_0} \end{pmatrix}, \quad (5.3)$$

where  $\mathcal{A}$  fulfills the conditions discussed in sections 3.1 and 3.4 and Liouville's theorem is applicable. For the Radon transform this means that the original transform  $p(\varphi, s)$  is converted to a transform  $p(\varphi, \theta, s, t)$ . Since the conditions for Liouville's theorem is fulfilled the density distribution along  $z$  does not change. Therefore, for a given density distribution  $\mathcal{F}(x, x', z_0)$  in Fig. 5.2 it holds that

$$\mathcal{F}(x, x', z_0) = \mathcal{F}(x, x', z_i) = \mathcal{F}(x, x', z_j) = \mathcal{F}(x, x', z_n). \quad (5.4)$$

Now, Eq. (5.2) can be rewritten with Eqs. (3.30), (5.3) and, (5.4) as

$$p(\xi, z_i) = \iint \mathcal{F}(x, x', z_0) \cdot \delta(\mathcal{A}_{11}x + \mathcal{A}_{12}x' - \xi, z_0) dx dx', \quad (5.5)$$

<sup>1</sup>The integral over the delta function is 1, while the function itself has only at position 0 a non-zero value. This is comparable to a rectangle function with area 1. If the rectangle becomes smaller it contemporaneously increases height to conserve the area 1. It is possible to shift the zero point with  $\delta(x - b)$ . Inside an integral the  $\delta$ -function behaves equally: multiplying a function  $f(x)$  with the  $\delta$ -function the value of  $f(0)$  (or  $f(b)$  if shifted) is provided

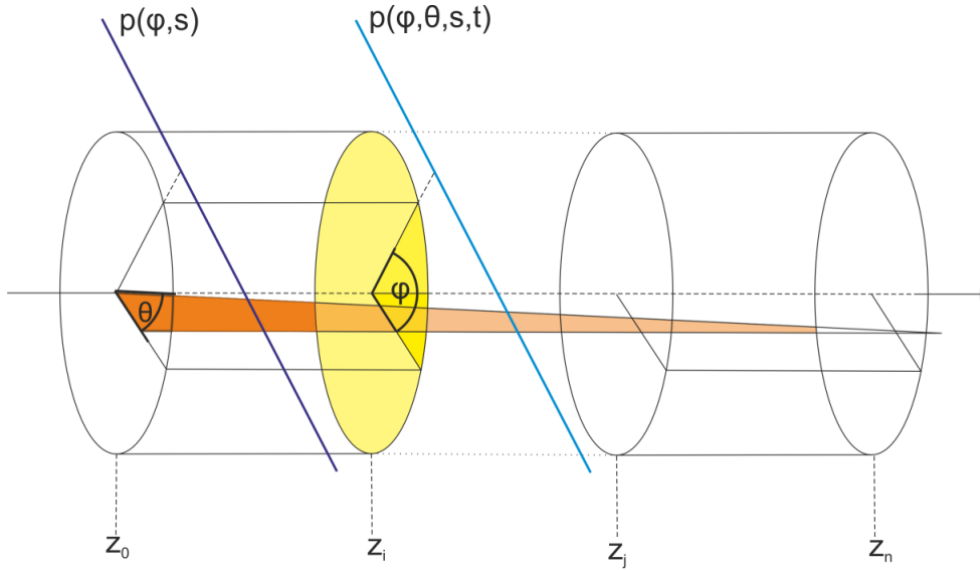


Figure 5.2: For the backprojection of the phase space transforms  $p(\varphi, \theta, s, t)$  along  $z$  are considered to create the Radon plot.

with

$$\mathcal{A} = \begin{pmatrix} \mathcal{A}_{11} & \mathcal{A}_{12} \\ \mathcal{A}_{21} & \mathcal{A}_{22} \end{pmatrix}. \quad (5.6)$$

As known from section 3.4 traveling along a drift may change the displacement and the correlation factor or the divergence and the correlation factor of a particle. In the transfer matrix these changes are represented by the elements  $\mathcal{A}_{11}$  for the displacement and  $\mathcal{A}_{12}$  for the correlation factor.

In a last step it has to be defined, how this two elements change the measured transforms  $p(\varphi, s, z_i)$  to a transform  $p(\varphi, \theta, s, t, z_0)$  for the phase space reconstruction at position  $z_0$ . Having a look on the situation in Fig. 5.2, a particle placed at a point  $(x, y)$  in position  $z_0$ , might be shifted to a position  $(x_1, y_1)$  in position  $z_1$ . The shift is depending on the transfer matrix, and holds for all points of the distribution. Therefore, the whole projection of the phase space ellipse will be shifted by factor  $t$  and maybe rotated by an angle  $\theta$ . For the original transform, in ordinary space tomography  $t$  as well as  $\theta$  are set to zero. Exactly interpreted, the ordinary space tomography then turns out to be a special case of the phase space tomography as adumbrated in section 3.3.1. It has to be noted that angle  $\theta$  is an azimuthal angle on the tomography angle  $\varphi$  as can be seen in Fig. 5.2. In Fig. 3.1 the divergence of the particle trajectory  $x'$  was defined as the slope of the particle trajectory  $x' = \arctan\left(\frac{dx}{dz}\right)$ . But it is also possible to define this slope from the other direction by using the azimuthal angle  $\theta$  relative to the tomography angle  $\varphi$  as shown in Fig. 5.3. Redrawing Fig. 3.3 for the general case, it has to be considered that  $t$  and  $\theta$  are non-zero, such that the phase space ellipse is not centered, and it's main axes are not obligatory parallel to the coordinate axes. The geometrical situation now can be seen in Fig. 5.4. The shift of a point in the coordinate system in Fig. 5.4 is completely defined by the length

## 5 Emittance Determination

---

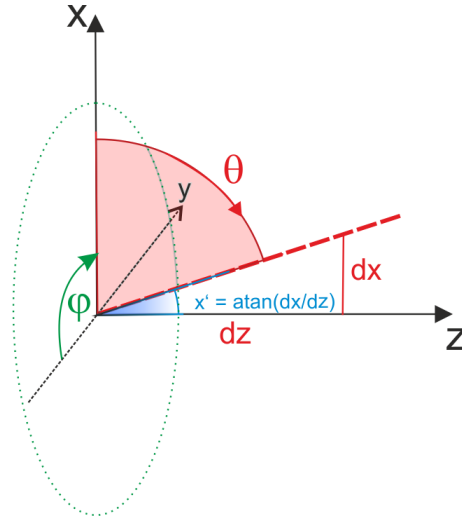


Figure 5.3: The slope of the trajectory explained in Fig. 3.1 can also be defined as the azimuthal angle  $\theta$  on the tomography angle  $\varphi$

and direction of vector  $\vec{t}$  from the origin  $(0,0)$  to a point  $P(x_1, x_1')$ . The length of  $\vec{t}$  is denoted by

$$t = \sqrt{x_1^2 + x_1'^2}, \quad (5.7)$$

which is, according to Eq. (5.5)

$$t = \sqrt{\mathcal{A}_{11}^2 + \mathcal{A}_{12}^2}. \quad (5.8)$$

The direction of  $\vec{t}$  is given by its slope, which is the azimuthal angle  $\theta$  on  $\varphi$

$$\theta = \arctan\left(\frac{x_1'}{x_1}\right), \quad (5.9)$$

which is, according to Eq. (5.5)

$$\theta = \arctan\left(\frac{\mathcal{A}_{12}}{\mathcal{A}_{11}}\right). \quad (5.10)$$

The filtered projection for the phase space backprojection at an angle  $\theta$  according to Eq. (5.5) is then given by [SD06]

$$p\left(\frac{x}{t}, \theta, z_i\right) = \frac{1}{t} \iint \mathcal{F}(x, x', z_0) \delta\left(x \cdot \cos(\theta) + x' \cdot \sin(\theta) - \frac{x}{t}, z_0\right) dx dx', \quad (5.11)$$

which can be interpreted as follows:

the measured transform at position  $z_i$  is the result of a transformation by the transport matrix, which can be recomputed by applying a scaling factor  $t$  on the inner argument of the transform and the whole transform itself, then applying it in the Radon plot at the position of the phase space rotation angle  $\theta$ . The inner and outer scaling with factor  $t$ , can be performed by a horizontal and vertical scaling of the measured transform.



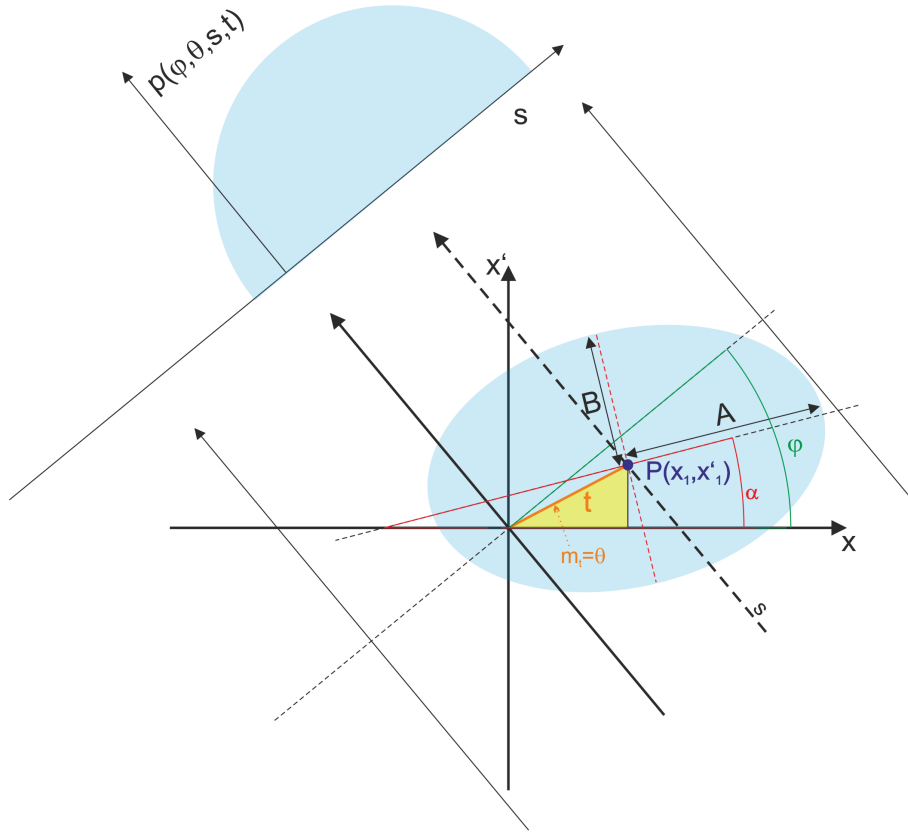


Figure 5.4: Generalization of Fig. 3.3. If a particle is transformed by a drift matrix, its position in phase space will be shifted. Now, not only the projection lines  $s = x \cdot \cos(\varphi) + x' \cdot \sin(\varphi)$  have to be considered for the Radon transform, but also a scaling factor  $t$  and a rotation angle  $\theta$ . This shift is exemplarily shown for the center point, but also holds for all points inside the ellipse.

## 5.2 RMS-Emittance

In Eq. (3.7) it was shown that the phase space density distribution along a time  $t$  does not change. Revisiting the behavior of particles in Fig. 3.2, their motion can be described by a time-dependent harmonic oscillator. In terms of a Hamiltonian this is given by [Gre08]

$$\mathcal{H}(q_i, p_j, t) = \frac{1}{2} \sum_{i=1}^n p_i^2 + \frac{1}{2} \omega^2(t) \sum_{i=1}^n q_i^2, \quad (5.12)$$

where  $\omega^2(t)$  is an arbitrary and not necessarily periodic, differentiable function. Applying

$$\frac{\partial \mathcal{H}}{\partial p_i} = \frac{dx_i}{dt} \quad \text{and} \quad \frac{\partial \mathcal{H}}{\partial x_i} = -\frac{dp_i}{dt} \quad (5.13)$$

## 5 Emittance Determination

---

gives

$$\omega^2(t)x_i = -\frac{d^2x_i}{dt^2}. \quad (5.14)$$

Now, given a pair of distinct particles, their motion can be expressed by Hill's equation [Str10]

$$\ddot{x}_1 + \omega^2(t)x_1 = 0 \quad (5.15)$$

$$\ddot{x}_2 + \omega^2(t)x_2 = 0, \quad (5.16)$$

the non trivial integral of motion for both particles

$$D = x_1\dot{x}_2 - x_2\dot{x}_1, \quad (5.17)$$

turns out to be an invariant that corresponds to the conservation of the angular momentum in a central force field

$$\begin{aligned} \frac{dD}{dt} &= x_1\ddot{x}_2 + \dot{x}_1\dot{x}_2 - x_2\ddot{x}_1 - \dot{x}_2\dot{x}_1 \\ &= -x_1\omega^2(t)x_2 + x_2\omega^2(t)x_1 \\ &\equiv 0. \end{aligned} \quad (5.18)$$

It has to be noted, that the particles energy is not invariant. For a beam as a collective of n pairwise distinct particles it holds

$$\begin{aligned} D_x &= \frac{1}{2n^2} \sum_{i=1}^n \sum_{j=1}^n (x_i\dot{x}_j - x_j\dot{x}_i)^2 \\ &= \frac{1}{2n^2} \sum_{i=1}^n \sum_{j=1}^n (x_i^2\dot{x}_j^2 - 2x_i\dot{x}_i x_j\dot{x}_j + x_j^2 + \dot{x}_i^2 x_j^2) \\ &= \frac{1}{2n} \sum_{i=1}^n (x_i^2\overline{\dot{x}^2} - 2x_i\dot{x}_i\overline{x\dot{x}} + \dot{x}_i^2\overline{x^2}) \\ &= \frac{1}{2n} \left( \overline{\dot{x}^2} \sum_{i=1}^n x_i^2 - 2\overline{x\dot{x}} \sum_{i=1}^n x\dot{x} + \overline{x^2} \sum_{i=1}^n \dot{x}_i^2 \right) \\ &= \overline{x^2} \overline{\dot{x}^2} - (\overline{x\dot{x}})^2. \end{aligned} \quad (5.19)$$

Rewriting  $\dot{x}$  by  $x'$  this turns out to be

$$D_x = \overline{x^2} \overline{x'^2} - (\overline{xx'})^2 \equiv \epsilon_x^2, \quad (5.20)$$

which is a common notation for the square of the above mentioned RMS-emittance in the  $(x, x')$ -phase space. Relating to the previous discussion, this RMS-emittance is invariant in time, as long as the particle motion is approximated by a linear equation of motion and the number of particles is conserved.  $\overline{x^2}$ ,  $\overline{x'^2}$  and  $\overline{xx'}$  are the second moments as already introduced in Eq. (3.30) as statistical parameters, that define the phase space ellipse for any given distribution.

### 5.3 Discretisation of the RMS-Emittance for Phase Space Tomography

In this section it will be shown, how the RMS-emittance can be discretely computed from the phase space picture, which is obtained by phase space tomography discussed in section 5.1.

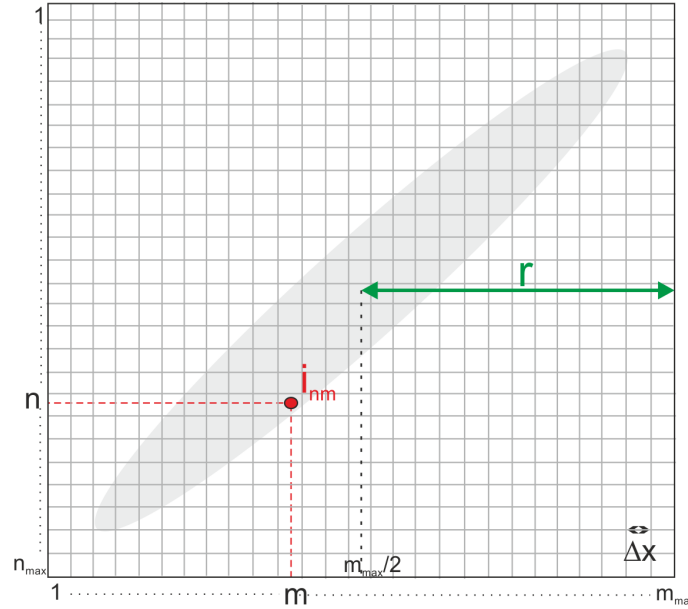


Figure 5.5: Schematic representation of a backprojected phase space picture.

In Fig. 5.5 a schematic image  $P$  of a backprojected phase space is shown. Without loss of generality it is assumed that there are  $m_{\max}$  pixel in  $x$  direction and  $n_{\max}$  pixel in  $x'$  direction, where all possible relations  $m \leq n$  or  $n < m$  are allowed. The size of a pixel given in mm is  $\Delta x$ . The intensity value of a pixel at position  $(x, x')$  is given by  $i_{xx'}$ .  $r$  is the radius of  $P$  in mm, denoted by

$$r = \frac{m}{2} \cdot \Delta x. \quad (5.21)$$

The first thing to do is to normalize  $P$  by

$$\forall i_{nm}^0 \in P^0 : i_{nm} = \frac{i_{nm}^0}{\max\{P^0\}}, \quad (5.22)$$

where  $P^0$  denotes the not-normalized image with values  $i_{nm}^0$ . In the following  $i_{nm}$  and  $P$  denote the normalized image and values. The total intensity  $I_P$  of  $P$ , now is given by

$$I_P = \sum_{n=1}^{n_{\max}} \sum_{m=1}^{m_{\max}} i_{nm}. \quad (5.23)$$

Since for the computation of the emittance the central second moments are needed, the center of gravity according to (4.7) has to be subtracted. Therefore, it has to be computed for the two dimensions  $n$

## 5 Emittance Determination

---

and  $m$  by

$$P_n = \sum_{n=1}^{n_{\max}} n \cdot \frac{i_{nm}}{I_P} \quad P_m = \sum_{m=1}^{m_{\max}} m \cdot \frac{i_{nm}}{I_P}. \quad (5.24)$$

The discrete versions of the second moments are

$$\overline{x^2} = \frac{1}{M} \sum_{m=1}^{m_{\max}} \sum_{n=1}^{n_{\max}} m^2 \cdot i_{nm} \quad (5.25)$$

$$\overline{x'^2} = \frac{1}{N} \sum_{m=1}^{m_{\max}} \sum_{n=1}^{n_{\max}} n^2 \cdot i_{nm} \quad (5.26)$$

$$\overline{xx'} = \frac{1}{NM} \sum_{m=1}^{m_{\max}} \sum_{n=1}^{n_{\max}} nm \cdot i_{nm}. \quad (5.27)$$

Because of the whitening from the centroid and to convert the pixel values in mm and mrad values a little detour has to be made. First whitening and conversion have to be performed [Str08]

$$\begin{aligned} x_{RMS} &= r \cdot \sqrt{\frac{\sum_n \sum_m n^2 \cdot i_{nm}}{I_P} - P_m^2} \\ x'_{RMS} &= r \cdot \sqrt{\frac{\sum_n \sum_m m^2 \cdot i_{nm}}{I_P} - P_n^2} \\ xx'_{RMS} &= r^2 \cdot \left( \frac{\sum_m \sum_n nm \cdot i_{nm}}{I_P} - P_m P_n \right). \end{aligned} \quad (5.28)$$

The values  $x_{RMS}$  and  $x'_{RMS}$  correspond to the maximum spreads  $x_{\max}$  and  $x'_{\max}$  of Fig. 3.4 given in mm. Then the emittance can be computed according to Eq. (5.20)

$$\epsilon_x = \sqrt{x_{RMS}^2 \cdot x'^2_{RMS} - xx'^2_{RMS}}. \quad (5.29)$$

According to [Sac71] the equivalence of the behavior of two particle beams with different distributions can be described by RMS-values. Therefore the RMS-emittance allows to trace back emittance ellipses with arbitrary distributions to behavioral equivalent ellipses with uniform distribution for the beam transport [Sit95].

### 5.4 Effective Emittance

Effective emittance is defined as the smallest phase space area that is necessary to describe the occupied phase space area by an ellipse which is given by Eq. (3.26). Therefore, the twiss-parameters have to be determined. The first possibility is to use the result of the computation of the RMS-emittance as described in the section before. According to table 3.1 it can be denoted

$$\begin{aligned} x_{RMS} &= \sqrt{\epsilon_x \cdot \beta} \\ x'_{RMS} &= \sqrt{\epsilon_x \cdot \gamma}, \end{aligned} \quad (5.30)$$

## 5.5 Direct Determination of Effective Emittance

with Eq. (5.28), (5.29) and (5.30) the twiss parameters can be computed by

$$\begin{aligned}\beta &= \frac{\sqrt{x_{RMS}}}{\epsilon_x} \\ \gamma &= \frac{\sqrt{x'_{RMS}}}{\epsilon_x}.\end{aligned}\tag{5.31}$$

The twiss parameter  $\alpha$  can be obtained by the normalization condition for the emittance ellipse

$$\begin{aligned}\beta\gamma - \alpha^2 &= 1 \\ \Rightarrow \alpha &= \sqrt{\beta\gamma - 1}.\end{aligned}\tag{5.32}$$

Under the influence of non-linear forces the shape of the occupied phase space area might be distorted, although the emittance ellipse contour remains as discussed in section 3.2. As a consequence the ellipse, surrounding the distorted phase space area, has to be larger, while inside the ellipse there may be areas enclosed that are not occupied (see Fig. 5.6).

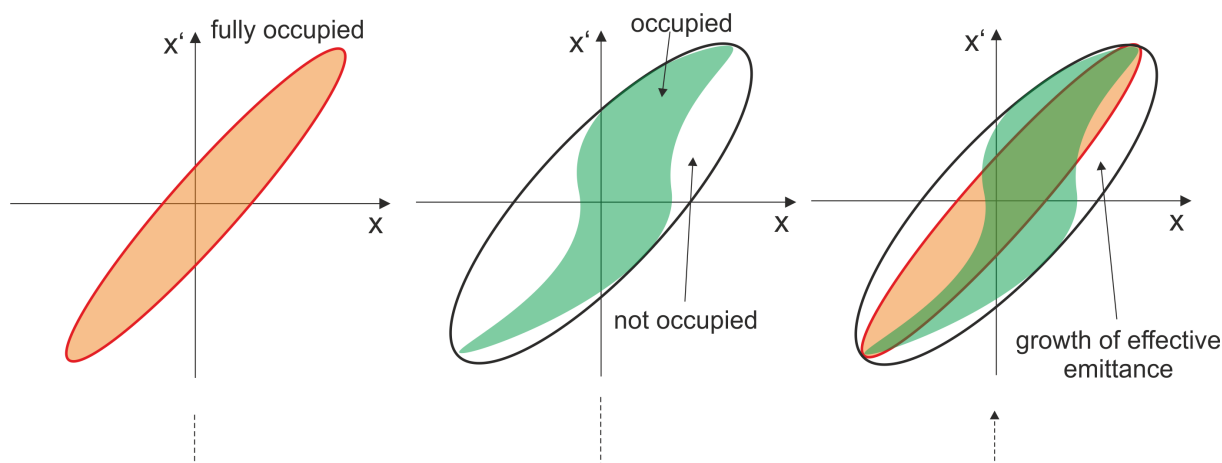


Figure 5.6: Non-linear forces cause a distortion of the occupied phase space area. The ellipse of the effective emittance, then has to be larger to enclose the total distribution, since inside the enclosing ellipse there are non-occupied areas. The result is an apparent emittance growth, that is not real, but an effect of the representation of the distribution as an elliptic area.

In this case the effective emittance has been increased, although the real occupied phase space area remains the same. This enlargement is not compatible to Liouville's theorem .

## 5.5 Direct Determination of Effective Emittance

In the last paragraph it was shown, how the effective emittance can be determined using the twiss-parameters which can be computed after the determination of the RMS-emittance. The effective emittance can also be computed directly using at least three measured beam profiles, from different

## 5 Emittance Determination

---

longitudinal positions [Str06, Sit95]. In sections 3.2 and 3.4 it is shown, how the phase space ellipse is transformed depending on the configuration of the beam guide system. This modification can also be described in terms of a transformation of the twiss-parameters. Given a start position  $z_0$  and an end position  $z_1$  in which the phase space ellipse is transformed by the optical system, the transformation can simply be written as

$$\begin{pmatrix} \beta_{z_1} \\ \alpha_{z_1} \\ \gamma_{z_1} \end{pmatrix} = \mathcal{A} \begin{pmatrix} \beta_{z_0} \\ \alpha_{z_0} \\ \gamma_{z_0} \end{pmatrix}. \quad (5.33)$$

In section 3.4 the transformation of the drift  $\mathcal{A}_d$  and the thin lens  $\mathcal{A}_l$  were derived as  $(2 \times 2)$  matrices. Since there are three twiss-parameters the matrices have to be converted into  $(3 \times 3)$  matrices as in the following

$$\begin{pmatrix} \sigma_{11} & \sigma_{12} \\ \sigma_{21} & \sigma_{22} \end{pmatrix} \Rightarrow \begin{pmatrix} \sigma_{11}^2 & -2\sigma_{11}\sigma_{12} & \sigma_{12}^2 \\ -\sigma_{11}\sigma_{21} & \sigma_{11}\sigma_{22} + \sigma_{12}\sigma_{21} & -\sigma_{12}\sigma_{22} \\ \sigma_{21}^2 & -2\sigma_{21}\sigma_{22} & \sigma_{22}^2 \end{pmatrix}. \quad (5.34)$$

Applying (3.35) and (3.41) to (5.34) for the simple drift it can be obtained

$$\mathcal{A}_{d(3)} = \begin{pmatrix} 1 & -2d & d^2 \\ 0 & 1 & -d \\ 0 & 0 & 1 \end{pmatrix}. \quad (5.35)$$

For the thin lens the result is

$$\mathcal{A}_{l(3)} = \begin{pmatrix} 1 & 0 & 0 \\ \frac{1}{f} & 1 & 0 \\ \frac{1}{f^2} & \frac{2}{f} & 1 \end{pmatrix}. \quad (5.36)$$

Note that this ellipse transformation assumes that Liouville holds. According to  $\mathcal{A}_{d(3)}$  and  $\mathcal{A}_{l(3)}$  the behavior of the beam can be described by the behavior of its boundary. In short this means, that the effective emittance can be computed out of the knowledge of the profile width at different longitudinal positions, or for different focal lengths of a thin lens. From Tab. 3.1 and Fig. 3.4 it is obvious, that the profile width  $P_{z_i}$  at a position  $z_i$  is given by

$$P_{z_i} = 2 \cdot x_{\max} = 2 \cdot \sqrt{\epsilon \cdot \beta_{z_i}}. \quad (5.37)$$

Solving this for  $\beta_{z_i}$  gives

$$\beta_{z_i} = \frac{P_{z_i}^2}{4\epsilon}. \quad (5.38)$$

Substituting  $\beta_{z_i}$  in (5.33) leads to

$$\begin{pmatrix} \frac{P_{z_i}^2}{4\epsilon} \\ \alpha_{z_1} \\ \gamma_{z_1} \end{pmatrix} = \begin{pmatrix} a_{11} & a_{12} & a_{13} \\ a_{21} & a_{22} & a_{23} \\ a_{31} & a_{32} & a_{33} \end{pmatrix} \begin{pmatrix} \beta_{z_0} \\ \alpha_{z_0} \\ \gamma_{z_0} \end{pmatrix}. \quad (5.39)$$

This can be written in three equations

$$\frac{P_{z_i}^2}{4\epsilon} = a_{11}\beta_0 + a_{12}\alpha_0 + a_{13}\gamma_0 \quad (5.40)$$

---

## 5.5 Direct Determination of Effective Emittance

$$\alpha_{z_i} = a_{21}\beta_0 + a_{22}\alpha_0 + a_{23}\gamma_0 \quad (5.41)$$

$$\gamma_{z_i} = a_{31}\beta_0 + a_{32}\alpha_0 + a_{33}\gamma_0. \quad (5.42)$$

Under assumption of the normalization condition (section 3.3.2) the four unknowns  $\beta_0, \alpha_0, \gamma_0$  and  $\epsilon$  can be reduced to three quantities that can be determined with (5.40) by a profile width measurement at different longitudinal positions  $z_i$  from which the emittance  $\epsilon$  then can be obtained. Given at least three positions  $z_1, z_2$  and  $z_3$  and the corresponding profile widths  $P_{z_1}, P_{z_2}$  and  $P_{z_3}$  that are measured one can set up the following system of equations

$$a_{11,z_1} \cdot \epsilon \cdot \beta_0 + a_{12,z_1} \cdot \epsilon \alpha_0 + a_{13,z_1} \cdot \epsilon \gamma_0 = \frac{P_{z_1}^2}{4}, \quad (5.43)$$

$$a_{11,z_2} \cdot \epsilon \cdot \beta_0 + a_{12,z_2} \cdot \epsilon \alpha_0 + a_{13,z_2} \cdot \epsilon \gamma_0 = \frac{P_{z_2}^2}{4}, \quad (5.44)$$

$$a_{11,z_3} \cdot \epsilon \cdot \beta_0 + a_{12,z_3} \cdot \epsilon \alpha_0 + a_{13,z_3} \cdot \epsilon \gamma_0 = \frac{P_{z_3}^2}{4}. \quad (5.45)$$

Note, that there are three different transformation matrices involved  $\mathcal{A}_{z_1}, \mathcal{A}_{z_2}$  and  $\mathcal{A}_{z_3}$  since the three profiles are taken under different distances  $d$  or focal lengths  $f$ . This may change the matrix components  $a_{jk,z_i}$ . The system of equations can be solved by setting up the following determinants

$$\mathcal{D} = \begin{vmatrix} a_{11,z_1} & a_{12,z_1} & a_{13,z_1} \\ a_{11,z_2} & a_{12,z_2} & a_{13,z_2} \\ a_{11,z_3} & a_{12,z_3} & a_{13,z_3} \end{vmatrix}, \quad (5.46)$$

$$\mathcal{D}_x = \begin{vmatrix} \frac{P_{z_1}^2}{4} & a_{12,z_1} & a_{13,z_1} \\ \frac{P_{z_2}^2}{4} & a_{12,z_2} & a_{13,z_2} \\ \frac{P_{z_3}^2}{4} & a_{12,z_3} & a_{13,z_3} \end{vmatrix}, \quad (5.47)$$

$$\mathcal{D}_y = \begin{vmatrix} a_{11,z_1} & \frac{P_{z_1}^2}{4} & a_{13,z_1} \\ a_{11,z_2} & \frac{P_{z_2}^2}{4} & a_{13,z_2} \\ a_{11,z_3} & \frac{P_{z_3}^2}{4} & a_{13,z_3} \end{vmatrix}, \quad (5.48)$$

$$\mathcal{D}_z = \begin{vmatrix} a_{11,z_1} & a_{12,z_1} & \frac{P_{z_1}^2}{4} \\ a_{11,z_2} & a_{12,z_2} & \frac{P_{z_2}^2}{4} \\ a_{11,z_3} & a_{12,z_3} & \frac{P_{z_3}^2}{4} \end{vmatrix}, \quad (5.49)$$

Now it can be written

$$\begin{aligned} \epsilon\beta_0 &= \frac{\mathcal{D}_x}{\mathcal{D}} \\ \epsilon\alpha_0 &= \frac{\mathcal{D}_y}{\mathcal{D}} \\ \epsilon\gamma_0 &= \frac{\mathcal{D}_z}{\mathcal{D}}. \end{aligned} \quad (5.50)$$

## 5 Emittance Determination

Applying the normalization condition from section 3.3.2, the effective emittance then can be determined by

$$\epsilon_{eff} = \sqrt{\frac{\mathcal{D}_x \mathcal{D}_z - \mathcal{D}_y^2}{\mathcal{D}^2}}. \quad (5.51)$$

In the following two concrete examples to apply this method are explained.

### 5.5.1 Effective Emittance with Three Profiles in Longitudinal Direction

The three different profiles necessary to determine the effective emittance with the method described before, can be obtained by a measurement in three different longitudinal positions along a simple drift (Fig. 5.7). Three intensity profiles at three distances  $d_1$  at position  $z_1$ ,  $d_2$  at position  $z_2$  and  $d_3$  at

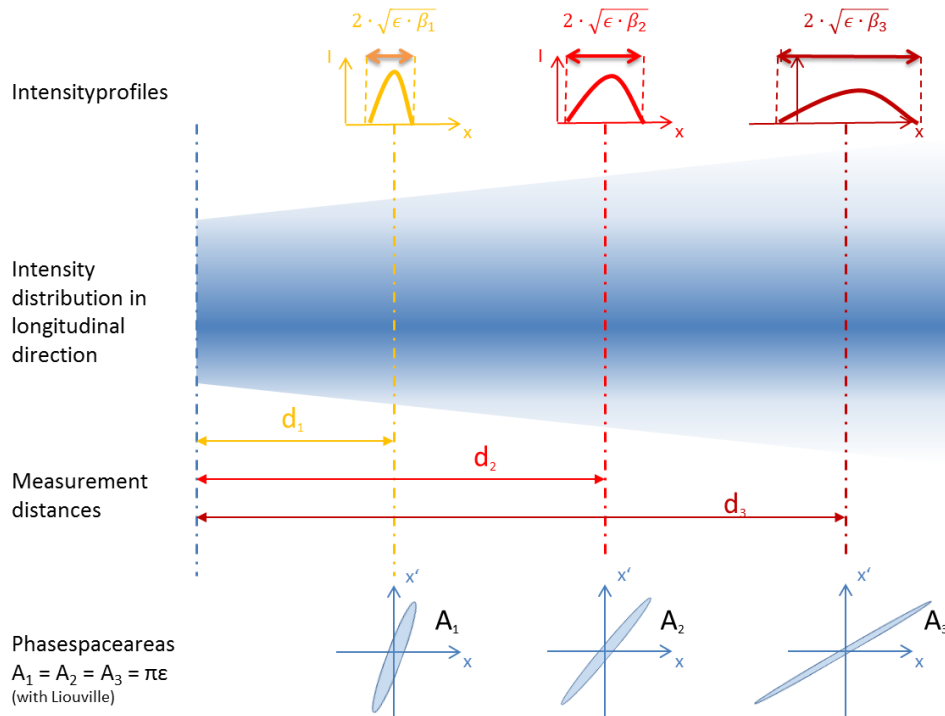


Figure 5.7: The determination of three profile widths along a simple drift.

position  $z_3$  are measured. While the phase space area is conserved under the assumption of Liouville, the ellipse adjustment changes as explained in detail in section 3.4.1, but also can be seen in Fig. 5.7 at the bottom. As a consequence the amplitude of the profile will be lowered while the profile width will be extended for a defocussed beam in this example (for a focussed beam this will be the other way round). The profile widths  $P_{z_1}, P_{z_2}$  and  $P_{z_3}$  can either be computed as a RMS-profile width  $x_{RMS}$  by the second moment of  $x$  as explained in section 5.3 or as a distance between two corresponding ABE's according to (3.58) in Definition 3.5.2. To solve the determinants derived in the last paragraph, one



has to determine all  $a_{jk,z_i}$ . From (5.35) it is known

$$\begin{aligned} a_{11,z_1} &= 1 & ; & & a_{12,z_1} &= -2d_1 & ; & & a_{13,z_1} &= d_1^2, \\ a_{11,z_2} &= 1 & ; & & a_{12,z_2} &= -2d_2 & ; & & a_{13,z_2} &= d_2^2, \\ a_{11,z_3} &= 1 & ; & & a_{12,z_3} &= -2d_3 & ; & & a_{13,z_3} &= d_3^2. \end{aligned} \quad (5.52)$$

Applying these values to the determinants (5.46) to (5.49) will lead to a completely solvable equation in (5.51).

### 5.5.2 Effective Emittance with Three Different Focal Lengths of a Thin Lens

Another way to determine the three profiles is to use a thin lens with different focal length settings (Fig. 5.8). To determine the emittance at the place of determination one has to take the drift before

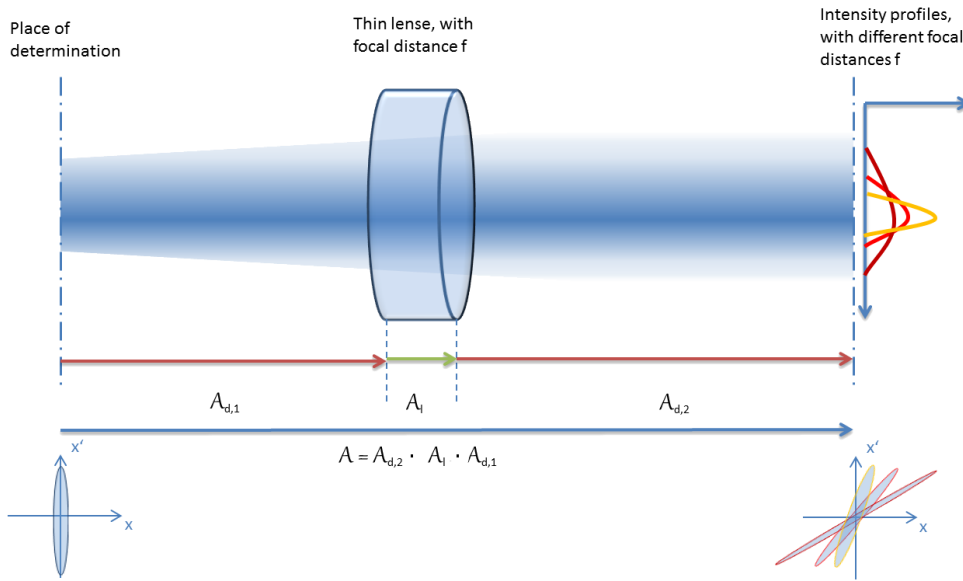


Figure 5.8: The determination of three profile widths with a thin lens. The three parts of the optical system drift, lens, drift have to be taken into consideration in the transformation matrix.

the lens, the lens itself and the drift after the lens into consideration. The complete transformation matrix for the total distance then is the matrix product of these three components

$$\mathcal{A} = \mathcal{A}_{d,2} \cdot \mathcal{A}_l \cdot \mathcal{A}_{d,1}. \quad (5.53)$$

For every profile measurement, the two drift sections stay the same, but the lens section will change with the modification of the focal length. Applying (5.35) and (5.36) to (5.53) under the assumption that  $d_1$  is the length of the drift section  $A_{d,1}$  and  $d_2$  is the length of the drift section  $A_{d,2}$  gives

$$\mathcal{A} = \begin{pmatrix} 1 & -2d_2 & d_2^2 \\ 0 & 1 & -d_2 \\ 0 & 0 & 1 \end{pmatrix} \cdot \begin{pmatrix} 1 & 0 & 0 \\ \frac{1}{f} & 1 & 0 \\ \frac{1}{f^2} & \frac{2}{f} & 1 \end{pmatrix} \cdot \begin{pmatrix} 1 & -2d_1 & d_1^2 \\ 0 & 1 & -d_1 \\ 0 & 0 & 1 \end{pmatrix}. \quad (5.54)$$

## 5 Emittance Determination

---

Expanding  $\mathcal{A}$ , it is obtained

$$\mathcal{A} = \frac{1}{f^2} \cdot \begin{pmatrix} f^2 - 2d_2f + d_2^2 & -2(d_1f^2 + d_2f^2 - d_2^2f - 2d_1d_2f + d_1d_2^2) & d_1^2f^2 + d_2^2f^2 + 2d_1d_2f^2 - 2d_1d_2^2f - 2d_1^2d_2f + d_1^2d_2^2 \\ f - d_2 & f^2 - 2d_1f - 2d_2f + 2d_1d_2 & -d_1f^2 - d_2f^2 + 2d_1d_2f - d_1^2d_2 \\ 1 & -2(d_1 - f) & f^2 - 2d_1f + d_1^2 \end{pmatrix}. \quad (5.55)$$

For every fixed focal length  $f_i$ ,  $i = 1, 2, 3$  one can determine the the determinant components according to (5.55) by

$$\begin{aligned} a_{11,f_i} &= 1 - \frac{2d_2}{f_i} + \frac{d_2^2}{f_i^2} \\ a_{12,f_i} &= -2d_1 - 2d_2 + \frac{2d_2^2}{f_i} + \frac{4d_1d_2}{f_i} - \frac{2d_1d_2^2}{f_i^2} \\ a_{13,f_i} &= d_1^2 + d_2^2 + 2d_1d_2 - \frac{2d_1d_2^2}{f_i} - \frac{2d_1^2d_2}{f_i} + \frac{d_1^2d_2^2}{f_i^2}. \end{aligned} \quad (5.56)$$

Note that the  $a_{jk,f_i}$  correspond to the  $a_{jk,z_i}$  in the determinants (5.46) to (5.49), since the different focal lengths substitute the different longitudinal positions. Again the different measured profile widths can be determined by RMS-values or ABE's. All necessary values for the computation of the effective emittance now are determined.

### 5.5.3 Effective Emittance with More than Three Profiles

In many cases the attempt to use this method with three profiles will lead to the experience, that the determined value of the emittance will be the square root of a negative number. This result is meaningless related to the determination of emittance, since it has no physical correspondence. The reason for this is, that the profile measurements are defective. The determined matrices represent the behavior of the beam edges, but the determination of the beam edges may not fit exactly this behavior, since three profile widths may not be representative enough to compensate even small errors. Three profiles are the minimum to solve the linear equation system in (5.43) to (5.45). The solution with three profiles is non-ambiguous but may not fit exactly the beam edge, such that Eq. (5.51) can not be solved reasonably. A solution for this problem is to use as much profiles as possible to find an optimized solution that is more robust against defective profile width measurements. In order to perform this, one collects  $m$  profiles ( $m \gg 3$ ) [Str06]. This can be done either by different profiles in longitudinal direction or with different focal lengths of a thin lens. For this profiles  $m$  corresponding equations will be set up with the following scheme

$$\frac{P_{z_i}^2}{4} = a_{11,i}\epsilon\beta_0 + a_{12,i}\epsilon\alpha_0 + a_{13,i}\epsilon\gamma_0, \quad (5.57)$$

where  $i = 1, \dots, m$ ,  $P_{z_i}$  are again the measured profile widths and  $a_{11,i}$ ,  $a_{12,i}$  and  $a_{13,i}$  are coefficients given by the transport matrix for measurement  $i$  according to (5.52) or (5.56). Minimizing the Euclidean norm of the error for this equation system

$$\min(\mathcal{L}_{lsqf}) = \min \left( \sum_{i=1}^m \left[ \frac{P_{z_i}^2}{4} - (a_{11,i}\epsilon\beta_0 + a_{12,i}\epsilon\alpha_0 + a_{13,i}\epsilon\gamma_0) \right]^2 \right), \quad (5.58)$$

## 5.5 Direct Determination of Effective Emittance

is a method that already was found by C.F.Gauss and is called *method of least squares*. Since the term  $a_{11,i}\epsilon\beta_0 + a_{12,i}\epsilon\alpha_0 + a_{13,i}\epsilon\gamma_0$  has continuous partial derivatives for  $\epsilon\beta_0$ ,  $\epsilon\alpha_0$  and  $\epsilon\gamma_0$  the necessary constraint for the minimization of  $\mathcal{L}_{lsqf}$  can be given by

$$\begin{aligned} \frac{\partial}{\partial\epsilon\beta_0} \sum_{i=1}^m \left[ \frac{P_{z_i}^2}{4} - (a_{11,i}\epsilon\beta_0 + a_{12,i}\epsilon\alpha_0 + a_{13,i}\epsilon\gamma_0) \right]^2 &= 0, \\ \frac{\partial}{\partial\epsilon\alpha_0} \sum_{i=1}^m \left[ \frac{P_{z_i}^2}{4} - (a_{11,i}\epsilon\beta_0 + a_{12,i}\epsilon\alpha_0 + a_{13,i}\epsilon\gamma_0) \right]^2 &= 0, \\ \frac{\partial}{\partial\epsilon\gamma_0} \sum_{i=1}^m \left[ \frac{P_{z_i}^2}{4} - (a_{11,i}\epsilon\beta_0 + a_{12,i}\epsilon\alpha_0 + a_{13,i}\epsilon\gamma_0) \right]^2 &= 0. \end{aligned} \quad (5.59)$$

Performing the partial derivation gives

$$\begin{aligned} \frac{\partial}{\partial\epsilon\beta_0} \mathcal{L}_{lsqf} &\rightarrow 2 \sum_{i=1}^m \left[ \frac{P_{z_i}^2}{4} - (a_{11,i}\epsilon\beta_0 + a_{12,i}\epsilon\alpha_0 + a_{13,i}\epsilon\gamma_0) \right] \cdot a_{11,i} = 0 \\ &\rightarrow \sum_{i=1}^m \frac{P_{z_i}^2}{4} a_{11,i} - \sum_{i=1}^m a_{11,i}^2 \epsilon\beta_0 - \sum_{i=1}^m a_{11,i} a_{12,i} \epsilon\alpha_0 - \sum_{i=1}^m a_{11,i} a_{13,i} \epsilon\gamma_0 = 0, \end{aligned} \quad (5.60)$$

$$\begin{aligned} \frac{\partial}{\partial\epsilon\alpha_0} \mathcal{L}_{lsqf} &\rightarrow 2 \sum_{i=1}^m \left[ \frac{P_{z_i}^2}{4} - (a_{11,i}\epsilon\beta_0 + a_{12,i}\epsilon\alpha_0 + a_{13,i}\epsilon\gamma_0) \right] \cdot a_{12,i} = 0 \\ &\rightarrow \sum_{i=1}^m \frac{P_{z_i}^2}{4} a_{12,i} - \sum_{i=1}^m a_{11,i} a_{12,i} \epsilon\beta_0 - \sum_{i=1}^m a_{12,i}^2 \epsilon\alpha_0 - \sum_{i=1}^m a_{12,i} a_{13,i} \epsilon\gamma_0 = 0, \end{aligned} \quad (5.61)$$

$$\begin{aligned} \frac{\partial}{\partial\epsilon\gamma_0} \mathcal{L}_{lsqf} &\rightarrow 2 \sum_{i=1}^m \left[ \frac{P_{z_i}^2}{4} - (a_{11,i}\epsilon\beta_0 + a_{12,i}\epsilon\alpha_0 + a_{13,i}\epsilon\gamma_0) \right] \cdot a_{13,i} = 0 \\ &\rightarrow \sum_{i=1}^m \frac{P_{z_i}^2}{4} a_{13,i} - \sum_{i=1}^m a_{11,i} a_{13,i} \epsilon\beta_0 - \sum_{i=1}^m a_{12,i} a_{13,i} \epsilon\alpha_0 - \sum_{i=1}^m a_{13,i}^2 \epsilon\gamma_0 = 0. \end{aligned} \quad (5.62)$$

Now the system of equations from (5.60), (5.61) and (5.62) can be written as

$$\begin{pmatrix} \sum_{i=1}^m a_{11,i}^2 & \sum_{i=1}^m a_{11,i} a_{12,i} & \sum_{i=1}^m a_{11,i} a_{13,i} \\ \sum_{i=1}^m a_{11,i} a_{12,i} & \sum_{i=1}^m a_{12,i}^2 & \sum_{i=1}^m a_{12,i} a_{13,i} \\ \sum_{i=1}^m a_{11,i} a_{13,i} & \sum_{i=1}^m a_{12,i} a_{13,i} & \sum_{i=1}^m a_{13,i}^2 \end{pmatrix} \begin{pmatrix} \epsilon\beta_0 \\ \epsilon\alpha_0 \\ \epsilon\gamma_0 \end{pmatrix} = \begin{pmatrix} \sum_{i=1}^m a_{11,i} \frac{P_{z_i}^2}{4} \\ \sum_{i=1}^m a_{12,i} \frac{P_{z_i}^2}{4} \\ \sum_{i=1}^m a_{13,i} \frac{P_{z_i}^2}{4} \end{pmatrix}. \quad (5.63)$$

This system can be solved with usual methods giving  $\epsilon\beta_0$ ,  $\epsilon\alpha_0$  and  $\epsilon\gamma_0$ . The effective emittance then can be determined by

$$\epsilon_{eff} = \sqrt{\epsilon\beta_0 \cdot \epsilon\gamma_0 - (\epsilon\alpha_0)^2}. \quad (5.64)$$

This method determines an optimized solution for  $\epsilon\beta_0$ ,  $\epsilon\alpha_0$  and  $\epsilon\gamma_0$  depending on the number of used profiles.

## 5 Emittance Determination

### 5.5.4 Estimation of Expected Angle Resolutions

In the following the question will be discussed, to what extent an angle can be resolved by the method described above using a CCD-camera. It will be seen, that this depends less on the resolution of the camera chip than on the longitudinal measurement length and the extent of the angles that have to be measured. A CCD-camera image is a  $n_{px} \times m_{px}$  arrangement of pixel that is a projection of the residual gas radiation in a transverse direction and a longitudinal direction of fixed length. The real lengths of this directions  $n_{mm} \times m_{mm}$  have to be determined depending on the distance of the camera chip to the place of exposure and the properties of the objective lens. Now the *pixel resolution* is given by

$$res_{px} = \frac{n_{mm}}{n_{px}} [\text{mm/px}] = \frac{m_{mm}}{m_{px}} [\text{mm/px}]. \quad (5.65)$$

Here it is assumed, that a pixel has an equal latitude in transverse and longitudinal direction. The first question is: what is the minimal angle that can be resolved at a given longitudinal length? This will be called *minimal angle resolution* for a given distance. Having a look on Fig 5.9a one can reduce this problem to the question: At a given distance, which angle is necessary for the isolumen to cross the pixel row? Turning this question around one also can argue: When the isolumen crosses the pixel row,

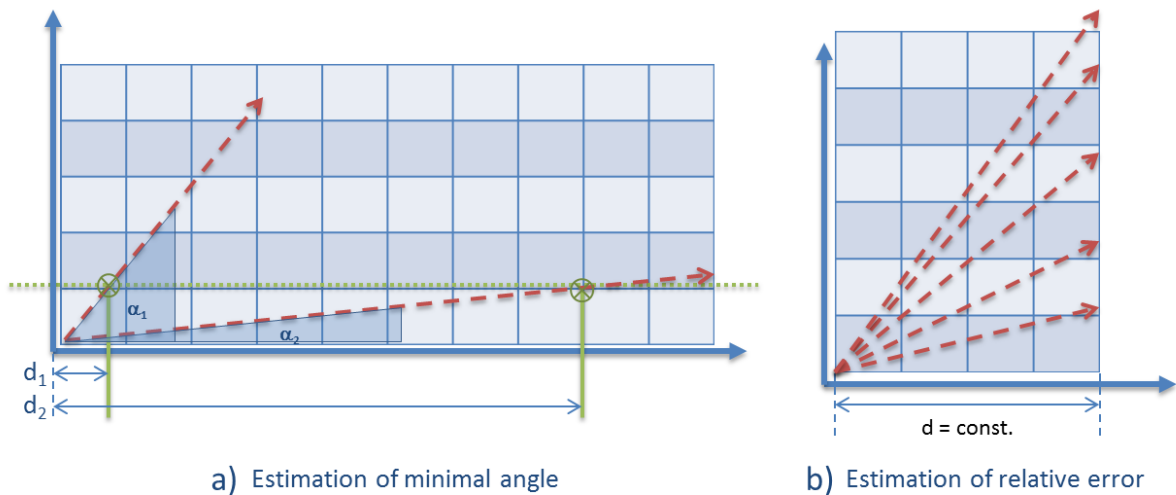


Figure 5.9: a) The minimal angle for a given distance means that the isolumen under this angle crosses the pixel row at the given distance. b) Given a fixed distance, and the knowledge of the minimal angle resolution for it, one can determine the relative error for preset angles, that can be measured at this distance.

this is the first time where one can distinguish between two angles, the one that is too small to cross the pixel row, and the one which is large enough to do it. The larger the distance that can be observed, the smaller an angle can be that has to be resolved. In Fig 5.9a the angle  $\alpha_1$  is very precipitous. It crosses the pixel row in the small distance  $d_1$ . From this distance the angle can be distinguished and its value is called the *minimal angle resolution* for distance  $d_1$ . Angle  $\alpha_2$  is comparatively flat. It takes

## 5.5 Direct Determination of Effective Emittance

pixel resolution simulation/measurement					
	$n_{px} \times m_{px}$	$n_{mm} \times m_{mm}$	$res_{px}$	$\Delta_{abs}\alpha$	$\Delta_{rel}\alpha$ (1 mrad)
simulation	511 px $\times$ 511 px	40 mm $\times$ 40 mm	0.0783 mm/px	$\pm 1.957$ mrad	195.7%
measurement	1600 px $\times$ 1200 px	60.97 mm $\times$ 52.44 mm	0.0437 mm/px	$\pm 0.625$ mrad	62.5 %

Table 5.1: Pixel resolution for images from simulation and measurement and their error estimation in relation to 1 mrad angle resolution at maximum image distance.

the long distance  $d_2$  to cross the pixel row, before it can be distinguished. In Fig. 5.10 the distance in relation to the minimal angle resolution  $\Delta_{abs}\alpha$  is plotted. It can be determined by

$$\Delta_{abs}\alpha = \arctan\left(\frac{res_{px}}{d}\right). \quad (5.66)$$

The pixel resolution for the simulated and measured beams in this work can be seen in Table 5.1.

Assumed that the emittance has to be determined at the left edge of the image (premised that the particles of the beam move from left to right) the minimal angle resolution at the right edge of the image will be 1.957 mrad for the simulated image with a pixel resolution of 0.0783 px/mm and 40 mm distance, and 0.625 mrad for the measured image with a pixel resolution of 0.0437 mm/px at a distance of 69.97 mm. That means that every angle at this distances can be measured with an absolute error  $\Delta_{abs}\alpha$  of  $\pm 1.957$  mrad for the simulation and  $\pm 0.625$  mrad for the measurement.

In the next step it can be noted, that larger angles at the same distance can be determined with better accuracy than smaller ones. Fixing a distance and knowing the absolute error given by the minimal angle resolution  $\Delta_{abs}\alpha$  makes it possible to determine the relative error  $\Delta_{rel}\alpha$ , that is made while measuring different angles  $\alpha$  (Fig. 5.9b), by

$$\Delta_{rel}\alpha = \frac{\Delta_{abs}\alpha}{\alpha}. \quad (5.67)$$

Resolving an angle of  $\alpha = 1$  mrad at the two distances leads directly to a relative error of 195.7% for the simulation (the angle can not be distinguished from this distance) and an error of 62.5% for the measurement (it can be distinguished but the accuracy is very bad). Opening the angle to a larger extend will increase the accuracy. In Fig. 5.11 it can be seen that the characteristics is nearly  $\arctan(1/d)$  and  $1/\alpha$ .

As a consequence at an angle  $\alpha = 10$  mrad, the relative error is reduced to 19.57% for the simulation and 6.25% for the measurement. At  $\alpha = 60$  mrad, the accuracy for the simulation is 3.262% and 1.042% for the measurement. Comparing this to the expected values (Table 1.1) this result is not very satisfying.

The result can be optimized in different ways. The first possibility is to enlarge the measurement distance. The second is to increase the image resolution (number of pixel increased at fixed length), that means to decrease the pixel resolution such, that the isolumen can cross the pixel row earlier. The

## 5 Emittance Determination

---

third one is to enlarge the divergence angles. Which of this strategies works best in the framework of the given setting? Fig. 5.12 shows the characteristics of the first possibility.

Again for 40 mm  $\Delta_{rel}\alpha = 195.7\%$  and for 70 mm  $\Delta_{rel}\alpha = 62.43\%$  are marked. Measuring a 1 mrad angle with the given pixel resolutions at an accuracy of 10% needs an elongation of the measurement distance to 437 mm for the measurement and 783 mm for the simulation. For a 5% error one has to enlarge the measurement distance to 874 mm, respectively 1566 mm. For the measurement with a pixel resolution of 0.0437 mm/px an accuracy of 1% for dissolving a 1 mrad angle can nearly be reached having a measurement distance of 4370 mm.

Considering the constricted proportions at the end of the LEBT, and the boundedness of the camera aperture the simple enlargement of the measurement distance seems not to be an adequate solution on its own. Another possibility is to increase the image resolution, which means to increase the number of pixel at a constant measurement length. The pixel resolution will become smaller and an isolumen can cross earlier to the next pixel row. In Fig. 5.13 the relation between the change of pixel resolution and the development of the relative error for 1 mrad is shown.

Again the relative errors for 1 mrad at a distance of 40 mm / 69.97 mm at a pixel resolution of 0.0783 mm/px / 0.0437 mm/px are marked. The relation in this case is  $\arctan(res_{px}/d)$  and depends on the measurement distance at a fixed pixel resolution. Though, massive changes can not be expected within a pixel resolution between 0.01 and 0.1. As a consequence a decrease of pixel resolution has to be appreciable to optimize the measurement accuracy. At a pixel resolution of 0.01 mm/px the accuracy at a distance of 40 mm amounts to 25% for a distance of 69.97 mm to 14.29%. Having a look on the overview in the top left corner, this means about 4000 px respectively 7000 px. For an accuracy of 50% (40 mm)/25%(69.97 mm) still about 2000 px/3250 px are needed at a pixel resolution of 0.02 mm/px.

As can be seen from Fig. 5.13 the pixel resolution acts approximately linear on the optimization of the relative error in this measurement range, when determining the angle divergence, while measurement distance (Fig. 5.12) and angle divergence (Fig. 5.11) take an advantageous influence of approximately  $\arctan(1/d)$  and  $1/\alpha$ . Before following up the last two optimization strategies, Fig. 5.14 shows the relation between distance, pixel resolution, divergence angle and relative error.

## 5.5 Direct Determination of Effective Emittance

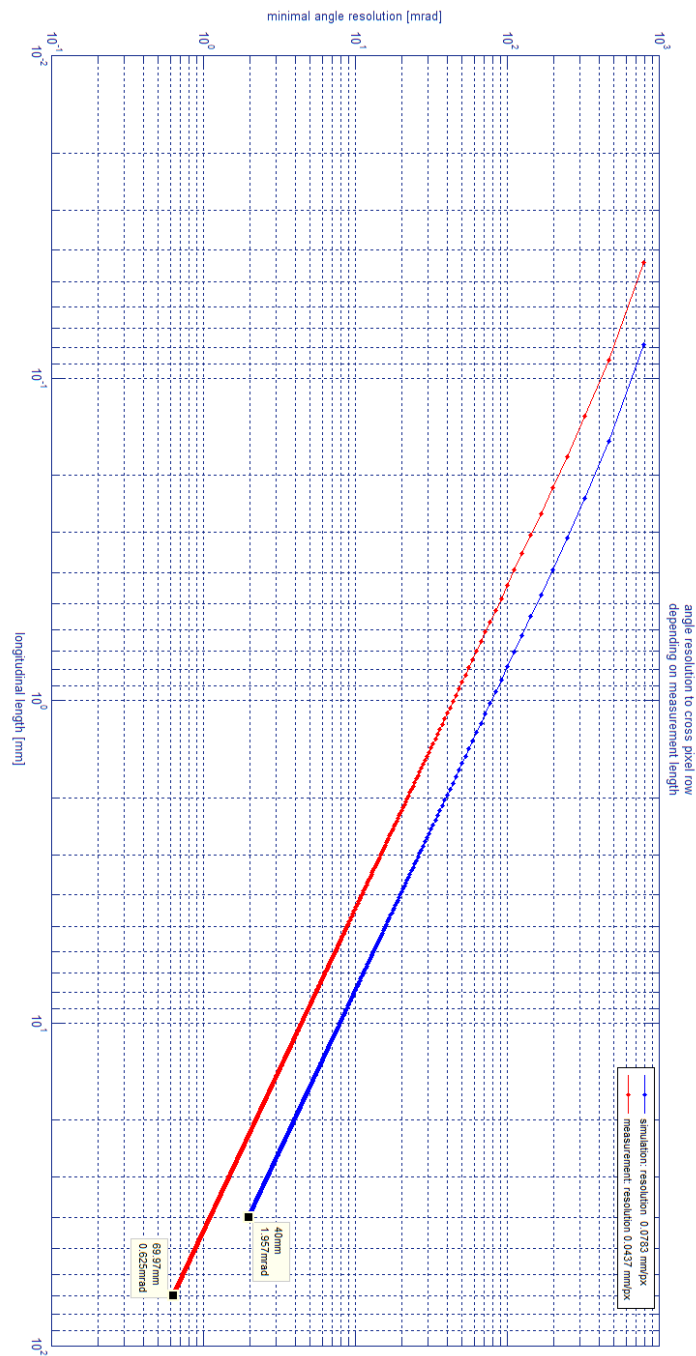


Figure 5.10: Minimal angle resolution in relation to measurement length if the place of emittance determination is the left edge of the CCD-camera image.

## 5 Emittance Determination

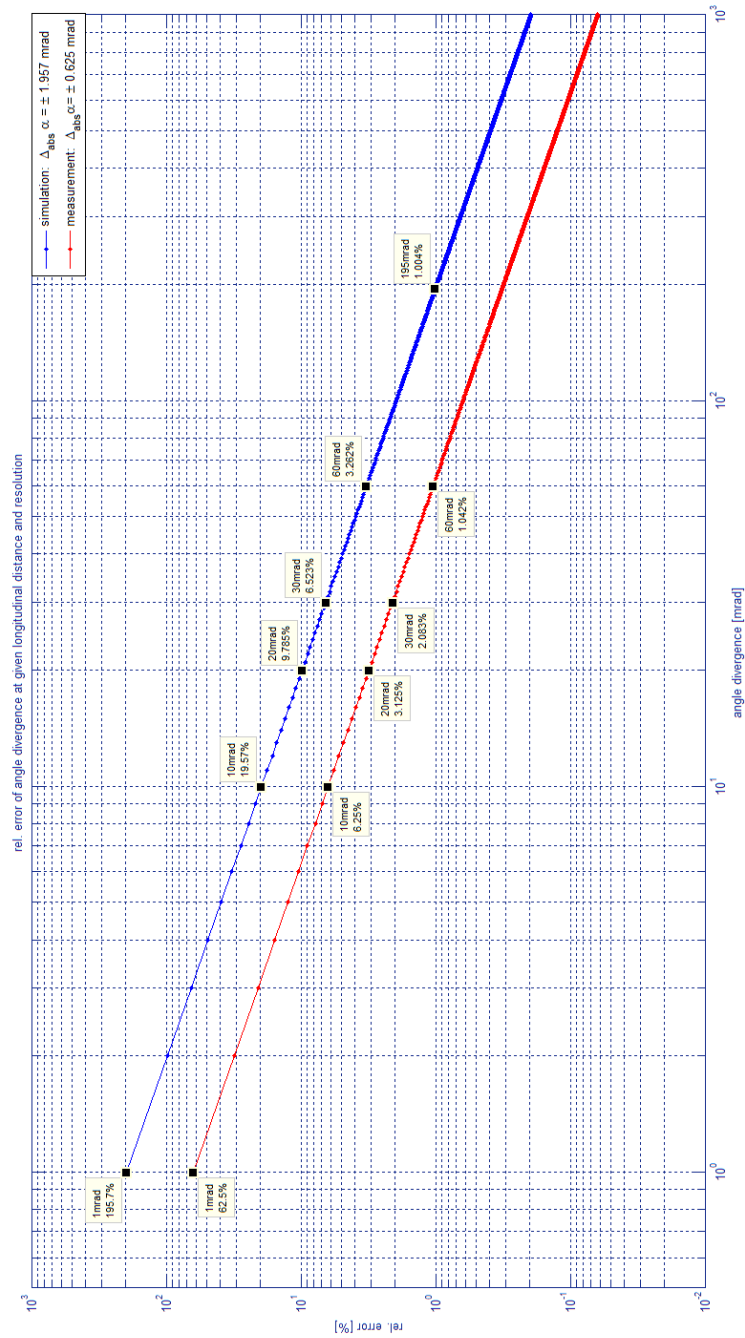


Figure 5.11: Characteristic of relative error at a fixed distance in relation to an angle  $\alpha$  that has to be measured. Distances as shown in Table 5.1



## 5.5 Direct Determination of Effective Emittance

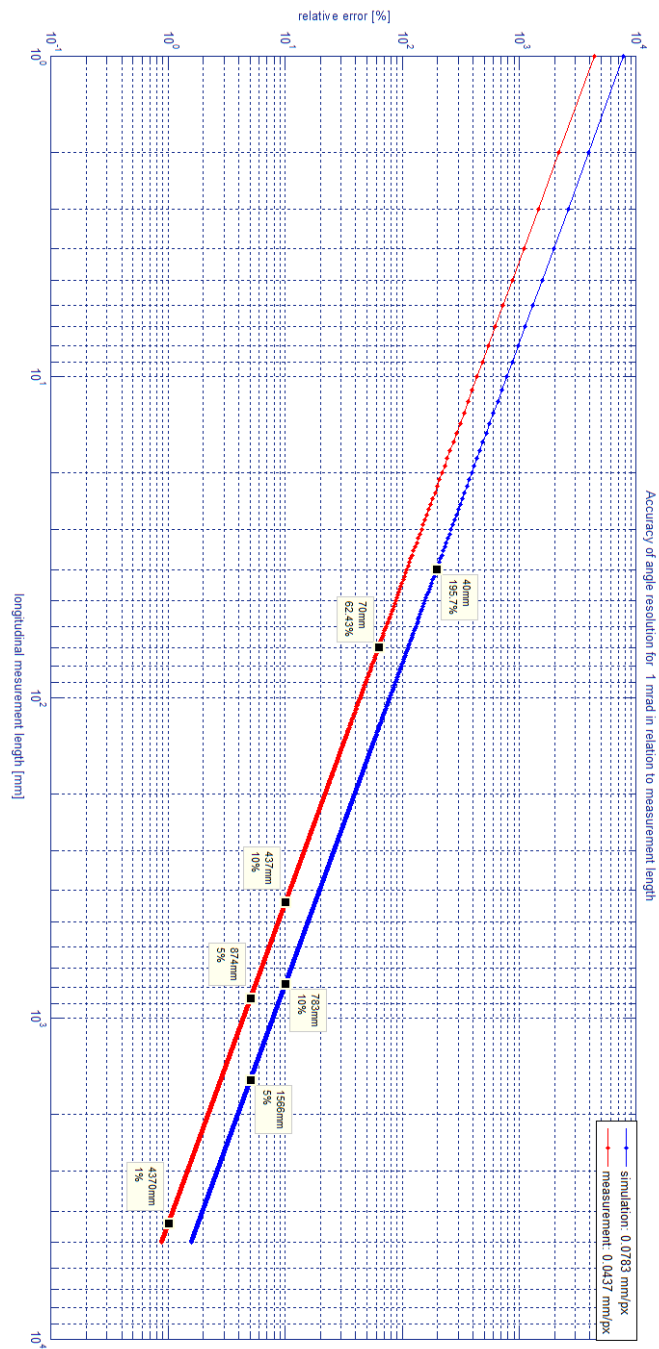


Figure 5.12: Optimization of measurement accuracy for an angle  $\alpha = 1$  mrad by elongating the measurement distance.

## 5 Emittance Determination

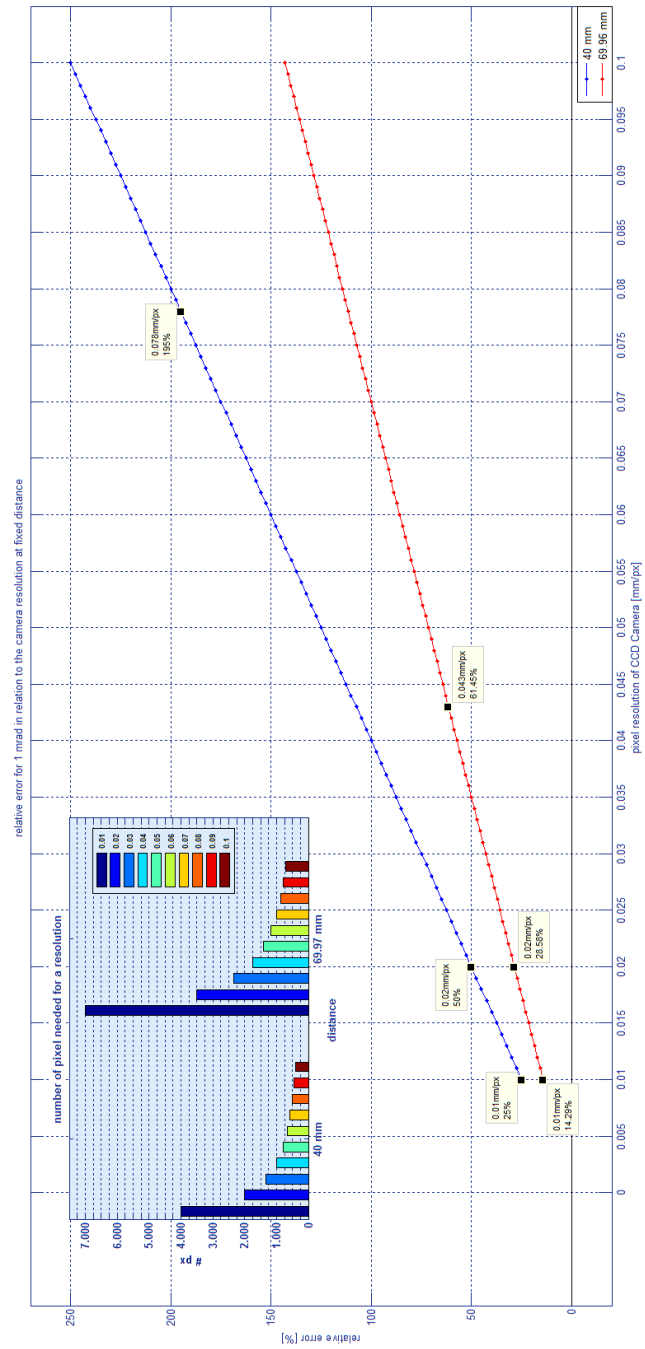


Figure 5.13: Optimization of measurement accuracy for an angle  $\alpha = 1$  mrad by increasing image resolution/decreasing pixel resolution.

## 5.5 Direct Determination of Effective Emittance

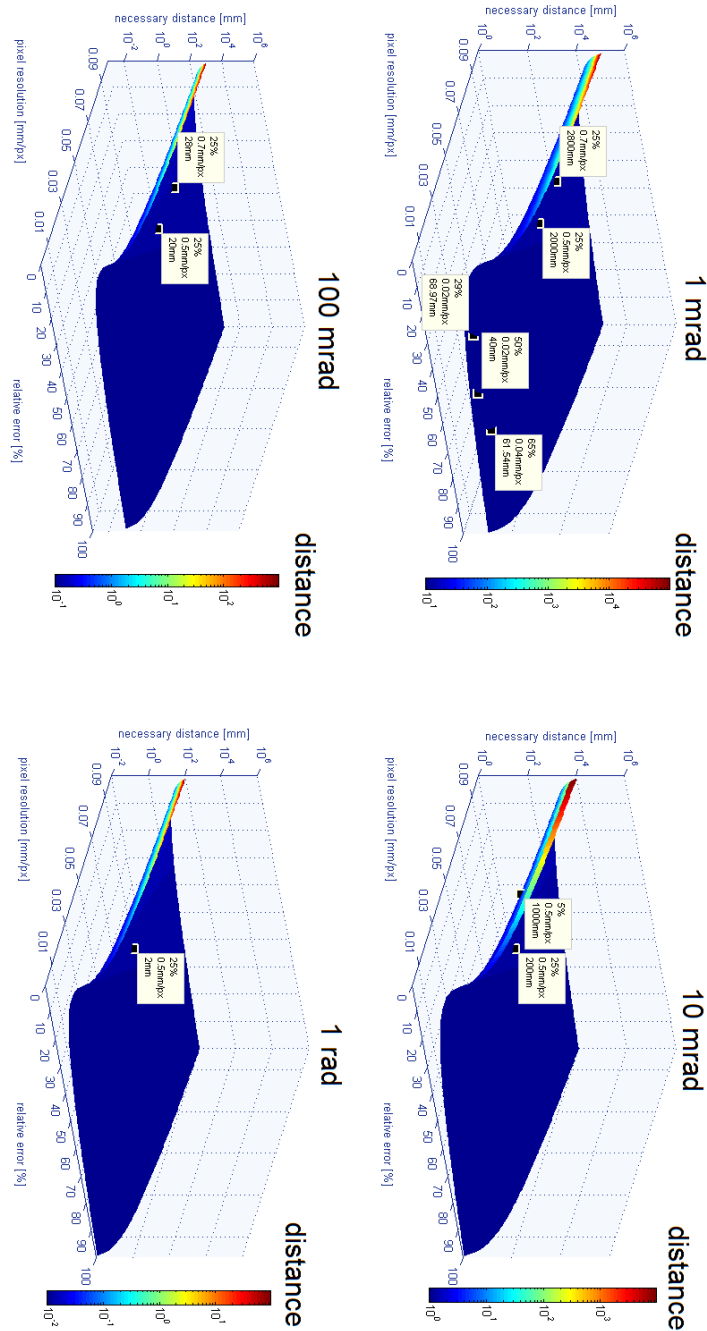


Figure 5.14: The relation between distance, pixel resolution, divergence angle and relative error shows, that the distance and the divergence angle have an influence of nearly  $\arctan(1/d)$  and  $1/\alpha$  on the relative error, while the pixel resolution just has a approximately linear one in this measurement range.

### 5.6 Determining Effective and RMS-Emittance

Given a projection from one direction, one can compute the phase space by using all profiles of this projection. In the case of effective emittance, for every profile the linear equation is computed, then the set of equations is solved as shown in Eq. (5.63) and Eq. (5.64) to obtain the effective emittance. In the case of RMS-emittance, first the scaling factor (Eq. (5.8)) and the phase space rotation angle (Eq. (5.10)) is computed. The profiles are scaled and the tomography algorithm is performed with the scaled profiles and the phase space rotation angles. Then the RMS-emittance is determined on the reconstructed phase space image. All following emittances are determined as  $\pi\epsilon$  emittances normalized by

$$\begin{aligned} \nu_i &= \sqrt{\frac{2 \cdot e \cdot E}{m_i}} \\ \beta &= \frac{\nu_i}{c}, \quad \gamma = \frac{1}{\sqrt{1 - \beta^2}} \\ \epsilon_{norm} &= \beta \gamma \epsilon_{measure} \end{aligned} \quad (5.68)$$

where  $e$  is the elementary charge,  $m_i$  the proton mass and  $c$  the light velocity.  $E$  is the beam current. An example of the result of the reconstruction is given in Fig. 5.15. If the beam is crossing the

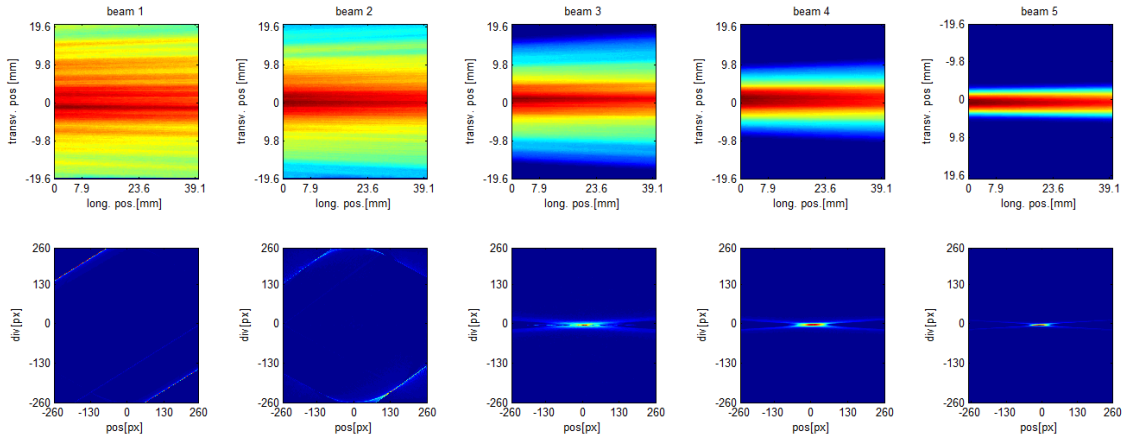


Figure 5.15: Result of phase space tomography performed on projections of five different beams.

projection edge as can be seen in beam one and two of this example, the discrete FBP can not resolve the reconstruction. Having a look on the different reconstruction situations in beam 2 and beam 5 shown in Fig. 5.16 it can be seen that the filtering for the profile in projection 2 is failing. The integration for the filtered Fourier transform  $Q_\theta = \int_{-\infty}^{\infty} S_\theta(w) |w| e^{i2xwt}$  must be carried out over all spacial frequencies, where  $S_\theta(w)$  are the samples of the Fourier transform and  $|w|$  is the frequency response of the filter [Kak88]. If now the frequencies of the complete profile are clipped at the image edge, the true spectrum could not be resolved. This is a quite similar effect as shown for the image defects in section 2.3.4 Fig. 2.26.

Since there are projections from many projection angles, the methods to determine the emittance can be performed on every of them. As in the case of profile width determination, one can then choose

## 5.6 Determining Effective and RMS-Emittance

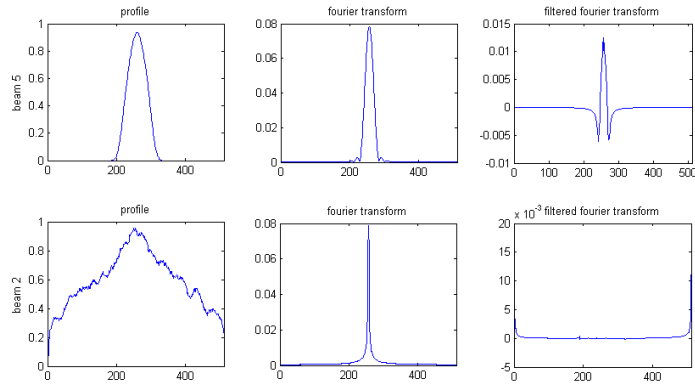


Figure 5.16: Different reconstruction situation for beam 2 and beam 5. The Filtering for beam 2 is failing.

the best fitting. The question is, which one this is. Is it the maximum as given in the case of profile width determination, the minimum or the mean over all emittances? First a look on the profile method will be taken. In Fig. 5.17 the two beam example is revisited to obtain the effective emittances for every projection and fractions between 0.1 to 1.0. For every fraction now the minimum, the maximum

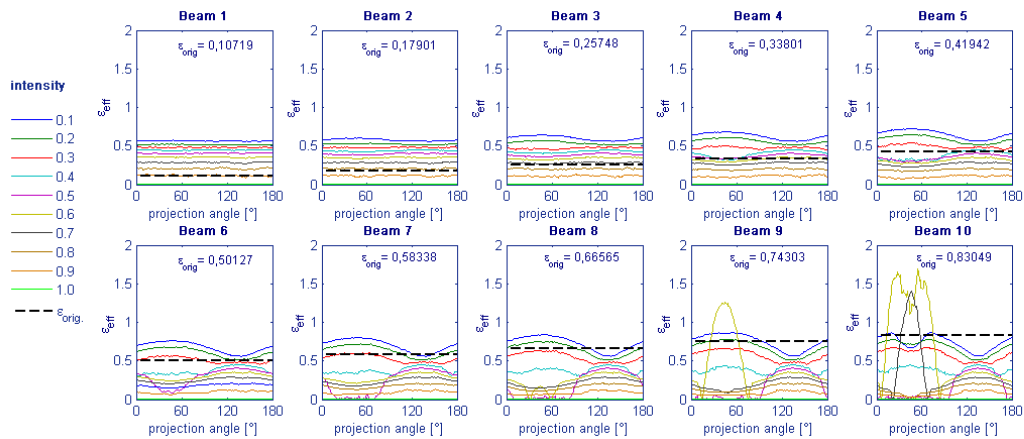


Figure 5.17: The effective emittances for all beams of the two beam example in every fraction from 0.1 to 1.0. The emittance of the original distribution is shown by the black dashed line.

and the mean is taken. This is done by example for beam 1 and beam 10 in Fig. 5.18. For beam 1 the aberration from the original emittance is quite high, and is approximating only in very high intensity fractions<sup>2</sup>. The critical fraction for beam 10 is 0.6, this is equal to the example of beam 7 (Fig. 4.1) where at this intensity the main transverse beam axis changes. Intensities that are higher or

<sup>2</sup>intensity fraction: is the fraction of the maximal intensity in the image. An intensity fraction of 1.0 corresponds to the maximal intensity. An intensity fraction of 0.9 corresponds to an intensity value that is 90% of the maximal intensity and so forth.

## 5 Emittance Determination

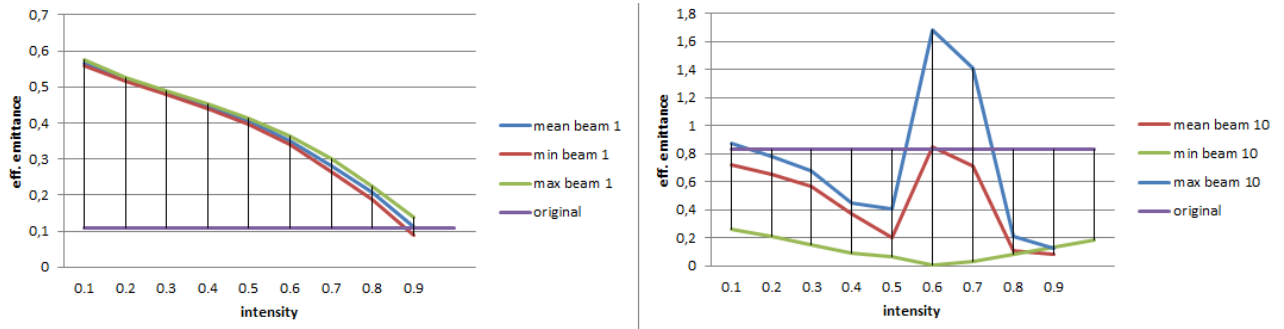


Figure 5.18: Comparison of the characteristics for the minimum, maximum and mean of emittances from all projection directions.

smaller than 0.6 are behaving quite equally as a collective, but the edge of the intersection of the two particle ensembles is crucial. Again having a look on Fig. 5.17, the minimum and maximum emittance of beam 10 are placed in the direction around  $50^\circ$  which is the direction of the main beam axis of the core of the beam. For the critical fraction of 0.6 the emittance in Fig. 5.18 on the right hand side, is best approximated by the mean value of emittances from all directions. Having determined the mean emittance for all fractions and beams with this mean effective emittance, one can have a look on the error. The error is determined as an RMS-error by

$$e_{RMS} = \sqrt{\frac{(\epsilon_{measure} - \epsilon_{orig})^2}{2}}. \quad (5.69)$$

The characteristic of the error over all beams and fractions can be seen in Fig. 5.19 For the beams 1

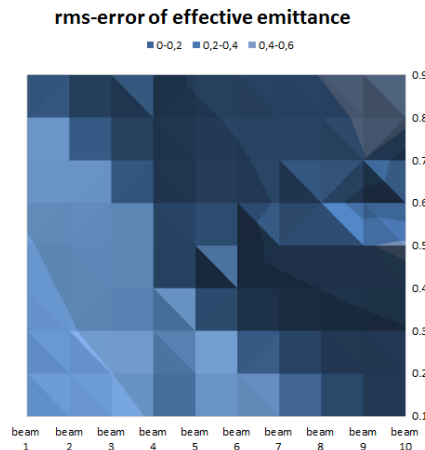


Figure 5.19: Characteristic of RMS-error over all 10 beams and all fractions of the two beam example.

to 3 the RMS-error is quite high. It is decreasing for the following beams. The reason is, that the determination of the emittance can be performed with higher accuracy with increasing angle aberration,

## 5.6 Determining Effective and RMS-Emittance

as is shown in section 5.5.4. The original emittances for all datasets of the two beam example are given in Fig. 5.20.

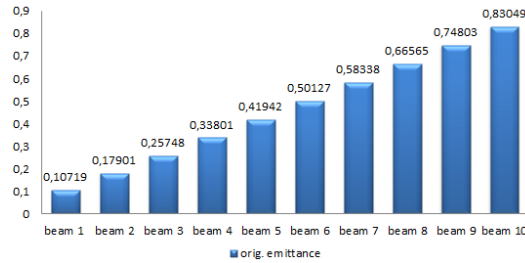


Figure 5.20: Emittances of the original distributions of the two beam example.

To obtain and analyze the the RMS-emittance of the beam, one first have to reconstruct the phase space and then perform the algorithm. In Fig. 5.21 and 5.22 the result is shown for beam 1 and beam 8 of the two beam example for each of these directions.

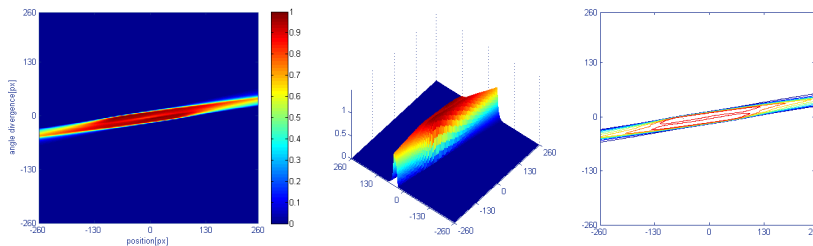


Figure 5.21: Reconstructed phase space for beam 1 of the two beam example.

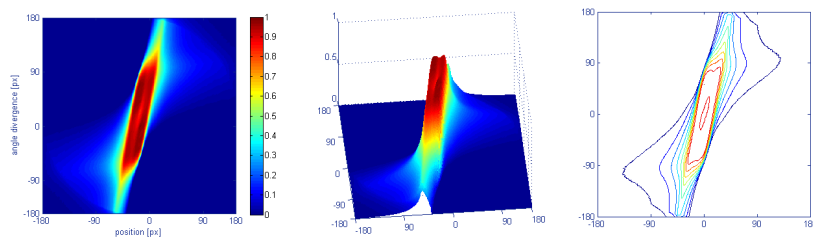


Figure 5.22: Reconstructed phase space for beam 8 of the two beam example.

The emittance then can be observed from all this directions. It can be computed for all projections from every direction. Afterwards, the RMS-emittance can be computed with the method introduced in section 5.3. For beam 1, which is nearly rotational symmetric in all slices, this emittance is quite equal within the different projection angles and can be compared in their characteristics with those of the effective emittance for beam 1 shown in Fig. 5.17. For beam 8 there are more irregularities within one fraction in the different directions. A characteristics for the RMS-emittance of the different

## 5 Emittance Determination

fraction from all directions is given in Fig. 5.23. The further methods now can be adopted as already

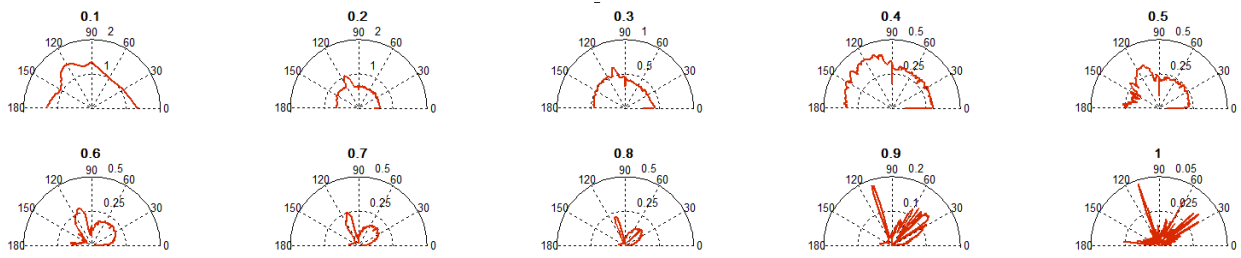


Figure 5.23: RMS-emittances of beam 8 for fractions 0.1 to 1.0 from all reconstructed directions.

shown for the effective emittance. The reconstructions shown in Fig. 5.21 and 5.22 are not single reconstructions, but they are a normalized sum of all reconstructed phase spaces from each direction. This is a second possibility for the RMS-emittance method with phase space tomography to create a mean over all directions. Nevertheless, it is quite helpful to first have a look on the RMS-error of the determined RMS-emittances of each direction in Fig. 5.24. Although beam 1 and beam 8 have

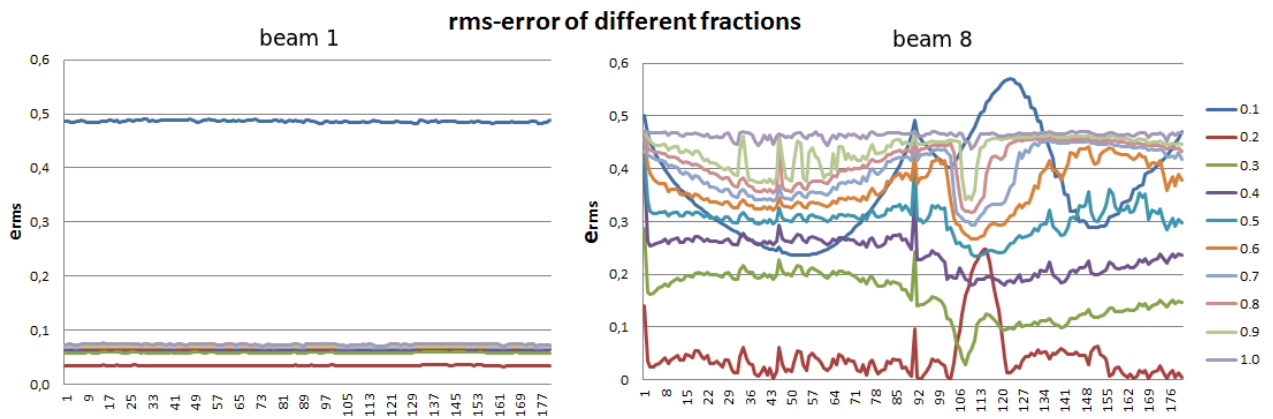


Figure 5.24: RMS-error of RMS-emittance for beam 1 and beam 8 for different fractions taken from 180 directions around the beam.

different characteristics, the fraction of 0.2 is for both beams the best choice. It is common to use a 80% RMS-emittance in many applications, which is equal with a fractional emittance of 0.2. For intensities that are smaller then 0.2 the signal to noise ratio in most cases is too low, to get reliable results out of a statistical measure as it is given by the RMS-emittance. On the other hand, the 80% RMS-emittance is a comparably reliable measure precisely because it is a statistical measure. This can be seen if comparing it with the characteristics of the effective emittance in Fig. 5.25. In both cases the RMS-emittance at an intensity level of 0.2, which is corresponding to the 80% RMS-emittance fits best for both cases. The maximum and minimum error of the effective as well as the RMS-emittance is better for beam 8 then for beam 1, for the reason that the larger divergence angle of beam 8 can be measured with higher accuracy then the smaller divergence angle of beam 1. Although in the shown examples



## 5.6 Determining Effective and RMS-Emittance

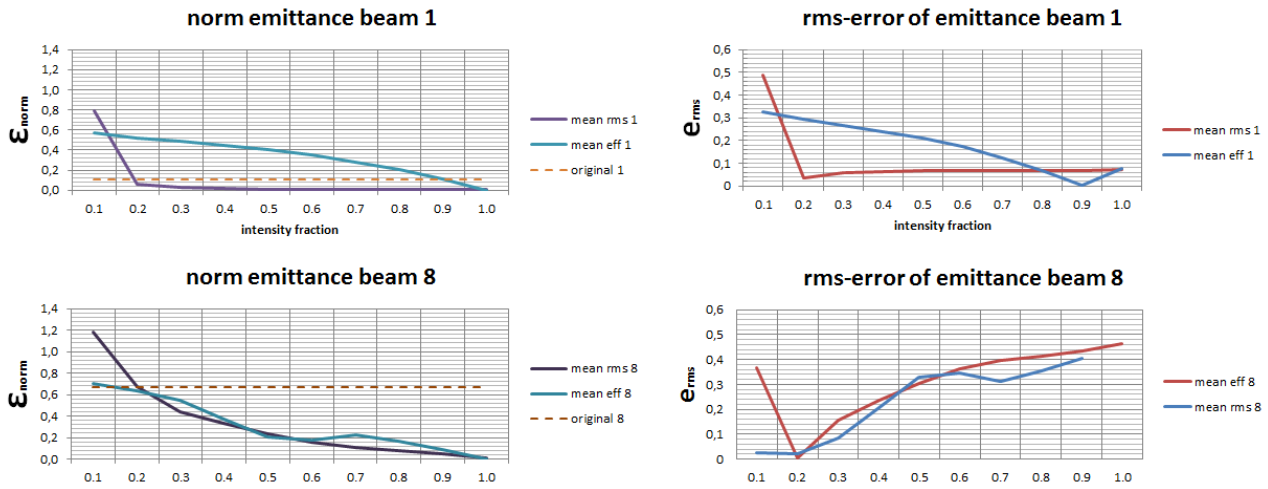


Figure 5.25: Comparison of effective emittance and RMS emittance for beam 1 and beam 8 with the corresponding RMS-error for different fractions.

the determination worked quite well, there are also situations in which the determination using phase space reconstruction with FBP fails. The reason is, that the computed phase space rotation angles, that are computed from the transport matrix, have the characteristics of the arc tangent not a linear equidistant one. Therefore the intensities of the values of the filtered profiles can be allocated in wrong positions in the reconstructed phase space. In this case using the maximum entropy method with less profiles may be a better choice. If the divergence angles are not too small, one also can use the profile method to determine the effective emittance. Finally, an example for the computation of the RMS-emittance on the basis of the measured data set 1 is shown in Fig. 5.26. In order to obtain clear

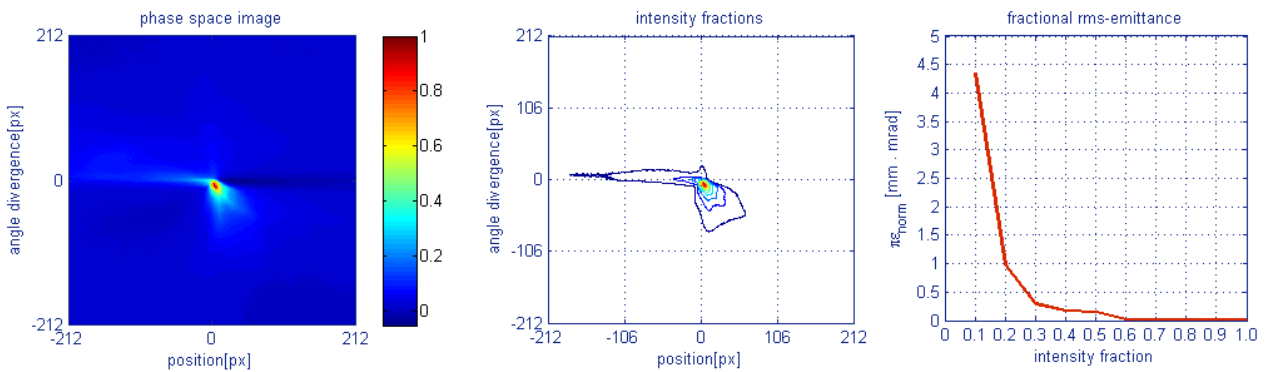


Figure 5.26: Determining the RMS-emittance for measured dataset 1. The sum of all phase space reconstructions from all directions is used to suppress scattering effects.

## 5 Emittance Determination

---

fractional differences and to avoid scattering effects, as already shown for techniques of beam profiling in chapter 4, the phase space is computed for all directions and then summed up to one phase space image on which the emittance determination is performed. If the projections are not too noisy it is also possible to use the mean emittance from all directions. The effective emittance also can be computed on the measurement data with the techniques shown above.

# 6 Summary and Outlook

A general and systematic approach to implement tomography for beam diagnostics has been invented and exemplarily shown for the invention of beam tomography for the Frankfurt Neutron Source. Following the diagnostic pipeline the first step was to prepare the data basis for the tomography reconstruction. At the beginning the purpose for which the tomography will be used has to be specified, since this has influence on the complete setup. Generally, the purpose is placed between the application for an non-interceptive online-tomography for controlling standard beam parameters during acceleration operation (monitoring) and detailed analyses of beam dynamics (Fig. 6.1 left side). For the monitoring,

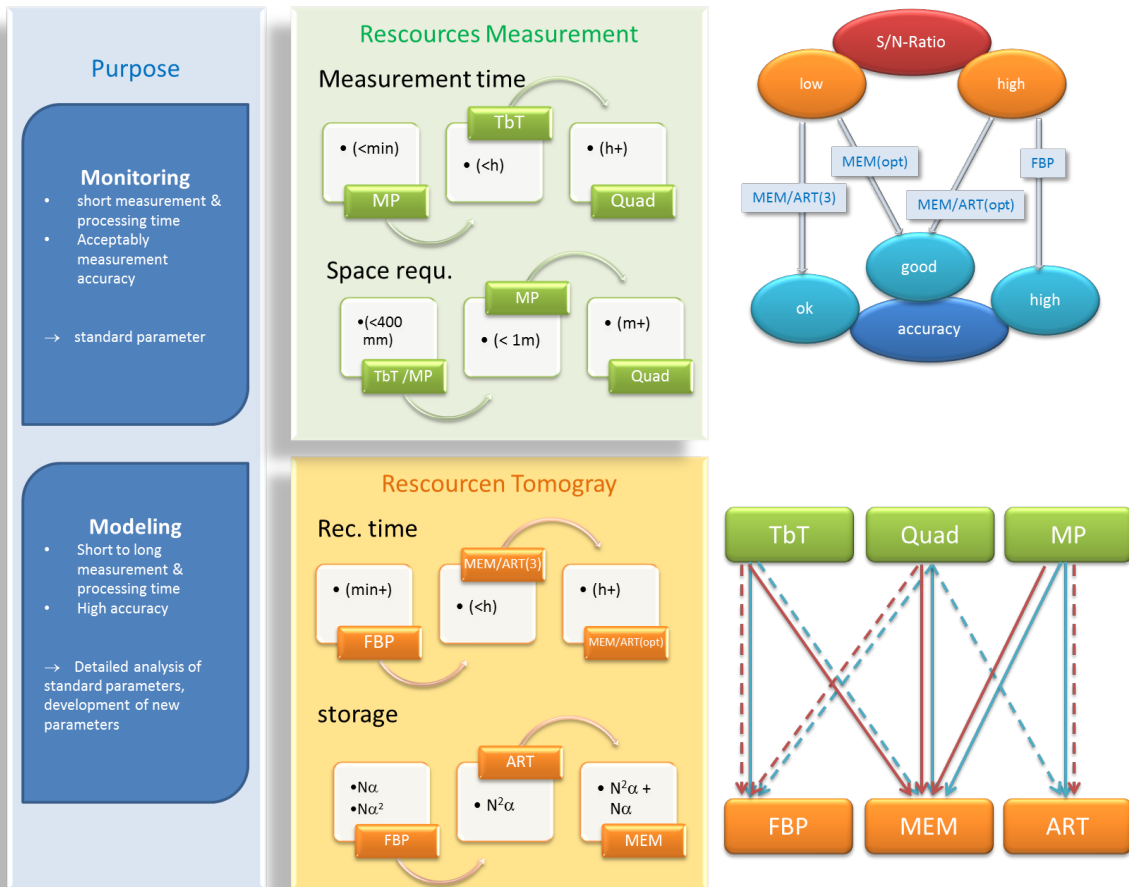


Figure 6.1: Decision systematics for the implementation of beam tomography.

standard parameters have to be obtained with sufficient accuracy. Very important in this case is that

## 6 Summary and Outlook

---

the measurement and processing time is as short as possible. For the analysis of beam dynamics, a high accuracy is needed and the measurement and processing time has to be sufficiently small. In the context of this work, tomography has been kept as flexible as possible. Firstly, it will be used for the analysis of beam dynamics but also for the further development of beam tomography for routined utilization. Later on it will have to serve as a monitoring system at the end of the LEBT of FRANZ. For this reasons the physical space of the device has to be very small on the one hand. On the other hand the number of projections for a high accuracy and has to be very high. Up to now, there was a discrepancy between these two demands, which is now closed by the development of the rotatable vacuum chamber that makes it possible to serve both of them.

The accuracy of the of the reconstruction is considerably influenced by the signal-to-noise ratio of the measurement data in relation the choice of reconstruction algorithm (top right). For this reason, in chapter 4 the data preparation for tomography was demonstrated step by step. In chapter 2 the filtered backprojection (FBP) algorithm was derived to show the basic idea of tomography which is contained in all forms of tomography algorithms. In connection with data exhibiting a high signal to noise ratio the FBP obtains the result with the highest accuracy, beyond that the accuracy can be controlled by the number of projections. The algebraic reconstruction (ART) and maximum entropy (MEM) approach were outlined in a nutshell. Both algorithms are able to deal with a very few number of projections. Comparing the maximum performance their accuracy is lower as it it the case for FBP. Additionally the accuracy of these two algorithms, can not be configured freely as it is in the case of FBP, but depending on the condition of the data there is an optimum of projections. Increasing the number of projections higher than this optimum will decrease the quality of the reconstruction result. Nevertheless they are a good choice if the number of projections or the signal-to-noise ratio is too low for FBP.

Another question has to be considered for the right choice of an algorithm. There is a coherence between the choice of the algorithm, the measurement technique and the space that has to be reconstructed (bottom right). There is a qualitative difference in the use of algorithms for ordinary space and phase space. In ordinary space (blue arrows) the reconstruction result taken on data taken by the TbT (Turn-by-Turn) with a sufficient S/N-ratio will show the best quality (solid line) of all possibilities. Using the Quad (Quad-Scan-Method) the result also will be quite good, but the problem is (dashed line) that the rotation angles are obtained by applying different currents on the quadrupoles, the angle distances are potentially not equidistant as it is necessary for the FBP. Therefore the MEM will be an option for improving the reconstruction results. For the measurement by MP (multi port) only ART and MEM are applicable, because of the low number of projections. In phase space (red arrows) the situation for the application of the FBP is different to the application in ordinary space. The phase space rotation angles which are used for the reconstruction are determined from the transport matrix by an arc tangent function. The consequence is, that the reconstruction angles are not equidistant. Therefore, if the FBP do not provide sufficient accurate results, the MEM is the better choice, because it is not depending on the equidistance of the reconstruction angles.

By the introduction of the diagnostic pipeline in combination with the decision systematics the basis for a routined utilization of tomography in ion beam diagnostics have been established and exemplarily demonstrated on the introduction of beam tomography for FRANZ. A rotatable vacuum chamber has been developed to close a gap between the availability of projections to use the FBP and the small physical space on which they have to be determined.

---

Now it will be important to improve the systematic approach to beam tomography by the following investigations:

1. *improvement of measurement speed*

At the moment the measurement speed for the TbT technique is not high enough for serving as solution for beam monitoring in an online tomography. In general a significant enhancement for the TbT technique is possible.

2. *improvement of processing speed*

The FBP is the fastest of all algorithm which is also requiring the smallest storage capacity (Fig. 6.1 orange box). For an online-tomography it will be quite helpful to implement it as parallel algorithm. Modern graphic cards are able to provide massive parallel computing power so that they are very good candidates to use them as computing platform for beam tomography.

3. *introduction of longitudinal phase space reconstruction for FRANZ*

FRANZ in operation mode will work in non-pulsed as well as in pulsed mode. For this reason it is obligatory to invent a longitudinal phase space reconstruction. It also is desirable to include the main points into the decision systematics to provide it to a the general set up of beam tomography.

4. *joining FBP with projection angles exhibiting an arc tangent distance function* It will be a great advantage, if a method or algorithm is developed, which makes it possible for the FBP to deal properly with angles that exhibit an arc tangent distance function. The advantage will be that the accuracy in phase space can be controlled as good as in the ordinary space, which will increase the possibilities to use it for detailed analysis of beam dynamics in this space.



# Appendix

## Contents

---

<b>1</b>	<b>Simulated Datasets</b>	<b>141</b>
1.1	Seven-Point Extraction (S1)	141
1.2	Single Direction Projection (S2)	142
1.3	Two Dispersing Beams (S3)	142
<b>2</b>	<b>Measured Datasets</b>	<b>147</b>
2.1	Preliminary Measurement (M1)	147
2.2	First Measurements with Rotatable Vacuum Chamber (M2)	147

---

## 1 Simulated Datasets

### 1.1 Seven-Point Extraction (S1)

This dataset consists of a particle distribution of 10,000 particles under the assumption of a seven-point extraction, whereby each of the seven points is nearly Gaussian distributed.

#### Example of Lateral View

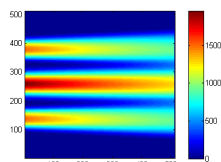


Figure 2: Example of seven-point extracted beam at angle  $24^\circ$

#### tomographic Backprojections

In Figure 3 the first column shows the first slice of the back projected volume. The second column shows the last slice. The summarized intensity distribution of all backprojected slices of the volume is shown in the third column. Other possible representations for a backprojected volume are shown at the end of section 2.2.2

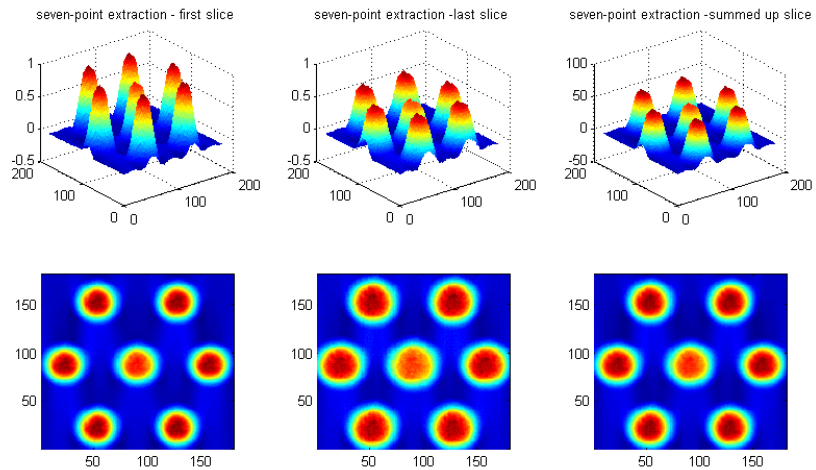


Figure 3: back projection of the seven-point extracted beam

### 1.2 Single Direction Projection (S2)

For this dataset projection from one single direction were simulated with 10.000 particles in order to only change one characteristics of the beam, which is the beam width. A series of 5 beams were created shown in fig.

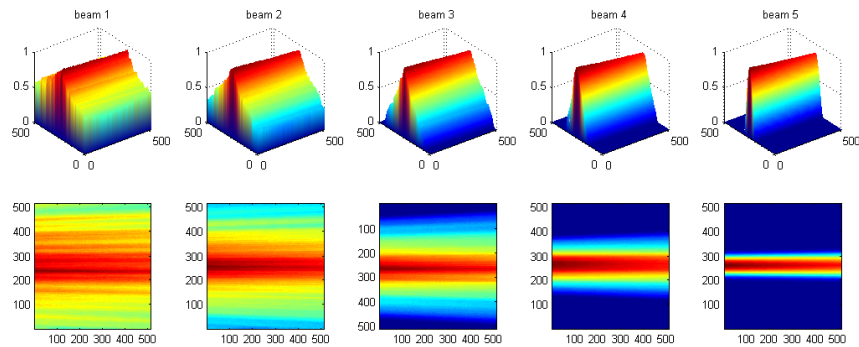


Figure 4: Simulation of a beam from only one direction. The characteristics of the beam width has been decreased in this example.

### 1.3 Two Dispersing Beams (S3)

This dataset is based on two beams consisting each of 10.000 particles with a Gaussian distribution. In a series of ten states, this two beams start with their center at the same x-y position in state one, and then one of the beams is moving to the right bottom edge until it crosses the image edge.



### Example of Lateral View

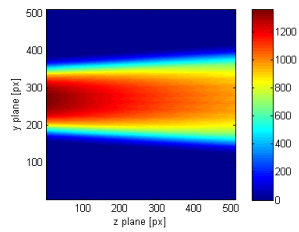


Figure 5: example of beam 1 at angle  $0^\circ$

### Tomographic Backprojections

In the following the first column shows the first slice of the back projected volume. The second column shows the last slice. The summarized intensity distribution of all backprojected slices of the volume is shown in the third column.

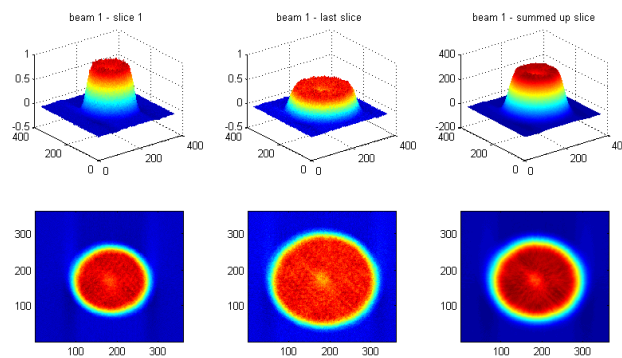


Figure 6: back projection of the two beams in state 1, called beam 1

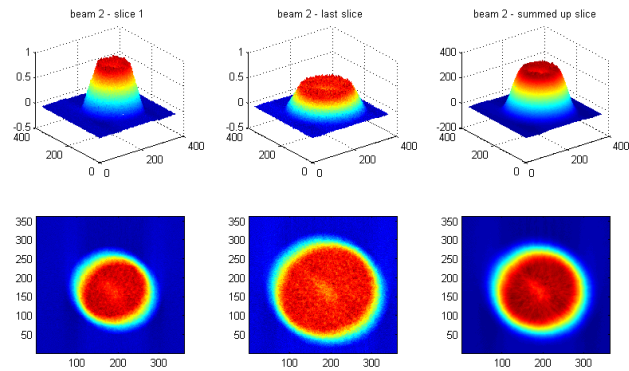


Figure 7: back projection of the two beams in state 2, called beam 2

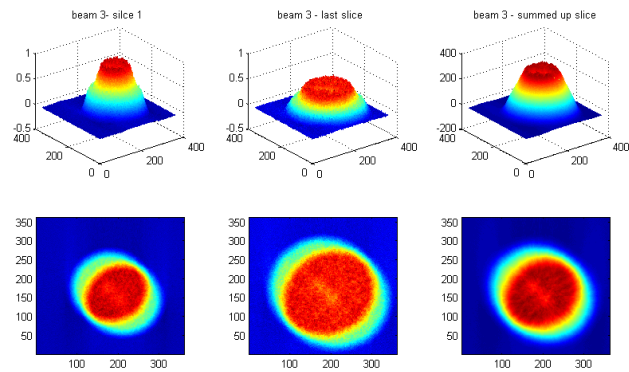


Figure 8: back projection of the two beams in state 3, called beam 3

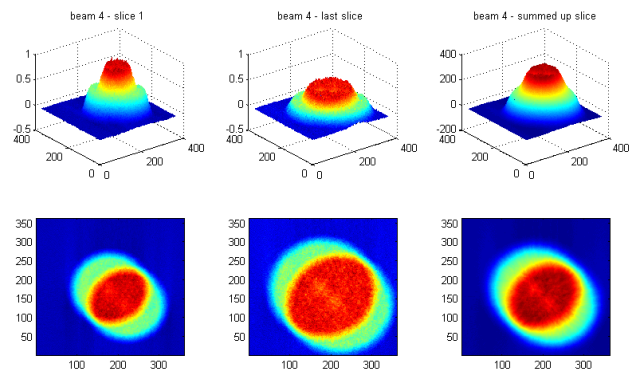


Figure 9: back projection of the two beams in state 4, called beam 4

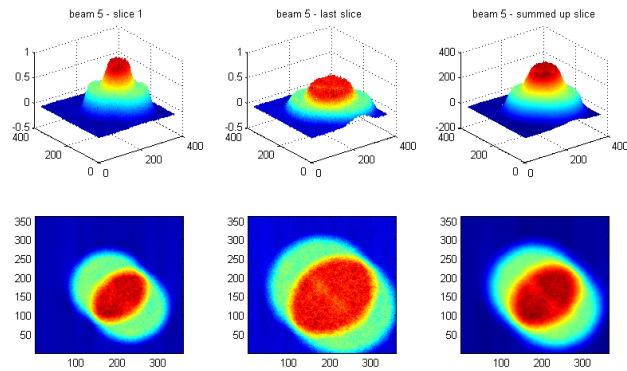


Figure 10: back projection of the two beams in state 5, called beam 5

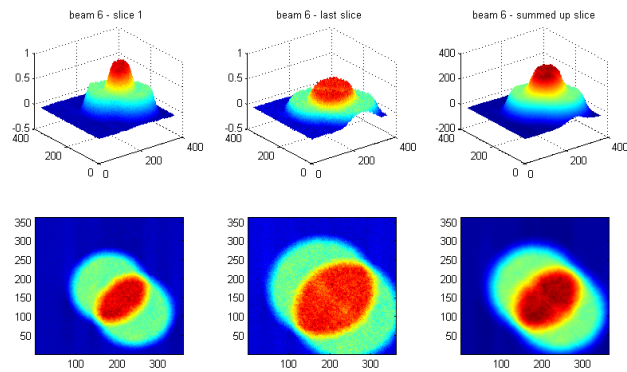


Figure 11: back projection of the two beams in state 6, called beam 6

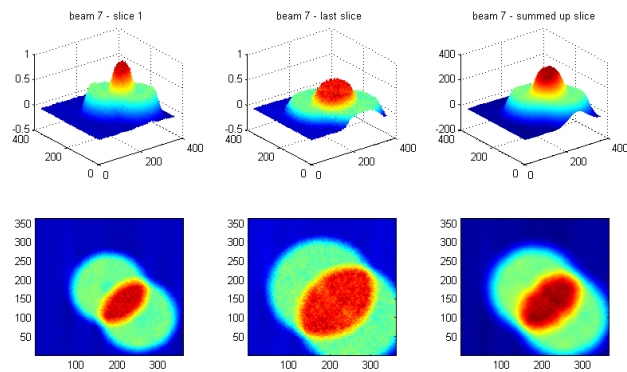


Figure 12: back projection of the two beams in state 7, called beam 7

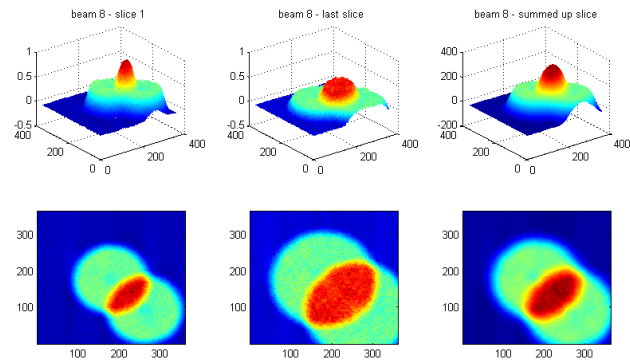


Figure 13: back projection of the two beams in state 8, called beam 8

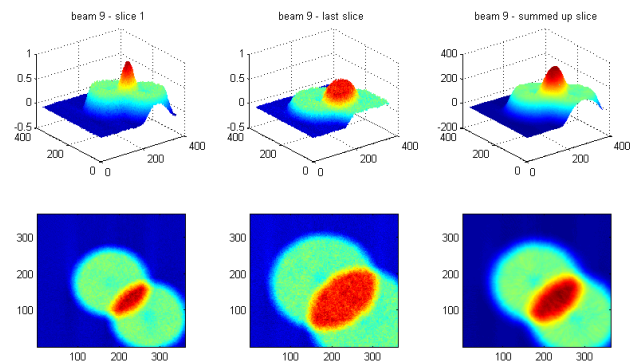


Figure 14: back projection of the two beams in state 9, called beam 9

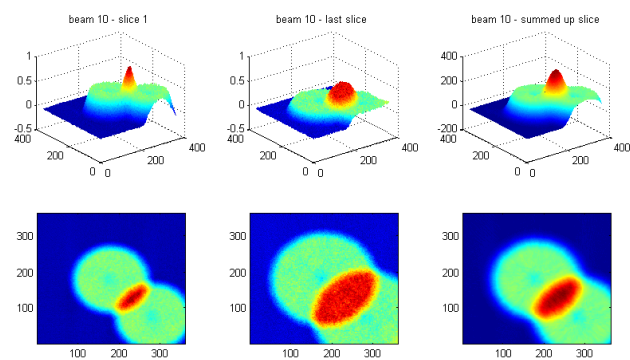


Figure 15: back projection of the two beams in state 10, called beam 10

## 2 Measured Datasets

### 2.1 Preliminary Measurement (M1)

A number of preliminary measurements on a teststand with fixed camera [Wag11] has been taken to investigate the influences of vacuum pressure, residual gas and shutters peed. An example of these preliminary measurements is used in section 3.5.3 showing the difference between two beams under approximately equal conditions but with different residual gases. The measurements shown in fig. 16 have been taken at a beam current of 20 keV at a vacuum pressure of  $5 \cdot 10^{-6}$  mbar and a shutters peed of 10 seconds.

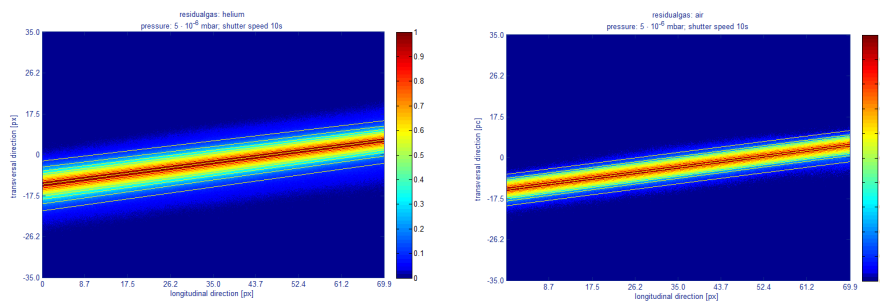


Figure 16: Measurement from one projection angle under approximately equal conditions but with different residual gases

### 2.2 First Measurements with Rotatable Vacuum Chamber (M2)

The measurements were taken at the teststand described in section 1.3.2. The beam was a  $H^+$  beam with a current of 10 keV. The residual gas was nitrogen at a vacuum pressure of about  $10^{-6}$  mbar. The chosen shutters peed of the camera was 5000 ms with a pixel resolution of  $1200 \times 1600$  px. An example of the projection can be seen in fig.17.

#### Example of Lateral View

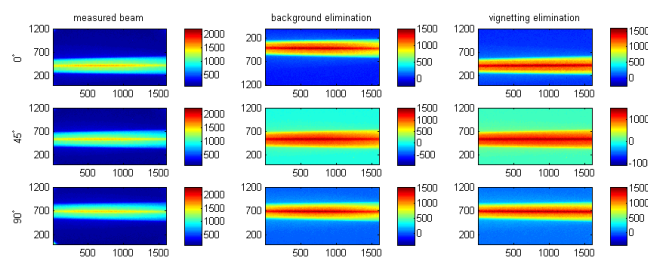


Figure 17: Example projections from the teststand taken at an angle of  $0^{\circ}$  and their related preprocessing

## Appendix

---

The steps of preprocessing are shown in section 1.5.

### Tomographic Backprojections

Two measurements have been performed under these conditions. The backprojections have been computed for all 1600 slices in longitudinal direction using filtered backprojection with hamming window.

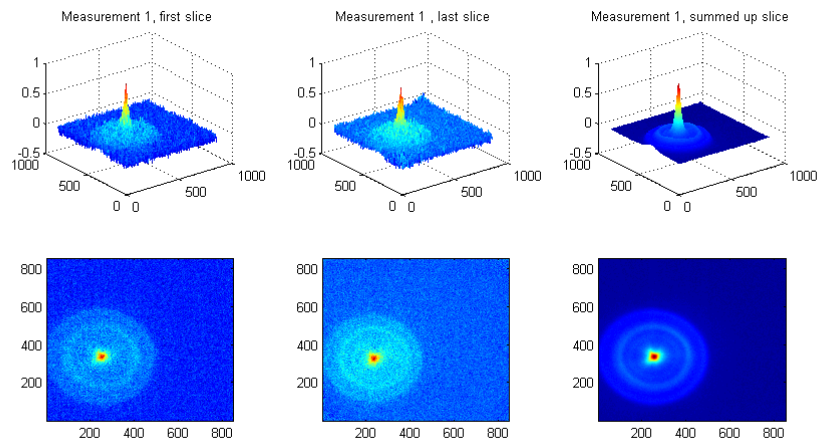


Figure 18: Backprojection results for first measurement. (M2-A)

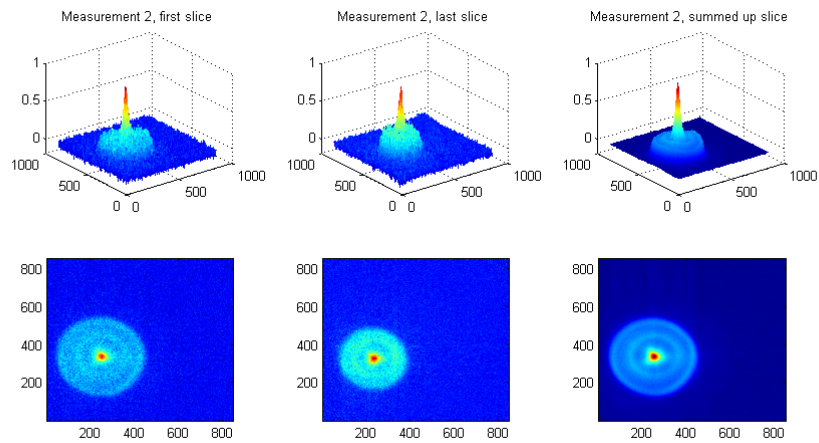


Figure 19: Backprojection results for second measurement. (M2-B)

# List of Tables

1.1	Specification of beam parameters that have to be determined by the diagnostic device at the end of the LEBT section. . . . .	7
3.1	The four important points of a phase space ellipse, can be represented by different notations, depending on the task, that have to be solved. . . . .	69
4.1	Beam width of beam in Fig. 4.5, determined in the two transverse directions $x$ at $0^\circ$ and $y$ at $90^\circ$ . . . . .	93
4.2	Diameter (maximal beam width) of the beam in Fig. 4.5, determined in the two transverse directions $x$ at $0^\circ$ and $y$ at $90^\circ$ in comparison with the viewing angles for the minimum ( $137^\circ$ ) and maximal diameter ( $43^\circ$ ) with respect to the normalized diameter .	94
4.3	diameters of $x$ , $y$ , min and max direction of a measured beam. . . . .	98
5.1	Pixel resolution for images from simulation and measurement and their error estimation in relation to 1 mrad angle resolution at maximum image distance. . . . .	123





# List of Figures

1	Rotierbare Vakuumkammer . . . . .	iv
2	Aufbereitete Projektion einer Messung für die Verwendung in der Tomographie. . . . .	iv
3	Die Grundlage für jede Form der Tomographie bildet das Fourier-Scheiben-Theorem. . . . .	vi
4	Auswirkungen der verschiedenen untersuchten Filter auf das Rekonstruktionsergebnis im Vergleich zur Entfernung des Hintergrundes. . . . .	vi
5	Bestimmung unterschiedlicher Profildicken für unterschiedliche Richtungen . . . . .	ix
6	Abweichung der Hauptstrahlachse . . . . .	x
7	Relation zwischen Messlänge, Bildauflösung, Winkeldivergenz und dem zu erwartenden relativen Fehler . . . . .	xii
8	Allgemeines Schema von Entscheidungen die für eine spezifische Implementierung der Tomographie getroffen werden müssen. . . . .	xiii
1.1	FRANZ scheme . . . . .	5
1.2	Rotatable Vacuum Chamber . . . . .	9
1.3	Parts of Rotatable Vacuum Chamber . . . . .	10
1.4	Teststand . . . . .	13
1.5	Activation Piloting . . . . .	14
1.6	Wavelength for optoelectronic measurements . . . . .	15
1.7	Inverse Abel transformation . . . . .	17
1.8	The Banana Measurement Distortion . . . . .	18
1.9	Correction for Banana Shape Measurements . . . . .	19
1.10	Angle Aberration of measurements . . . . .	20
1.11	Diagnosis Pipeline . . . . .	23
1.12	A Priori Knowledge and Information . . . . .	24
1.13	Semantic stages of an ion beam and the micro-macro relations containing information determined in this work. . . . .	26
1.14	The beam as a collection of moving particles, each tracing its own trajectory. . . . .	27
2.1	Tomography in Medicine and Beam Diagnostics . . . . .	31
2.2	Initial Geometrical Situation for Beam Tomography . . . . .	32
2.3	Creating a Radon Plot . . . . .	33
2.4	Fourier Slice Theorem . . . . .	33
2.5	Fourier Space Distortion . . . . .	35
2.6	Filtered Backprojection Algorithm . . . . .	36
2.7	Single Projection Example . . . . .	37
2.8	Radon plot Example . . . . .	37

## List of Figures

---

2.9	Filtered Backprojection in Examples . . . . .	38
2.10	Difference between Discrete FBP and Matlab-Function iRadon . . . . .	39
2.11	Visualization of a volume by the first slice, the last slice and a sum up over all slices. . . . .	40
2.12	Iso-surface at an intensity of 0.9(left) and Iso-surface at an intensity of 0.5 (right) . . . . .	41
2.13	Possibilities to visualize the computed beam volume by 3d-representations. . . . .	41
2.14	Unfiltered Backprojection . . . . .	42
2.15	Shepp-Logan Filter Optimization . . . . .	43
2.16	Comparison of Different Filters . . . . .	44
2.17	Test picture with a full range of intensity levels . . . . .	45
2.18	Filter results for Test picture . . . . .	45
2.19	Filtering with Absence of Noise . . . . .	46
2.20	Adding Noise to Image to Proof Influence of Filtering . . . . .	46
2.21	Filtering for Measured Datasets . . . . .	47
2.22	Ghost Particles . . . . .	48
2.23	Reconstruction Noise from Ghost Particles . . . . .	48
2.24	Evolution of Reconstruction Noise . . . . .	49
2.25	Distortions caused by loss of projections . . . . .	50
2.26	Consequences of Data loss Inside Profiles . . . . .	51
2.27	Algebraic Reconstruction . . . . .	53
2.28	Maximum Entropy . . . . .	55
3.1	Slope of Trajectory angle . . . . .	64
3.2	Particles Traveling in a Harmonic Oscillator . . . . .	65
3.3	Geometrical Situation of phase space Ellipse . . . . .	67
3.4	Four Characteristic Points of the Phase Space Ellipse . . . . .	68
3.5	Transformation by Drift . . . . .	72
3.6	Effects of a Thin Lens on Particle Trajectory . . . . .	73
3.7	Transformation by Thin Lens . . . . .	74
3.8	Particle Motion at End of Solenoid . . . . .	75
3.9	Influences on Particles at the End of a Solenoid . . . . .	76
3.10	Profile Width Determination with FWHM . . . . .	80
3.11	Isolumen . . . . .	81
3.12	Two Problems at Profile Width Determination . . . . .	81
3.13	Problem of Ambiguity at the Determination of Profile Width . . . . .	82
3.14	The IRF-method determines isolumen sensitive to information . . . . .	84
3.15	Clipping Outliers in IRF-Method . . . . .	85
3.16	Comparison of ABEs of beams under quite equal conditions but with different residual gases. . . . .	87
3.17	Fractional profile widths for the situation of Fig. 3.16. Helium as residual gas causes a higher excitation. . . . .	87
4.1	Determining Intensity Fractions for Beam Diameter . . . . .	90
4.2	Evaluation of beam diameters using different ABEs and fractions. . . . .	91

4.3	Difference in profile determination using the maximum of each row or the maximum of the complete slice to define the FWHM threshold. . . . .	92
4.4	The beam width according to different characteristics is observed from all 360 angles of view around the reconstructed density distribution. . . . .	92
4.5	In the case of a not rotational symmetric beam the diameter will differ according to the direction the beam profile was taken from. . . . .	93
4.6	Characteristic profiles of the beam shown in Fig. 4.5, taken at an viewing angle of $0^\circ$ (x-direction) and the orthogonal angle $90^\circ$ (y-direction) . . . . .	94
4.7	Characteristic Profiles of beam 7 of the Two Beam Example . . . . .	95
4.8	Comparison of profiles in direction $42^\circ$ and $137^\circ$ . . . . .	95
4.9	Problems with Reconstruction of One Slice From Measured Projections . . . . .	96
4.10	Improvement of Fractional Intensity Differentiation in a Measured Beam . . . . .	96
4.11	Diameters obtained from viewing angles by step-width $1^\circ$ . . . . .	97
4.12	Determining the minimal and maximal diameter for the measured reconstructed distribution. . . . .	97
4.13	Comparison of minimal and maximal diameter. The differences are marginal. . . . .	98
4.14	Three dimensional centroid . . . . .	99
4.15	Axes of Gravity of Beam 1 of the Two Beam Example . . . . .	102
4.16	Center of Gravity and Main Beam Axes for Beam 1 . . . . .	103
4.17	The relation between the direction of the eigenvectors and their corresponding eigenvalues. . . . .	104
4.18	Centroid Movement . . . . .	104
4.19	Aberration of Main Beam Axis in the Two Beam Example . . . . .	105
4.20	Aberration of main beam axis from longitudinal direction of beam 7. . . . .	105
5.1	Integrating $x'$ over the phase space distribution $\mathcal{F}(x, x')$ leads to the projection $p(x)$ in a given location $z_i$ . . . . .	108
5.2	For the backprojection of the phase space transforms $p(\varphi, \theta, s, t)$ along $z$ are considered to create the Radon plot. . . . .	109
5.3	Trajectory Slope as Azimuthal Angle . . . . .	110
5.4	Transformation of original Phase Space Ellipse . . . . .	111
5.5	Schematic representation of a backprojected phase space picture. . . . .	113
5.6	Non-linear Forces and Effective Emittance . . . . .	115
5.7	The determination of three profile widths along a simple drift. . . . .	118
5.8	Determination of three Profile Width with a Lens . . . . .	119
5.9	Influence of Minimal Angle and Fixed Distance for the Relative Error . . . . .	122
5.10	Minimal Angle Resolution with respect to Measurement Length . . . . .	125
5.11	Characteristics of relative error at fixed distance . . . . .	126
5.12	Optimization of Measurement Accuracy by Distance Elongation . . . . .	127
5.13	Optimization of Measurement Accuracy by Increasing Image Resolution . . . . .	128
5.14	Relation Between Pixel Resolution, Divergence Angle and Relative Error . . . . .	129
5.15	Result of phase space tomography performed on projections of five different beams. . . . .	130
5.16	Different reconstruction situation for beam 2 and beam 5. The Filtering for beam 2 is failing. . . . .	131

## List of Figures

---

5.17	Effective Emittance of the Two Beam Example . . . . .	131
5.18	Comparison of the characteristics for the minimum, maximum and mean of emittances from all projection directions. . . . .	132
5.19	Characteristic of RMS-error over all 10 beams and all fractions of the two beam example.	132
5.20	Emittances of the original distributions of the two beam example. . . . .	133
5.21	Reconstructed phase space for beam 1 of the two beam example. . . . .	133
5.22	Reconstructed phase space for beam 8 of the two beam example. . . . .	133
5.23	RMS-emittances of beam 8 for fractions 0.1 to 1.0 from all reconstructed directions. . .	134
5.24	RMS-error of RMS-emittance for beam 1 and beam 8 for different fractions taken from 180 directions around the beam. . . . .	134
5.25	Comparison of Effective Emittance and RMS-Emittance for Beam 1 . . . . .	135
5.26	Determining the RMS-Emittance for Measured Dataset . . . . .	135
6.1	Decision systematics for the implementation of beam tomography. . . . .	137
2	Example of seven-point extracted beam at angle $24^\circ$ . . . . .	141
3	back projection of the seven-point extracted beam . . . . .	142
4	Single Direction Projection . . . . .	142
5	example of beam 1 at angle $0^\circ$ . . . . .	143
6	back projection of the two beams in state 1, called beam 1 . . . . .	143
7	back projection of the two beams in state 2, called beam 2 . . . . .	144
8	back projection of the two beams in state 3, called beam 3 . . . . .	144
9	back projection of the two beams in state 4, called beam 4 . . . . .	144
10	back projection of the two beams in state 5, called beam 5 . . . . .	145
11	back projection of the two beams in state 6, called beam 6 . . . . .	145
12	back projection of the two beams in state 7, called beam 7 . . . . .	145
13	back projection of the two beams in state 8, called beam 8 . . . . .	146
14	back projection of the two beams in state 9, called beam 9 . . . . .	146
15	back projection of the two beams in state 10, called beam 10 . . . . .	146
16	Measurement from one projection angle under approximately equal conditions but with different residual gases . . . . .	147
17	Example Projections of Measurement with Preprocessing . . . . .	147
18	Backprojection results for first measurement. <b>(M2-A)</b> . . . . .	148
19	Backprojection results for second measurement. <b>(M2-B)</b> . . . . .	148

## Bibliography

- [AC07] **Soria J. Atkinson C.H.** *Algebraic Reconstruction Techniques for Tomographic Particle Image Velocimetry*. In 16th Australian Fluid Mechanics Conference, Australia. Laboratory for Turbulence Research in Aerospace and Combustion, Department of Mechanical Engineering, 2007.
- [And02] **Rosenzweig J.B. Anderson, S.G.** *Space-charge Effects in High Brightness Electron Beam Emittance Measurements*. Physical Review Special Topics - Accelerators and Beams, 5, 2002.
- [Ban66] **A.P. Banford.** *The Transport of Charged Particle Beams*. E&F.N Spon Ltd., 1966.
- [Bel87] **J.S. Bell.** *Hamiltonian Mechanics*. CAS Oxford, England, CERN 87-03, page 35, 1987.
- [Bie04] **F.M. et al Bieniosek.** *Diagnostics for Intense Heavy Ion Beams in the hif-vnl*. International Symposium on Heavy Ion Inertial Fusion, 2004.
- [Bri53] **L. Brillouin.** *The Negentropy Principle of Information*. Journal of Applied Physics, 24:1153, 1953.
- [Bri62] **L. Brillouin.** *Science and Information Theory*. New York Academic Press, 1962.
- [Cai96] **Cai, Z. B. Lai W. Yun E. Gluskin D. Legnini P. Illinski G. Srajer** *Measurement of Stored Electron Beam at the Aps Storage Ring Using Pinhole Optics*. Rev. Sci. Instrum., 67(9), 1996.
- [Chau08] **Chau L.P. et.al.** *One Nano-second Bunch Compressor for High Intense Proton Beam* Proceedings of EPAC, Genoa, Italy, 2008, THPP091,3578-3580
- [Com01] **Comblin, J.F. Sanchez Alvarez J.L. Hancock.S.** *A Pedestrian Guide to Online Phase Space Tomography in the Cern PS Complex*. Technical Report, European Organization for Nuclear Research, 2001.
- [Con00] **Connolly, R. Michnoff R. Moore T. Shea T. Tepikian S.** *Beam Profile Measurements and Transverse Phase-Space Reconstruction on the Relativistic Heavy-Ion Collider*. Nucl. Instr. and Methods in Phys. Res. A, 413, 2000.
- [Con02] **Connolly. R. et al.** *Laser Beam-Profile Monitor Development at BNL for SNS*. 10th Beam Instrumentation Workshop, 2002.
- [Fra78] **J.S. Fraser.** *Beam Tomography or Art in Accelerator Physics*. Los Alamos Scientific Laboratory Report LA-7498-MS, 1978.

## Bibliography

---

- [Fra79] **J. S. Fraser.** *Beam Analysis Tomography.* 26(1):1641–1645, 1979.
- [Gre08] **Greiner W.** *Klassische Mechanik: Teilchensysteme, Lagrange-Hamiltonsche Dynamik.* Verlag Harry Deutsch, 2008.
- [Hac89] **Hackbusch W.** *Integralgleichungen-Theorie und Numerik.* Teubner, 1989.
- [Ham73] **Hamming, W.R.** *Numerical methods for scientists and engineers.* McGraw-Hill, 1973.
- [Han97] **Hancock S.** *A Simple Algorithm for Longitudinal Phase Space Tomography.* Technical Report, European Laboratory for Particle Physics, 1997.
- [Han99] **Hancock, S. Jansson A. Lindroos M.** *Tomographic Reconstruction of Transverse Phase Space from Turn-by-Turn Profile Data.* Proceedings of PAC, 1999.
- [Han00] **Hancock, S. Lindroos M.** *Longitudinal Phase Space Tomography with Space Charge.* Phys.Rev. ST. Accel. Beams, 3, 124202, 2000.
- [Hes93] **Hess W.** *Digitale Filter.* B.G. Teubner, 1993.
- [Hin08] **Hinterberger F.** *Physik der Teilchenbeschleuniger und Ionenoptik,* Volume 2. Springer Verlag Berlin Heidelberg, 2008.
- [Hol06] **Holder D.J. et al.** *A Phase Space Tomography Diagnostic for PITZ.* Proceedings of EPAC, 2006.
- [Hon05] **Honkavaara K. et al.** *Transverse Electron Beam Diagnostics at the VUV-FEL at Desy.* Proceedings of the 27th International Free Electron Laser Conference, 2005.
- [Hue02] **Hühning M.** *Analysis of Surface Roughness Wake Fields and Longitudinal Phase Space in a Linear Electron Accelerator.* Dissertation, Universität Hamburg, 2002.
- [ISO] **ISO 11146:2005/04** *Lasers and Laser-Related Equipment – Test Methods for Laser Beam Widths, Divergence Angles and Beam Propagation Ratios, Part 1 - Part 3.*
- [Jac87] **Jackson G.** *A Phase Space Tomography (PST) Monitor for Adjusting Bunch Rotation During Coalescing.* Technical Report, Fermi National Accelerator Laboratory, 1987.
- [Jac93] **Jackson G.** *Design, Implementation and Results from a Longitudinal Phase Space Tomography (PST) Monitor in the Fermi Lab Main Ring.* In Proceedings PAC, 1993.
- [JC03] **Chen J. Rongli Geng Yuantao Ding Kui Zhao Baocheng Zhang Shengwen Quan Anjia Gu.** *Emittance Measurement by Using Duo Image Pattern of Cherenkov Radiation.* Proceedings of the Particle Accelerator Conference, 2003.
- [Joh80] **Joho W.** *Representation of Beam Ellipses for Transport Calculations.* Technical Report, Swiss Institute for Nuclear Research, 1980.
- [Kac37] **Kaczmarz S.** *Angenäherte Auflösung von Systemen Linearer Gleichungen.* Bull. Acad.Pol.Sci.Lett.A, 6-8A:335–357, 1937.

- 
- [Kak88] **Slaney M. Kak, A.C.** *Principles of Computerized Tomographic Imaging*. IEEE Press, 1988. Ref2 Fourier Slice Theorem.
- [Kam06] **Kroschel K. Kammeyer, K.-D.** *Digitale Signalverarbeitung*. B.G.Teubner, 2006.
- [KH66] **Kogelnik H. Li T.** *Laser Beams and Resonators*. Applied Optics, 5:1550–1567, 1966.
- [Kos01] **Kostial S.** *Transversale Phasenraum-Tomographie des Elektronenstrahls am S-DALINAC*. Dissertation, Technische Universität Darmstadt, 2001.
- [Koz01] **Kozioł H.** *Beam Diagnostics for Accelerators*; 2005 ed. (CERN-PS-2001-012-DR):44 p, May 2001.
- [Kue90] **Kueppers B.O.** *Information and the Origin of Life*. MIT Press, 1990.
- [LB74] **Logan B.F. Shepp L.A.** *Reconstructing Interior Head Tissue from X-ray Transmissions*. IEEE Trans. Nucl. Sci., page 21:228236, 1974.
- [LB75] **Logan B.F. Shepp L.A.** *Optimal Reconstruction of a Function from its Projections*. Duke Mathematical Journal, 42, No.4:645ff., 1975.
- [Man97] **Mane, V. Wei J. Peggs S.** *Radon Reconstruction in Longitudinal Phase Space*. Particle Accelerator Conference. Proceedings, 2:2158 – 2160, 1997.
- [McK95] **McKee, C.B. Madey J.M.J. O’Shea.P.G.** *Phase Space Tomography of Relativistic Electron Beams*. Nuclear Instruments and Methods in Physics Research, A 358, 1995.
- [Mes06] **Meschede D. editor.** *Gerthsen Physik*, Volume 23. Springer Verlag Berlin Heidelberg, 2006.
- [Met73] **Metzger C.** *The 800 Mev Measurement Line of the Cern P.S. Booster*. IEEE Trans. Nucl.Sci., NS-20, No. 3, 1973.
- [Meu08] **Meusel O. et.al.** *A Coupled RFQ-Drift Tube Combination for FRANZ*. Proc. LINAC, 2008, Victoria, Canada, MOP002, 49-51
- [Min77] **Minerbo, G.N. Sanderson J.G.** *Reconstruction of a Source from a Few (2 or 3) Projections*. Los Alamos Scientific Laboratory informal report LA-6747-MS, 1977.
- [Min79] **Minerbo G.N.** *Ment: A Maximum Entropy Algorithm for Reconstructing a Source from Projection Data*. Computer Graphics Image Proc., 10, 1979.
- [Min81] **Minerbo, G. N. Jameson R. A Sander O.R.** *Four-Dimensional Beam Tomography*. Nuclear Science IEEE, 28,3:2231 – 2233, 1981.
- [Mot85] **Mottershead C.T.** *Maximum Entropy Beam Diagnostic Tomography*. IEEE Transactions on Nuclear Science, NS-32 No.5:1970–1972, 1985.
- [Neu67] **Neumann W.** *Spektroskopische Methoden der Plasmadiagnostik, in: Ergebnisse der Plasmaphysik und Gaselektronik*. Akademie-Verlag, 1967.
-

## Bibliography

---

- [Nie97] **Niemoller, N. Schulz-von der Gathen V. Stampa A. Dobele H.F.** *A Quasi-Optical 1 mm Microwave Heterodyne Interferometer for Plasma Diagnostics Using a Frequency-Tripled Gunn Oscillator.* Plasma Sources Sci. Technol., 6:478–483, 1997.
- [Pan83a] **Pan S.X. Kak-A.C.** *A Computational Study of Reconstruction Algorithms for Diffraction Tomography.* IEEE Trans. Acoust. Sig. Proc., ASSP-31:pp. 12621275, 1983. Refl Fourier Slice Theorem.
- [Pan83b] **Pan S.X./Kak A.C.** *A Computational Study of Reconstruction Algorithms for Diffraction Tomography; Interpolation vs. Filtered-Backpropagation.* IEEE Trans. Acoust. Speech Signal Processing, ASSP-31:1262–1275, 1983.
- [Pas10] **Pastorino M.** *Microwave Imaging.* John Wiley & Sons, 2010.
- [Pet01] **Petz D.** *John von Neumann and the Foundation of Quantum Physics,* Chapter Entropy von Neumann and the von Neumann Entropy. Springer Netherlands, 2001.
- [Poz00] **Pozimski, J. Jakob A. Lakatos A. Klein H. Meusel O.** *Non Destructive Determination of Beam Emittance for Low Energy Ion Beams Using CCD-Camera Measurements.* Proceedings 7th EPAC, 2000.
- [Rad17] **Radon J.** *Über die Bestimmung von Funktionen durch ihre Integralwerte längs gewisser Manigfaltigkeiten.* Sächsische Akademie der Wissenschaften, 1917.
- [Ram71] **Lakshminarayan A.V. Ramachandran, G.N.** *Three-Dimensional Reconstruction from Radiographs and Electron Micrographs: Application of Convolutions Instead of Fourier Transforms.* Proc. Natl. Acad. Sci., page 63:22362240, 1971.
- [Rei08] **Reiser M.** *Theory and Design of Charged Particle Beams.* Wiley-VCh, 2008.
- [Rei10] **Reichau, H. Meusel O. Ratzinger U. Wagner C.** *Estimation of Profile width in Hybrid Ionbeam Tomography.* Proc. Beam Instrumentation Workshop, 2010.
- [Ren70] **Renyi A.** *Probability Theory.* American Elsevier Publishing Company, 1970.
- [Ros60] **Edwards; B. Rose D.N.** *An Extension of the Transfer Matrix Method to a Beam Transport System Containing a Solenoid.* Nuclear Instruments and Methods, 7:135, 1960.
- [Ros82] **Rosenfeld A.C. Kak A.** *Digital Picture Processing.* NY Acadmemic Press, 1982.
- [Sac71] **Sacher F.J.** *Rms Enveloppe Equations with Space Charge* IEEE Trans. Nucl. Sci., 1971.
- [Sch08] **Schulte K.** *Untersuchung von Messmethoden zur Parameterbestimmung eines nichtneutralen Plasmas.* Diplomarbeit, Goethe Universität Frankfurt am Main, 2008.
- [SD06] **Stratakis D. et al** *Tomography as a Diagnostic Tool for Phase Space Mapping of Intense Particle Beams.* Physical Review Special Topics - Accelerators and Beams, 9, 2006.
- [SD07] **Stratakis D. et al** *Phase Space Tomography of Beams with Extreme Space Charge.* Proceedings of PAC07, 2007.



- 
- [Sen09] **Senger V.** *Ionenstrahldiagnose mit Zellularen Neuronalen Netzen.* Diplomarbeit, Goethe Universität Frankfurt am Main, 2009.
- [Sha49] **Shannon, C.E. Weaver W.** *The Mathematical Theory of Communication.* Illinois Press, 1949.
- [Sit95] **Sittinger F.** *Untersuchungen zu Optischen Profil- und Emittanzmessungen an Niederenergetischen , Intensiven Ionenstrahlen.* Dissertation, Goethe Universität Frankfurt am Main, 1995.
- [Siv06] **Sivia, D.S. Skilling J.** *Data Analysis - A Bayesian Tutorial.* Oxford Science Publications, 2006.
- [SJ96] **Safranek J.Stefan P.M.** *Emittance Measurement at the Nsls X-Ray Ring.* Proc. EPAC, 1996.
- [SL74] **Shepp L. A. Logan B. F.** *Reconstructing Interior Head Tissue from X-ray Transmissions.* 21(1):228–236, 1974.
- [Sny57] **Courant E.D. Snyder H.S.** *Theory of the Alternating-Gradient Synchrotron.* Annals of Physics, 281:360–408, 1957.
- [Ste65] **Steffen K.G.** *High Energy Beam Optics.* Interscience Publishers, 1965.
- [Sto06] **Stockli M.P.** *Measuring and Analyzing the Transverse Emittance of Charged Particle Beams.* Proceedings of 12.BIW, 2006.
- [Str06] **Strehl P.** *Beam Instrumentation and Diagnostics.* Springer Verlag Berlin Heidelberg, 2006.
- [Str08] **Stratakis D.** *Tomographic Measurement of the Phase Space Distribution of a Space-Charge-Dominated Beam.* PhD thesis, University of Maryland, 2008.
- [Str10] **Struckmeier J.** *Statistical Description of Charged Particle Beams and Emittance Measurements.* HICforFAIR Workshop, 2010.
- [Tan71] **Tanabe K.** *Projection Method for Solving a Singular System.* Numer.Math., 17:203–214, 1971.
- [Tho94] **Thomson M.** *Side-on Messungen der Balmerlinie H-alpha in einem Plasma hoher Dichte.* Diplomarbeit, Christian-Albrechts Universität, Kiel, 1994.
- [Tol38] **Tolman R.C.** *The Principles of Statistical Mechanics.* University Press, Oxford, Great Britain, 1938.
- [Wag11] **Wagner C.** *Entwicklung eines Teststandes für die Optische Strahltomographie.* Bachelorarbeit, Universität Frankfurt am Main 2011.

## Bibliography

---

- [Wie10] **C. Wiesner**, L. P. Chau, H. Dinter, M. Droba, M. Heilmann, N. Joshi, D. Mader, A. Metz, O. Meusel, I. Muller, D. Noll, H. Podlech, U. Ratzinger, H. Reichau, R. Reifarth, A. Schempp, S. Schmidt, W. Schweizer, K. Volk, and C. Wagner. *Proton Driver Linac for the Frankfurt Neutron Source* AIP Conference Proceedings, 1265(1):487–492, 2010.
- [Yak03] **Yakimenko V. et al** *Electron Beam Phase Space Measurement Using a High-Precision Tomography Technique*. Physical Review Special Topics - Accelerators and Beams, 6, 2003.

# Acknowledgements

---

Writing this thesis would not have been possible without the advice and encouragement of a lot of people.

I am especially grateful to Prof. U.Ratzinger for the way he fulfilled his role as advisor. He made it possible, that this work could successively be completed within the last three years, by showing the right mixture of confidence and review, to motivate and challenge me.

I am deeply indebted to Prof. J.Struckmeier for countless hours of discussion and teaching. Thanks for the continuous commitment during the last two years of my research, and always being open to my questions and thoughts.

I wish to give many thanks to Dr. O.Meusel to provide a positive and open environment within our research group in which a progressive research has become possible. Thanks for providing inspiration, spending a lot of time for discussions, simulations, corrections and ideas.

Since writing a thesis can be very lonely despite of good advice and encouragement of advisors, supervisors, and tutors, I am very grateful to the companionship of all of my colleagues. Namely I wish to give thanks to Christopher Wagner, Kathrin Schulte, Christoph Wiesner, Long-Phi Chau, Rudolf Tiede, Stefan Schmidt, Marcel Lotz, Hannes Dinter, Daniel Noll, Vanessa Senger, Martin Eichler, Gunter Geis, Frank Gollas, Karl Schnell, and Frank Ranostaj for small and great favors, questions, discussions, laughs and cups of coffee. I especially wish to thank C.Wagner for providing measurement and simulation support and his restless technical engagement. I am especially grateful to my family, which backed me in this time of intense work and study, in particular I want to thank my son Don and my daughter Amy to cheer me up and to persuade me to have a rest for the real important things in life.

I wish to thank Dr. A.Bechthold of the Neue Technologien GmbH (NTG) for his excellent collaboration, consulting and service during the development of the rotatable vacuum chamber.

I am grateful to Dr. Müller who did not tire to review linguistic and formal errors, and not sparing me to correct them.





# Curriculum Vitae

---

## personal

Name Hermine Reichau  
Born 04.10.1975  
Place of Birth Gummersbarch

## education

1983 - 1987 GGS Bursten, Bergneustadt  
1987 - 1989 Realschule Bergneustadt  
1989 - 1995 Wüllenwebergymnasium Bergneustadt  
1995 Vocational College of Commerce Gummersbach

## academic development

### diploma studies in computer science

9/2000 - 6/2006 at J.W. Goethe University Frankfurt Main  
main subjects Artificial Intelligence, Graphic Data Processing  
auxiliary subjects Philosophy, Cognitive Linguistics  
23.07.2011 Diplomathesis  
Title *Untersuchung Nicht-Deterministischer Lambda-Kalküle zur Implementierung der Montague-Semantik*  
Supervisor Prof.Dr.Schmidt-Schauss

### research assistant in physics

from 07.2006 Research at Institute of Applied Physics, University Frankfurt  
Contents Statistical Signal Analysis, Data Processing, Mathematical Physics




### doctoral studies in physics




from 02.2007 Admission to doctoral studies in physics  
Title *Fundamentals for Routined Utilization of Tomography in Beam Diagnostics*  
Supervisor Prof.Dr.U.Ratzinger

---






## academic teachers






### mathematics

 Prof.Dr. J.Baumeister  
 Prof.Dr. G.Kersting  
 Prof.Dr. H.Luckhardt




 Prof.Dr. A.Wakolbinger  
 Prof.Dr. C.-P.Schnorr  
 Prof.Dr. M.Sieveking



### computer science

 Prof.Dr. R.Brause  
 Prof.Dr. T.Hagerup  
 Prof.Dr. D.Krömker  
 Prof.Dr. R.Kunz  
 Prof.Dr. R.Mester






 Prof.Dr. M.Schmidt-Schauss  
 Prof.Dr. G.Schnitger  
 Prof.Dr. K.Waldschmidt  
 Prof.Dr. D.Wotschke  
 Prof.Dr. R.Zicari





### philosophy / linguistics

 Prof.Dr. W.Detel  
 Prof.Dr. W.k.Essler  
 Prof.Dr. G.Grewendorf

 Prof.Dr. H.Leuninger  
 Prof.Dr. T.E.Zimmermann

### physics

 Prof.Dr. H.Appelshäuser  
 Prof.Dr. W.Aßmuss  
 Prof.Dr. M.Huth  
 Prof.Dr. A.Lacroix  
 Prof.Dr. U.Ratzinger

 Prof.Dr. H.Roskos  
 Prof.Dr. J.Struckmeier  
 Prof.Dr. R.Tetzlaff  
 Prof.Dr. M.R.Valenti